THE MECHANICS OF CARBON-FOAMS AND DESIGN OF MODULE SUPPORTS FOR THE ATLAS-UPGRADE INNER TRACKER

Koral Toptop

THE MECHANICS OF CARBON-FOAMS AND DESIGN OF MODULE SUPPORTS FOR THE ATLAS-UPGRADE INNER TRACKER

PROEFSCHRIFT

ter verkrijging van
de graad van doctor aan de Universiteit Twente,
op gezag van de rector magnificus
prof.dr. T.T.M. Palstra
volgens besluit van het College voor Promoties
in het openbaar te verdedigen
op donderdag 4 juli 2019 om 16:45 uur

door

Koral Toptop

geboren op 15 december 1988
te Istanbul, Turkije

Dit proefschrift is goedgekeurd door:

de promoter:	Prof. Dr. Ing.	B. van Eijk
de co-promoter:	Dr.	N.P. Hessey

The Mechanics of Carbon-Foams and Design of Module Supports for the ATLAS-Upgrade Inner Tracker
PhD. thesis, University of Twente, Enschede, the Netherlands

Cover design : Atifet Sena Şerifoğlu
Printed by : Gildeprint, Enschede
ISBN : 978-90-365-4326-2
DOI : 10.3990/1.9789036543262

Promotiecommissie:

Voorzitter:	Prof. Dr.	J.L. Herek
Promoter:	Prof. Dr. Ing.	B. van Eijk
Co-promoter:	Dr.	N.P. Hessey
Leden:	Prof. Dr. Ir.	A.H. van den Boogaard
	Prof. Dr. Ir.	H.J.M. ter Brake
	Prof. Dr.	A.P. Colijn
	Prof. Dr.	H.G. Raven
	Dr. Ir.	H.J.M. Geijselaers
	Dr. Ir.	A.A. van der Stelt
	Dr.	F.R. Cadoux

This research was granted and funded by the *European Commission Research Executive Agency* under the FP7 MC ITN "TALENT" (project grant 289161 Training for Career Development in High-Radiation Environment Technologies) and *Stichting voor Fundamenteel Onderzoek der Materie (FOM)*, which is part of the *Nederlande Organisatie voor Wetenschappelijk Onderzoek (NWO)*. The work was carried out at the *Nationaal Instituut voor Subatomaire Fysica (Nikhef)*.

Contents

Introduction

> *Is matter continuous or discontinuous? That is, if you could break apart a piece of chalk as long as you wanted, would you ever reach some ultimate particle beyond which further division was impossible? Or could you keep up that process of division forever? [1]*
>
> *Democritus (c.470-c.380 BC)*

The nature of matter was already questioned in ancient times by Democritus, a Greek philosopher who named the fundamental units the world is made of *atomos*, which means "*indivisible*" in Greek [2]. In doing so, he introduced the first atomic theory of the universe, without any scientific or experimental support. The theory of atoms took more than two millennia to evolve, but would ultimately be proven true by scientists at the end of 19th century.

In the last several decades, scientists have begun asking a new set of questions by scoping the sub-atomic world to discover truths beyond the known physics of the universe. Research at the sub-atomic scale requires the use of advanced experimental mechanisms and measuring tools. Thus, particle accelerators and precise detectors were built to fulfil those needs. A particle accelerator generates particle beams at almost the speed of light; it aligns and focuses beams to bring in collision with a second particle beam. After the collision of high-energy particles, new particles may be produced. Detecting mechanisms are being used to precisely record subsequent events following the collision. Later, recorded data are processed by software to map trajectories of released particles, together with their subsequent decays. Finally, scientists analyse the collected information to solve the mysteries behind matter's behaviour and extend physical models of the universe.

At the Large Hadron Collider (LHC) at CERN, particles collide at the highest energy level ever achieved [3]. The ATLAS detector, one of the detectors residing at the LHC machine, records collision events [4].

Collisions at a center of mass energy at 13 TeV were first recorded in 2015 [3]. The increase in center of mass energy raised the possibility to produce new more massive particles. Detection chance of these rare particles can be increased by collecting more

collisions per unit time, in the other words by increasing data rate i.e. luminosity. Therefore, the LHC will run at higher luminosities. Currently, the LHC is in Run-2 phase; it will shut down in 2019 for improvements. The luminosity after 2021, in Run-3 phase, is expected to be more than two times higher than in Run-2.

Increasing luminosity will introduce higher radiation loads to the detector system than at present, and will be far beyond what the current tracker can stand up to. Radiation will lead to deterioration of the particle tracker performance with time. Future operating conditions require use of far higher radiation tolerant construction. The Inner Detector receives very high radiation loads, which makes it one of the most critical sectors of the ATLAS detector for radiation hardness. Consequently, the ATLAS team has decided to replace the entire Inner Detector, prior to Run-4 [5].

Inner trackers measure charged particle trajectories. They should minimise multiple scattering of the charged particles, photon conversion to electron-positron pairs, and bremsstrahlung from electrons to increase accuracy in reconstruction of particle trajectories. All three are minimised by reducing the fractional radiation length, known as $\%X_0$, of the detectors, supports and services. Low $\%X_0$ is achieved with low atomic number (Z) materials, such as carbon ($Z = 6$), and minimising the amount of all materials used. At the same time, the supports must be stiff to prevent motion which would blur the precision of position measurements, setting a lower limit to the amount of material needed. Furthermore, the detector has to survive more than 10 years in a very high radiation environment. This limits the choice of materials to those that do not deteriorate with the expected radiation dose.

The detectors are held on thermo-mechanical support units known as Petals. In the early part of this development, a new petal design was made by the DESY group [6]. This required studies to verify it will meet the requirements, and to see if further optimisations are possible.

The new detector will operate at low temperature (around $-30^{\circ}\mathrm{C}$) to minimise leakage current in the silicon sensors. The petals cool the modules with evaporative CO_2 flow in a cooling tube surrounded by carbon foam and embedded in the Petal. The thermal contraction of the tube will exert forces on the carbon-foam. There is a risk that these forces will lead to fractures at the tube/foam interface, which would result in deterioration of the thermal performance. Similarly, resistance of the carbon-foam against deformation will result in forces on the tube. This might also fracture the tube, which will cause coolant to leak out and cause complete failure of the detectors. Since preventing mechanical damage is crucial for maintaining thermal properties, there is a particular interest in the fracture mechanics of the graphitic carbon-foam.

Addressing the problems defined above, the first target of research is improving the ATLAS Petal design in terms of its radiation length. The second is verifying mechanical reliability of the tube/foam interface, an essential element of the Petal, regarding structural risks.

This thesis presents a study focusing on the mechanics of the Petal, the tube-foam

structure and graphitic foams. Investigations are primarily based on computational analyses on developed finite element models (FEM). Experimental studies are carried out to confront the predictions made via the models. Overall, this thesis presents technical information to be used in the designs of the support structures in the ATLAS Inner Detector. Another researcher, Afroditi Koutoulaki, also from the Nikhef group, is currently investigating the Petal in terms of thermal properties [7].

The outline of the thesis is as follows.

The LHC accelerator complex at CERN is briefly described in **chapter 1**, along with the ATLAS detector and its innermost sub-detector, the Inner Detector, and a design of the Petal. Rough operation plan of the LHC is presented clarifying the motivation behind the detector upgrade.

Chapter 2 is dedicated to introducing the necessary underlying information regarding materials used in the Petal. Candidate materials for upgrade are presented.

Mechanics of the Petal is investigated and design improvements are introduced in **chapter 3**. A computational FEM was developed based on the Nikhef Petal prototype, and outcomes of structural analyses were verified by experimental measurements. This model was then adapted to the DESY design, which will be used in the ATLAS detector. An analytic model for a simple Petal was developed to compare several materials which are candidates for the design, and used to select the optimal ones. Selections were implemented in the computer model to evaluate overall performance.

Fracture mechanics of graphitic carbon-foams is investigated in **chapter 4**. A series of experiments were performed to study elastic and destructive behaviour in compression and shear modes. Then a computational micro-scale model was developed to reproduce measured compressive behaviour. The outcomes of both measurements and analyses were used to construct a macro-scale continuum model of the foam.

Mechanical reliability of the tube-foam structure is studied in **chapter 5**. A computational model of the structure was developed by using a macro-scale foam model, and used to analyse stresses arising due to thermal contraction of the tube. The results were used to ensure no fractures will occur.

Chapter 6 gives a summary of the main results of this research.

Chapter 1

Tracking at the LHC

CERN, the European Organization for Nuclear Research, is the largest particle physics research center in the world, and the CERN accelerator complex hosts a set of particle accelerators, of which the Large Hadron Collider (LHC) is the world's largest and most powerful particle accelerator and collider. This chapter gives a brief description of the LHC, and the ATLAS detector, which records particle collision events at one collision point of the LHC.

Silicon detectors are used for particle tracking purposes in high energy physics. After the particle collision, a released particle travels through the tracker, losing energy in the silicon detectors. This energy ionizes silicon atoms producing free charges [8]. These charges flow through an electric field between two poles of the diode sensor, and generate detectable signal. Thermo-mechanical support structures (i.e. Petal and Staves) carry the detector modules and position them inside the ATLAS detector.

This chapter presents the fundamental design of the detector support unit (Petal). Key considerations in the design of these units, especially the radiation length of the structure, are described to understand the structural design process. An operation plan of the LHC is presented to indicate future conditions, which have to be taken into consideration when upgrading the ATLAS tracking detector.

1.1 The Large Hadron Collider

The LHC began operation in 2008 and led to the discovery of the Higgs boson in 2012 [11, 12]. Fig. 1.1 illustrates the CERN accelerator complex. First of all, a particle beam passes through the injector chain consisting of a series of accelerators. Each accelerator machine boosts the energy of the particles, and injects a beam into the next accelerator. After subsequent acceleration steps, beams can successfully be injected into the LHC, where proton-proton (p-p), heavy ion-ion (A-A) or proton-ion (p-A) beam collisions take place.

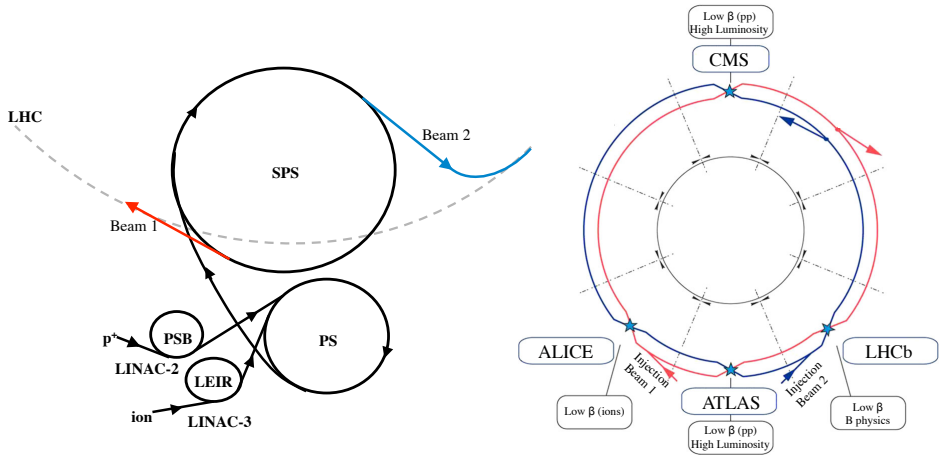

Fig. 1.1: Scheme of machine layout at CERN accelerator complex, the LHC injector complex at left and the main accelerator of the LHC at right. Protons are released and further accelerated by the Linear Accelerator (LINAC-2), Proton Synchrotron Booster (PSB), Proton Synchrotron (PS) and Super Proton Synchrotron (SPS), and injected to the main accelerator LHC at two injection sections (blue and red arrow at left). Two beams circulate in opposite directions and intersect at four points, where the ALICE, ATLAS, CMS and LHCb detectors are (at right). [9, 10]

A particle collision experiment starts with an injection of a beam from the proton source, which is located at one end of the Linear Accelerator 2 (LINAC-2). A simple bottle of hydrogen gas is used as the proton source. The hydrogen atoms are passed through an electrical field, which extracts electrons and leaves the protons. Generated protons have a 90 keV kinetic energy and enter into the LINAC-2, which is the first accelerator of the injector chain system. There the protons reach 50 MeV energy. They are injected into a circular accelerator machine, Proton Synchrotron Booster (PSB), where the energy is increased to 1.4 GeV. The protons pass through the next accelerator Proton Synchrotron (PS) and attain 25 GeV. Then, the beam is injected into the Super Proton Synchrotron (SPS) for a further increase in energy to 450 GeV. [4, 12]

The LHC consists of a 27 km long ring of superconducting magnets, located at a depth of about 175 meters under ground. The magnets contain two vacuum pipes, one for each beam direction. The SPS injects a beam into those two pipes in different circulation directions (at right in fig. 1.1). In the LHC, the protons are accumulated and accelerated to maximum energy, travelling almost at the speed of light. In 2012, the process up till filling the LHC rings with proton beams took around 4 mins, and it took 20 mins to ramp to an energy level of 4 TeV per beam [12]. The vacuum pipes of the LHC have four intersections, where the two counter-circulating proton beams collide. The detectors were constructed in the halls at the collision points to record sub-atomic events occurring after collision. Seven types of experiment, named ALICE, ATLAS, CMS, LHCb, TOTEM, LHCf and MoEDAL are conducted in these collision points [4].

	Nominal	1st Run	2nd Run	3rd Run	4th Run	Units
Period	-	2010-12	2015-18	2021-23	2026-	
Center of Mass Energy (*p-p*)	14	7-8	13-14	14	14	TeV
Average Luminosity	1.0	0.6	1.0	2.2	5.0-7.0	$\times 10^{34}$ cm^{-2}s^{-1}
Integrated Luminosity	80-120	30	150	300	3000	fb^{-1}

Table 1.1: Performance of the LHC. The nominal data is taken from [13, 14], recorded data comes from [14] and expected performance in future is taken from [15, 16]. The LHC is shutdown for maintenance between the runs.

Protons are not the only particles used in the LHC experiments. Heavy ion (*A-A*) collisions can also be tested. In such tests, lead ions coming from a vaporised lead source enter the Linear Accelerator-3 (LINAC 3), which accelerates and injects them into the Low Energy Ion Ring (LEIR) and into the PS. The ions then follow the same route as for the protons.

1.2 Operation Plan of the LHC

The LHC was designed to reach 14 TeV center of mass collision energy at a design luminosity[1] of 10^{34} cm^{-2}s^{-1}. In the LHC, each beam consists of around 2080 bunches of particles, and each bunch containing up to around 1.1×10^{11} protons are separated 25 ns. Around 40 million bunch collisions occur every second. Furthermore, the LHC is also capable of performing heavy ion collisions at up to 5.5 TeV per nucleon pair at 10^{27} cm^{-2}s^{-1} design luminosity. While the collision energy affects the character of subsequent events and the type of emerged particles, the luminosity determines the number of events. [12–14]

During the first run period, the machine successfully ran *p-p* collisions each 50 ns, with 7 and 8 TeV center of mass energy; and 0.36 and 0.77×10^{34} cm^{-2}s^{-1} peak luminosities were reached in 2011 and 2012 [14]. At the end of the first run, the LHC had delivered 30 fb^{-1} integrated luminosity to each of ATLAS and CMS, and underwent a long shutdown for maintenance and upgrade. In the second run, the machine is expected to reach its nominal performance by delivering 150 fb^{-1} integrated luminosity at the end of the run.

Higher integrated luminosity gives more events of interest. This allows rare processes, including production of discovered particles, to be studied. It also allows properties of particles, especially the newly discovered Higgs, to be measured with a greater accuracy. Where no new phenomena are found, it allows more stringent limits to be set on their

[1] The instantaneous luminosity (L) is a commonly used term to describe beam intensity. The integrated luminosity ($\mathscr{L} = \int L dt$) is the total number of interactions per unit cross-section during an operation period. The integrated luminosity is generally used to specify aggregated radiation on detectors and define lifespan of the equipment. A collision process with a cross sectional area of σ will produce events of that process at a rate $L\sigma$.

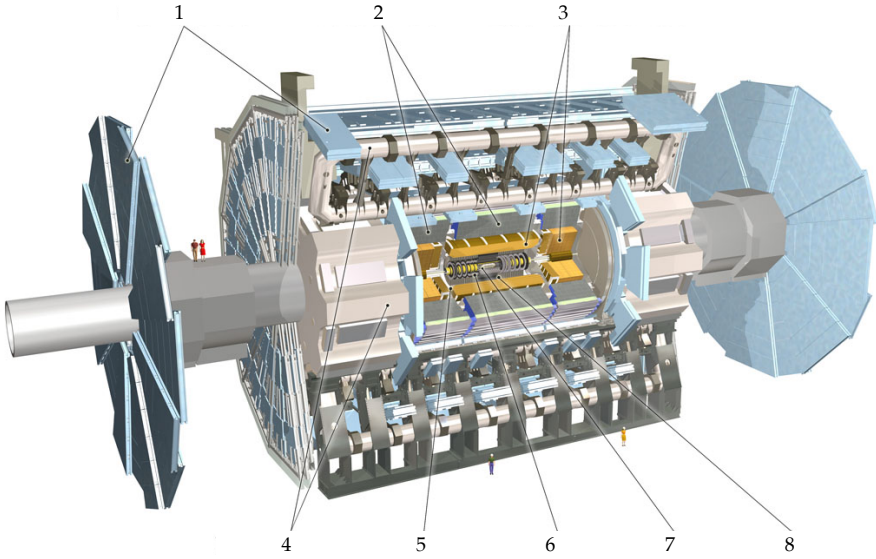

Fig. 1.2: Cut-away view of the ATLAS detector and sub-components. Muon Chamber Detectors (1), Calorimeters (2-3): Tile Calorimeter (2) and Liquid Argon Calorimeter (3), Toroid Magnets (4), Soleniod Magnets (5), Inner Detector (6-8): Semiconductor Tracker (SCT, 6), Pixel Detector (PD, 7), Transition Radiation Tracker (TRT, 8). [14]

existence. For these reasons, the LHC has a long term plan to increase luminosity and eventually deliver at least 3000 fb^{-1} to each of ATLAS and CMS detectors. The machine was planned to operate at ∼2 and ∼5 times nominal luminosity in its third and fourth runs, by delivering integrated luminosity of 300 and 3000 fb^{-1} at the end of each operation period [15, 16]. Table 1.1 indicates recorded LHC performance together with future expectations over the run periods.

1.3 The ATLAS Detector

ATLAS (A Toroidal LHC ApparatuS) is one of the two general-purpose detectors that have been built to record collisions at one station (the other is CMS, Compact Muon Solenoid). The ATLAS detector is 25 m high and 44 m long. It consists of many subsystems, which aim to detect different groups of sub-atomic particles: From the innermost to the outermost layer, these are the Inner Detector, Calorimeter and Muon Spectrometer (fig. 1.2). The Inner Detector tracks charged particles and their decay products by measuring their direction, momentum and charge. The Calorimeter measures the energy a particle loses due to interaction with matter, while it travels through the detector. It is made to completely stop or absorb most of the particles, thus it behaves

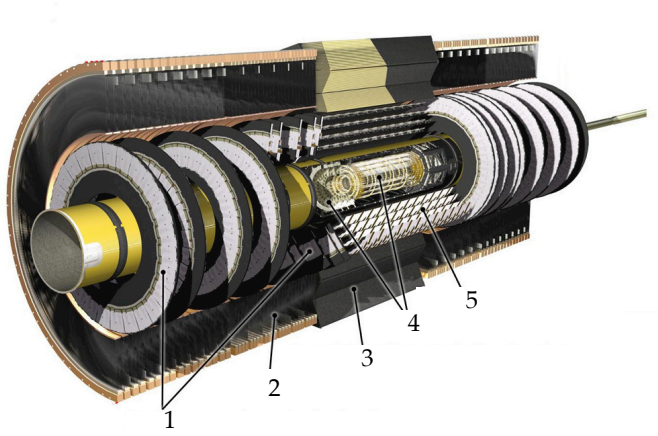

Fig. 1.3: Cut-away view of the Inner Detector (components 6-8 in fig. 1.2) and sub-sections, used in the first run of the LHC. The Pixel Detector (PD, 4), Semiconductor Tracker (SCT): End-cap SCT (1) and Barrel SCT (5), Transition Radiation Tracker (TRT): End-cap TRT (2) and Barrel TRT (3). [14]

as a filter to the outer layers. Only muons (in addition to neutrinos that leave the detector unobserved) can travel through the inner two layers without losing much energy, and the Muon Spectrometer is built to track this group of particles. Magnets are constructed between some sectors containing Inner Detector and Muon Spectrometer to bend the track of charged particles. [17]

When particles hit semiconductor sensors, they can displace atoms from the lattice and cause other damage sites, resulting in higher leakage current and thus increased heat dissipation. This inherently deteriorates measurement performance in long-term use, thereby limiting the detector lifespan. The Inner Detector has the highest track density and thus is exposed to high radiation loads per unit area.

1.4 The Inner Detector

The Inner Detector is 2.1 m in diameter and 7.0 m in length. It consists of three complementary sub-sections, which are from inside to out: the Pixel Detector (PD), Semiconductor Tracker (SCT) and Transition Radiation Tracker (TRT). Each consists of a central "barrel" section, and two "end-cap" sections at the front- and back-ends of the barrel (along the beam line). The sub-components and integrations are shown in fig. 1.3 with a cut-away view of the Inner Detector.

As mentioned, the LHC is planned to run at higher luminosities, requiring detectors

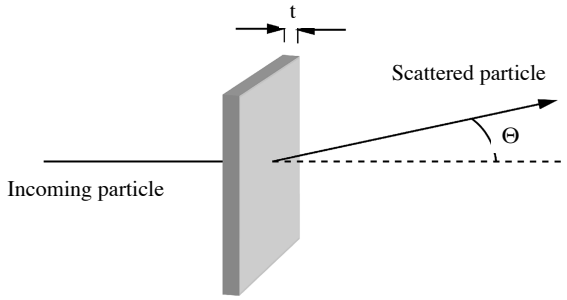

Fig. 1.4: Particle-material interactions. When a charged particle penetrates matter, multiple scattering occurs. The particle interacts with electrons and nuclei of atoms on its pathway, and loses energy and changes direction. Figure is taken from [21].

to be designed to handle extreme radiation conditions. The ATLAS team has decided to design a completely new Inner Detector, called Inner Tracker, ITk [18]. In the new design, additional layers are added to the Pixel Detector for better track seeding. The TRT and SCT are replaced by silicon strip detectors. Similar to the former design, the new pixel and strip detector sections each consist of a barrel and two end-cap parts.

The strip barrels are made of long rectangular panels, called "Staves", assembled in a cylindrical frame horizontally around the beam axis. The strip end-caps are built from disc-shaped modular sub-sections arrayed along the beam axis, with 32 V-slice panels, called "Petals" forming each disc. The petals were assembled in a support frame perpendicular to the beam axis [19, 20].

The Petals carry the detector modules. They are equipped with silicon sensors for particle detection, and chips and electronics to process data. Furthermore, cables are also installed on panels in order to transmit data to the main computer. The panels ease the installation of modules to the tracker. They also provide structural reinforcement to keep them stable at a well defined location, and have an integrated cooling system in the panel core. The panels thus serve as thermo-mechanical support structure for the modules.

1.5 Considerations in Design of ITk Support Structures

When a charged particle penetrates matter, it interacts with electrons and nuclei of atoms, and loses energy. Interaction causes change in the particle direction (i.e. Multiple Scattering, MS), fig. 1.4. Atoms become ionised producing free charge carriers in the semiconductor sensors, generating an electrical signal. However, particle-material interactions negatively affect the precision with which the particle properties can be

measured (energy and momentum). In addition, the radiation loads may cause damage to semiconductor sensors and support structures. Therefore, the detector systems require use of material and structures that minimize the interaction with particles. In this way, measurement errors and radiation loads can be reduced.

A charged particle travelling through a material with thickness t acquires a mean angular deviation Θ as in eq. (1.1), (fig. 1.4) [21]. The descriptions of the terms in the equations below are given in appendix, section A.1.

$$\sqrt{\langle \Theta^2 \rangle} = \frac{k}{P c \beta} (20\,\mathrm{MeV}) \sqrt{\frac{t\rho}{X_0}} \tag{1.1}$$

where X_0 is the radiation length in g/cm^2 and is the amount of material needed for an electron to lose all but $1/e$ of its energy by bremsstrahlung [22].

$$\frac{1}{X_0} \approx 4\alpha r_0^2 Z(1+Z) \left(\frac{N_A}{A_r}\right) \ln\left(\frac{183}{Z^{1/3}}\right) \tag{1.2}$$

In eq. (1.1), the $t\rho/X_0$ term is independent from the particle properties, and comes from the material and structural properties. Scientists define this material and structure dependent term as the fractional radiation length $\%X_0$ (i.e. $\%X_0 = t\rho/X_0 \times 100\%$) in order to characterise the tendency of a structure to interact with charged particles and quantitatively define structure contribution on the angular deviation Θ. Eq. (1.2) was written to formulate $\%X_0$ only by taking the structure dependent parameters into consideration:

$$\%X_0 \approx d \left(\frac{\rho t Z(1+Z)}{A_r}\right) \ln\left(\frac{183}{Z^{1/3}}\right) \tag{1.3}$$

where d is the parameter containing constant factors and terms depending on the particle properties.

The future tracker require use of structures with $\%X_0$ as low as possible to improve measurement quality (i.e. to minimise Θ). This can be achieved by either lowering the number of atoms on particle pathway or the atomic number of each. In other words, the structures have to be thinner (t), and selected material has to be lower in both density (ρ) and atomic number (Z), eq. (1.3). Less material also reduces the production of new charged particles from nuclear interactions, pair production and delta rays, which in turn reduces the amount of radiation damage in the outer layers of the tracker.

Since the detectors and electronics are not very flexible regarding design issues, most of the effort around design configuration and $\%X_0$ optimization is focused on the support panels: the Staves and Petals. However, any new configuration must satisfy structural and thermal performance needs.

As another requirement of measurement quality, a support panel has to keep sensor modules stable in position. This necessitates use of rigid support structure with precise fixation to the support frame. To achieve these design goals, the support panels

are constructed as a sandwich structure, comprised of ultra-high-modulus thin facings glued on both sides of a low-weight core material.

Stability of the modules also requires the support structure to have high level of temperature stability (i.e. use of materials having low thermal expansion coefficient) to not cause any movement due to temperature change. Lifespan of the detectors improves with low running temperature, requiring use of thermally conductive materials. All structures have to have high radiation resistance to sustain their performance without any degradation.

1.6 Overview of the Petal Design

Fig. 1.5 shows a bare petal (i.e. without modules) prototyped by the Nikhef team. The interior structure is shown in fig. 1.6. We now describe the petal, labelling components according to fig. 1.6.

Fig. 1.5: Top view of the bare Petal, LoI design.

The petal is a sandwich structure, made of high-modulus thin facings glued on both sides of a light core material. The facings (1) give rigidity to the petal, while the core (2) material contributes to overall structural stiffness by keeping facings apart[2]. The facings need to be as thin as possible to reduce $\%X_0$. Facings are made of carbon fibre-reinforced composites due to the materials' high specific modulus. Carbon-fibres also have high thermal conductivity in the direction of fibres and support cooling by transporting heat. The petal has to be flat to minimise glue use for module mounting, and keep modules as close as possible to their nominal position. In case of non-flat form, hollows can contain extra glue, deteriorating conductivity at the facing-module interface and design in terms of $\%X_0$ criteria. Prepregs (pre-impregnated fibres) are the most suitable carbon-fibre reinforced composite material for this application, thanks to their optimized weight and mechanical properties (explained in chapter 2).

[2]Eq. (3.22) will provide a better understanding about the contribution of the components to structural behaviour.

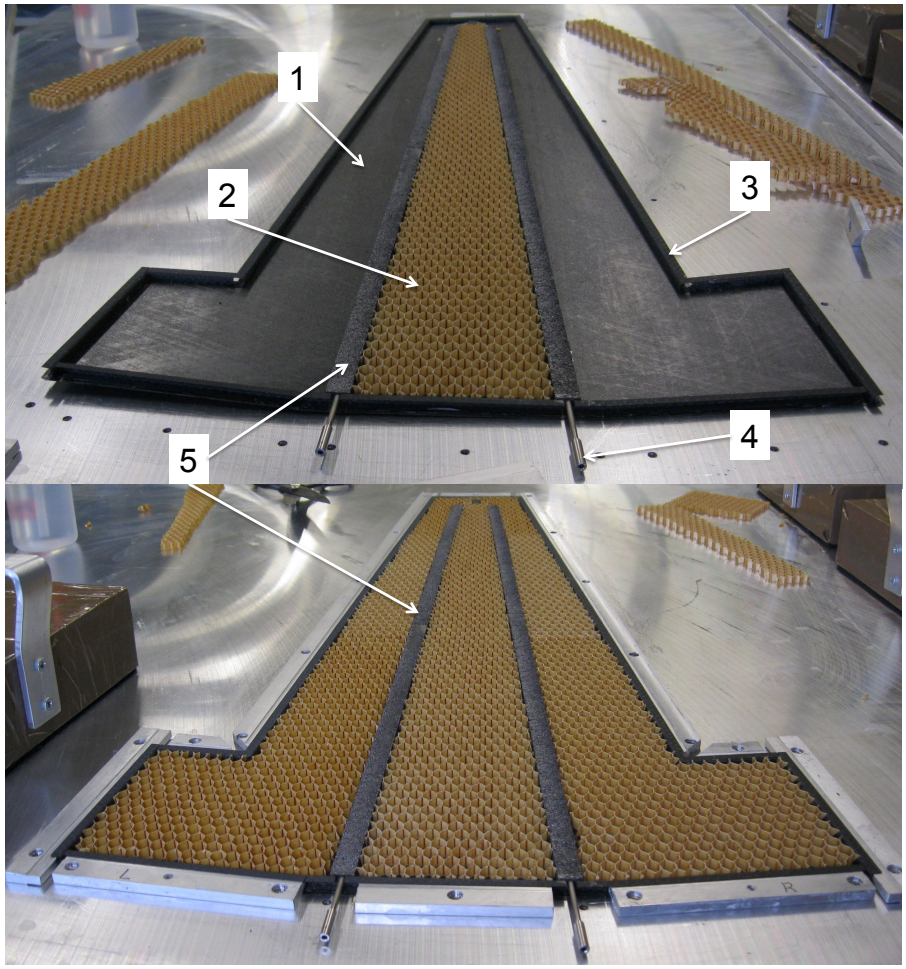

Fig. 1.6: Components of the petal. One facing is removed to show open structure. Components are facing (1), structural honeycomb core (2), close-outs (3), tube (4) and thermal transportation foam core (5). At bottom image, the close-outs are fixed to the work table with aluminium bars.

Honeycomb materials have ultra-low density, and the most suitable materials for use as a core (2). Composite-made honeycomb cores are preferred for their lower density and thermal expansion coefficient compared to metallic honeycombs. Due to the honeycomb cell gaps, facing-to-core bonding strength is low, causing facings to be peeled off easily at the edges. To avoid this, U-shaped ''close-outs'' (3) are bonded around the perimeter of the petal. Other than this, the close-outs do not have any significant effect on overall stiffness. Thanks to strength-to-weight advantage, good adhesion quality and low radiation damage, carbon-fibre reinforced composites are generally preferred to

make the close-outs.

Moreover, over the life of sensors, retaining quality in measurements relies on removing heat from the sensors and chips. This in turn calls for use of an efficient cooling mechanism integrated into the petal. In today's designs, CO_2 coolant fluid is circulated through a tube (4) passing through the petal. The tube that carries the fluid is surrounded by thermally conductive low density carbon foam (5) to transfer heat from the facings. The titanium cooling pipe was designed to be extremely thin (around 0.15 mm in wall thickness) to lower $\%X_0$.

When the system is cooled down, the tube contracts and may break. Therefore, the tube has to be made of a strong material to handle the risks arising from its thin structure. The current design uses titanium alloy. Thermally conductive core material does not contribute to overall stiffness of the petal; however, it has to be structurally strong enough not to sustain damage from the internal loads caused by contraction of the tube. Furthermore, it also has to stand up to loads during the assembly and machining process; mechanical damage would result in deterioration in thermal performance. In addition, material should be radiation resistant. Generally, carbon or graphitic foams are the most convenient material for this purpose thanks to their high specific thermal conductivity (around 7 times higher than copper [23]), while they present moderate mechanical properties. This type of material also exhibits very low thermal expansion [24] and is relatively transparent to radiation.

This thesis deals with two Petal designs. The Nikhef[3] team produced a design known as Petal-LoI, which met the requirements of the design at the time of the Letter of Intent [15]. Later, the ITk layout was improved by the Layout Task Force. The DESY[4] team then made the Petal-LTF design meeting the new requirements. The two designs have slight differences in geometry and materials, but the functional components and the design concepts are similar. Tables 3.1 and 3.2 provide details about properties of both Petal designs.

Fig. 1.7 shows the most recent design, known as the Petal-LTF (Layout Task Force), including modules mounted on. The petal is divided into 6 ring sections; while the first 3 inner sections contain 1 module each, the 3 outer rings host 2 modules placed side by side, giving in total 9 modules on each side. The bus tape layer is glued on the facings to transport power and data. The modules are glued on the bus tape. Each module consists of sensors, hybrids (electronic circuit boards), ASICs (read-out chips) and DC-DC converter [20]. The end of the substructure (EoS) board is used to combine data coming from modules and transmit it to the main computer (not shown in fig. 1.7). Fig. 1.8 shows a cross-sectional view of the petal along with modules. Material selections are still in discussion, and further improvements are still needed.

[3]National Institute for Subatomic Physics, Amsterdam, Netherlands

[4]Deutsches Elektronen-Synchrotron, A Research Center of Helmholtz Association, Hamburg, Germany

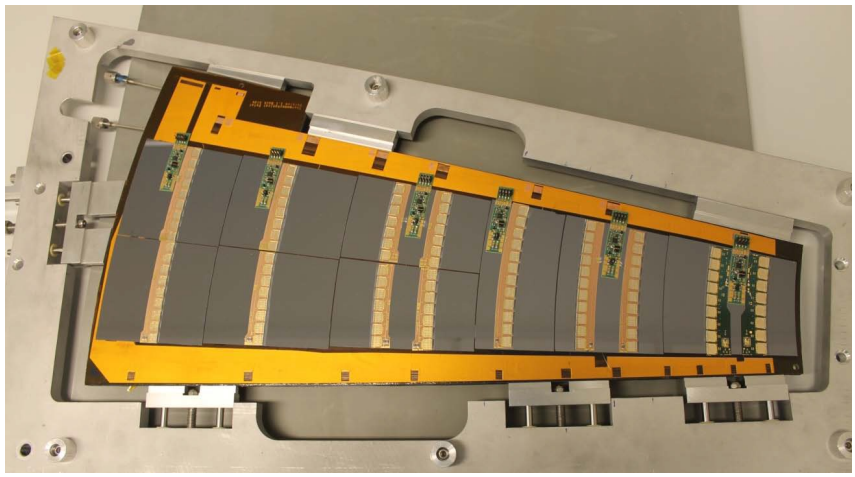

Fig. 1.7: The LTF-Petal with modules mounted on, shown in assembly process [6]. Bus tape (orange), Si-sensors (grey), hybrids (brown) and ASICs (square yellow) are shown. One face of the petal contains 6 rings of modules. The outer 3 rings (left hand side) have 2 sensor modules side by side.

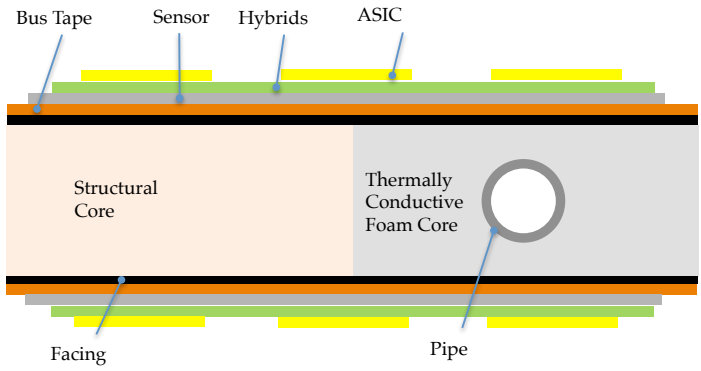

Fig. 1.8: Cross-sectional view of a Petal along with modules. The components are glued to the core. The thin glue layers are not shown in this view.

Chapter 2

Materials for the ATLAS Support Structures

Carbon is a unique element, with a low atomic number (Z) that makes it light-weight and relatively transparent to radiation. Carbon atoms offer strong inter-atomic bonds and can be made crystalline (depending on the engineering process), resulting in good mechanical and thermal properties. These advantages make carbon-based materials an excellent choice for advanced applications, and they are preferentially used in ATLAS support structures.

This chapter presents materials used in the petal design, along with brief background information to clarify main aspects of their physical and mechanical properties. Specifically, these materials are: carbon-fibre reinforced composites, structural honeycomb cores and graphitic carbon-foam cores. Specific products that are used in the current prototype or are candidates for a subsequent design are described. Their effective physical, mechanical and thermal properties are given (summarised in table 2.2), and will be used in the next chapters.

2.1 Carbon-Fibre Reinforced Composites

Broadly defined, the term "composite material" refers to a combination of two or more materials. The properties of the composite depend on the combined behaviour of the constituents, and ideally are better than the properties of the individual constituents used alone. In contrast to metallic alloys, each constituent maintains its own properties.[26] A laminated composite is made through stacking of layers, i.e. plies (fig. 2.1). The carbon-fibre reinforced composites (CFRCs) are one of the most advanced composite materials, offering a high strength-to-weight ratio. As the name suggests, the carbon fibres act as reinforcement, and give rigidity and strength to the composite. As well, this type of material offers excellent heat transfer. However, those contributions are unidirectional, and overall composite properties depend on orientation and quantity of fibres. The matrix binds fibres to transfer load between them and protects against

exterior effects (e.g. corrosion). Also, it affects thermal and mechanical behaviour in the fibre's transverse direction. Since the resin thermal conductivity is very low, the composites also have very low conductivity in the fibre transverse direction. Hence substances are sometimes added into the matrix to improve composite properties. In particular, diamond powders are used to increase thermal conductivity through the matrix. Thermosetting polymer resin such as epoxy is generally used as a binding agent. Generally, fibres with a smaller diameter yield higher strength thanks to having fewer surface defects and more homogeneous micro-structure throughout the cross-section. Moreover, smaller fibres are more flexible, therefore easily formed in a cast [26], and a better choice for producing complex shapes. This type of composite can be produced by following the steps listed below:

- Fibres or "wovens" (the woven form of a fibre) are laid up in a cast. The number of layers and ply directions can be adjusted to obtain the desired stiffness.
- The matrix is prepared by mixing resin with its corresponding hardener material.
- The matrix is presented to fibres in a cast and left for curing.

When the hardener is added into resin, it starts to coalesce with resin molecules and creates cross-link. After a while, the mixture solidifies and forms an almost homogeneous molecular web structure. This process is called curing, and can be achieved at various temperatures depending on resin and hardener type.

For advanced applications, prepregs are developed via the same overall process with a slightly different method. "Prepreg" is a term for pre-impregnated fibres, where the resin is already presented to fibres by the manufacturer and partially cured. Further curing is prevented or slowed by storing in a cold environment. Thus the manufacturer controls fibre and resin content by weight, and imperfections caused by the user are

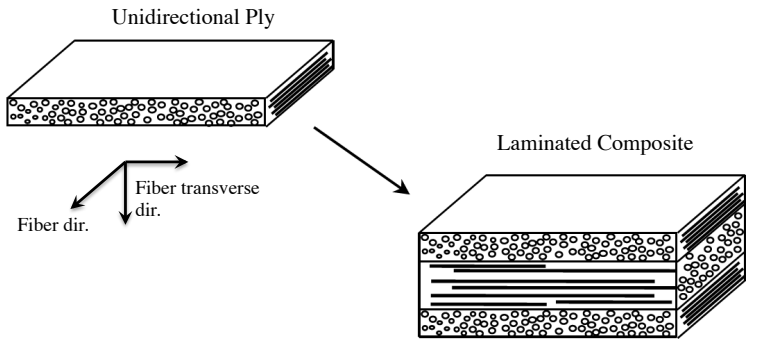

Fig. 2.1: Illustration of a ply and a laminated composite formed of multi-plies. In the example above, the ply consists of parallel randomly distributed fibres. Fibre distribution changes depending on fibre packing method. The image is taken from [25].

prevented. The final product contains minimal resin and is extremely flat thanks to uniform distribution of resin. For the prepregs, resins with high curing temperatures are preferred in order to sustain wet storage. Therefore, prepregs have to be cured with an autoclave (pressure chamber providing elevated temperature). Although there are many advantages of prepreg, it is only available in a flat form, and is thus not applicable to be used with all geometries.

Carbon fibres can yield a very broad range of properties, which are highly dependent on the fabrication technique used. The carbon fibres are derived from precursors through various heat treatment processes (e.g. oxidative stabilization, carbonization and graphitization). Mechanical properties of the end fibre product depend on the type of precursor, conditions during the heat treatment (e.g. rate of temperature increase and duration) and other processing steps such as stretching and surface treatment [27, 28]. Polyacrylonitrile (PAN) fibres are the most common precursor used in the fabrication of carbon fibres. PAN-based carbon fibre can exhibit tensile modulus from 230 up to 580 GPa, along with strength varying from 0.38 to 7.00 GPa [28, 29]. Carbon fibres made of mesophase-pitch precursor can yield tensile modulus between 170 and 960 GPa, along with strength between 1.38 and 3.00 GPa [28].

By taking the typical mechanical values for CFRC reported by Hexcel Inc. [30] as an example, the compressive strength in the fiber direction is about 65 % of the tensile strength for the high and intermediate modulus carbon-fiber made unidirectional prepregs with epoxy resin. For the same prepreg systems, the in-plane shear strength is 4-5 % of the tensile strength. For $0/90^\circ$ fabric prepregs, the compressive strength is about 88 %, and the in-plane shear strength is about 9 % of the tensile strength.

CFRC properties are affected by temperature change. Low temperature effects on unidirectional carbon-fiber/epoxy-resin composites have been studied in [31]. It is shown that the Young's modulus in the fiber direction increases when the temperature is decreased to $-50^\circ\mathrm{C}$, while the tensile strength decreases about 7 %. The decrease in strength is due to thermal expansion mismatch between fibre and resin[5], which induces residual stresses at the fiber-matrix interface. This causes micro-cracks and interface weakening, and fiber debonds from the matrix [31, 33]. Furthermore the matrix becomes more brittle.

In [33], low temperature effects on quasi-isotropic $(+45/-45/0/90^\circ)$ and cross-ply $(0/90^\circ)$ carbon-fiber/epoxy laminates have been investigated. The studies showed that the temperature drop from ambient to $-60^\circ\mathrm{C}$ did not have a significant affect on composite elastic modulus, which remained almost unaffected. The tensile strengths dropped about 25 % and 5 % for quasi-isotropic and cross-ply laminates. This difference comes from how much the matrix and the fiber dominates the measured response of the composite: there are more plies with off-axis orientation in the quasi-isotropic laminate, and the matrix has more effect on the mechanical properties in the loading direction.

[5]Some example numbers for the thermal expansion coefficients are: about 70 ppm/K for epoxy resin [32] and about -1 ppm/K for carbon fiber.

In [34], damping properties of composite beams made of graphite fiber and epoxy resin have been characterized by measuring the damping loss factor[6]. The composite beams were made of unidirectional plies either only longitudinally or only transversely laid-up in the beam axis. The reported measured damping loss factor is 1.7-2.9 $\times 10^{-3}$ for the beam made of longitudinal plies, and 6.6-14.7 $\times 10^{-3}$ for the beam made of transverse plies. The studies showed that the damping of the composite is higher in the fiber transverse direction. In another study [37], the damping loss factor of the composite is modelled based on the fiber orientation, and the model suggests that the highest damping properties are obtained with fiber aligned with angle above 30°, and the maximum is obtained at 45°. The loss factor quantities given above lie in the medium-damping range according to tabular data given in [35] summarizing loss factors for many other types of materials e.g. metals and ceramics.

2.2 Structural Honeycomb Cores

Honeycomb cores make use of a cell structure as shown in fig. 2.2, thus minimizing the weight of the structure. This type of core can be based on either metal or composite sheets. Composite offers a higher stiffness-to-weight ratio, better gluing properties which make core-to-skin adhesion stiffer, and lower fractional radiation length. All these properties make composite honeycombs an excellent choice.

Firstly, chopped fibre or woven fibre sheets are laid up one on top of the other. A thermosetting adhesive is used to bond these sheets at the nodes. Another sheet is laid

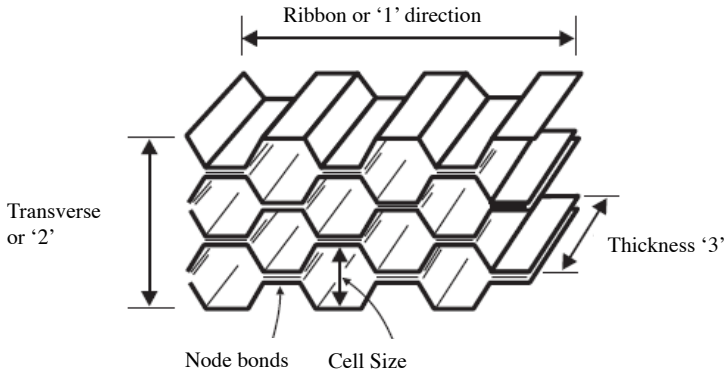

Fig. 2.2: Hexagonal cell honeycomb and material directions.[38]

[6]The damping loss factor η is one of the measures to characterize the damping properties of a structure. $\eta = tan(\phi)$, where ϕ is the loss angle i.e. lag of strain behind stress [35]. The loss angle can be related to the damping ratio ζ with the following equation [36]: $tan(\phi/2) = \zeta/\sqrt{1-\zeta^2}$. For reported loss factor quantities above, $\eta \approx 2\zeta$.

on and bonded at different nodal locations. This process continues until enough layers have been added. Then all sheets are pulled up in the lay-up direction and a hexagonal cell structure is formed. Finally, the block is dipped into resin and cured. Slices are cut in desired thickness from the large block. The distance between the nodes in the pull-up direction gives the cell size. This process can produce a hexagonal cell network with a wide range of cell sizes, thicknesses and densities. The final structure can also have different cell shapes, such as rectangular. The fibres have to be reasonably flexible to form hexagonal structures. Fig. 2.2 illustrates hexagonal cell honeycomb by indicating ribbon (1), transverse (2) and thickness (3) directions of the panel. The lay-up or pull-up direction is in the transverse ribbon direction.

Since the cell gaps are effective in the ribbon and transverse direction, this type of core does not have any axial rigidity in the same directions ($E_1 \approx E_2 \approx 0$). Therefore, its shear properties (i.e. G_{13} and G_{23}) have more effect on the structural behaviour in these directions. The core has reasonably high compression modulus in the thickness direction (E_3), so it keeps facings apart without any crushing under ideal use. Honeycomb core has a very low shear modulus in the in-plane direction ($G_{12} \approx 0$).[38] The Poisson's ratios in the thickness direction are very close to zero ($\nu_{13} \approx \nu_{23} \approx 0$) [39]. The in-plane Poisson's ratios under loading in the thickness direction are very similar ($\nu_{31} \approx \nu_{32}$), and they are about 0.33 [39]. They can have different values based on orientation of lay-ups within the cell walls. The other in-plane Poisson's ratio (ν_{12}) is very sensitive to cell geometry, is usually around one, and can take values up to three (see fig. 1 in [40]). Mechanical behaviour of the honeycomb core depends on type of fibres and resin, number of cells per unit area and cell wall thickness.

2.3 Carbon and Graphitic Foams

Graphitic carbon foam is an emerging material with a very high thermal conductivity to density ratio that is approximately seven times higher than copper [23]. This raises the possibility to make ultra-light and efficient thermal management systems. Highly-aligned graphitised-carbon base material (with 800-1900 W/m·K thermal conductivity) [41] brings high bulk thermal-conductivity to graphitic foams (135-245 W/m·K) [23, 24], while the porous structure reduces density. Furthermore, bulk material exhibits very low thermal expansion [24], is transparent to radiation thanks to having low atomic number, and has high modulus-to-density ratio [42] compared to other foams.

2.3.1 History and Fabrication

Carbon-foam development started in the late 1960s, in the form of carbonization of existing thermosetting organic polymer foams with a simple heat treatment. The foam obtained via this technique is called reticulated vitreous carbon (RVC) foam (fig. 2.3.a). The base foams are usually from polyurethane, polyester or phenolics. The resultant

bulk material is an excellent thermal insulator, and has uniform cell size and intermediate mechanical strength [43]. The very first graphitic foams were obtained by coating the RVC foam with graphite powder to improve final foam properties. Recently, this process has been improved with a new technique called chemical vapor decomposition (CVD), used to place pyrolytic graphite on the ligaments [44] (fig. 2.3.b). Furthermore, RVC foams were coated via the same process to produce a foam from alternating compositions such as refractory metals (e.g. niobium, tungsten, tantalum) and their ceramic compounds (e.g. oxides, nitrides, silicides) [45]. While the skeleton structure of the base foam offers a highly porous structure, the final density and behaviour of the substance is determined by the coating composition and the thickness.[23]

The graphitic RVC foam made via the CVD process is commercialised by Ultramet Corp. under the tradename Ultrafoam® [23]. Allcomp Inc. also manufactures a similar type of foam [46]. Energy Research and Generation Inc. (ERG) produces RVC foam via a similar coating process and has commercialised their product under the tradename Duocel® [47].

In the early 1990s, carbon foams also have begun to be fabricated from alternative low-cost thermoplastic precursors such as coal, coal solvent extracts, coal-derived pitches and petroleum-derived pitches. Synthetic petroleum-derived pitches are obtained from the residues of petroleum cracking. Since this pitch precursor is isotropic in nature, the oxidative stabilization process results in a non-graphitizable structure (fig. 2.3.e). In another method developed at West Virginia University and commercialised by Touchstone Research Lab, pitches are extracted from bituminous coal via various processes and used to produce carbon foam. The foam is then subjected to heat treatment for graphitization; however, the final structure is only partially graphitic, containing small crystalline regions dispersed among non-crystalline regions (fig. 2.3.d). The resultant foams from pitches and coal extracts (fig. 2.3.c) have high strength but low thermal conductivity due to their non-graphitic structure. These foams are used as thermal insulator or filters for corrosive products.[23]

Alternatively, the same mesophase-pitch precursors used to produce high-modulus carbon fibres have been used to produce foams [23], resulting in anisotropic properties with moderate strength and high thermal conductivity.

The most commonly used mesophase pitches are Mitsubishi AR and Conoco pitches. There are several ways to produce carbon foam from a mesophase-pitch precursor. The first is a traditional blowing technique. The mesophase is melted in a vessel and saturated with a blowing agent. Next, a sudden pressure drop causes the blowing agent gases to form foam. The foam is then stabilized with oxygen at an elevated temperature to prevent remelting during the carbonization and graphitization steps. This technique has been licensed by MER Corporation.[23]

Another method has been developed at Oak Ridge National Laboratory (ORNL) and licensed by Poco Graphite Inc. Process starts with heating mesophase pitch to 50°C above its softening point in an oxygen-free environment under high pressure. Once liquified,

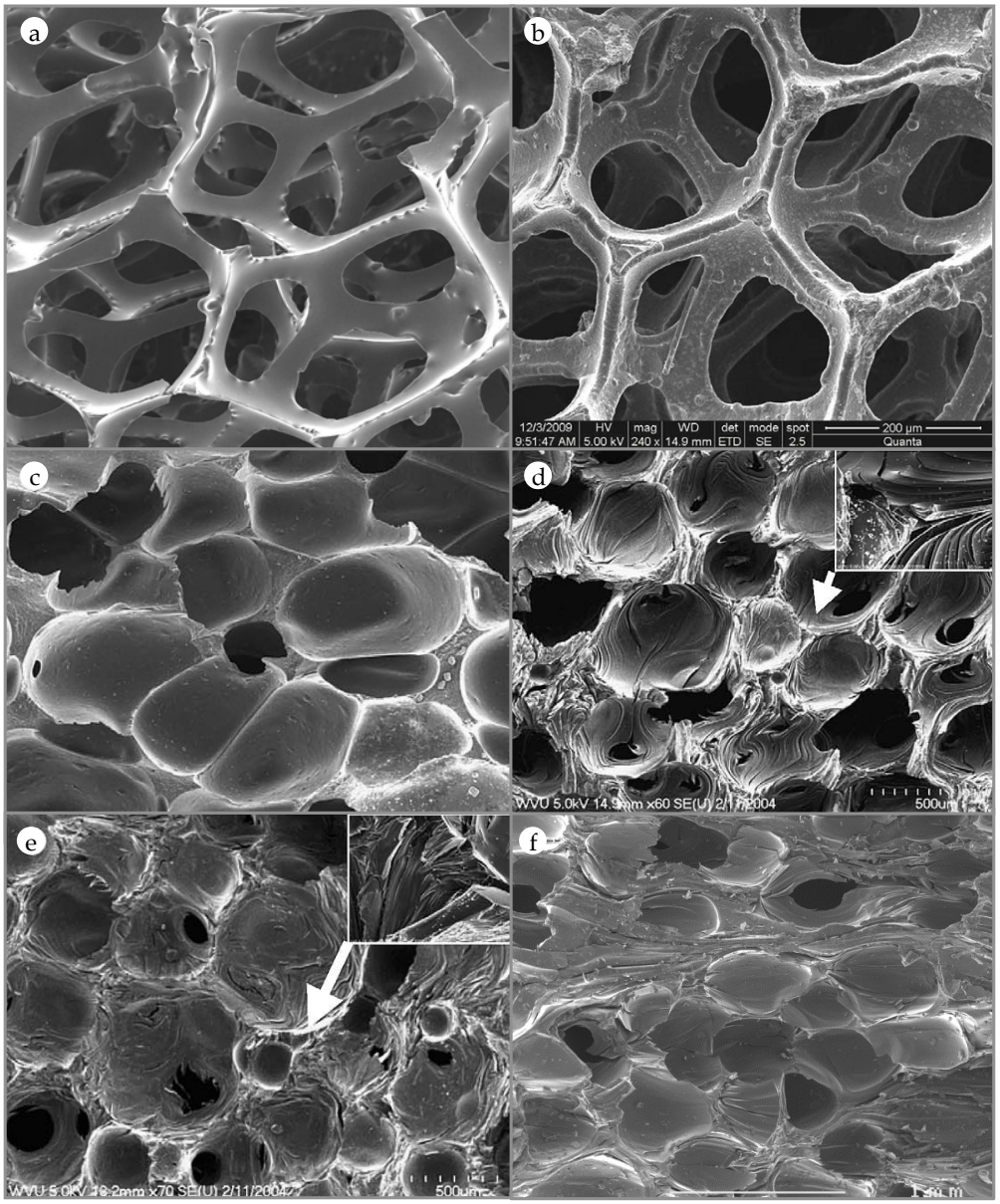

Fig. 2.3: SEM images of carbon and graphitic foams from various precursors. RVC foam (a), RVC foam coated with pyrolytic graphite via CVD (b) and foams made of coal solvent-extracts (c), coal tar pitch (d), petroleum pitch (e) and mesophase-pitch (f), images were taken from [43, 45, 46, 48]. RVC, graphite-coated RVC and mesophase-pitch based foams were produced by ERG, Allcomp and PocoGraphite Inc., respectively.

the mesogens are randomly oriented. Further raising the furnace temperature converts the volatile components of the pitch into gas. This forms bubbles which float upwards, aligning mesogens vertically. Evaporation of low molecular mass components leaves behind an increasingly higher viscosity material. Simultaneously, the mesogens start to polymerise and crosslink. Increasing viscosity tends to capture bubbles in place and the upward flow in a viscous liquid leads to elongated bubbles. If the gas fraction exceeds a certain level, these bubbles start to interconnect and create an open-cell foam. The temperature is further raised until the foamed mesophase sufficiently cross-links and has high viscosity, thus the foam turns into an infusible structure. Next the foam is carbonised by heating between 600 and 1000°C to yield a pure carbon foam. Finally, it is graphitised with heat treatment above 2800°C . The final product is an open cell foam with an interconnected network of graphitic ligaments (fig. 2.3.f). This process is free of oxidative stabilization step used in the fabrication of carbon-foams made by MER Co. and carbon-fibres. This allows much larger mesophase crystals than in carbon fibres, which after graphitization gives much higher thermal conductivity in the foam ligaments than in carbon fibres.[23, 44]

Thanks to their highly graphitic structure, these foams are classified as graphitic foam and have been reported as having the highest thermal conductivity among all carbon-based foams. Recently, thermal conductivity has been improved up to 245 W/m·K . By combining thermal performance with a porous structure, the latest generation of foams presents up to approximately 300 $(W/m \cdot K)/(g/cm^3)$ specific thermal conductivity (i.e. thermal conductivity to density ratio). This is around 7 times higher than pure copper and 15 times higher than the copper foam with similar relative density [24, 44].

Fig. 2.3 illustrates the structure of the foams produced from various precursors with images recorded with scanning electron microscopy (SEM). Table 2.1 lists bulk properties of various carbon foams in comparison with thermal conductor or structural core metallic and ceramic foams.

2.3.2 Micro-Structure

Mesophase-Pitch Based Graphitic Foam (Poco-HTC)

The precursor and processing details affect the internal structure of the end product, which in turn determines the bulk properties. The structure of a graphitic foam produced from mesophase pitch is illustrated with scanning electron microscopy records given in figures 1 and 2 in [48] (attached in page 155) . Poco-HTC® foam sample produced by PocoGraphite Inc. was used for capturing these images. This figure highlights what the terms ligaments, junctions, cell-openings (pores), micro-cracks on walls and around cell-openings, and layer-spacings around folded layers refer to. Due to the foaming process, the resultant material has bubbles elongated in the vertical (out-of-plane) direction.

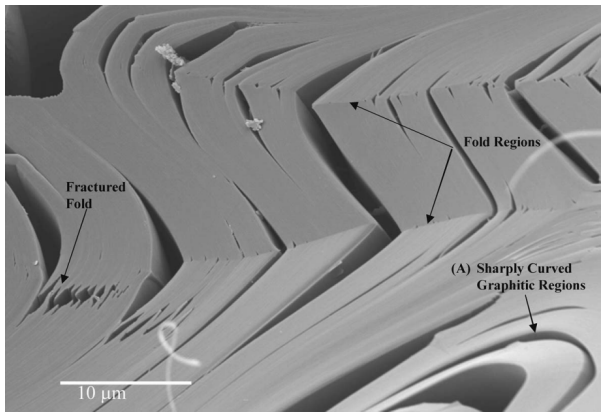

Fig. 2.4: SEM image illustrating graphitic planes within the junction region, containing large number of cleavages, taken from [44].

PocoHTC consist of highly graphitic material. The cell walls at mid-height of the bubble have graphite planes parallel to the bubble walls, and these planes are perfectly compacted. Where these planes meet at the top and bottom of the bubble (junctions), the graphite structure folds and has many micro-defects. Figure 2 in [48] (attached in page 155) shows that the molecular layers are much less well aligned at junctions, and containing cleavages between planes of graphite. These plane separations are illustrated in fig. 2.4 with higher magnification. It was reported in [44] that higher graphitization rate exhibits micro-cracks as separation of the graphitic layers. In contrast, lowering the graphitization rate will allow layers to relieve stress and reduce the cracks. These micro-defects are possibly caused by the thermal expansion mismatch between in and out-of-plane directions of graphitic layers in the structure [43]. These layer-spacings run parallel to the planes of graphite, and affect neither crystal length nor thermal conductivity. Besides, the folded sectors may lead graphitic planes to fracture and limit crystal size.

There are also cracks and defects in the cell-walls probably caused by thermal stresses arising during the heat treatment process. These cracks occur at the boundaries of the planes. However, wall cracks are much less than the micro-defects at the junctions.

If the gaseous volume is large enough, the bubbles join at openings in the cell walls, making an open-cell foam. At formation these openings are smooth and circular. However, later heat treatments can lead to fracture and micro-cracks at cell openings.

Graphite Coated RVC Foam (Allcomp)

The micro-structure of pyrolytic graphite-coated RVC foam is illustrated in fig. 2.5 by using SEM images of Allcomp foam. As can be clearly seen, the RVC structure shows a strut type network instead of the cell-wall formation seen in Poco-HTC. Thus it exhibits very high porosity. Since the graphitic layer is obtained via coating, it shows

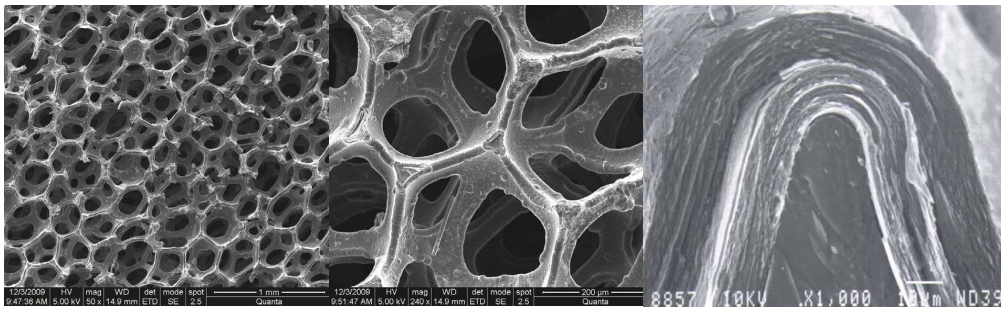

Fig. 2.5: SEM image illustrating micro-structure of Allcomp, pyrolytic graphite-coated RVC foam. Macro-, meso- and micro-scale views appear respectively from left to right. [46]

more continuous structure and contains less defects than mesophase pitch-based foams. However, the coating thickness limits the amount of graphitic structure contained.

2.3.3 Properties

The resultant bulk properties of carbon and graphitic foams vary in a wide range. They can be thermally conductive or insulating, and structurally strong or weak. The precursor and processing conditions have a huge impact on the bulk properties, thus determining the purpose and uses of the foam.

While the RVC foams offer the highest porosity i.e. lowest density, they have significantly lower bulk thermal properties. The isotropic precursors (e.g. petroleum-derived pitches) give ligaments with non-graphitic structure, resulting in high strength and low thermal conductivity. The anisotropic pitch precursors (e.g. mesophase pitches) create foam with anisotropic properties along with highly graphitic ligaments, presenting excellent thermal and electrical conductivity with intermediate mechanical strength.

The heat treatment increases crystal size, thereby increasing thermal conductivity. As stated above, heat treatment and graphitization rate can lead to micro-defects, which have a major impact on bulk material properties as compared to what would result from perfect graphite. Since the layer-spacings and cracks are possibly caused by the thermal expansion difference of graphitic planes, this is more likely to happen in foams made by anisotropic pitch precursors. Those defects in turn weaken the foam mechanically; however, they are not expected to reduce thermal transportation [52]. In contrast, folded sectors and fracture due to sharp folds result in reduction in both thermal and mechanical properties. Probably most of the thermal resistance of the bulk material is due to resistance at the junctions [44]. Consequently, when the structure becomes more graphitic, it has larger crystal sizes, making it more thermally and electrically conducive. Conversely, it becomes structurally weaker due to micro-defects.

Manufacturer and Foam -	Precursor and Type -	Average Bulk Density g/cm^3	Relative Density -	Compressive Strength MPa	Compressive Modulus MPa	Thermal Conductivity W/(m.K)	Ref.
Carbon Foams							
ERG - Duocel®	RVC	0.049	%3	0.48	62	0.050	[23, 47]
Ultramet - Ultrafoam®	RVC	0.042	-	0.76	-	0.085	[23, 45]
Touchstone - CFOAM® 30	Coal-derived Pitch	0.48	-	22.10	830	0.30	[49]
-	Petroleum Pitch	0.34	%17	3.90	-	-	[43]
Graphitic Foams							
MER	Mesophase Pitch	0.62	-	7.00	-	210	[45]
ORNL	Mesophase Pitch	0.57	%27	2.10	144	180	[23, 44]
PocoGraphite - Pocofoam®	Mesophase Pitch	0.61	%27	2.66	135	182	[23]
PocoGraphite - PocoHTC	Mesophase Pitch	0.90	%39	5.90	111*	245	[23, 24]
Allcomp - K9-130 ppi	RVC & CVD coating	0.25	%12$^\bullet$	2.17	380	35	[50]
Other Foams							
ERG - Duocel®	Aluminum foam	0.22	%8	2.53	103	5.8	[51]
ERG - Duocel®	Copper foam	0.72	%8	0.90	736	10.1	[51]
-	Copper foam	2.24	%25	-	-	45	[44]
ERG - Duocel®	SiC Ceramic Foam	0.26	%8	1.38	2760	5.28*	[51]

Table 2.1: Properties of various carbon and graphitic foams in comparison with metallic and ceramic foams. 'ppi' refers to 'pores per linear inch'. Strengths, moduli and conductivities are given in the out-of-plane directions of the foams. $^\bullet$ is estimated by scaling the foam bulk density with a perfect graphite density. Since RVC skeleton is not graphitic, the actual relative density is slightly larger than the evaluated. * is taken from measurements performed in next chapters. * is for temperature dependent value and given at 250°C.

In addition, the high porosity foams tend to have more micro-defects due to thinner wall structure [52]. Moreover, the melting point and viscosity of melted precursor also affect the bulk properties of the substance. The low viscous domain will allow mesogens to flow and re-orient easily. This in turn gives better alignment of mesogens at ligament and cell-walls, resulting in improved thermal and mechanical properties [52]. It is stated in [43] that the precursor with the higher fluidity generates the stronger foam. Also, a melted precursor with low viscosity results in smaller pore size; thus it gives denser foam.

Both the elongation of bubbles and the alignment of graphite planes along the bubble walls lead to anisotropic behaviour of the bulk material. Note that the micro-cracks tend to be in the out-of-plane direction, also contributing to anisotropy in foams.

2.4 Products for Use in the Petal

Effective properties of the products and their constituents mentioned in this section are summarised in table 2.2.

2.4.1 Carbon-Fibre Composites

K13D2U-RS3 Unidirectional Prepreg

Unidirectional (UD) refers to a prepreg that contains fibres oriented only in one direction (fig. 2.1). The left and right side of the product designation specify the fibre and resin. According to the supplier (TenCate Co.), the prepreg has 80 g/m^2 fibre areal weight and 29 % resin content by weight. This gives 63 μm thick single ply. K13D2U is a coal-tar pitch-based carbon-fibre. Thanks to its carbon content of over 99 % and high-graphitic structure, it is one of the highest modulus carbon fibres (935 GPa). It has 2.2 g/cm^3 density [53], very close to the compacted graphite density reported by Klett et al. in [44]. RS-3, toughened cyanate ester resin, has epoxy-like processing at 177°C curing temperature [54]. It has low modulus loss after radiation, making it an excellent resin choice in ATLAS applications. Due to resin and fibre type combination, this prepreg is also called cyanate graphite prepreg. The prepreg has longitudinal tensile strength of 2.2 GPa reported by the ALICE group [55].

K13C2U-EX1515 Unidirectional Prepreg

K13C2U is a coal-tar pitch based carbon-fibre like K13D2U and offers similar mechanical properties, with just a slight difference [53]. EX-1515 is toughened cyanate ester resin, and has high radiation resistance and optimal mechanical properties. It has a curing temperature between 107 and 121°C with 1.17 g/cm^3 density [56]. The prepreg

has 45 g/m^2 fibre areal weight, giving lower stiffness and ply thickness (around 50 μm) compared to K13D2U-RS3 prepreg. However, the ply thickness is not as low as expected due to higher resin content. This could be reduced using absorbent peel ply during curing if desired.

M55J Carbon-Fibre Bidirectional Woven

Bidirectional woven is practically equivalent to two plies of fibres oriented in the 0°/90° directions. Due to the friction between transversely aligned fibres, the overall behaviour shows a slight difference to the 0°/90° layer model. M55J carbon fibres are based on PAN (polyacrylonitrile) precursor [57]. The ultimate strain is 0.8%, two times higher than the coal-tar pitch-based fibre K13D2U. It has 540 GPa tensile modulus and 1.91 g/cm^3 density [29].

2.4.2 Honeycomb Cores

Goodfellow Nomex

Nomex® is the brand name of a series of meta-aramid fibre (polymetaphenylene isophthalamide, an aromatic polymer) based honeycombs. The fibres are bonded with phenolic resin. The product with the code AR312810 was supplied by Goodfellow, it has 0.024 g/cm^3 core density, 6 mm cell size and 0.05 mm wall thickness. The shear moduli are 25 and 14 MPa in the ribbon and transverse directions. [58]

Plascore Kevlar N636

PK2 Kevlar® N636 is a honeycomb core made by impregnating para-aramid fibre papers with phenolic resin. It has higher shear moduli than the equivalent density of Nomex® honeycomb cores; therefore it is a strong candidate to replace the structural core for the new petal design. PK2-3/16-2.0, supplied by Plascore Inc., was considered as a sample product from Kevlar class cores. It has 0.032 g/cm^3 density and 4.76 mm cell size. The shear moduli are 70 and 42 MPa in the ribbon and transverse directions. [59]

Ultracor Carbon-Fibre

Ultracor honeycomb core with UCF-TBD-1/4-3.0 product designation is an alternative material choice for the new design. It is made of YSH50A-75 pitch-based carbon-fibre fabrics impregnated with EX-1515 cyanate ester resin. It has 0.048 g/cm^3 density, and

the shear moduli[7] are 228 and 119 MPa in the ribbon and transverse directions. Other mechanical properties of the honeycombs are given in table 2.2.

2.4.3 Thermal Management Foam Cores

Poco-HTC

Poco-HTC® is a graphitic foam made from mesophase-pitch precursors. It offers one of the highest thermal conductivities and light structure among the available graphitic foams in the market. Therefore, it is used in the ATLAS applications as a thermal transportation element. The bulk foam exhibits anisotropic properties; therefore the final thermal behaviour of the structure is highly dependent on the foam direction. It has 245 and 70 W/m·K thermal conductivity in the out-of-plane and in-plane directions. It has 0.9 g/cm^3 density with 61 % total porosity, i.e. fraction of empty volume to bulk volume. Open porosity, i.e. fraction of interconnected empty volume to total empty volume, is 95 %. [24]

Allcomp

Allcomp graphitic foam is made by coating and annealing RVC foam with pyrolytic graphite via CVD technique. The final bulk foam is isotropic and has high-modulus ligaments. Allcomp K9-130 ppi foam along with 0.25 g/cm^3 density has 35 W/m·K thermal conductivity.[46] It has 2.17 MPa compressive strength and 380 MPa compressive modulus [50]. It exhibits one of the highest porosities among available graphitic foams. The porosity is around 88% [8]. Other properties are listed in table 2.2.

2.4.4 Adhesives

Araldite AY 103-1 / HY-991

This is a low-viscosity two-component adhesive system obtained by mixing Araldite® AY 103-1 epoxy resin and HY-991 hardener. It can bond a wide variety of materials and cures at room temperature. The final properties depend on the mixing ratio of the components, curing temperature and duration. According to the supplier tests, adhesive with 2/1 volumetric mixing ratio (resin-to-hardener vol.) and cured at 40°C during 16 hours has the following properties at ambient temperature: 1.0 g/cm^3 density, 1.7 GPa

[7] This material is a special order from the DESY group; therefore online data presenting material properties were not found. Mechanical properties were taken from another similar carbon fibre honeycomb core UCF-304-3/8-2.0.[60]

[8] This is estimated by scaling the foam density with a perfect graphite density. Since RVC base skeleton is not graphitic, the actual porosity is slightly lower than the evaluated porosity.

Young's modulus, 38 MPa tensile strength, 0.4 GPa shear modulus and 15 MPa lap shear strength. [61]

Hysol EA9396

Hysol® EA9396 is supplied by Henkel Co. and is a low viscosity epoxy adhesive for structural applications. It is a two-component mixture with a 100/30 optimal mix ratio by weight, which is practically equivalent to an 84/30 volumetric mix ratio. The final resin mix has 1.14 g/cm^3 density. The nominal mechanical performance can be achieved by curing for 3 to 5 days at 25°C . According to the supplier datasheet, it has 2.75 GPa tensile modulus, 35.2 MPa tensile strength, 3.4% breaking elongation and 24.1 MPa tensile lap shear strength after optimal curing conditions. [62]

DC SE4445 CV

Dow Corning® SE4445 CV is a moderate-viscosity two-component thermally conductive silicon (polydimethylsiloxane) gel. This gel is generally used for thermal applications such as potting electronic modules to a base or gap-filling between heat sources and sinks. The optimal mixing ratio is 1/1, and the final mixture has 2.36 specific gravity after curing. It exhibits 1.34 W/m·K thermal conductivity and low modulus after curing. Since it is used for thermal systems, the structural properties are not given.[63]

2.4.5 Other Materials

T40 Titanium Alloy

T40 is an α-type pure titanium alloy. It has 4.51 g/cm^3 density, 115 GPa Young's modulus, 460 MPa ultimate tensile strength and 350 MPa yield strength at ambient temperature [64, 65]. The tube made of this alloy will operate at −30°C . Therefore, material properties also has to be investigated for this temperature.

PEEK

PEEK (Polyether-ether ketone) is a semi-crystalline organic thermoplastic polymer used in engineering applications as a stiff and strong plastic. It also has a low density, which makes it a good choice for low-weight and rigid structures. It resists against radiation damage and chemicals. It can contain reinforcement substances such as glass or carbon to improve mechanical properties. Unreinforced PEEK has 1.32 g/cm^3 density, 3.6 GPa Young's modulus and 100 MPa tensile strength. [66]

PAI

PAI (Polyamide-imide) is an amorphous organic thermoplastic polymer, with better adhesion properties, lower thermal expansion coefficient and generally higher mechanical performance than PEEK. It is recommended for Petal mounts and inserts. Torlon® 4203L is an unreinforced PAI. It has 1.42 g/cm^3 density, 4.9 GPa tensile modulus and 152 MPa tensile strength [67].

2.5 Conclusion

Carbon-fibre composites, composite made structural honeycomb cores and graphitic carbon-foams are the key components used in the ATLAS Inner Detector support structures. Physical, mechanical and thermal properties were briefly described. Since effective properties of all these materials are direction dependent, given information is necessary to understand the petal design, which is described in the previous chapter and studied more in detail in the next chapter.

Furthermore, technical details of the products, which are used in the current petal prototype and candidates for the new design, were given and summarised in table 2.2. These properties will be used in the finite element models developed in the next chapters.

Material	Property	Value	Unit
RS3/K13D2U UD Prepreg [55]	Fiber Areal Weight	80	g/m^2
	Resin Content by Weight	29	%
	Ply Thickness	63	μm
	Tensile Strength (fiber dir.)	2.2	GPa
EX1515/K13C2U UD Prepreg	Fiber Areal Weight	45	g/m^2
	Ply Thickness	50	μm
K13D2U Carbon-Fiber [53]	Density	2.2	g/cm^3
	Tensile Modulus	935	GPa
	Tensile Strength	3.7	GPa
	Ultimate Elongation	0.4	%
	Thermal Conductivity	800	W/(m.K)
	Carbon Content	> 99	%
K13C2U Carbon-Fiber [53]	Density	2.2	g/cm^3
	Tensile Modulus	900	GPa
	Tensile Strength	3.8	GPa
	Ultimate Elongation	0.42	%
	Thermal Conductivity	620	W/(m.K)
	Carbon Content	> 99	%
M55J Carbon-Fiber [29]	Density	1.91	g/cm^3
	Tensile Modulus	540	GPa
	Tensile Strength	4.0	GPa
	Ultimate Elongation	0.8	%
	Carbon Content	> 99	%
RS-3 Resin [54]	Density	1.19	g/cm^3
	Tensile Modulus	3.0	GPa
	Tensile Strength	80	MPa
	Ultimate Elongation	4.9	%
EX1515 Resin [56]	Density	1.17	g/cm^3
Silicon Wafer [68]	Density	2.33	g/cm^3
	Young's Modulus	129.5	GPa

Table 2.2 – continues to next page.

Material	Property	Value	Unit
Goodfellow Nomex® Polyaramid Honeycomb AR312810 [58]	Density	0.024	g/cm^3
	Cell Size	6	mm
	Wall Thickness	0.05	mm
	Compressive Strength (thickness dir.)	0.7	MPa
	Shear Modulus (ribbon dir.)	25	MPa
	Shear Modulus (transverse ribbon dir.)	14	MPa
	Shear Strength (ribbon dir.)	0.7	MPa
	Shear Strength (transverse ribbon dir.)	0.35	MPa
Plascore PK2 Kevlar® N636 Para-Aramid Fiber Honeycomb PK2-3/16-2.0 [59]	Density	0.032	g/cm^3
	Cell Size	4.76	mm
	Compressive Strength (thickness dir.)	1.03	MPa
	Shear Modulus (ribbon dir.)	70	MPa
	Shear Modulus (transverse ribbon dir.)	42	MPa
	Shear Strength (ribbon dir.)	1.0	MPa
	Shear Strength (transverse ribbon dir.)	0.62	MPa
Ultracor Carbon Fiber Honeycomb, UCF-TBD-1/4-3.0	Density	0.048	g/cm^3
	Cell Size	6.35	mm
Ultracor Carbon Fiber Honeycomb, UCF-304-3/8-2.0 [60]	Compressive Modulus (thickness dir.)	134	MPa
	Compressive Strength (thickness dir.)	1.34	MPa
	Shear Modulus (ribbon dir.)	228	MPa
	Shear Modulus (transverse ribbon dir.)	119	MPa
	Shear Strength (ribbon dir.)	1.05	MPa
	Shear Strength (transverse ribbon dir.)	0.56	MPa
T40 Titanium Alloy [64, 65]	Density	4.51	g/cm^3
	Young's Modulus[(a)]	115	GPa
	Poisson's ratio[(a)]	0.32	-
	Yield Strength [(a)]	350	MPa
	Thermal Expansion Coefficient[(a)]	9.2	ppm/K
PEEK Unreinforced [66]	Density	1.32	g/cm^3
	Young's Modulus[(a)]	3.6	GPa
	Tensile Strength[(a)]	100	MPa
PAI Unreinforced, Torlon® 4203L [67]	Density	1.42	g/cm^3
	Tensile Modulus[(a)]	4.9	GPa
	Tensile Strength[(a)]	152	MPa

Table 2.2 – continues to next page.

Material	Property	Value	Unit
Poco-HTC® [24]	Density	0.9	g/cm^3
	Ligament Density	2.23	g/cm^3
	Total Porosity	61	%
	Open Porosity	95	%
	Average Pore Diameter	400	μm
	Compressive Strength (out-of-plane dir.)	5.9	MPa
	Thermal Conductivity (out-of-plane dir.)	245	W/(m.K)
	Thermal Conductivity (in-plane dir.)	70	W/(m.K)
	Thermal Expansion$^{(b)}$ (out-of-plane dir.)	-1.07	ppm/K
	Thermal Expansion$^{(b)}$ (in-plane dir.)	1.02	ppm/K
Allcomp K9-130ppi [50]	Density	0.25	g/cm^3
	Compressive Strength (out-of-plane dir.)	2.17	MPa
	Compressive Modulus (out-of-plane dir.)	380	MPa
	Thermal Conductivity (out-of-plane dir.)	35	W/(m.K)
Araldite® AY 103-1/HY 991 Two Components Epoxy Adhesive [61]	Volumetric Mixing Ratio	2/1	-
	Density	1.00	g/cm^3
	Young's Modulus$^{(a,c)}$	1.7	GPa
	Tensile Strength$^{(a,c)}$	38	MPa
	Shear Modulus$^{(a,c)}$	0.4	GPa
	Lap Shear Strength$^{(a,c)}$	15	MPa
Hysol® EA9396 Epoxy Paste [62]	Volumetric Mixing Ratio	84/30	-
	Density	1.14	g/cm^3
	Tensile Modulus $^{(a,d)}$	2.75	GPa
	Tensile Strength $^{(a,d)}$	35.2	MPa
	Ultimate Strain $^{(a,d)}$	3.4	%
	Lap Shear Strength $^{(a,d)}$	24.1	MPa
	Thermal Conductivity	0.21	W/(m.K)
Dow Corning® SE4445 CV Silicon Gel [63]	Volumetric Mixing Ratio	1/1	-
	Density	2.36	g/cm^3
	Thermal Conductivity	1.34	W/(m.K)

Table 2.2: Materials used in petal and their physical, mechanical and thermal properties. [a] is for values measured at ambient temperature. [b] is for values measured between at 50-150°C . [c] is for values by curing resin at 40°C during 16 hours. [d] is for values by curing resin at 25°C during 5 days. The direction of properties are specified in paranthesis. The data were taken from datasheets published by manufacturer or suppliers.

Chapter 3

The ATLAS Petal Design Studies

This chapter is dedicated to analytical, experimental and computational studies on structural mechanics of the ATLAS Petal designs. The studies introduce clear understanding of the influence of the materials on the structural performance. This understanding allows reliable studies of possible improvements to the petal design, resulting in recommendations for changing facing and core material.

Firstly, we give a brief description of the petal prototype made at Nikhef to the LoI-design, and of another petal prototype made at DESY to the LTF-design.

The theory section describes bending behaviour of the petal by simplifying the design to a rectangular sandwich structure consisting only of two facings and a core. Mass and mechanical properties were derived for a unidirectional prepreg, and these were used to calculate overall mechanical properties of a facing, i.e. composite laminate consisting of multi-directional layers. Then composite calculations and sandwich theory were used to evaluate petal bending stiffness.

Calculations based on the theory part were used to compare angular configuration of the facings, other prepregs for use in facings, and core materials. The results were interpreted in terms of contributions to overall mass properties and structural bending stiffness of the panel. The aim was to improve bending stiffness, while removing excessive material and improving the design regarding fractional radiation length $\%X_0$. Materials were selected to further improve the petal design for use in the future tracker.

Bending tests were performed to measure structural stiffness of the LoI-Petal prototype, and experimental modal analysis was conducted to measure frequencies and shapes of free vibration modes. A finite-element model of the design was developed to reproduce these measured characteristics. Having verified this model on the LoI-Petal design, it was adapted to the LTF-Petal design, which also includes sensor modules. This model was used to evaluate final performance of the design with current and recommended material configurations.

Evaluations based on the theory section and material selection are presented in section 3.6. Computed performance of the LTF design is given in section 3.7.

3.1 LoI-Petal

The LoI-Petal design is illustrated in figs. 1.5 and 1.6 with dimensions given in fig. A.4. It is symmetrical around the centre line; a horizontal line passes through middle of the petal and the nominal beam line. The petal edges have U-shaped close-outs having 5 mm depth; the outer edges of the honeycomb core are reduced by this amount. Fig. A.5 shows the cooling pipe position in the petal, and fig. A.6 sketches the cross-section of the tube-foam structure.

The material configuration for the bare petal prototype used for measurements (without modules in place) is listed below:

- Facings are made of 3 plies of a K13D2U/RS3 unidirectional prepreg laid up in $60^\circ/0^\circ/-60^\circ$ angles from the petal longitudinal axis.
- Nomex® (polyaramid) AR312810 hexagonal honeycomb with $0.024\,\mathrm{g/cm^3}$ density was used as structural core material.
- The close-outs were made into a U-shaped bar using a single layer of bidirectional weave of M55J carbon-fibres by impregnating with room temperature cure Araldite AY-103-1/HY-991 two-component adhesive. Hand lay-up was preferred to create the final shape. Fibres used here are reasonably flexible (i.e. able to elongate more before breakage) to handle the corners while the component is in the mould.
- The cooling tubes were made of T40 titanium alloy.
- Poco-HTC® graphitic foam was used as a thermal conductor core element.
- Thanks to its bonding capability with a wide range of materials, the adhesive used in close-outs was also used to glue core to facings and tube to foam.

The components are summarized in table 3.1 along with materials, layer thicknesses

Component	**Material**	**Thickness** (mm)	**Mass** (g)
Facings	K13D2U/RS3 $[60/0/-60]^\circ$	*0.19	79.00
Structural Core	Nomex AR312810 Honeycomb	5.12	11.90
Thermal Core	Poco-HTC graphitic foam	5.12	42.50
Close-outs	M55J $[0/90]^o$ + Araldite AY-103-1/HY-991	0.28	7.03
Cooling Pipe	T40 Titanium	0.15	6.92
Glue (in total)	Araldite AY-103-1/HY-991	-	*20.50
Bare Petal		5.50	167.85

Table 3.1: The components along with materials, layer thicknesses and total masses for LoI-Petal. *: calculated value. Thickness is given for one layer, while mass is the total amount for the same type of components, e.g. the thickness is given for one facing, while the mass is given for 2 facings.

and weights. The facing thickness was taken from the prepreg properties. Total weight of all parts was subtracted from the prototype weight to calculate amount of adhesive used. It is hard to measure how the glue is distributed over the structure. Section A.3 in appendix describes how the petal prototype is made at Nikhef, and gives some information about glue use. There are 4 main sections where most of the adhesive was used: The first is the core to facing bond, applied by dipping the honeycomb in glue; the others are the foam-facing, foam-foam and foam-tube interfaces. Since the foam has high open-porous structure, the glue leaks through the pores and creates additional undesired weight. As well, there is a thin layer of adhesive between the facings and the close-outs; however, its weight is negligible compared to the other sections.

3.2 LTF-Petal

The LTF-Petal design differs from the LoI-design: It has only one EoS ear, different materials and different dimensions. Fig. A.7 gives the 2D sketch of facings along with dimensions, and fig. A.8 gives the cooling pipe position with respect to the facings. The cross-section of the tube-foam structure is the same as the LoI-design given in fig. A.6. Fig. 1.7 illustrates the modules containing silicon sensors and electronic boards positioned on the base structure, and fig. A.9 gives the wireframe view. The design was updated in 2016; this design already contains the facing selection discussed in section 3.6. Conference presentation in [6] describes the details of a prototype made at DESY. Later on, presented masses were corrected by the same author [69], and corrected values are used in this thesis. The components are listed in table 3.2 along with materials, layer thicknesses and total masses.

- The facings are 3 plies of a 45 gsm K13C2U/EX1515 unidirectional prepreg laid up in $0°/90°/0°$ angles from the petal longitudinal axis.
- Carbon-fibre hexagonal honeycomb core with product designation of UCF-TBD-1/4-3.0 having $0.048\,\mathrm{g/cm^3}$ density was used as a structural core.
- The close-outs are made of a rectangular bar of a PEEK structural plastic material. The weight is minimized via holes in the bars. The locking components are also made of PEEK.
- Allcomp K9-130 ppi graphite foam having $0.23\,\mathrm{g/cm^3}$ density was used as thermal conductor core.
- Hysol EA9396 was used to glue facings to the close-outs, honeycomb core and foam.
- The cooling tube is made of CP2 titanium. It has a 2.0 mm inner diameter and 0.14 mm wall-thickness.
- The bus tape is a shieldless tape of polyimide containing two copper conductor layers. The prepregs were co-cured with bus tape on; thus the tape is bonded to the facing without using any additional layer of adhesive. However, this

Component	Material	Thickness (mm)	Mass (g)
Facings	K13C2U/EX1515 [0/90/0]°	0.15	56.91
Structural Core	UCF-TBD-1/4-3.0	5.00	23.67
Thermal Core	Allcomp K9-130 ppi	5.00	18.09
Close-outs (incl. locks)	PEEK	-	27.44
Cooling Pipe	Titanium CP2	0.14	5.78
Glue (Facing to Core)	Hysol EA9396	0.10	10.81
Glue (Total In Bare Petal)	Hysol EA9396	-	15.60
Bus Tape	Polyimide/Cu	0.20	51.37
Glue (Module to Bus)	DC SE4445	0.14	36.60
Modules (Wafer, Hybrids)	-	-	212.11
EoP	Circuit Board	0.30	50.00
Bare Petal		5.50	147.50
Petal incl. modules and bus		-	497.60

Table 3.2: The components along with materials, layer thicknesses and total masses for LTF-Petal, taken from [6]. Thickness is given for one layer, while mass is the total amount for the same type of components. Masses given in [6] were later corrected by the same author, and corrected masses are given above. In the same document, glue between module and bus tape is included in the module mass, and mass of the bus tape is included in the bare Petal mass.

configuration required use of prepreg with higher resin content, which also caused additional weight.

- The sensors (0.320 mm thick wafers) are made of silicon and glued onto the bus tape with DC SE4445 thermally conductive adhesive having 0.14 mm thickness. Hybrids are polyimide containing copper planes and silicon ASICs, and glued on the sensor with Epolite FH5313. Sensors and hybrids together form the module assembly.
- The end of petal (EoP) is a multilayer circuit board, 0.3 mm thick, with several chips on. It is glued onto the bus tape with DC SE4445 adhesive as well.

3.3 Theory

In this section, various theoretical approaches are used to formulate properties of the composite in the facings and bending behaviour of the petal. The first part is dedicated to producing properties of a single lamina based on the properties of the constituents (fibre and resin). These properties are calculated for prepregs used in the petal facings, and used in finite element modelling of the petal (in section 3.5). In the second part, composite theory is used to derive the elastic constants for a laminated composite as a whole by transforming properties of multi-directional plies to a common direction. In

the third part, sandwich theory is used to describe bending behaviour of the petal by simplifying it as a rectangular panel.

3.3.1 Lamina Properties

A lamina or ply is used to describe a single layer of a laminated composite formed of multi-plies. Fig. 2.1 shows a lamina made of unidirectional fibres.

Mass Properties

In general, composites are defined in terms of the weight contributions of the constituents. The most-used parameters are the areal weight AW (i.e. weight per unit area) and content by weight CW (i.e. fraction of density to total density). Fibre areal weight and resin matrix content by weight are usually reported by the suppliers. These can be converted to volumetric properties of a single ply as follows.

Consider a composite plate with mass m and area A. The subscripts f and m denote fibre and resin matrix. The subscript i identifies different components. Then, $\sum m_i = m$, $AW_i = m_i/A$ and $CW_i = m_i/m$, so that $AW_i/CW_i = m/A$, which is independent of constituent i.

For two-component facesheet, $AW_f/CW_f = AW_m/CW_m$ and $CW_f + CW_m = 1$. Hence, the matrix areal weight is:

$$AW_m = \frac{AW_f}{(1-CW_m)} CW_m \tag{3.1}$$

Dividing areal weights by densities ρ gives equivalent layer thicknesses, $t_i = AW_i/\rho_i$. The sum of both layer thicknesses gives the single ply thickness:

$$t = \frac{AW_f}{\rho_f} + \frac{AW_m}{\rho_m} \tag{3.2}$$

Dividing equivalent thicknesses to the ply thickness gives volumetric fraction V of the constituents:

$$V_f = 1/\left(1 + \frac{AW_m}{AW_f}\frac{\rho_f}{\rho_m}\right) \quad and \quad V_m = 1 - V_f \tag{3.3}$$

Micromechanics

A piece of unidirectional composite shown in fig. 3.1 consists of randomly distributed fibres and matrix, and it is simplified to a block as a combination of two volume elements parallel to each other in fibre axis [25]. In the figure, 1-axis refers to a lamina in-plane longitudinal direction parallel to fibres (0°), 2-axis is in-plane transverse direction perpendicular to the fibres (90°) and 3-axis is normal to the lamina, also

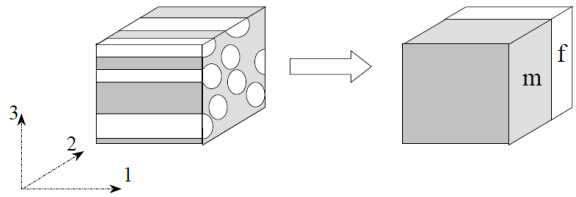

Fig. 3.1: Composite simplified in representative fibre and matrix volume.[25]

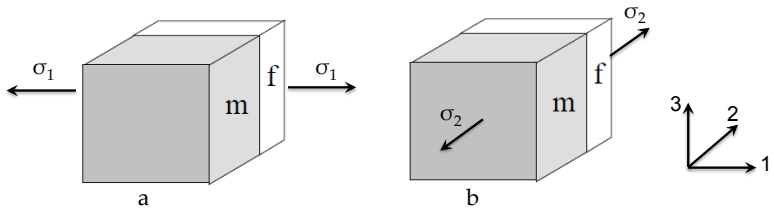

Fig. 3.2: Fibre and matrix representative volume element connected in, a) parallel for the in-plane longitudinal and b) series for in-plane transverse loading.[25]

called out-of-plane or stacking direction. The subscripts 1, 2 and 3 are used to show material directions. The fiber is assumed to be orthotropic material, so its properties differ depending on direction. The matrix is isotropic and so does not need directional subscripts. A homogeneous model for a lamina is derived as follows.

Fig. 3.2 (a) shows loading in the fibre direction. The relation between the longitudinal stress (σ) components is $\sigma_1 A = \sigma_{f1} A_f + \sigma_m A_m$, where A is the cross-sectional area of the components on the loading face. The component-to-composite area ratios give volumetric fractions, $V_i = A_i/A$. It is assumed that deformations are linear with stress, and $\sigma_i = E_i \varepsilon_i$ is substituted. The strain (ε) in the force direction is equal for all constituents, assuming no slipping occurs between them. Young's modulus of the composite in the fibre direction E_1 is found as a function of elastic modulus and volumetric fraction of both constituents [25]:

$$E_1 = E_{f1} V_f + E_m V_m \tag{3.4}$$

This method is called the rule of mixture.

Analytic models can be used to obtain the transverse modulus E_2 of a composite based on fibre transverse and matrix properties. In the simple approach, the fibre and matrix representative volumes are considered in series as shown in fig. 3.2 (b). This implies stress equality over components ($\sigma = \sigma_f = \sigma_m$); the transverse modulus is derived by using this relation: $1/E_2 = V_f/E_{f2} + V_m/E_m$. The final relation is called the inverse rule of mixture. Actually, the resin is not distributed over the cross-section uniformly, so the stress is not either. Therefore, the serial model is generally not sufficient to predict the

transverse modulus of a composite [25]. Some models adjust this relation by considering parallel-series connections together, and by introducing other assumptions and effects such as spherical matrix inclusion [70].

Another difficulty of these approaches is that the prediction is based on fibre transverse modulus E_{f2}, which is difficult to obtain reliably with traditional measuring techniques. Raman spectroscopy can be used; however, not all manufacturers use it, and it is difficult to obtain data. Instead, composite transverse properties are measured in macro-scale. Then the data are used in an analytic model to find the fibre transverse modulus. The closest predictive model is the Halpin-Tsai semi-empirical model given by [70, 71]:

$$\begin{aligned} E_2 &= E_m \frac{1+\zeta\,\eta\,V_f}{1-\eta\,V_f} \\ \eta &= \frac{\left(E_{f2}/E_m\right)-1}{\left(E_{f2}/E_m\right)+\zeta} \\ \zeta &\approx 2 \end{aligned} \tag{3.5}$$

The factor ζ is called the reinforcing factor and depends on the fibre cross-sectional geometry, and on packing[9] and loading conditions. Generally, it is found by curve-fitting of the experimental data. The ζ is 2 for fibres with circular cross-section (aspect ratio is 1) in a square array. In this work, we consider the ply as a square array pack of fibres instead of random distribution.

This method gives fibre transverse modulus more than 60 % higher than Raman spectroscopy (fig. 9 in [70]). Raman spectroscopy measured a transverse modulus of 10.4 GPa for fibres having 230 GPa longitudinal modulus [72]. For this work we make the assumption that the transverse-to-longitudinal modulus ratio μ is constant giving

$$\begin{aligned} E_{f2} &= \mu\,E_{f1} \\ \mu &\approx 10.4/230 \end{aligned} \tag{3.6}$$

Shear modulus G of the ply is also formulated by considering both constituents in series, fig. 3.2 (b). It suffers from the same difficulties as the transverse modulus [25]. The Halpin-Tsai semi-empirical model describes shear modulus in the same form as

[9] Fibre packing affects the glue distribution and fibre-to-fibre contact in composites. In rectangular or square packing, each fibre layer goes onto another layer. In triangular packing, the fibres are placed between 2 fibres of the bottom layer. Fibres are randomly packed in common composites.

eq. (3.5) [71]:

$$\begin{aligned} G_{12} &= G_m \frac{1+\zeta\,\eta\,V_f}{1-\eta\,V_f} \\ \eta &= \frac{\left(G_{f12}/G_m\right)-1}{\left(G_{f12}/G_m\right)+\zeta} \\ \zeta &\approx 1 \end{aligned} \tag{3.7}$$

This time reinforcing factor ζ is 1 for the circular fibre with packing in square sequence.

However, the predictions are far from experimental results, and there is usually no data related to fibre shear modulus G_{f12}. Since the in-plane shear properties of the lamina are not the predominant factor in determining bending behaviour (see eq. (3.22)), we made an assumption and took shear modulus of the resin as the ply in-plane shear modulus:

$$G_{12} \approx G_m \tag{3.8}$$

While the composite is exposed to an axial load in the fiber axis, the resultant transverse deformation δ of the composite can be written as $\delta_2 = \nu_{12}\varepsilon_1 w$, where w is the width and ν_{12} is the Poisson's ratio of the composite. The transverse deformation of composite is the sum of the transverse deformations of both constituents. As mentioned, both constituents and composite have the same strain in the force direction in the parallel connection, fig. 3.1. Therefore, the relation can be written in reduced form as $\nu_{12}\,w = \nu_{f12}\,w_f + \nu_m\,w_m$. The ratio of component-to-composite widths give volumetric fractions i.e. $V_i = w_i/w$, and the following equation can be found [25]:

$$\nu_{12} = \nu_{f12}\,V_f + \nu_m\,V_m \tag{3.9}$$

The rule of mixture used to derive longitudinal modulus can be applied for the Poisson's ratio as well. Poisson's ratio for fiber is not available in product datasheets. A typical value of 0.19 can be used, which is taken from the measurements in [73].

In composites, fibre and matrix areal weights are usually known after manufacturing. By using this information in eq. (3.3) along with the mass properties of the constituents, one can find volumetric properties of a ply. The outcomes are used in eq. (3.4) with mechanical properties of the constituents to find equivalent longitudinal modulus E_1 of the ply. Eq. (3.6) is used to predict fibre transverse modulus, which is substituted in eq. (3.5) to calculate ply transverse modulus E_2. Eq. (3.8) gives in-plane shear modulus G_{12}, and eq. (3.9) is used to find Poisson's ratio ν_{12} of the ply. The properties of a single lamina are then used to compute the properties of a laminated composite as described in the next section. Some values are given in table 3.6.

3.3.2 Multi-directional Composite Properties

A laminate consists of multi-directional plies. Each ply contributes overall composite properties depending on its lay-up direction. First, we construct the compliance matrix for a single ply. This is then transformed from the ply axes to the composite axes. Next, classical laminate theory was used to combine contributions of all layers to obtain the stiffness matrix for the whole laminate. This matrix can be transformed to evaluate composite behaviour in different loading directions as well.

Stiffness Matrix of a Lamina

Hooke's law defines the relation between 1×6 stress $[\sigma]$ and strain $[\varepsilon]$ tensor as:

$$\begin{bmatrix} \varepsilon_{11} \\ \varepsilon_{22} \\ \varepsilon_{33} \\ 2\varepsilon_{12} \\ 2\varepsilon_{13} \\ 2\varepsilon_{23} \end{bmatrix} = [C] \begin{bmatrix} \sigma_{11} \\ \sigma_{22} \\ \sigma_{33} \\ \sigma_{12} \\ \sigma_{13} \\ \sigma_{23} \end{bmatrix} \tag{3.10}$$

where $[C]$ is the 6×6 material compliance matrix. $[C]$ is comprised of lamina elastic constants, which are three Young's moduli E, three shear moduli G and three Poisson's ratios ν; 9 constants in total. Our lamina has symmetric behaviour around 3-orthogonal planes having normals in the material axes; therefore, the lamina is an orthotropic material. In such materials, shear strains are only affected by the corresponding shear stress component, and the compliance matrix elements corresponding to remaining components in the stress tensor become zero. Furthermore, the laminate is assumed to be in plane stress state in the classical lamination theory [74]; this implies that out-of-plane shear (σ_{13} and σ_{23}) and normal stresses (σ_{33}) are zero. This relative lack of stress reduces $[\sigma]$ and $[\varepsilon]$ tensors to 1×3 and removes corresponding compliance matrix elements as well, simplifying to:

$$\begin{bmatrix} \varepsilon_{11} \\ \varepsilon_{22} \\ 2\varepsilon_{12} \end{bmatrix} = \begin{bmatrix} \frac{1}{E_1} & -\frac{\nu_{21}}{E_2} & 0 \\ -\frac{\nu_{12}}{E_1} & \frac{1}{E_2} & 0 \\ 0 & 0 & \frac{1}{G_{12}} \end{bmatrix} \begin{bmatrix} \sigma_{11} \\ \sigma_{22} \\ \sigma_{12} \end{bmatrix} \tag{3.11}$$

where $\nu_{21} = \nu_{12} E_2 / E_1$. The stiffness matrix $[K]$ is the inverse of the compliance matrix:

$$[K] = [C]^{-1} \tag{3.12}$$

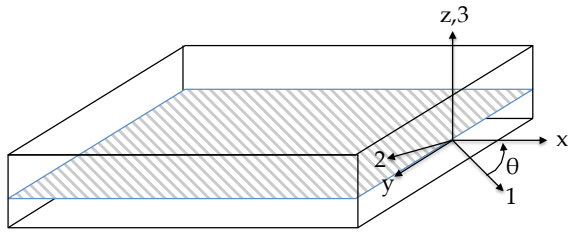

Fig. 3.3: A single rotated ply in laminate.

Ply Transformation

Fig. 3.3 illustrates one of the plies in a laminated composite having a fibre angle θ, which is the angle between the primary axis of the composite and the fibres of the ply. Composite orientation axes are labelled by x, y and z, while the ply orientation axes are labelled by 1, 2 and 3. The 3 and z-axes are the same for both. The material stiffness matrix $[K]$ is transformed from the ply 1 and 2-axes onto the composite x and y-axes as [25]:

$$[Q] = [T]\,[K]\,[R]\,[T]^{-1}\,[R]^{-1} \tag{3.13}$$

where $[T]$ is the transformation matrix in the clockwise direction:

$$[T] = \begin{bmatrix} c^2 & s^2 & 2cs \\ s^2 & c^2 & -2cs \\ -cs & cs & c^2 - s^2 \end{bmatrix} \; with \begin{cases} s = \sin\theta \\ c = \cos\theta \end{cases} \tag{3.14}$$

and $[R]$ is the Reuter matrix[10]:

$$[R] = \begin{bmatrix} 1 & 0 & 0 \\ 0 & 1 & 0 \\ 0 & 0 & 2 \end{bmatrix} \tag{3.15}$$

Classical Laminate Theory

Laminate theory considers a laminated beam under axial and flexural loading to construct a relation between internal force and moments, and strains and curvatures. The theory models the elastic behaviour of multi-plies as an equivalent single layer, using three matrices: These are extensional $[A]$, coupling $[B]$ and bending $[D]$ stiffness matrices, which are comprised of components of the transformed stiffness matrix $[Q]$ and geometric properties of each ply. Fig. 3.4 shows the cross-section of a laminated composite consisting of n plies. h is the composite thickness, t_k is the ply thickness, r_k

[10] Engineering shear components are twice the shear deformation tensor components, e.g. ε_4 or $\gamma_{12} = 2\varepsilon_{12}$, and Reuter matrix is used to correct strain transformations [25].

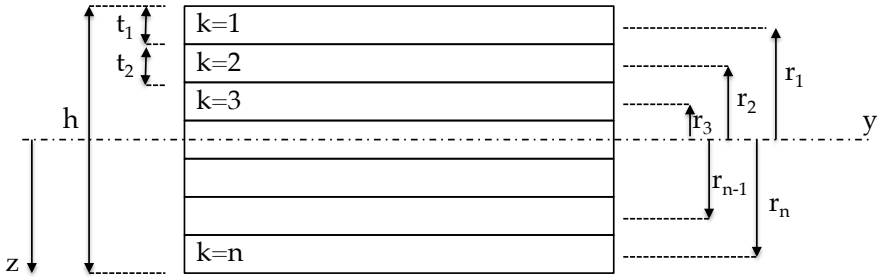

Fig. 3.4: Cross-section view of laminate.

defines the distance from ply mid-plane to the neutral axis of the composite, and the subscript k specifies the ply. The $[A]$, $[B]$ and $[D]$ matrices are [75]:

$$\begin{aligned}
[A] &= \sum_{k=1}^{n} [Q_k]\, t_k \\
[B] &= \sum_{k=1}^{n} [Q_k]\, (t_k\, r_k) \\
[D] &= \sum_{k=1}^{n} [Q_k] \left(\frac{t_k^3}{12} + t_k\, r_k^2 \right)
\end{aligned} \tag{3.16}$$

These matrices are used to write the relation between axial force $[N]$ and moment $[M]$, and strain $[\varepsilon]$ and curvature $[\kappa]$ tensors as:

$$\begin{aligned}
[N] &= [A]\,[\varepsilon] + [B]\,[\kappa] \\
[M] &= [B]\,[\varepsilon] + [D]\,[\kappa]
\end{aligned} \tag{3.17}$$

If $[B]$ is non-zero, there is a coupling between extensional and bending deformations. In-plane loads induce curvature in a laminate resulting in plate warping, while bending causes extensional strain [75]. For practical use, composite plates are usually designed to be symmetric about their mid-plane, thus the composite mid-plane coincides with the neutral plane and the coupling stiffness matrix $[B]$ becomes zero. Similarly, if the ply configurations in the facings of a sandwich structure are symmetric about the sandwich mid-plane, only $[A]$ and $[D]$ are important for the mechanical response of the whole sandwich. This simplifies the above equations giving:

$$\begin{aligned}
[\varepsilon] &= [a]\,[N] \\
[\kappa] &= [d]\,[M]
\end{aligned} \tag{3.18}$$

where $[a]$ is the extensional compliance matrix which is the inverse of the extensional stiffness matrix $[A]$, and $[d]$ is the inverted bending stiffness.

$$[a] = [A]^{-1} \tag{3.19}$$

The longitudinal and transverse Young's moduli, E_x and E_y, and the in-plane shear modulus G_{xy} and Poisson's ratio ν_{xy} are extracted from the components of the extensional compliance matrix as[11]:

$$E_x = \frac{1}{a_{11}\,h}\ ,\ E_y = \frac{1}{a_{22}\,h}\ ,\ G_{xy} = \frac{1}{a_{44}\,h}\ ,\ \nu_{xy} = -\frac{a_{21}}{a_{11}} \tag{3.20}$$

Firstly, elastic constants of a single ply found in section 3.3.1 are used in eq. (3.11) to construct the compliance matrix $[C]$, which is inverted to obtain stiffness matrix $[K]$. Then $[K]$ is transformed onto the primary axis (or any desired direction) of the composite respectively for each ply by using eq. (3.13). The transformed stiffness matrix $[Q]$ of each ply was substituted in eq. (3.16) along with geometric properties to combine individual contributions of all plies into matrices defining behaviour of a composite as a whole. The matrix $[A]$ is inverted to give the extensional compliance matrix $[a]$ of the composite, and elastic constants are extracted by using eq. (3.20).

Having derived the properties of the face-sheets, these can then be used to calculate bending of panels —analytically for rectangular panels as in the section 3.3.3 or as input to finite element model.

Composite Elastic Properties in Loading Direction

Eq. (3.19) gives the extensional compliance matrix $[a]$ in the composite x and y-axes. ϕ is the angle between loading direction and the primary axis of the composite in the clockwise direction. The matrix $[a]$ can be transformed on loading direction with matrix $[T]$, which is formed by using the angle ϕ in eq. (3.14). The transformed compliance $\widehat{[a]}$ matrix then becomes:

$$\widehat{[a]} = [R]\,[T]\,[R]^{-1}\,[a]\,[T]^{-1} \tag{3.21}$$

$[R]$ is given in eq. (3.15). By using components of $\widehat{[a]}$ instead of $[a]$ in eq. (3.20), one can find the elastic constants of a composite along any loading axis. This method is then used in section 3.6 to calculate the Young's modulus of a composite in several loading axes, see fig. 3.19.

[11] The notations used here to specify the components of $[a]$ matrix are considered for the 6×6 compliance matrix. For a_{ij}, $i\,\&\,j = 1,2,...,6$.

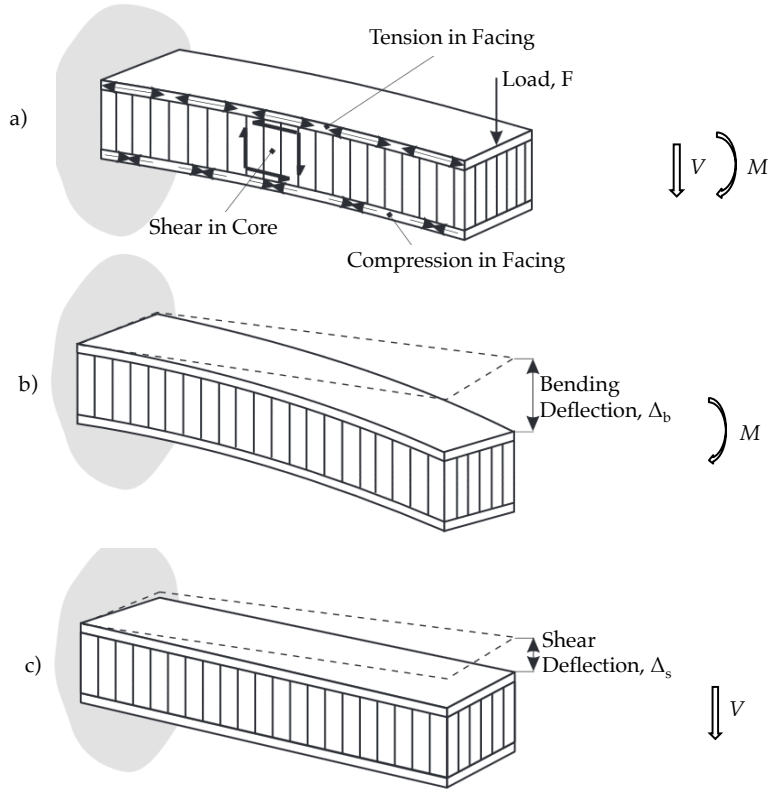

Fig. 3.5: Bending of sandwich panel due to vertical loading F and internal forces and moments [38]. b) bending deflection Δ_b of facings due to internal moment M and axial forces. c) shear deflection Δ_s in the core due to shear force V in the panel thickness direction.

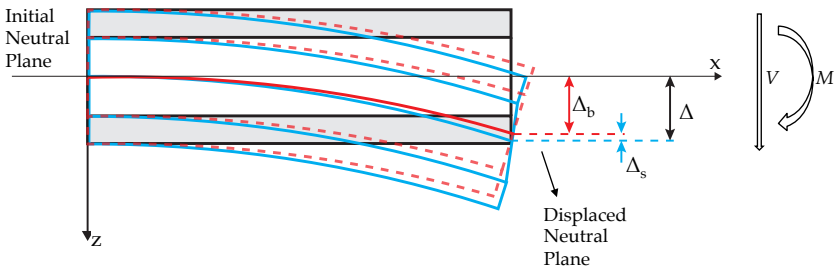

Fig. 3.6: A bent section of sandwich structure. Black shape is the initial, red dashed shape is for the pure bending deformation due to moment M, and blue shape is for the beam, including core shear deformation caused by vertical shear force V. The image is based on online source [76] and was modified.

3.3.3 Description of Sandwich Bending

Sandwich structures are comprised of thin facesheets made of high-modulus material separated by a low-density, thick core material. The sandwich theory generally describes bending behaviour of beam and plate sandwich structures. The theory makes the following assumptions [77]:

- The facing-core interface is rigid; hence the facings do not slide on the core.
- The facings are extremely thin, so no shear deformation occurs in the thickness direction.
- The core has small in-plane stiffnesses compared to the facings, so it does not carry forces in the same direction.
- The core has high stiffness in the panel thickness direction and does not crumple in. Therefore, distance between the facings remains the same as it was initially.

The petal model was simplified to a rectangular panel to ease applying the theory. Since we are only interested in longitudinal bending behaviour, width effects were ignored, and the model was reduced to a beam problem. Fig. 3.5 (a) shows a sandwich structure and internal forces and moments in the components due to vertical loading. The applied force F results in a bending moment M around the neutral plane and a shear force V in the vertical direction. The moment causes tension and compression forces in the upper and lower facings, while there is no axial force on the neutral plane, which remains undeformed. This in turn causes the beam to bend (b). Simultaneously, another phenomenon occurs. The vertical shear force V causes a sliding displacement of the neutral plane, caused by shear deformation in the core (c). The vertical displacement of the neutral plane due to pure bending is Δ_b and the sliding displacement is Δ_s. The total beam deflection is the sum of both, and is shown as $\Delta = \Delta_b + \Delta_s$ in fig. 3.6.

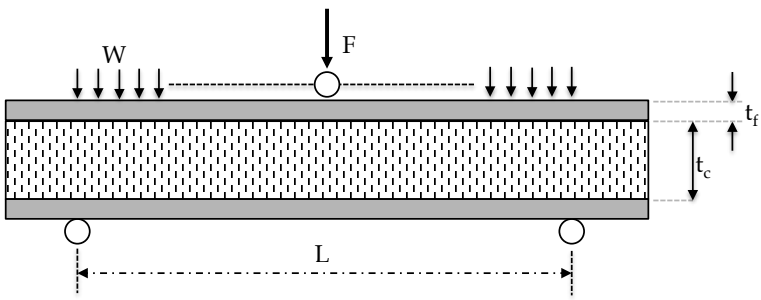

Fig. 3.7: Simply supported sandwich beam, supported at both ends, and loaded by concentrated force F at centre and uniformly distributed load W.

Three-Point Bending for Simply-Supported Case

Fig. 3.7 shows a sandwich beam loaded by a concentrated force F at its center and a uniformly distributed load W, and supported at both ends. w is the width of the beam, L is the distance between the supports, and t specifies the thickness of components. The subscripts f and c define the facing and core. The force diagram and deformations are shown in fig. 3.6.

The applied loads F and W are used to derive the resultant bending moment M and shear force V, which then give the pure bending Δ_b and shear Δ_s deformations. Maximum deformation occurs at beam centre, and is [77, 78]:

$$\Delta = \underbrace{\frac{1}{48}\left(\frac{FL^3}{D_f}\right) + \frac{5}{384}\left(\frac{WL^3}{D_f}\right)}_{\Delta_b} + \underbrace{\frac{1}{4}\left(\frac{FL}{D_c}\right) + \frac{1}{8}\left(\frac{WL}{D_c}\right)}_{\Delta_s} \tag{3.22}$$

where D_f is the bending rigidity of facings, and D_c is the core shear rigidity. The rigidity terms are:

$$\begin{aligned} D_f &= E_f I_f \\ D_c &= G_c A_c \end{aligned} \tag{3.23}$$

where E_f is the Young's modulus of facing in the beam longitudinal axis and I_f is the area moment of inertia of both facings around the neutral plane. G_c is the shear modulus of core in thickness direction and A_c is the core cross-sectional area. By integration over the panel geometry,

$$I_f = \frac{wt_f^3}{6} + wt_f\frac{(t_c+t_f)^2}{2} \tag{3.24}$$

The left term (containing t_f^3) is much smaller than the right term for the structures; with $t_c \gg t_f$, this simplifies the above equation into the form $I_f \cong wt_f t_c^2/2$.

Eq. (3.22) shows that deformation depends on material properties — Young's modulus of facings and shear modulus of the core, sample geometry, and loads applied. The numeric coefficients result from the position of applied load and boundary conditions (i.e. type of support such as simply-supported, clamped at two ends, clamped at one end etc.). Depending on geometry, shear deformation can dominate. For example, four-point bending test on a short beam measures shear behaviour of the core.

Young's modulus, E_f or E_x, of the facing in the beam direction is found from eq. (3.20). Area moment of inertia, I_f, is calculated by using eq. (3.24) and substituted in the first formula in eq. (3.23) along with modulus to find bending rigidity of the facings, D_f. Similarly, shear modulus of core in the panel thickness direction, G_c, and the cross-sectional area, A_c, are used in the second formula in eq. (3.23) to find core shear

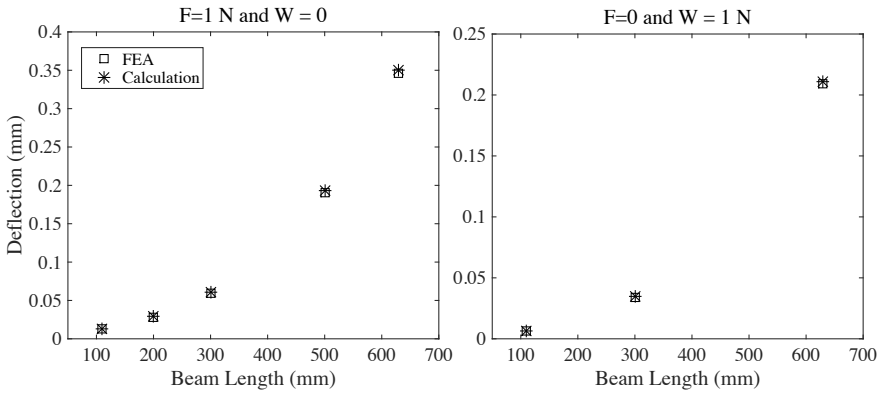

Fig. 3.8: Comparison of the deflections calculated via eq. (3.22) and computed via FEM at various beam lengths. Calculations made by only considering concentrated force F (at left), and by only using uniformly distributed load W (at right).

rigidity D_c. Both rigidity terms, D_f and D_c, are substituted in eq. (3.22), along with panel length L, weight W and concentrated force F to calculate maximum deflection Δ at the mid-length of the beam.

Theory Verification Via FEA

Bending deflection calculated via eq. (3.22) was compared with computational results from a simple finite-element model of a sandwich beam. The model cross-sectional geometry[12] and material properties, such as the facing's Young's modulus to core shear modulus ratio, were kept as in the petal (see table 2.2 for material properties). Two different loading conditions are used: In the first, only concentrated force is accounted for ($F = 1$ and $W = 0$), and in the second, only uniformly distributed load is considered ($F = 0$ and $W = 1$). Thus, precision of the equation is tested for each loading term individually. The deflections were calculated at various beam lengths.

Fig. 3.8 gives results of the study, all calculations agree within 3 % with computational results. Precision may be affected by the active deflection component. Fraction of pure bending to core shear deflection , Δ_b/Δ_s, changes from 0.1 at 110 mm to 4.6 at 630 mm beam length for the concentrated load case. This suggests that both deflection terms play an active role in determining overall bending behaviour, and both are accurately calculated. Consequently, the analytic model is reliable enough to be used as a simple petal model.

This model is then used in section 3.6 to compare several face-sheet configurations and choice of core materials, see fig. 3.20.

[12] Core and facing thicknesses were 5.00 and 0.19 mm, and beam width was 20 mm.

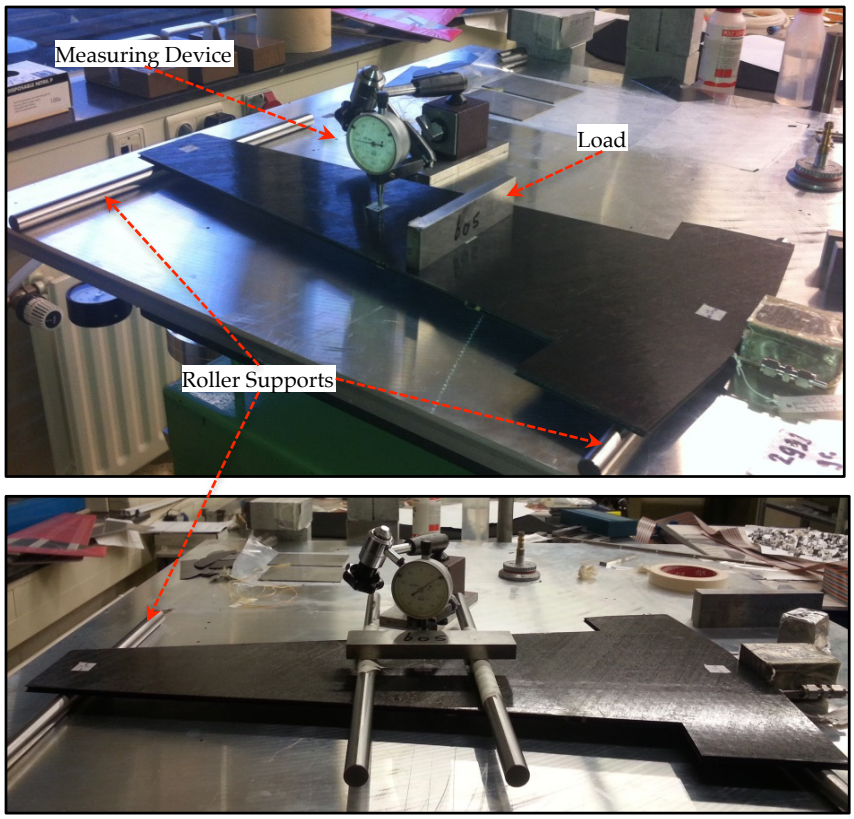

Fig. 3.9: Configuration of bending tests; three-point at top and four-point at bottom. Look fig. 3.10 and table 3.3 for more information.

3.4 Measurements - LoI Petal

This section reports measurements of the mechanical behaviour of the petal. Two different experimental set-ups were used for two different characteristics. In the first, the bending deflection was measured with three- and four-point bending tests, and bending stiffness was calculated. In the second, modal frequencies and corresponding modal shapes were measured. Tests were performed on a bare LoI-Petal prototype without any modules, shown in fig. 1.5.

3.4.1 Bending Tests

The bending tests are performed to measure and characterise overall bending behaviour of the structures. Three-point bending test refers to a structure loaded along one line,

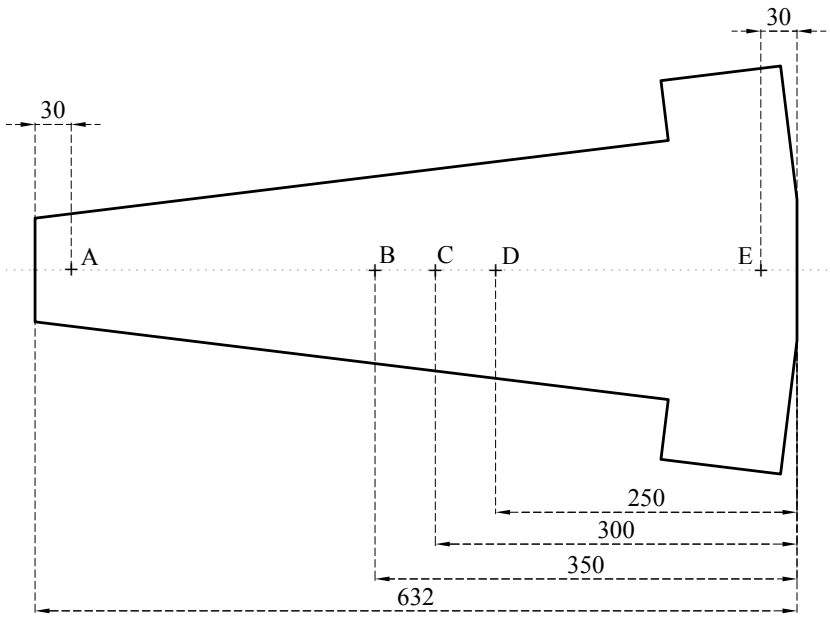

Fig. 3.10: Positions of markers used to define roller supports, loading and data reading points. All dimensions are in mm. Sketch is from fig. A.4.

and supported along two lines. In the four-point test, load is applied along two lines simultaneously, while the structure is also supported along two lines.

Fig. 3.9 shows the configurations of the three- and four-point bending tests. Test types are summarised in table 3.3, along with markers used to define location of loads, supports and reading the displacement. Fig. 3.10 gives the positions of these markers on the sketch of a petal.

The petal was supported by cylindrical rollers along two lines. The cylindrical rollers were longer than the petal width to prevent deflections between edge and centre. The system was set up on a flat table. No attempt was made to measure the gravitational sag due to petal's own weight: the measuring device was positioned on the petal surface and calibrated to zero. The device measures the vertical movement of the tool tip and

Test Type	**Loading**	**Supports**	**Data Read**
3-Point	D	A and E	C
4-Point	B and D	A and E	C

Table 3.3: Type of bending tests along with markers used to define locations of support, loading and deflection measurement. Fig. 3.10 gives the marker positions.

had 10 μm resolution. In the three-point bending case, external masses were placed at the loading point and the tool displacement was recorded for each. Each mass increment was around 600 g. For the four-point bending case, bottom supports were kept the same, but the load was applied via two cylinders with equal weights. The measuring device was calibrated to zero with both cylinders in place. External masses were then added on top of the two cylinders, and the tool displacement was recorded at each increment.

3.4.2 Experimental Modal Analysis

Experimental modal analysis is a method used to measure natural frequencies by artificially exciting the vibration modes of a structure. Each mode is defined by a natural frequency, modal damping and mode shape.

- Force is instantaneously applied to a body at a point to excite vibration modes.
- The corresponding operating deflection shape (ODS) is determined by measuring and combining motions at two or more locations.
- The frequency response is found via fourier transform of the motion, where the peaks give the natural frequencies of the activated modes. [79, 80]

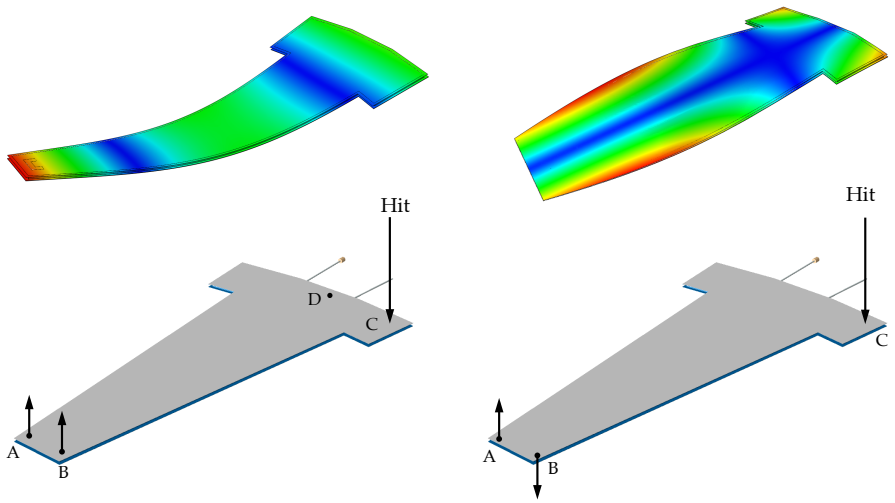

Fig. 3.11: The first bending and torsional modal shapes (top left and right). The corresponding excitation location (shown by hit arrow at C or D) and nodal movements (shown by arrows at A and B).

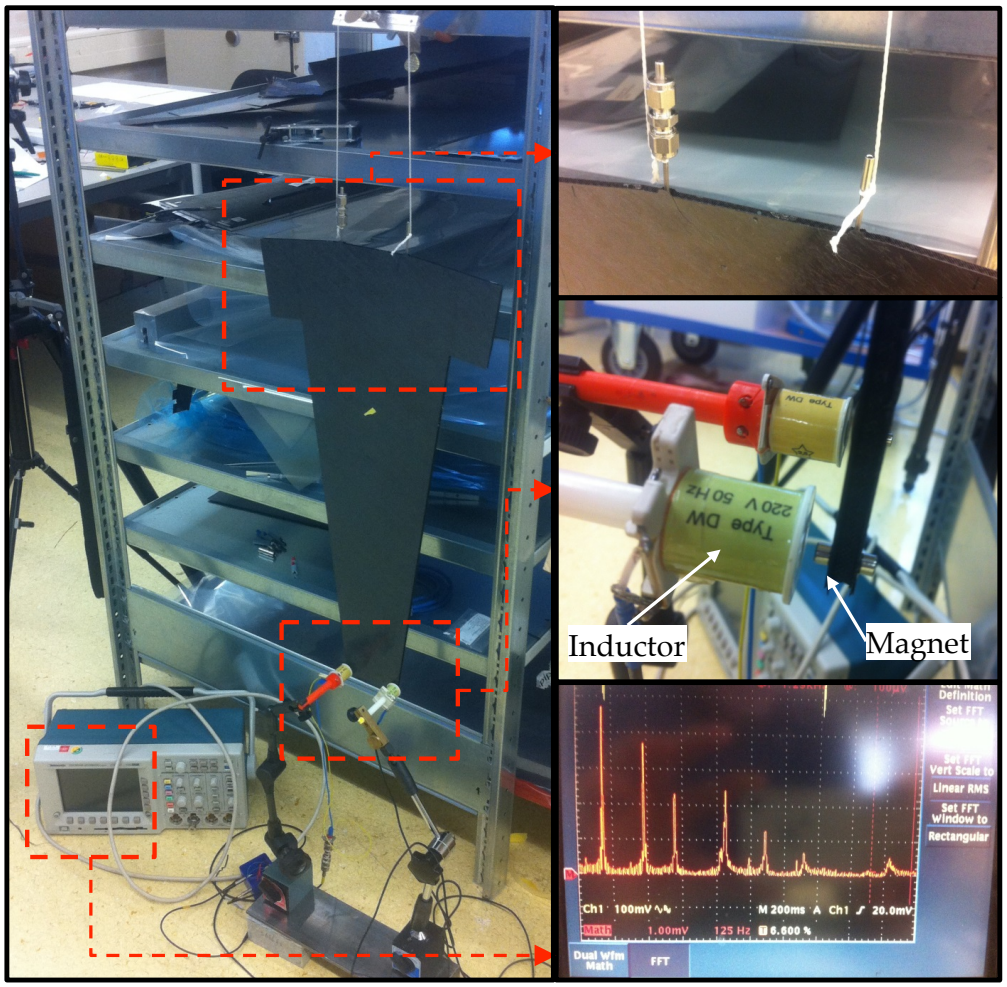

Fig. 3.12: Experimental modal analysis test set-up. The petal is tied to a frame to freely suspend it (top right inset). Magnets are placed at the bottom (middle right inset). Inductors are placed in front of the magnets to read displacement, and the signal is processed (combine, subtract, fourier-transform, etc.) by the oscilloscope (bottom right inset).

The frequencies depend on the effective stiffness of the ODS and mass distribution. Comparing frequencies of different designs helps in optimisation. Another great benefit, particularly important here, is that FEA models give precise prediction of the frequency spectrum, allowing stringent test of the models.

In general, the lowest frequencies of a panel structure belong to bending, torsional and cross-bending modes. Fig. 3.11 gives the first bending and torsional mode shapes, with

the corresponding excitation location and nodal motions. The blue regions have no displacement. Tapping (applying instantaneous force) at these regions will not excite the concerned modes. The red area has the highest displacement in the mode shape, and is the best section to excite the mode and read data. The green has moderate displacement. All modes mentioned above can be excited by tapping at node *C*. We measure at point *A* and *B* because here both modes have large motion, and also the motion is different: in bending *A* and *B* vibrate in the same phase, while in the torsional mode they vibrate with the opposite phases.

Fig. 3.12 gives the experimental set-up in the test facility. The petal was vertically suspended by two strings on the cooling pipe. Small magnets were placed on nodes *A* and *B*. Inductor coils were located in front of the magnets: motion of the magnets induces a current in these coils. The inductors were connected to the oscilloscope, where the generated signals were processed via fourier transform to obtain frequency response.

The excitation force was applied by knocking with a stiff bar at node *C*. The signals coming from nodes *A* and *B* were summed to identify bending modes, and subtracted to recognize only torsional modes. Furthermore, the force was applied to node *D* to excite only bending modes (fig. 3.11).

3.4.3 Results

Fig. 3.13 shows the load versus deflection behaviour of the petal for the three- and four-point bending tests. The slopes give the overall petal bending stiffness, and are

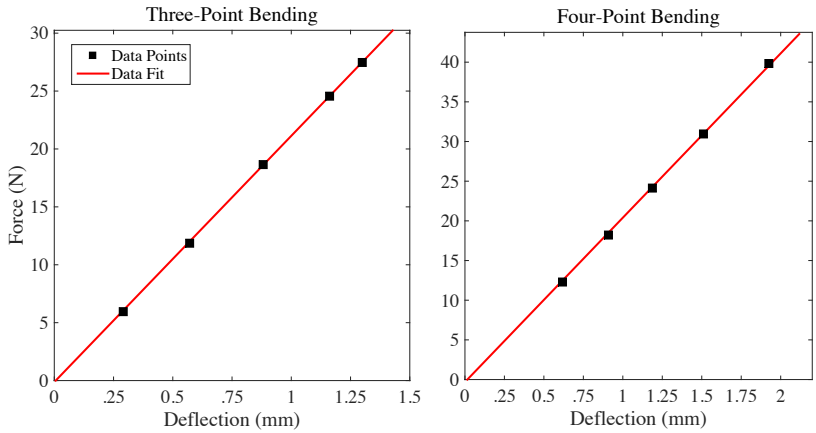

Fig. 3.13: Measured force vs. deflection behaviour of the LoI-Petal with three-point bending (left) and four-point bending (right) tests. Data points are fit to obtain a linear curve, and slope gives the overall bending stiffness, which is 21.26 N/mm for three-point and 20.71 N/mm for four-point bending.

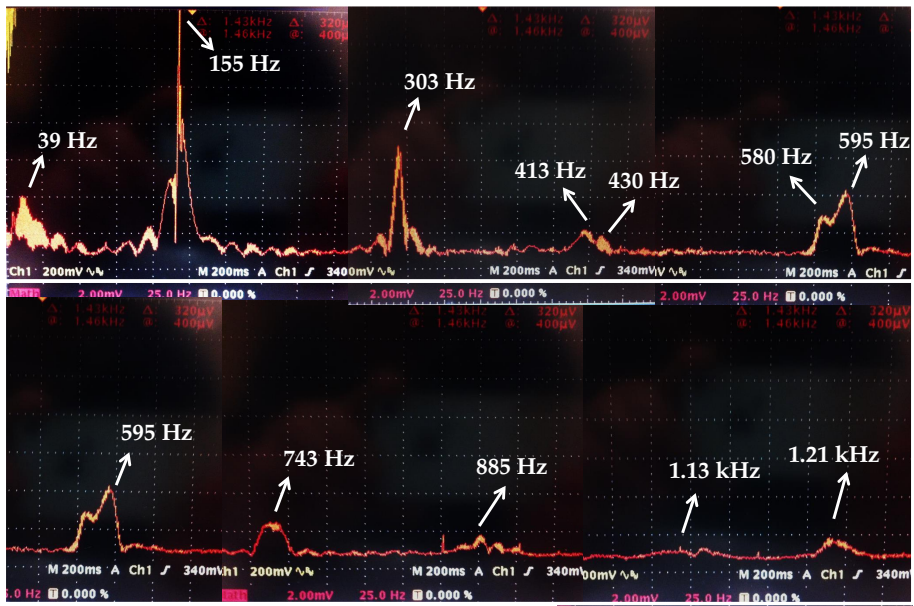

Fig. 3.14: Frequency response of a signal from node *A*, containing all vibration modes, obtained by hitting at node *C*. The response is up to 650 Hz at top and 1300 Hz at bottom. Corresponding modal shapes are listed in table 3.4.

	Natural Frequencies (Hz)			
Bending Modes	155	413	743	1130
Torsional Modes	303	595	885	1210
Cross-Bending Modes	580	-	-	-

Table 3.4: Identified modal shapes and frequencies upto 1.3 kHz from fig. 3.14.

21.26 N/mm for three-point and 20.71 N/mm for four-point bending tests. These are compared with predictions from FEA model in section 3.5.4.

Fig. 3.14 is the frequency response of a signal recorded at node *A* after knocking at point *C*. As mentioned, this signal contains all the vibration modes. The peaks give the resonance frequencies. After careful inspection by knocking at different nodes along with different combination of signals, the corresponding modal shapes of each peak were identified. Consequently, one cross-bending, four bending and four torsional modes were found up to 1.3 kHz, and are listed in table 3.4 along with the natural frequencies. The lowest frequency in the spectrum belongs to the first bending mode, and measured 155 Hz.

The broad peak at 39 Hz is due to the pipe connector (7.5 g), added to this prototype for cooling test (see left pipe at right top inset in fig. 3.12). The effect of the connector was checked via the finite-element model, giving a similar frequency.

3.5 Finite Element Model - LoI Petal

A computational finite-element model of the LoI-Petal was developed to re-produce its measured mechanical behaviour. Abaqus CAE software was used for the modelling. Computations made via this model are compared with measurements to verify the model. This model will be modified for the LTF-Petal design for further studies.

The petal must keep modules in a stable position, so the structure can have only small deformations. Therefore, we are interested in modelling linear elastic behaviour. The model should predict bending behaviour and natural frequencies. The first requires accurate modelling of the mechanical structure, and the second requires correct weight distribution in addition. These two key properties are the main scope of the model.

The first section describes a computer-aided design (CAD) model of the petal. Next, details of the FEM will be explained, along with appropriate section definitions, assigned material types, elements and boundary conditions. Finally, bending stiffness of the petal and natural frequencies will be evaluated, and compared with measurements to check model agreement.

3.5.1 CAD Model

A CAD model of the petal was developed in Abaqus CAE as an assembly of components. All components are 3D deformable solid parts, assembled without any clearances. Tie constraints were defined between all pairs of adjoining surfaces, e.g. outer surface of tube and inner surface of foam, or bottom of facing and top of core. This forces nodes from the different parts lying on the same interface to move together. In practical use, this means the components are bonded perfectly, so the interface is very stiff. CAD assembly of the petal is illustrated in fig. 3.15 as an expanded view, and core-foam-tube connection is shown in fig. 3.16.

The dimensions given in fig. A.4 were used to draw facings. The same sketch with a 5.00 mm internal offset was used to draw the core sketch. The thickness of the facings was based on table 3.1. The cooling tube was designed according to the tube features given in fig. A.5 and fig. A.6. The core was divided into two sections; an offset 5 mm on both sides from the tube (fig. A.6) was defined as the foam region, and the remaining part was the honeycomb core. Meanwhile, the tube was subtracted from the foam part to obtain proper foam geometry. The U-shaped close-outs were added to the sides of the core.

As stated before, the petal contains 20.5 g glue (table 3.1), the distribution of which is not well known. There are four main places where most of the glue is: facing-core, facing-foam, foam-foam and tube-foam interfaces. In order to add the weight of glue at the facing interfaces, the core thickness was taken as 5.00 mm, and two 0.06 mm thick layers were added on top and bottom of the core. Thus the distance between inner

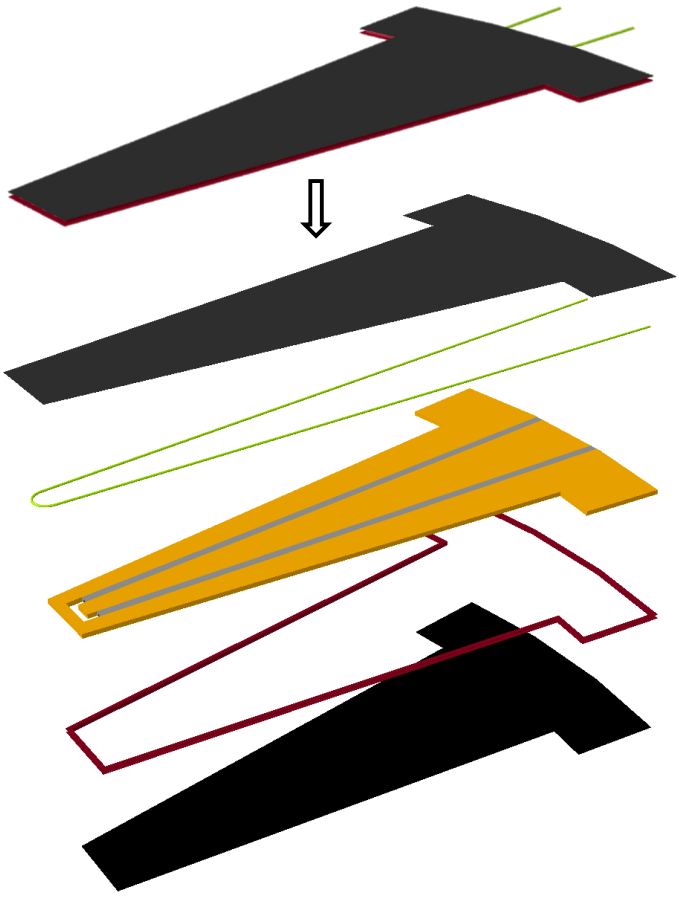

Fig. 3.15: Expanded view of Petal. Respectively from top to bottom, the components are: top facing (black), tube (green), structural core (orange) and foam (grey), close-outs (red) and bottom facing (black). The glue layers between components are not shown above.

sides of facings is 5.12 mm, as in table 3.1. The glue at the foam-foam and foam-tube interfaces is distributed over a very small area; therefore it is highly concentrated. The foam part was divided into two sub-sections, and additional weight was added into a 0.5 mm thick layer near the tube (dark grey in fig. 3.16).

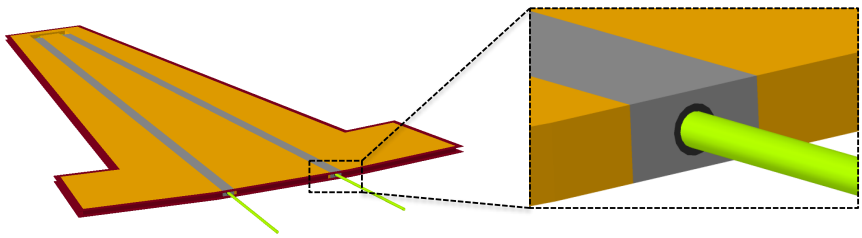

Fig. 3.16: CAD assembly without facings at left. Dashed box with a larger magnification at right: close-outs are removed for a clear view of part connections; dark grey is the inner foam, where the additional glue weight was included.

3.5.2 Property Assignment and Mesh

In Abaqus, the behaviour of a geometrical part is determined by defining its material properties, section and element types. If a material property is direction-dependent, the material orientation has to be defined as well.

Table 3.1 gives the materials used in the components. The majority of the material elastic constants are given in table 2.2, which is based on datasheets from the suppliers. Densities were also taken from table 2.2; however, they were slightly adjusted to agree with the measured weights given in table 3.1. The total glue was distributed over two regions: facing-core interface and inner foam regions, having 14.5 and 6.0 gr glue respectively.

Table 3.5 summarises part geometry, section, material and element types used for each component.

Component	Part	Section	Material	Element	Orientation
Facing	3D	Composite Shell	Lamina	SC8R	Required
Close-outs	3D	Composite Shell	Lamina	SC8R	Required
Honeycomb	3D	Homogeneous Solid	Orthotropic	C3D8R	Required
Foam	3D	Homogeneous Solid	Isotropic	C3D8R	Not Required
Tube	3D	Homogeneous Shell	Isotropic	SC8R	Not Required
Glue Layer	3D	Homogeneous Shell	Isotropic	SC8R	Not Required

Table 3.5: Summary of Petal components with assigned geometry, section, material properties and suitable element types used in Abaqus CAE software.

	A Single Layer of		
	K13D2U-RS3	M55J-AY103	
Fibre-to-Resin Volumetric Ratio	57 / 43	40 / 60	-
Young's Modulus in 0°	531.74	217.00	GPa
Young's Modulus in 90°	10.78	4.00	GPa
In-Plane Shear Modulus	1.13	0.63	GPa

Table 3.6: Fibre-to-resin volumetric ratios used and resulting properties of a single ply. Although the close outs are made from a weave, they are modelled as two layers of unidirectional ply.

Composite Sections

Abaqus composite shell section with a lamina type material is capable of modelling thin composite structures. This section model ignores stress in the normal direction, reducing the problem and requiring the use of shell elements. The lamina-type material is defined by six elastic constants: the ply longitudinal and transverse Young's moduli, three shear moduli and one Poisson's ratio. The shear properties in the normal direction are also included to capture transverse shear deformation, although this kind of deformation is unlikely to happen in sandwich structures with very thin skins. Elastic constants of a lamina were calculated by following section 3.3.1, and are presented in table 3.6.

The orientation of the material was described for the facings, where the axis-1 is pointing in the longitudinal direction of the petal, axis-2 is perpendicular to the axis-1 in the width direction, and axis-3 is in the thickness direction of the petal. The facings were defined as a composite shell section comprised of 3 unidirectional plies having 0.33/0.34/0.33 relative section thicknesses. Each layer was oriented in $60°/0°/-60°$ angles in relation to the axis-1, with top and bottom facesheets symmetric about the mid-plane.

Close-outs at petal edges were split into straight beams. Material orientations were defined by taking the beam axis as the material axis-1. Axis-3 was always the thickness direction. The beams were also defined as a composite shell section consisting of 2 unidirectional plies, each having 0.5 relative section thickness and oriented in $0°/90°$ angles with respect to axis-1. Since the close-outs were made via hand layup, the resin content is much higher than that of the prepreg. The fibre-to-resin volumetric ratio was taken as 40/60.

Homogeneous Sections

Honeycomb core is an orthotropic material [81], so a homogeneous solid section with orthotropic material properties was assigned. The orientation of the material was defined by three axes: axis-1, 2 and 3 lie along the ribbon, transverse ribbon, and

thickness directions. The core is arranged in the petal with the ribbon direction along the petal longitudinal direction. The mechanical properties are defined by 9 elastic constants: 3 Young's moduli, 3 shear moduli and 3 Poisson's ratios. Two shear moduli in the panel thickness directions (G_{13} and G_{23}) are given in table 2.2. Honeycomb core has a very low shear modulus in the in-plane direction (G_{12}); therefore it was set to 1% of G_{13}. The Young's modulus in the thickness direction E_3 was taken as 100 MPa to make it stiff enough to keep core thickness constant during simulation, and is reasonable by comparing the compressive modulus given for various honeycomb materials [82]. Since the honeycomb core does not have any axial rigidity in the ribbon and transverse ribbon directions, the other two Young's moduli (E_1 and E_2) were kept very close to zero. The Poisson's ratios in the thickness direction (ν_{13} and ν_{23}) are very close to zero, however small non-zero values were used[13]. The Poisson's ratios in the in-plane directions under loading in thickness direction (ν_{31} and ν_{32}) were assumed 0.33 taken from [39]. The effect of in-plane Poisson's ratio (ν_{12}) is negligible on sandwich panel stiffness (see fig. 2 in [40]), and it is assumed the same as ν_{31}.

The foam contributes to bending stiffness by keeping the distance between the facesheets constant and through its shear modulus. The prototype has Poco-HTC foam, with no Young's modulus given[14]. Instead we used properties of Pocofoam, which is similar. The overall effect of the foam is small, and so it is modelled simply as a homogeneous isotropic material, with properties given in table 2.1.

Since the tube is very thin, it was modelled as a shell homogeneous section with isotropic material properties. The glue layers between the facing and the core were defined as a shell homogeneous section with isotropic material properties as well. The Young's modulus of the glue was kept the same as the honeycomb modulus in the thickness direction. This allows adjustment of the weight distribution without affecting the stiffness.

Element Choice and Meshing

Abaqus gives a wide range of choice for element types.

For the shell sections, we selected general purpose continuum-shell elements with 8 nodes, reduced integration, called SC8R. Continuum-shells capture response of the thin structures in the thickness direction better, and component needs to be meshed with a single element layer. Reduced-integration elements need less computational effort. The facesheet and glue layers were meshed into 70,836 elements.

[13] If the FEA program calculates other Poisson's ratio by $\nu_{ji} = \nu_{ij}E_j/E_i$, zero value for ν_{ij} will also result in zero for ν_{ji}, and will cause non-diagonal components in the compliance matrix to be zero. Instead, we calculated ν_{13} and ν_{23} by using ν_{31} and ν_{32}, returning very small values (close to zero). Then, we calculated components of the stiffness matrix for orthotropic material, and directly defined components in the FEA program as material properties.

[14] Later, the Young's modulus of Poco-HTC will be measured, see section 4.1

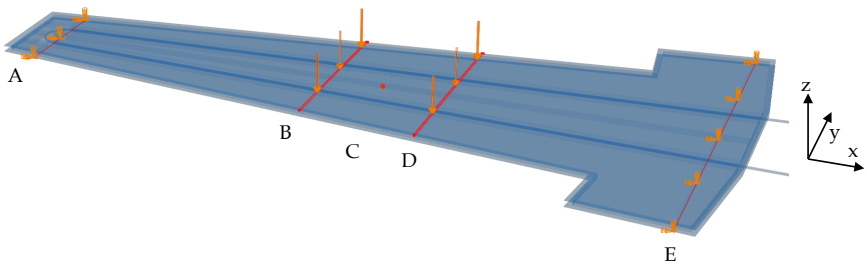

Fig. 3.17: Boundary conditions for four-point bending analysis. See fig. 3.10 for position of lines. It is supported from the bottom facing along A and E, and loads were applied to the top facing along B and D.

For the solid sections, continuum 3D, 8-node, reduced integration, linear elements, called C3D8R were selected. These work well with the planar straight-edged geometry of a petal, with no need for more complicated element shapes, such as tetrahedral element, that are better suited to capture complex geometries. The honeycomb and foam were meshed into 185,218 elements. In total, including the remaining components, the model has 287,553 elements.

3.5.3 Boundary Conditions

The simulations emulated the tests in table 3.3. Fig. 3.17 shows the petal with applied boundary conditions for the four-point bending test, with the axes of directions. Concentrated force may lead high deformation (similar to crumpling) at the forced node, applied force is distributed over an area by using uniform pressure to avoid this. All the loads and supports were applied across the full width in order to prevent deformation along y. The following boundary conditions and loads were applied:

- One end of the bottom facing (A) was pinned by prescribing zero displacements to all directions, i.e. $u_x = 0$, $u_y = 0$ and $u_z = 0$.
- The other end of the bottom facing (E) was constrained by prescribing zero displacement in the vertical and width directions, and leaving the structure free to slide along the longitudinal direction, i.e. $u_x =$ free, $u_y = 0$ and $u_z = 0$.
- Uniform pressure was applied along the loading lines on the upper facing: B and D for four-point and only D for three-point. The width in x of the pressurized region was 1 mm to keep load concentrated in a small area. In four-point bending test, pressures were adjusted to keep applied forces equal along both lines, $F_B = F_D$.

No boundary conditions were defined for the free-body modal analysis.

	Bending Stiffness		Units
	3-Point	4-Point	
Measurement	21.26	20.71	N/mm
FEA	21.80	20.83	N/mm
Relative Error	2.5	0.6	%

Table 3.7: Results of the three and four-point petal bending tests and analyses. The predictions are very close to the measured values.

	B_1	B_2	B_3	B_4	T_1	T_2	T_3	T_4	CB_1	
Measurement	155	413	743	1130	303	595	885	1210	580	Hz
FEA	162	405	722	1045	290	562	833	1082	553	Hz
Relative Error	4.3	-2.0	-2.9	-8.1	-4.5	-5.9	-6.2	-11.8	-4.5	%

Table 3.8: Natural frequencies from measurement and free-body modal analysis. B, T and CB refer to bending, torsional and cross-bending mode shapes. Subscripts indicate the sequence of the modal shape. The model is correct within 5 % for the lowest mode in each mode shape, worsening with frequency to ~ 10 % for B_4 and T_4. The lowest frequency belongs to the first bending mode B_1, which is the most critical mode for the petal design.

3.5.4 Model Verification

Results of the bending and modal analyses were compared with measurements to check model agreement.

Bending deflection (Δ) was read at the node-C in fig. 3.17. The applied pressures were multiplied with the corresponding application area to give the force (F) on the body. The bending stiffness is F/Δ. The bending stiffness for both bending analyses are given in table 3.7 along with the results from the measurements. The predictions of the bending stiffness are within 2.5 % agreement.

The lowest four bending modes, four torsional modes and one cross-bending mode frequencies were evaluated in the free-body modal analysis, and are given in table 3.8 in comparison with measurements. The lowest natural frequencies of each modal shape are within 5 % agreement, getting slowly worse with the increasing number of waves in the modal shapes. In conclusion, the model is verified at better than 5 % for bending and the lowest-frequency modes of each modal shape.

In table 3.8, while the first bending frequency is predicted high, the frequency of higher modes are predicted low. In the facesheets used in the prototype, fibers are not perfectly aligned parallel to each other. Misalignment of fibers has been shown in page 23 in [83] with large scale images, and the spread angle of fibers has been measured $\pm 2.8^\circ$. By using eqs. (3.20) and (3.21), the elastic modulus of the prepreg was calculated by aligning fibers with 2.8° angle; the modulus decreased around 50 %. In the model,

fibers are perfectly aligned, so the stiffness is over-predicted.

When the mode number increases, the effective length of the bent section gets shorter: L gets smaller in eq. (3.22). The pure bending deformation decreases, and the core shear deformation plays a more important role in the overall response of the structure. Consequently, the structural response becomes less sensitive to the properties of the facesheet, and is more dominated by the core shear properties. If the shear properties of the core in the model are lower than actual, the frequencies of the higher modes are under-predicted. Similarly, torsion and cross-bending modes are more affected by the core properties, and also these frequencies were under-predicted.

In order to verify this observation, another analysis was performed by increasing core shear moduli, while keeping the facesheet properties equal. When the first bending frequency remained the same, all the other frequencies increased.

3.6 Design Improvement

3.6.1 Design Targets and Constraints

As mentioned in section 1.5, the new tracker requires structures with very low fractional radiation length $\%X_0$ to reduce the deviation of the particle from its original trajectory and radiation loads accumulated on the structure. The fractional radiation length[15] of the earlier design was 0.54 %; the new design should have a lower value. As described by eq. (1.3), this goal can be achieved by using either thinner structures or materials with low-density and low atomic number. In conclusion, the new design should be made of less material; and the primary purpose of the study is to reduce the weight of the components. Since the amount of material in electronics, sensors and bus tape are very difficult to reduce, the focus on the improvement was moved to the composite facesheets and core components.

However, these two components are crucial for the rigidity of the structural support, and reconfiguration may disrupt position stability of the modules. Fig. 3.18 illustrates how the petals are installed in the Atlas tracker support frame. The petal is placed in a plane perpendicular to the beam axis with quasi-kinematic mounts at both ends, and the beam axis has a 2° slope. These mounts ensure the petals carry only their own weight. Since the petal is vertically placed, gravitational weight gives only in-plane loads, and negligible gravitational sag. The positional stability is related to dynamic behaviour of the structure. The maximum amplitude of a vibrational mode depends on the resonance frequencies, the power spectral density causing the excitation, and the damping characterizing energy dissipation. All modes which can be excited while the petal is fully equipped and installed in the Atlas Tracker are important,

[15] See section A.2 for the procedure followed to calculate the radiation length of composite materials, components and the whole structure.

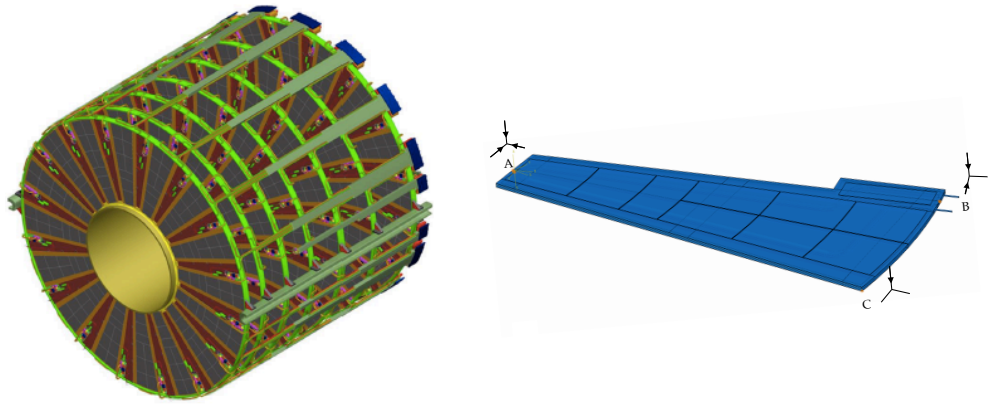

Fig. 3.18: At left, an example is given for the petal installation mechanism to the space-frame in the Atlas tracker. This is a proposed installation system taken from [85], and it is not the final design. At right, expected petal fixation mechanism is given. Quasi-kinematic mountings are located at marked points, and constrained translations are shown by arrows. The three mountings together restrict translational and rotational rigid body motion of the petal.

including bending and torsion. Underground laboratories tend to have 0-10 Hz as the important range of frequencies in the power spectral density [84], and we accepted 50 Hz as a very safe lower limit for frequencies of important modes in this work. In order to accomplish the design target — of both weight reduction and keeping positional stability safe — the method is to first improve overall stiffness of the structure, and then remove unnecessary material[16]. The measurements made on the bare LoI petal showed that the lowest natural frequency belongs to the bending deformation mode. Consequently, this mode is more critical over the torsion, and the stiffness improvement will be specifically made for this mode.

As described in eq. (3.22), the bending stiffness of the petal can be improved by increasing the bending rigidity of the facings and increasing the core shear rigidity. Using thicker core is one of the ways to improve the facing's bending rigidity. However, the modules on each side will get further apart, increasing the gap for a particle to pass through without hitting a second layer of sensor. Consequently, resolution of the tracker would get worse. Furthermore, implementing thicker core will worsen the thermal performance with current tube configuration. Changing the core thickness will affect the physics performance and is beyond the scope of this study.

The temperature differences between curing, assembly and operation lead to internal

[16]The relation between the natural frequency ω, stiffness k and mass m for a single degree of freedom mass-spring system is $\omega = \sqrt{k/m}$. Using less material in the facesheets decreases the bending stiffness. However, overall mass reduction in the sandwich structure will not be affected the same as stiffness. Therefore, the natural frequency will be lower. To avoid this, the main objective is to increase stiffness first.

stresses in the facesheets, and will cause deterioration of the flatness. To avoid this, symmetric lay-ups are required with respect to the petal mid-plane. Another design preference by the design team is to use either cross-ply laminate (consisting of only 0° and 90° plies, e.g. $0/90^\circ$) or quasi-isotropic laminate such as $-60/0/60^\circ$ or $45/-45/0/90^\circ$. From quasi-isotropic laminates, $-60/0/60^\circ$ is preferred due to its thinner form.

Another design issue is that reduction of facesheet material gives higher stresses along the fibers and in the matrix. Stresses must stay below the failure level.

3.6.2 Procedure

The petal was simplified to a rectangular sandwich panel consisting only of two facings and a core to ease application of eq. (3.22). Only concentrated loads were considered, and gravitational effects were ignored; this applies $W = 0$ in eq. (3.22). Equation was rearranged to give bending stiffness, F/Δ. The panel length and core thickness were assumed to be as in the petal; they are 632 and 5.12 mm (see fig. A.4 and table 3.1). The width is 240 mm, chosen to give bending stiffness similar to table 3.7. The facing consists of 3 plies of a prepreg, and its thickness was calculated according to the prepreg choice (by using eq. (3.2)). The bending stiffness was calculated for several material configurations for comparison.

We consider two different angular configurations for the facings:

- $[60/0/\text{-}60]^\circ$,
- $[0/90/0]^\circ$,

two types of unidirectional prepregs:

- 80 gsm K13D2U/RS3,
- 45 gsm K13C2U/EX1515,

and three types of honeycomb core materials:

- Goodfellow Nomex® AR312810,
- Plascore Kevlar® N636 PK2-3/16-2.0,
- Ultracore® UCF-208F-3/8-2.0 carbon fibre.

Firstly, angular configuration of the facings was changed to $[0/90/0]^\circ$ to improve the bending stiffness. This allowed to replace the facings with a thinner and lighter prepreg, which reduced $\%X_0$ but also lowered the bending stiffness. At the end, different core materials were compared.

3.6.3 Angular Configuration of the Facings

We get insight into the angular configuration of the facings by considering a symmetric lay-up, with no core. Two different configurations were considered: 6 layers, laid-up in

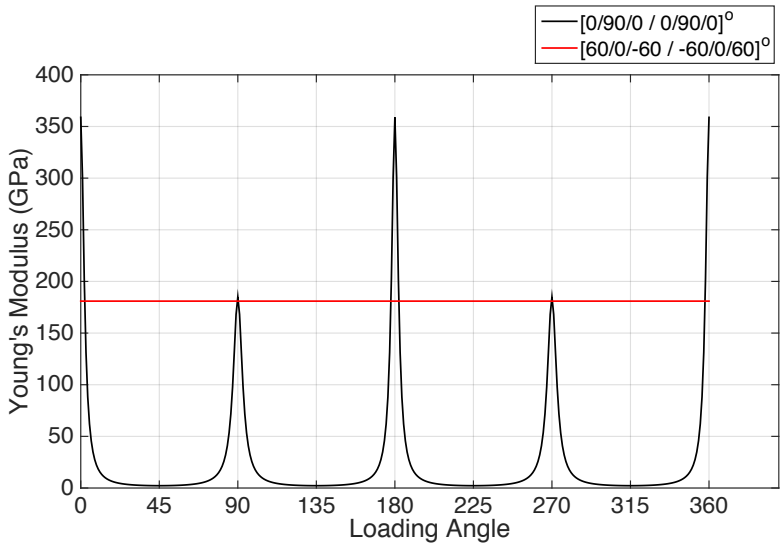

Fig. 3.19: The Young's modulus of the composite in the angular directions with respect to the longitudinal axis. The laminated composite consists of 6 plies and is symmetric around mid-plane. The 80 gsm K13D2U/RS3 unidirectional prepreg was used as a ply. Two different angular configurations were used in the composite. The $[60/0/-60]^\circ$ configuration (red line) has a constant modulus. The $[0/90/0]^\circ$ configuration (black line) doubles the modulus along 0°, and has similar modulus at 90°. However, it has almost zero Young's modulus in between these angles, suggesting low rigidity in torsional mode.

$[60/0/\text{-}60/\text{-}60/0/60]^\circ$ and $[0/90/0/0/90/0]^\circ$ configurations. The Young's modulus of the composites was calculated in all directions with respect to the 0° lay-up direction[17]. The calculated moduli are given in fig. 3.19.

As clearly seen in fig. 3.19, the $[60/0/\text{-}60]^\circ$ configuration gives isotropic in-plane properties. Changing to $[0/90/0]^\circ$ configuration almost doubles the longitudinal Young's modulus (at 0°), while the transverse modulus (at 90°) remains similar. In-between, the modulus is highly decreased. Consequently, $[0/90/0]^\circ$ configuration attains rigid structure in both longitudinal and transverse bending, while $[60/0/\text{-}60]^\circ$ configuration suggests better mechanical properties in the torsional modes. Note the thermal conductivities follow similar patterns, so the choice must also be checked for cooling performance. Since the lowest modal frequency is the longitudinal bending mode (see table 3.4), we are more interested in how to improve rigidity of this mode. Therefore $[0/90/0]^\circ$ lay-up configuration was selected for the new design.

[17] By following eqs. (3.20) and (3.21).

3.6.4 Facing Selection

As listed in table 3.1, 47 % of the bare petal weight comes from the facings, while only 7 % comes from the honeycomb core. This difference indicates that the $\%X_0$ is dominated by the facings, and further improvement to facings will improve the design more effectively than will changes to the other components.

Since the $[0/90/0]^\circ$ lay-up almost doubles the longitudinal Young's modulus (fig. 3.19), we study reducing the facings thickness. We consider a K13C2U prepreg with fibre areal weight of 45 gsm; this is a 44 % reduction with respect to the 80 gsm prepreg. The gain in facing tension stiffness due to angular configuration and the loss due to lower fibre areal weight almost cancel each other; thus the longitudinal bending behaviour remained very similar (see black dashed line and red line in fig. 3.20).

Calculated elastic, volumetric and mass properties of both prepregs are given in table 3.9. Using the 45 gsm prepreg with volumetric properties similar to 80 gsm prepreg (with 57/43 fibre-to-resin vol. ratio) is expected to lower the facing thickness and weight about 44 % as well. However, the 45 gsm prepreg has 41/59 fibre-to-resin volumetric ratio, i.e. contains more resin. As a result, reduction in the weight and fractional radiation length remain at 30 %, which is far from the expected improvement. The extra resin could be removed for further improvement, using for example an absorbent peel-ply during manufacturing. In this ideal case, the facing weight can be reduced 11 gr more. However, currently petal manufacture anticipates co-curing the bus tape with the facesheet. The extra resin allows this to work (but note this removes one of the prime motivations for co-curing, which was to avoid the facesheet to bus tape glue layer).

	K13D2U/ RS3	K13C2U/ EX1515	Change
Fibre Areal Weight (gsm)	80	45	−44 %
Ply Thickness, t (μm)	64	50	−22 %
Volumetric Resin Content (%)	43	59	37 %
Volumetric Fibre Content (%)	57	41	−28 %
Facings Weight (gr)	79	56	−30 %
Ply Young's modulus, E (GPa)	532	372	−30 %
Ply Stiffness (N/m$\times 10^6$)	33.9	18.4	−45 %
Ply Frac. Rad. Length (%)	0.24	0.17	−29 %

Table 3.9: Mass, volumetric and elastic properties of both prepreg. The Young's modulus (E) is given for a single ply of a unidirectional prepreg in the fibre direction. The ply stiffness is Ewt/l, where w and l is width and length of a ply, which are unit dimensions. Facing weight was calculated by considering the facing design in the LoI-Petal and given as sum of the two. By reducing fibre areal weight around 44 % resulted in a similar reduction in the ply stiffness, however overall weight reduction remained at 30 % due to higher resin content.

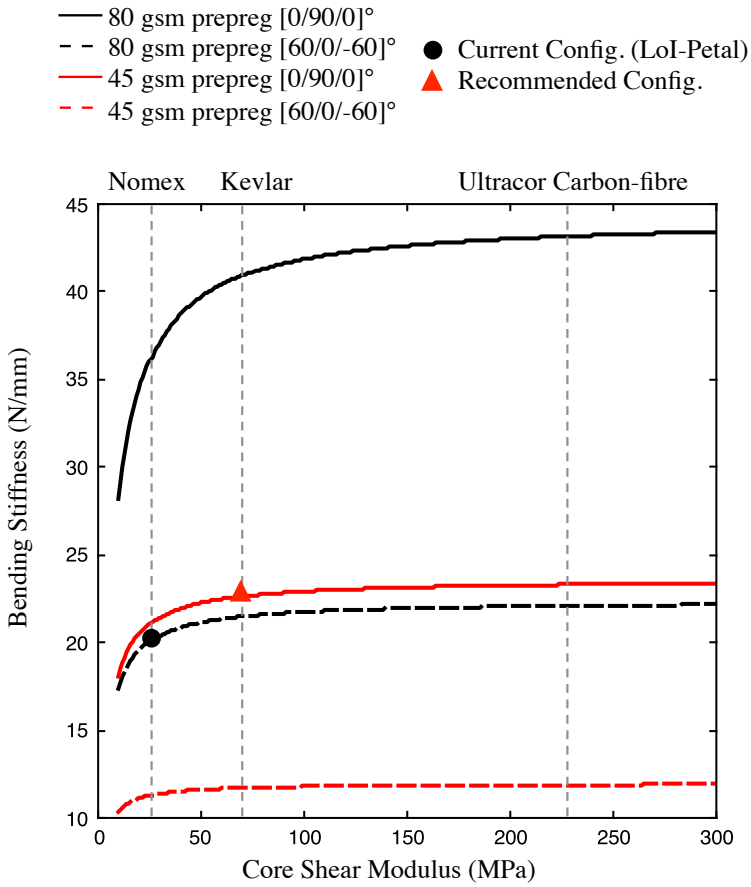

Fig. 3.20: Three-point bending stiffness versus core shear modulus in the panel longitudinal direction. Two different prepregs with two different angular lay-up configurations were modelled. 80 gsm prepreg is the K13D2U/RS3, and 45 gsm prepreg is the K13C2U/EX1515. Vertical dashed-lines correspond to available core materials of interest. Filled-markers indicate the original and recommended material configurations. Panel with stiffer facings (continuous black line) benefit more from higher core shear modulus. After about 70 MPa shear modulus, there is little improvement for the recommended facesheet material (continuous red line).

Panel bending stiffness can be increased with a thicker core (see eq. (3.24)), which will not create excessive additional weight. That would allow even lower fibre areal weight in the facings. However, the 45 gsm prepreg offers one of the lowest fibre areal weights on the market, and so we will continue the design process with this product. If new prepregs emerge in the future offering lower than this value, they are highly recommended for the new petal design.

3.6.5 Core Selection

Fig. 3.20 gives the longitudinal three-point bending stiffness with respect to the core shear modulus, from eq. (3.22), for various designs. The vertical dashed-lines on the graph correspond to specific honeycomb core materials of interest. The filled-markers give the old and recommended material configurations.

As seen in fig. 3.20, 80 gsm prepreg with $[0/90/0]^\circ$ configuration has the highest bending stiffness. Increasing core shear to about 70 MPa gives significant improvement in stiffness, reaching 95 % of the ultimate value (black line). For less rigid facesheet configurations, 95 % of the ultimate stiffness is reached with cores with shear modulus less than 70 MPa. This behaviour can be traced back to eq. (3.22), showing that rigid facesheets (large D_f) suppress the bending mode Δ_b, making the shear deformation Δ_s dominant. Panel bending stiffness is less sensitive to core shear for lower facesheet rigidity (red line).

By carefully examining fig. 3.20, we see that Plascore Kevlar® significantly improves the bending stiffness for most of the facing configurations. Improvement is around 14 % and 8 % for K13D2U/RS3 and K13C2U/EX1515 with $[0/90/0]^\circ$ configurations. Although Ultracore® carbon-fibre core offers almost 3 times higher shear modulus than Plascore Kevlar, it brings very little improvement in stiffness. Besides, it has 1.5 times higher density than the Kevlar, and costs far more. As a result, Plascore Kevlar is highly recommended for the new design.

3.7 Performance Evaluation

The finite-element model developed for the LoI-Petal (Nikhef prototype) was modified to model the LTF-design (section 3.2). The components of the bare petal were similar to fig. 3.15, except in a slightly different geometric form. The model was extended by adding the bus tape, sensor modules, EoP board and glue layers between them to account for weight and stiffness contributions. We ignored chips, electronics and DC-DC converters, since they do not have a significant influence on the bending stiffness. However, their weights were included in the sensor module components.

Extra resin in the facesheets of the LTF-design is used to glue bus tape to the facesheet. This glue would also be necessary to use in Nikhef-LoI configuration. Therefore, we attribute this extra glue to a separate layer between the facing and the bus tape, and we consider the facesheets with minimal resin content (about 57/43 fibre-to-resin vol. ratio). The bare petal model includes this glue layer.

The modified model is shown in fig. 3.21. Bus tape (orange) was continuous through the whole petal surface. Silicon detector layers (grey) were modelled as 9 separate modules on each side. Shell section was defined for both components, and a single layer of SC8R elements was used to mesh them. The close-outs were modelled as a

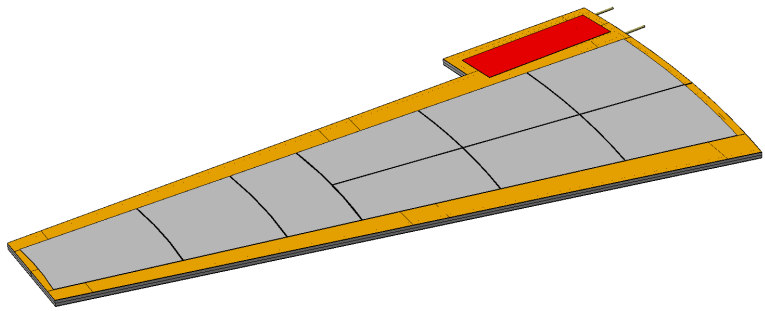

Fig. 3.21: Modified FEA model for the Petal LTF. The model is similar to the LoI-Petal in fig. 3.15. This model is extended by including bus tape (orange), silicon modules (grey), EoP board (red) and glue (not visible above) between the components.

rectangular continuous bar with homogeneous material[18], using C3D8R elements. The model contains 225,000 elements in total.

The sensors are made of silicon wafers, which have 129.5 GPa Young's modulus, given in table 1 in reference [68]. The bus tape, thermal management adhesive DC SE4445, and EoP polyimide circuit board have low modulus compared to the facings and Si-wafers; therefore they do not make a significant contribution to the structural behaviour. Their Young's moduli were set to 3 GPa.

The materials used are given in table 3.2. The LTF dimensions are given in fig. A.7. Note the LTF-Petal is shorter than the LoI geometry, making it stiffer and increasing its natural frequencies.

Three-point bending simulations were performed for both bare and fully-loaded petals to evaluate bending stiffness. The boundary conditions are described in appendix section A.4.

Free body modal analyses were performed to determine the lowest frequencies for the bending and torsional modes. These were carried out for both bare and fully-loaded petals. Additionally, constrained body modal analyses were carried out to assess petal performance when fixed in the completed end-cap. The boundary conditions for this assume kinematic mounting (more details in appendix section A.5).

For comparison, the LTF geometry was simulated with various facesheet and core material configurations: used in DESY LTF design, used in Nikhef-LoI prototype and as recommended in section 3.6. Table 3.10 summarises the cases studied, giving masses

[18] In the DESY prototype, the close-outs are made from PEEK with holes cut-out to reduce material. These holes were not modelled, justified since the close-outs have very little effect on petal bending stiffness: reducing the Young's modulus by a factor 10 reduced stiffness by only 1.7 % for the petal with modules.

of components used, and the results of the simulations. These results are discussed in the next two sections. The recommended configuration is compared with the Nikhef-LoI configuration in section 3.7.1, and with the DESY design in section 3.7.2.

3.7.1 Comparison with the Nikhef Configuration

Replacing the facing with 45 gsm K13C2U/EX1515 prepreg with low resin content reduces facesheet mass and fractional radiation length by about 42 %, table 3.10. The core replacement is heavier, the net reduction in weight and fractional radiation length were around 16 % for the bare petal. The reduction in the fractional radiation length over the fully-equipped petal (i.e. with modules, bus tape etc.) is much smaller.

The bending stiffness increases slightly (5 %) despite the thinner facesheet due to the switch to $[0/90/0]^\circ$ lay-up. When the modules are mounted, the silicon wafers contribute significantly to the bending stiffness, which almost doubles. The pure bending deformation reduces, and the shear deformation becomes more significant. The stiffness gain coming from the better core is higher for the fully loaded petal case, so that the recommended configuration is 10 % stiffer.

Stiffness gain along with weight reduction results in higher bending natural frequencies. The increase was around 9 % and 5 % for the constrained petal in both bare and fully loaded conditions.

In contrast, since the $[0/90/0]^\circ$ angular configuration has low rigidity away from 0 and 90°, the torsional stiffness drops with dramatic reduction in the corresponding resonance frequency for the bare petal (around 80 % reduction), and becomes the lowest frequency mode. In the fully loaded case, the wafers contribute to diagonal stiffness as well: the reduction in the torsional mode frequencies are less dramatic (about 25 %), and the bending mode remains the lowest frequency.

3.7.2 Comparison with the DESY 2016 Configuration

In another study, the recommended configuration was checked against the DESY configuration updated in 2016, table 3.10. The facings are the same, but the honeycomb is different. UCF carbon-fibre honeycomb is almost 1.5 times denser and has almost 3 times higher shear modulus than the Kevlar honeycomb, and was used in the DESY configuration. Changing to the recommended Kevlar saves 8 g or 5 % of bare petal mass.

The recommended configuration further improves the DESY design, and reduces the fractional radiation length by 5 %. It should be noted that these calculations were done by considering the use of plastic close-outs. It is possible to lower petal weight

	Nikhef	DESY	Recomm.
Material Configuration:			
Facing	K13D2U 80 gsm [60/0/-60]°	K13C2U 45 gsm [0/90/0]°	K13C2U 45 gsm [0/90/0]°
Core	Nomex	UCF	Kevlar
Shear Modulus in Ribbon Dir. (MPa)	25	228	70
Core Density (g/cm^3)	0.024	0.048	0.032
Masses (g)			
Facings	78.4	45.2	45.2
Core	11.8	23.7	15.8
Bare Petal (incl. bus-to-facing glue)	168	147	139
Petal (with bus, modules and EoP)	517	496	488
Bare petal :			
Bending Stiffness (N/mm)	20.4	21.9	21.4
Free body bending freq. (Hz)	177.0	197.1	199.6
Free body torsional freq. (Hz)	302.4	61.1	62.0
Constrained body bending freq. (Hz)	80.2	85.8	87.2
Constrained body torsional freq. (Hz)	188.9	40.0	40.7
Petal with bus, modules and EoP:			
Bending Stiffness (N/mm)	35.9	41.9	39.3
Free body bending freq. (Hz)	144.5	158.2	154.5
Free body torsional freq. (Hz)	271.1	215.6	196.0
Constrained body bending freq. (Hz)	60.5	65.3	63.7
Constrained body torsional freq. (Hz)	155.4	133.8	121.9
Fractional Radiation Lengths, $\%X_0$:			
$\%X_0$ of Facings	0.2374	0.1369	0.1369
$\%X_0$ of Core	0.0371	0.0718	0.0496
$\%X_0$ of the base petal	0.5421	0.4760	0.4536
Reduction in $\%X_0$	-	12 %	16 %

Table 3.10: Masses used and results of analyses for LTF-Petals with different facing and core configurations. See the text for discussion. 11 g bus-to-facing glue is included in the calculations for bare petal. At the last row section, calculated fractional radiation lengths are given.

around 20 g by making close-outs from carbon-fibre composite (see the difference between weights of close-outs in tables 3.1 and 3.2). We recommend reverting to carbon-fibre close-outs, retaining plastic only for mounting points and cooling-tube strain-relief. For this configuration, the fractional radiation length was calculated 0.4, improving the DESY configuration by 11 % more.

The shear modulus reduction (around 70 %) has very little effect on stiffness (around

2 %), as expected from fig. 3.20. The lighter core actually increases the natural frequencies for both bending and torsional modes of the constrained bare petal (around 2 %).

In case of the fully-loaded petal, the modules contribute to the bending rigidity of the skins (large D_f), making structure more sensitive to the core shear properties. The petal bending stiffness reduces around 6 %. As a result, the bending frequencies drop slightly (2 %), and the torsional mode frequencies have a more significant decrease (9 %).

All in all, the use of Kevlar honeycomb drops the weight 8 g at the cost of 2 % reduction in the lowest frequency for the petal constrained and fully-loaded. The Kevlar is also much more cost effective. On balance, we recommend the Kevlar core.

3.7.3 Design Verification

The thinner facesheets have higher stresses. Therefore the recommended design has to be checked for failure. It turns out the safety margins are more than a factor 100. We have made a simple FEA study to verify this (for example, not using the Tsai-Wu tensor polynomial failure criterion [86]).

In order to read ply-wise stresses, the FEA model was modified to use the Abaqus conventional shell section for the facesheets. A new set of simulations were performed on the petal. The same boundary conditions used for constrained body modal analysis were used in these analyses (see section A.5), and only gravitational loads were included. The loads were calculated by taking a 2° slope of the beam axis into account. Analyses were performed on the petal installed as in fig. 3.18 for 5 different position cases: petal positioned 0° (up-down position), 45°, 90°, 135° and 180° in the space-frame. For 0° and 180°, all load is carried by the mount at A. At other positions, some load is taken by the slot mount at B. Then, the ply-wise stresses were studied for each ply. The stress along the fiber direction was always the highest.

Figures 3.22 and 3.23 give the stress in the fiber direction for the longitudinal (0°) and transverse (90°) plies in the +z facesheet for five different installation cases. The other plies with the same alignment showed similar stress distributions.

For the longitudinal ply (fig. 3.22), the highest stress was obtained at mount A when the petal is positioned vertical (0° and 180° installation case), and was 2.4 MPa in compression mode for 0° installation and tension mode for 180° installation. The tensile fracture stress is 2.2 GPa for a unidirectional layer, table 2.2. Roughly adjusting it to a compression mode according to section 2.1 (by using the ratio of strengths given for a typical product) gives 1.43 GPa. Both evaluated stresses are very far from fracture.

For the transverse ply (fig. 3.23), the highest stress occurs at the mounting B, when the petal is positioned at 90°. The maximum stress was 3.9 MPa near the mounting.

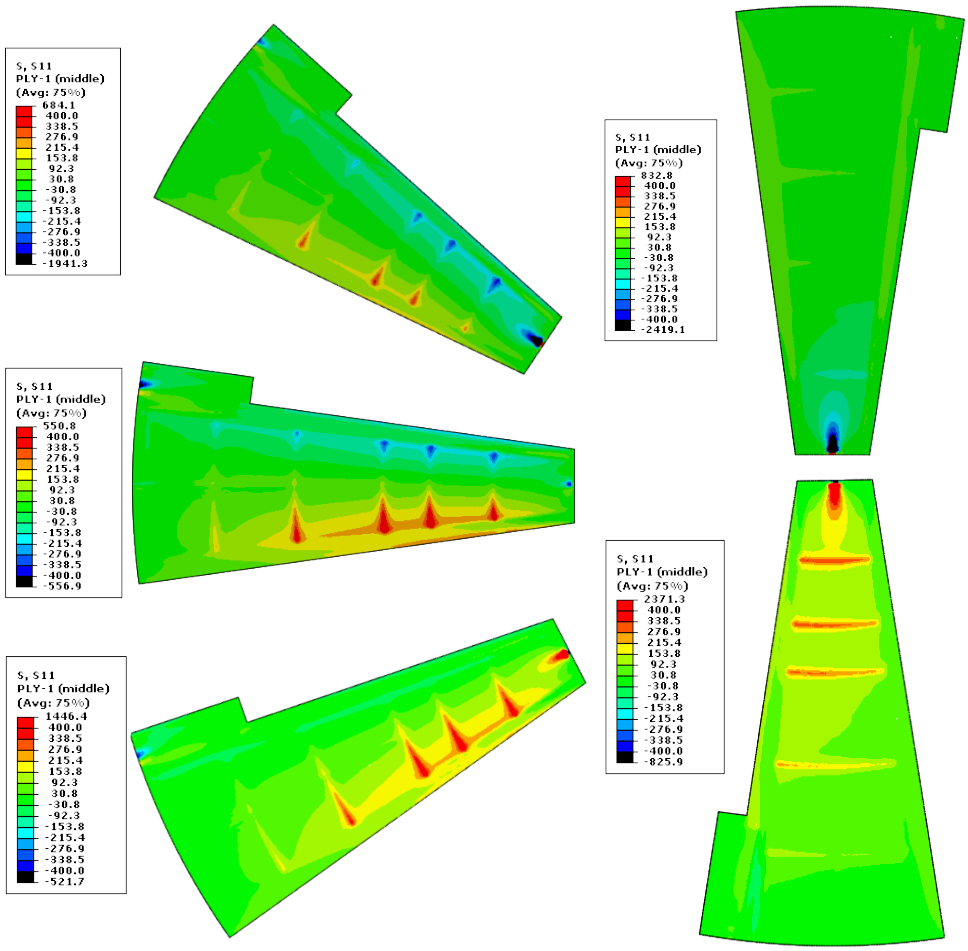

Fig. 3.22: Stress in the fiber axis for 0° ply for five different installation cases. Stresses are in kPa, for the recommended design.

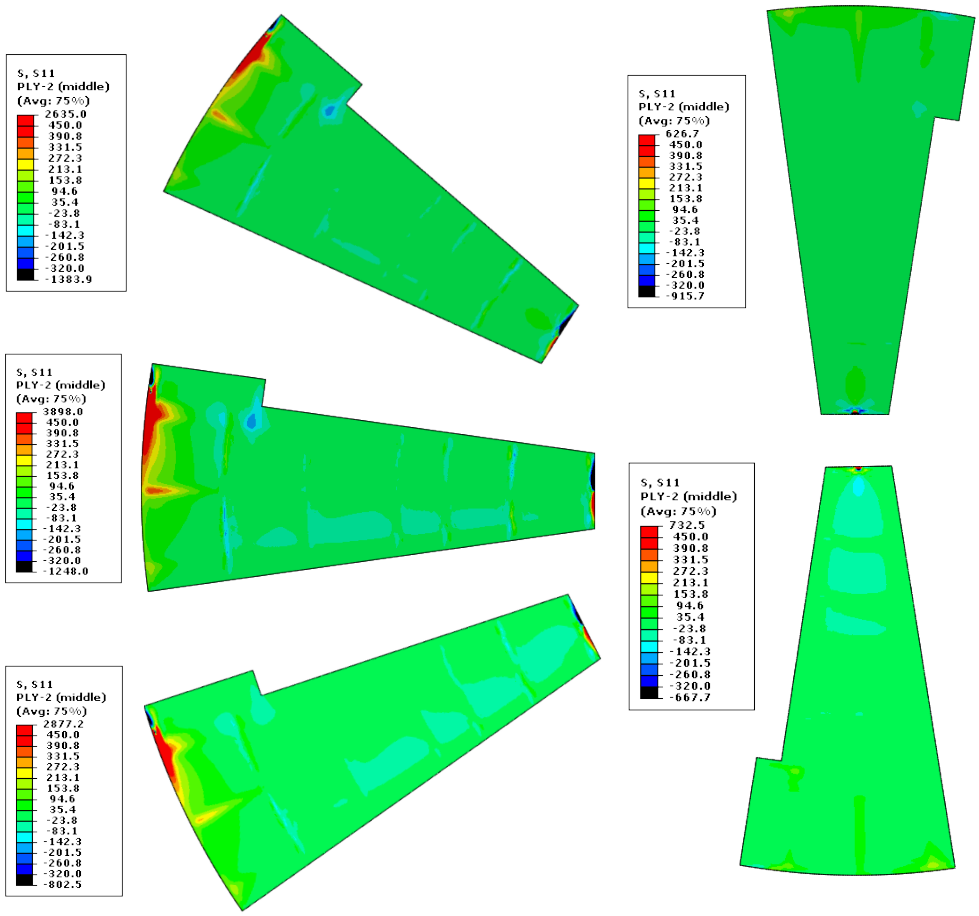

Fig. 3.23: Stress in the fiber axis for 90° ply for five different installation cases. Stresses are in kPa, for the recommended design.

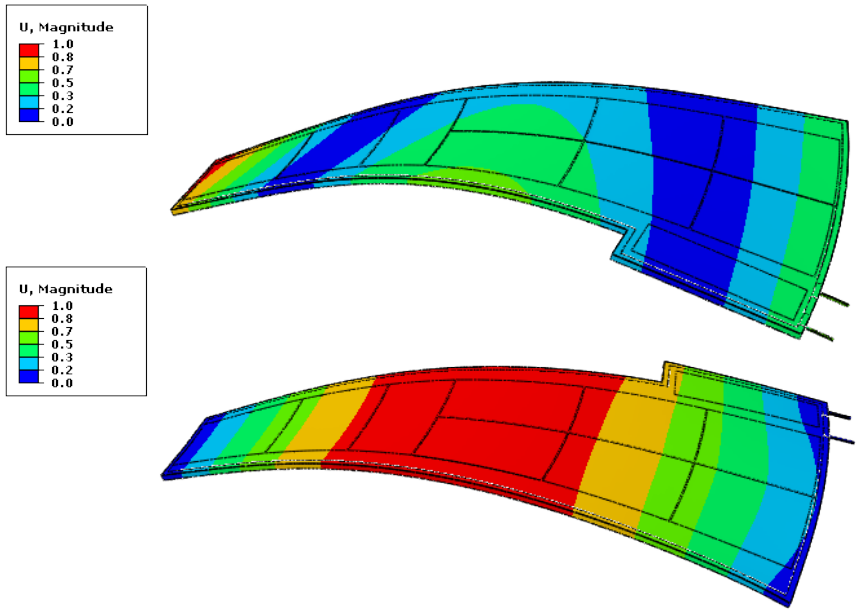

Fig. 3.24: The evaluated mode shapes of the first bending mode for the petal when it is freely suspended (at top) and constrained by kinematic mounts (at bottom). The waveshape of the motion is shorter while the petal is unconstrained, therefore the frequency of the motion is higher.

Another important design consideration is composite fractures at lower stresses at low temperatures. The reduction in the strength for $-50°C$ is about 5 % (see section 2.1) and still leaves a large safety factor.

3.7.4 Discussion on Mode Shapes

The mode shapes of the first bending mode evaluated by the free body and constrained body modal analysis are illustrated in fig. 3.24. The blue regions are where the motions are zero. When the petal is supported by its mountings, the whole body can move in the same direction. In contrast, while the petal is freely suspended, the center of gravity cannot move (no net force), so the center and the ends move in the opposite directions balancing the body. Therefore, the length of the motion's waveshape (distance between blue regions) is shorter, and the frequency of the vibration is higher compared to the constrained petal (table 3.10).

In order to study the difference between the free and constrained body modal analysis, modal frequencies were calculated for a simple beam structure for both cases in section A.6. The calculations showed that the modal frequency for unsupported beam is

~2.27 times higher than the simply-supported beam, table A.4. The ratio of evaluated bending frequencies for the petal is consistent with the calculation for a beam.

3.8 Conclusion

A FEA model of the Nikhef Petal prototype (LoI-design) was developed, which predicts structural stiffness and the lowest modal frequencies within 5 % agreement with the measurement. Later, this model was used for the DESY Petal (LTF-design), which is the actual product being used for the future ATLAS tracker. The model was extended by adding external modules (containing bus tape, sensor modules, EoP and adhesive) to predict the performance in use.

Improving the measurement performance of the future ATLAS inner tracker required lowering the fractional radiation length of the petal structure, while maintaining positional stability. An analytic model developed for the petal was used to compare different prepregs, angular configurations in the composite facesheets and core materials. First, a layup for facesheet and a core improving the bending stiffness were selected. Then the facesheet ply thickness was reduced. The improved design has been verified to meet strength, positional stability, and radiation length requirements. The study leads to the following recommendations:

- $[0/90/0]^\circ$ angular configuration almost doubled the longitudinal rigidity, but significantly reduced torsional rigidity. Since the longitudinal bending mode of the petal has the lowest natural frequency, this configuration is preferable to the $[60/0/-60]^\circ$ configuration.
- The improved facing rigidity from the above change allows thinner facings to be used. 45 gsm K13C2U/EX1515 prepreg is recommended.
- Core shear modulus has a diminishing contribution to bending stiffness; therefore it is not the predominant factor in determining bending stiffness of the petal beyond a specific modulus. As a result, we choose a core (Plascore Kevlar) having a moderate modulus and a lighter structure, giving considerable cost savings.

The recommended material configuration reduces the fractional radiation length of the base petal by 16 %. Finite element analysis of the recommended configuration in ATLAS (i.e. with modules mounted and constrained to the End-cap frame) gives the lowest natural frequency at 64 Hz (a 5 % improvement), sustaining stability requirements. In-plane stresses in the facesheet plies were evaluated, and indicated that the design is very far from the fracture point and safe to install.

The new facing configuration will affect the thermal performance of the petal. Another researcher from the Nikhef group, Afroditi Koutoulaki, studied and verified that the thermal performance remains sufficient even with the thinner facesheet [7].

It is possible to lower petal weight around 20 g by making close-outs from carbon-fibre composite instead of PEEK plastic. We recommend reverting to carbon-fibre close-outs, retaining plastic only for mounting points and cooling-tube strain-relief.

Chapter 4

Carbon-Foams

As mentioned in chapter 1, carbon foam is currently being considered in the development of a thermo-mechanical support structure for the upgrade of inner-tracker of the ATLAS detector. Carbon foam is used to transfer heat from electronics mounted on the facings to the cooling tube. Mechanical damage in the tube-foam interface can have adverse impacts on thermal properties of the structure and its long-term reliability. Therefore, there is a particular interest in studying the fracture mechanics of the foam.

This chapter is dedicated to studies performed on carbon foam to understand, characterise and reproduce its mechanical behaviour including fracture. Several tests were performed to characterise elastic and destructive compressive and shear behaviour of Poco-HTC samples. This work extends the understanding of the failure mechanism by presenting measurements made in both material directions, and made with different loading modes. A computational micro-scale model was developed to re-produce the characteristics of the measured behaviour. This work extends the existing models by incorporating local anisotropy and failure criteria to evaluate anisotropy, compressive strength and post-failure behaviour of foam. Several analyses were performed based on the model, and the outcomes were compared with the measurements to improve the model. Finally, measurements and the model were used to produce elastic constants required for developing a continuum model, i.e. a macro-scale foam model. This continuum model will be used to analyse tube-foam interface and to evaluate the design reliability in chapter 5.

4.1 Measurements

A series of destructive tests were performed to study fracture mechanics of Poco-HTC graphitic foam in compression and shear cases. Destructive compression (crush) tests were made in both in-plane and out-of-plane directions to characterise anisotropy. These tests were filmed to visually examine crack initiation and propagation at macro-scale. Images were captured via SEM from the fracture surfaces in crushed samples to

examine post-failure formation of material at micro- and meso-scale.

In another series of tests, cyclic compressive loads were applied in the elastic regime to characterise the elastic behaviour. These tests were used to extract elastic parameters, such as Young's modulus and elastic limits. Also, strengths were measured by subjecting some samples to continuous compression load up to destruction after the cyclic test.

Poco-HTC shows highly anisotropic behaviour in both elastic and fracture cases. It has higher modulus and strength in the out-of-plane direction. This comes from two separate effects: the graphite planes of carbon atoms are aligned along the out-of-plane direction; and the cells are elongated in the out-of-plane direction.

Measurements showed that the local fractures start at 3.0 and 1.5 MPa, and strengths are 5.3 and 3.5 MPa in the out-of-plane and in-plane directions. The Young's modulus was measured 113 and 75 MPa in the same directions. The shear strength is 1.8 MPa, measured with Iosipescu shear test.

The initial failure mode is cell-wall bending fracture (mainly called Mode-I fracture in the thesis) followed by propagation to nearby cells up to complete material separation.

In the out-of-plane (z) crushing, the fracture plane propagates diagonally in both in-plane (x and y) directions with a slightly larger component in the out-of-plane direction. This is very close to the 45° crack line in typical brittle shear failure.

In the in-plane (x) crushing, the propagation is horizontal in the out-of-plane (z) direction, while it is around 45° diagonal in the in-plane transverse (y) direction.

In the shear test (zx), cracks appear in the foam out-of-plane direction, as cleavages. These cleavages are probably due to separation of graphitic layers as a result of shear forces, and propagate along the planes. These observations showed that alignment of graphitic planes affects the behaviour of macro-cracks.

The SEM images of the fracture surfaces of the crushed samples indicate that the cracks initiate at cell-walls, becoming cleavages between graphitic planes at the junctions. These separations propagate along the planes and spread to neighbouring ligaments.

The methods of these experiments and the outcomes were published in *Results in Physics* [48]. This manuscript is reprinted in this thesis, page 155.

4.2 Computational Micro-Model of Graphitic Foam

In the literature, numerical modelling approaches to model foam behaviour are divided into two categories. In the first, called *the continuum model*, the foam is modelled as an homogeneous continuum material, and the constitutive equations are implemented to model macro-scale behaviour. These continuum models are based on experimental data; therefore they actually reproduce characteristics of the measured behaviour. Generally, these are developed from crushing low density metallic foams. Therefore, the models are limited with such materials and analysis cases, and not capable of handling complex conditions, e.g. inelastic deformation under transverse compression and shear modes. In the second method, called *micro-model*, a 3D representative CAD model is used to model porous structure of the foam, followed by application of the most suitable material model to the solid domains. In this approach, the model carries micro- and meso-scopic properties of the foam, and is used to evaluate macro-scopic scale properties. Therefore, internal material and the foam topological properties govern the bulk material response. These models bring with them the capability to study the effects of structural parameters (e.g. cell size, cell-wall thickness and density variation) on macro behaviour. Since these models use micro-structure, a large number of elements are required, limiting the model use in large-scale finite element analysis. Therefore, these models are intended to be performed in a small-scale analysis and extract foam macro-scale parameters to implement in a continuum model. [87]

Two common techniques have been described for micro-modelling. In the first, a representative unit-cell is developed and duplicated at symmetry planes to form a multi-cell foam object. This model homogenizes the foam structure, and is only applicable to foams having regular and periodic cells. In spite of the identical cell format, it is still possible to apply density variation by affecting wall thickness at different sectors via computer code. Another method, a super-cell model, is used to account for cell irregularity, and thereby for micro-structural variations. A multi-cell geometry is generated by taking the most representative unit-cell as a basis and developing an algorithm to randomize cell size and any other micro-structural parameters. In this method, cell parameters are usually measured with advanced sectional imaging tools, such as computer tomography (CT) or scanning electron microscopy (SEM), and fed into the algorithm. [88]

In the literature, most of the foam micro-models were developed for low-density ductile metallic foams and are barely applicable for brittle carbon foams with relatively higher density. However, existing methods still can constitute a basis for new carbon-foam materials. As a basis for the current unit-cell studies, Gibson and Ashby used simple-cubes model [87]. This model estimated the bulk Young's Modulus and plastic collapse strength for metallic foams. Later, this model was improved upon with use of a 3D tetrakaidecahedron unit-cell [87], also called Kelvin cell model. In these models, cells can be in either face or strut form to model closed- or open-cell foams. Santosa et al. [89] modelled closed-cell aluminium foam as an assembly of large and small closely packed

cells in the shape of a truncated cube and pyramid. This model also referred to a cruciform-pyramidal foam model, and has been a base for many other similar closed-cell foam studies. Meguid et al. [90] took cruciform-pyramidal cell and replaced the pyramid with a hemisphere, and Czekanski et al. [91] used another cell similar to the cruciform-pyramid to simulate crushing of closed-cell metallic foams. All these models involve the repetition of unit cells, and do not capture the micro-structural variations of the foam. By contrast, cell irregularity was included in the foam models with use of random Voronoi cell model [88]. Giorgi et al. [92] modified Kelvin cells by accounting for face curvature to model closed-cell aluminium foams, and also used randomly distributed shell ellipsoids in another study. Jang et al. [93] used micro-computed X-ray tomography to collect data from the cell structure of open-cell polyester urethane and aluminium foams. In their work, a multi-cell foam object was generated as a network of irregular polyhedra cells by defining cell sizes and ligament thicknesses according to the measurements.

Most of these models use either struts at edges or shells at cell-walls, giving a good representation of structure of metallic foams up to 10 % relative density. Since the RVC-based graphitic foams have a similar structure to open-cell metallic foams, Kelvin cell in strut form is an applicable method. For example, Gilchriese et al. [94] used a similar method to model Allcomp RVC foam. Although pitch-based graphitic foams are mostly in open-cell form, they have higher relative density (around $20-30\,\%$), and these methods are not capable of capturing solid sections in such carbon foams.

Several studies have focused on modelling the topology of carbon foams at higher relative densities. For example, Maruyama et al. [42] presented the serial internal section capturing technique to develop a 3D isosurface geometrical model of the foam. Similar to the super cell models above, Kirca et al. [95] developed a computer algorithm to place spherical bubbles in an enclosed volume to generate the porous structure of carbon foam. Lamontie et al. [96] and Bonad [97] also followed the same technique to obtain foam geometry. All these models gave topologically isotropic foam models, and need some modification to be adapted for anisotropic foams. As well, these models also used isotropic properties at solid sections to predict foam elastic constants, although the graphitic material exhibits anisotropic properties.

One of the most detailed studies on this topic was made by Sihn et al. [98]. They modelled a representative unit cell containing a junction and a few ligaments, and divided in different segments with different properties for each segment introducing variation of graphitic material. They performed several sensitivity studies to link modulus of a unit cell to segment properties. However, this model does not represent the actual foam geometry, and therefore does not properly predict its macro-scopic behaviour.

In another study, Choi et al. [99] made a micro-mechanical model of carbon-foam by taking a cube containing a spherical void as a unit cell and duplicated to create a multi-cell foam body. They defined tensile strength for the solid material to predict fracture toughness of the foam. However, this model is geometrically isotropic and not capable of capturing micro-structural variations, and does not account for anisotropy

at micro-scale and different fracture modes (e.g. compression).

Gilchriese et al. [94] used tetrakaidecahedron representative unit cells to model the topology of pyrolytic-graphite coated RVC-foam with low density. They combined elastic properties of both carbon skeleton and pyrolytic-graphite coating to calculate elastic modulus of the homogenised ligament, and defined isotropic properties. The model was used to predict the compressive modulus of the foam in the thickness direction, and the prediction was about 20 % higher than the trendline of the measured data points. However, variation in the measured foam properties makes accuracy of the model unclear. Furthermore, they defined flexural strength of the skeleton carbon material as a limiting stress at ligaments [100]. In the compression analysis, when an element in the ligament surface reaches the defined stress level, it was an indication of failure initiation, and they took the bulk load as compressive strength of the foam. The fracture initiation strength was predicted in good agreement with the measurements. However, the model does not predict the actual crushing strength i.e. maximum reachable stress state. Their work constitutes a good basis for future foam modeling studies.

Up till now, most carbon-foam studies have focused on deriving bulk elastic properties from micro-structural models with isotropic properties. A few studies have been published modelling the fracture case and variation of solid material properties; however, in contrast to metallic foams, there is no micro-model predicting crush strength and anisotropy of brittle carbon-foam.

In the following subsections, a new technique is presented which extends these models by incorporating local anisotropy and failure criteria in order to evaluate anisotropy, crush strength and post-failure behaviour of bulk material. The works of Kirca et al. [95] and Lamontie et al. [96] were improved by taking a prolate spheroid bubble as the unit-cell, and placing them in an enclosed volume via computer script by targeting a certain porosity. The cell dimensions were selected to match measurements on various Poco-HTC samples. Thus topological anisotropy and cell irregularity were accounted. The generated geometry was discretized to small elements, and material directions (i.e. alignment of graphitic planar molecules) were defined in each to introduce local anisotropy to predict macroscopic anisotropy. Failure criteria for finite elements are included in the model to predict strength.

Song et al. [101] conducted a study to identify fracture mechanisms at mesoscopic scale for brittle foams under compression. A few cell-sized samples made of Aluminium and Silicon based brittle metallic foam were crushed inside a SEM. Four major failure modes were characterised: Mode-I, compressive bending fracture of cell-walls and ligaments; Mode-II, direct brittle fracturing due to tension or shear; Mode-III, cracking in the cell-face and Mode-IV, friction and shear between fractured cells. Since the face cracks are caused by either compression or tension, the third mode is covered by the first and second modes. The fourth mode occurs under high deformations. Our model is not intended to describe high deformations, so the fourth mode is not necessary in this case. Therefore, only Mode-I and Mode-II fractures are considered in the model developed in this chapter.

4.2.1 Foam Representative CAD Geometry

The following steps are used to obtain a 3D geometric model to represent the actual topology of the foam:

- Cell geometric dimensions are measured by processing various SEM images.
- An algorithm is developed to position bubbles in an enclosed volume. The model has a free parameter that can be adjusted to give the desired density.
- The script is written for Abaqus CAE software. It generates the 3D porous structure using computer-aided design (CAD) commands by taking dimensions and calculated bubble positions as inputs.

Cellular Data Collection

Referring to fig. 4.1, cellular formations in Poco-HTC can be considered as an interconnected network of bubbles. Bubbles are elongated in the vertical (z) direction, with almost circular cross-section on the horizontal (xy) plane. They are therefore modelled as prolate spheroids with major axis near vertical, and both minor axes equal. The major axis can have a small tilt α away from the vertical axis. Bubbles are connected via pores (cell-opening) having width D_p to form an interconnected network. As such, a bubble is characterised as a prolate spheroid with the following parameters: major diameter (D_z), major/minor diameter ratio ($c = D_z/D_x$), bubble misalignment angle (α) and the pore width (D_p).

Cellular parameters were measured by processing SEM images of several Poco-HTC samples. The variation in cellular properties is presented in fig. 4.2. Furthermore,

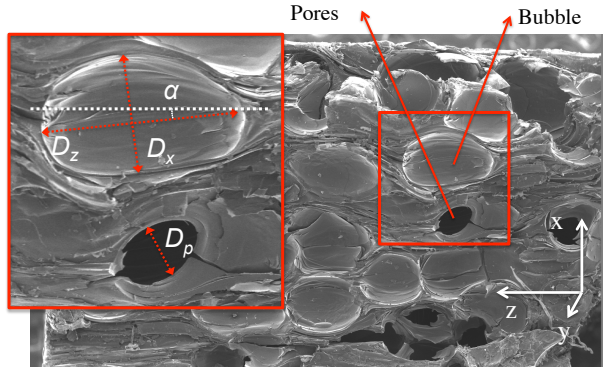

Fig. 4.1: SEM image illustrating cellular structural parameters for a bubble simplified as an ellipsoid in prolate spheroid form. Cells are elongated in the out-of-plane direction z. The cell parameters are indicated.

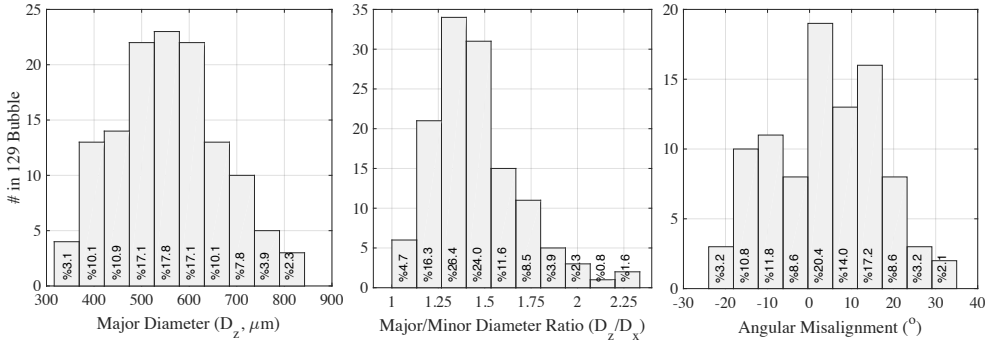

Fig. 4.2: Histogram of cellular parameters: major diameter (at left), major-to-minor diameter ratio (at middle) and angular misalignment (at right). The vertical axis gives the number of bubbles laying within the histogram bins from the 129 bubble samples. Number of bubbles were converted to percentages and are given in the bars.

distribution parameters such as mean and standard deviation were calculated and are listed in table 4.1.

The cellular parameters were measured using 129 bubble samples. The pore diameter distribution is rather difficult to measure due to inaccuracy caused by limited depth resolution. Measurement of the bubble diameters are given in fig. 4.3. Mean major and minor diameters are 557 and 390 μm, and they are correlated. Consequently, the ratio between major and minor diameters (c) is used as a cellular parameter. The ratio has a mean of 1.45, while 66.7% of the bubbles ratios are within the range 1.13-1.52 (at middle in fig. 4.2). Since the images are 2D, bubble angular misalignment was measured from the projected view onto the xz-plane. α varies up to around $\pm 24^\circ$ and shows slightly a symmetric distribution around the vertical axis with a 3° mean (at right in fig. 4.2).

	Unit	Max.	Min.	Mean	Std.
D_z	μm	842	316	557	111
D_x	μm	619	176	390	84
c	-	2.34	1.00	1.45	0.24
α	°	35	-24	3	13

Table 4.1: Cellular parameters based on 129 bubble samples. The last column is the standard deviation.

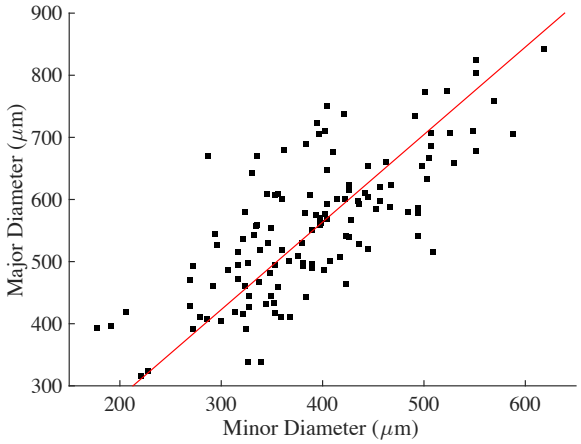

Fig. 4.3: Scatter plot of the major and minor bubble diameters. The red line is a linear fit.

Algorithm to Locate Bubbles

R_x, R_y and R_z are the radii of an ellipsoid bubble in x, y and z directions. R_z is the major radius, while R_x and R_y are the minor radii, taken equal. In case of variations in the in-plane formations, further work requires $R_x \neq R_y$; therefore, we kept characteristic ellipsoid equations non-reduced. Consider a bubble centered at the origin with major axis along z. A point on its surface can be represented in cartesian coordinates by

$$\Delta = (\Delta_x, \Delta_y, \Delta_z) \tag{4.1}$$

It can be defined in spherical polar coordinates as

$$\Delta = r(\theta, \phi) H(\theta, \phi) \tag{4.2}$$

where,

$$H(\theta, \phi) = \begin{bmatrix} s\theta\, c\phi \\ s\theta\, s\phi \\ c\theta \end{bmatrix} \tag{4.3}$$

Above, r, ϕ and θ are radial distance, azimuthal angle i.e. angle projected onto the xy-plane, and polar angle i.e. angle from the zenith direction (z-axis), respectively. The transformation is depicted in fig. 4.4. The radial distance is also a function of both angles. c and s are the abbreviations of *cosine* and *sine* of the relevant angles. Points satisfy generalized surface equation of the ellipsoid:

$$\left(\frac{\Delta_x}{R_x}\right)^2 + \left(\frac{\Delta_y}{R_y}\right)^2 + \left(\frac{\Delta_z}{R_z}\right)^2 = 1 \tag{4.4}$$

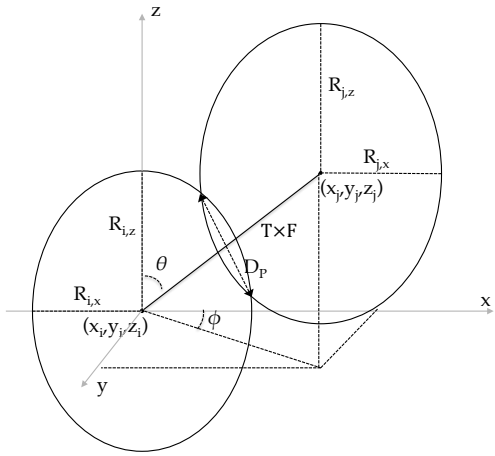

Fig. 4.4: Two adjacent prolate spheroid bubbles shown in 2D.

The angular misalignment of bubbles was not incorporated in these equations to reduce the complexity. Substituting eq. (4.2) in eq. (4.4) gives the radial distance to the point on the surface in the direction (θ, ϕ) from the origin:

$$r(\theta,\phi) = \left(\left(\frac{s\theta\, c\phi}{R_x} \right)^2 + \left(\frac{s\theta\, s\phi}{R_y} \right)^2 + \left(\frac{c\theta}{R_z} \right)^2 \right)^{-1/2} \tag{4.5}$$

Pores occur when two bubbles intersect. Consider a bubble i at the origin, and an intersecting bubble j centered at (x_j, y_j, z_j), which is in (θ, ϕ) direction (fig. 4.4). When the bubbles are just in touch, the separation of their centres is very close to the sum of both radial distances, $T \cong r_i(\theta,\phi) + r_j(\theta,\phi)$, if the major and minor diameters are relatively close to each other. Equality holds for spherical bubble and at $\theta = 0°, 90°$ and 180° for prolate spheroids. Since typically R_z is not much bigger than R_x, we took the equation in equality form as:

$$T_{ij} = r_i(\theta,\phi) + r_j(\theta,\phi) \tag{4.6}$$

When they intersect, the separation is less. Therefore, the separation distance T was scaled by a reduction factor F, where $0 < F < 1$, to obtain the true distance between the centres. This parameter is actually a function of the radial distance, both angles and the pore width. Since the pore width was not measured, the reduction factor was kept a free parameter in the CAD generation process, thus controlling the final relative density of the foam.

Consequently, the centre of the jth bubble can be written as:

$$\begin{bmatrix} x_j \\ y_j \\ z_j \end{bmatrix} = HFT_{ij} \tag{4.7}$$

Firstly, bubble sizes are randomly sampled to give the distributions in fig. 4.2, and the final foam dimensions are defined. Then, using the above equations, the following algorithm locates the bubbles:

1. Generate a first bubble and place it at a random position in the volume.
2. Generate a second bubble and place it at a distance FT_{12} from the centre of the first bubble, in a randomly selected direction.
3. Generate a new bubble (defined by subscript j).
4. Select the bubble with least number of intersecting bubbles as the first reference bubble.
5. By taking the first ref. bubble, calculate the separation distance T_{1j} with eq. (4.6) and scale by the reduction factor F.
6. Create a set of possible coordinates for the centre of the new bubble at various angular positions using FT_{1j} in eq. (4.7).
7. Select another bubble, which intersects the first or that can be considered as the nearest neighbour, as the second reference bubble.
8. Repeat step 5 for the second reference bubble to calculate another scaled distance, FT_{2j}.
9. Keep the coordinates within the set, which satisfy the distance FT_{2j} to the centre of the second bubble, and eliminate the rest,
10. Find the coordinates in the remaining set, which satisfy the distance to the centre of the other bubbles in the domain, and select one of them as the centre for the new bubble.
11. Repeat steps 3-10 until there is no more space left in the volume to place a bubble.

If the density differs from the target, the reduction factor F is adjusted and the process is repeated. Then, calculated coordinates are written to a file to use in a CAD script.

CAD Data Generation

The Abaqus CAE package was used to create desired foam geometry in CAD format. Since GUI commands are not sufficient for this task, a script was written in Python and run in Abaqus. The Abaqus script consists of CAD commands, which use bubble dimensions and calculated positions as input and return the foam geometry as an output.

In the first trial, 3D solid prolate spheroid parts were subtracted from a 3D box to obtain proper CAD geometry. However, this operation created unwanted edges and vertices, and sharp geometry at pores, which later resulted in the meshing operation

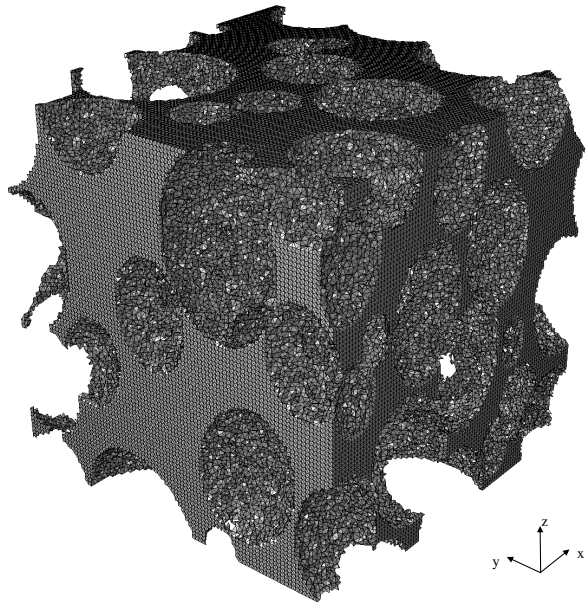

Fig. 4.5: Representative foam geometry as an orphan mesh part at 62 % porosity.

failure. Hence, another method was followed to create the porous geometry. An enclosed volume was first discretized using tetrahedral elements and then was converted to the mesh part (i.e. a part only containing elements), that facilitates the editing of each node and element individually. Finally, the elements that were present within the bubble regions were removed from the mesh part by applying following procedure:

- Select an element and find its centroid coordinates.
- Find the closest bubble to the selected element and calculate relative position Δ as in eq. (4.1).
- Transform Δ into a tilted bubble frame by using $\widehat{\Delta} = \Gamma_y(\text{-}\alpha_y)\,\Gamma_x(\text{-}\alpha_x)\,\Delta$, where Γ_x and Γ_y are the rotation matrices around x and y-axes, and α_x and α_y are randomly chosen from the distribution in fig. 4.2 (at right). Thus, bubble angular misalignment is accounted in the final geometry.
- Delete the element, if it is inside the bubble (use eq. (4.4) with the condition less than one).
- Repeat the previous steps for each element.
- Clean the mesh part by removing groups of elements with no connection to the main material, or with only a single nodal connection.

This method requires more generation time than the first. Furthermore, the geometry has poor discretization at cell-walls, which can be improved by reducing the element

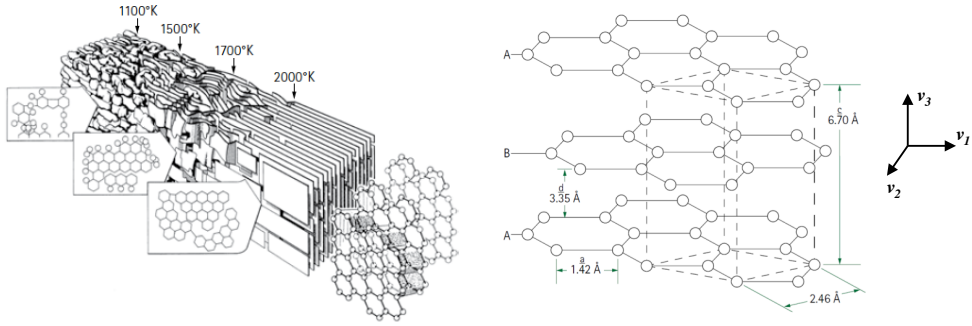

Fig. 4.6: Illustration of mesophase to graphite structure transition during heat treatment (left) and final molecular composition of graphitic planes (right), taken from [102]. Å is 10^{-10} m.

size. However, it generates geometry without any software error. Fig. 4.5 shows the foam mesh geometry.

4.2.2 Element Formulations

The heat treatment converts the mesophase to graphitic crystals, with layers of carbon atoms in a regular hexagonal pattern [44]. Fig. 4.6 illustrates change in crystal structure during heat treatment. Graphite is orthotropic, and has different material properties in the longitudinal (primary in-plane direction, $\vec{v_1}$), transverse (secondary in-plane direction, $\vec{v_2}$), and stacking (out-of-plane, $\vec{v_3}$) directions. Berinski et al. [103] showed that longitudinal and transverse Young's moduli are the same for graphene sheets, using a 2D linearized model to represent regular hexagonal molecular structures. This considerably simplifies the model.

As mentioned, the graphite planes tend to be aligned with cell-walls. Since graphite is orthotropic, this needs to be taken into account in the material properties of each cell. The next two subsections give details of the approach used here, and are together expected to model anisotropic elastic behaviour of the graphitic foam. Then, in the subsection on page 97, a factor defining the bending moment due to in-plane loads is used to evaluate compressive bending failure as Mode-I fracture, and the in-plane loads are used for the tensile failure criteria as Mode-II fracture.

Stiffness Matrix

Hooke's law defines the relationship between 1×6 stress σ and strain ε tensors as $\varepsilon = C\sigma$, where C is a 6×6 material compliance matrix. The compliance matrix involves three Young's moduli (E_1, E_2 and E_3), three Poison's ratios (ν_{12}, ν_{13} and ν_{23})

and three shear moduli (G_{12}, G_{13} and G_{23}). Based on Berinski et al. [103], the in-plane longitudinal and transverse properties are assumed to be the same for graphite layers, applying $E_1 = E_2$, $G_{13} = G_{23}$ and $\nu_{13} = \nu_{23}$. The resulting compliance matrix is :

$$C = \begin{bmatrix} \frac{1}{E_1} & -\frac{\nu_{21}}{E_1} & -\frac{\nu_{31}}{E_3} & 0 & 0 & 0 \\ -\frac{\nu_{12}}{E_1} & \frac{1}{E_1} & -\frac{\nu_{31}}{E_3} & 0 & 0 & 0 \\ -\frac{\nu_{13}}{E_1} & -\frac{\nu_{13}}{E_1} & \frac{1}{E_3} & 0 & 0 & 0 \\ 0 & 0 & 0 & \frac{1}{G_{12}} & 0 & 0 \\ 0 & 0 & 0 & 0 & \frac{1}{G_{13}} & 0 \\ 0 & 0 & 0 & 0 & 0 & \frac{1}{G_{13}} \end{bmatrix} \tag{4.8}$$

where $\nu_{21} = \nu_{12}$ and $\nu_{31} = \nu_{13} E_3/E_1$. The stiffness matrix K is the inverse of the compliance matrix, $K = C^{-1}$.

Material Orientation Vectors

During carbon-foam manufacture, the mesogens become vertically aligned and form parallel to the bubble walls. Thus graphite planes show great alignment with the cell walls. They are less well aligned with more folded structure at the junctions, where the graphitic sheets merge at top and bottom of the bubble. The optical microscopy image of the Poco-HTC section presented in fig. 4.7 shows a clear view of the material orientations at the cell-wall and junctions.

Since the graphitic planes align with the nearest cell wall, the cell parameters of this bubble are used to calculate the vectors defining the graphite planar directions. Consider a virtual ellipsoidal (or prolate spheroidal) surface passing through an element and centered at the origin of the nearest bubble, and with the same shape as the nearest bubble but enlarged. The surface tangents at the element coordinates give the in-plane directions of graphitic layers $\vec{v_1}$ and $\vec{v_2}$, while the surface normal gives the out-of-plane direction $\vec{v_3}$. The derivative of the position vector Δ of the element relative to the closest bubble centre with respect to the θ coordinate gives the surface tangent in the vertical plane. The derivative with respect to the ϕ coordinate gives the surface tangent in the horizontal plane. These vectors are rotated around the x and y-axes by the misalignment angle α to account for the tilt of the bubble. Finally, the surface normal was found from the cross product of both vectors. These three vectors define the graphite planar orientations :

$$\begin{aligned} \vec{v_1} &= \Gamma_x(\alpha_x)\Gamma_y(\alpha_y)\left(\frac{\partial \Delta}{\partial \theta}\right)/n_1 \\ \vec{v_2} &= \Gamma_x(\alpha_x)\Gamma_y(\alpha_y)\left(\frac{\partial \Delta}{\partial \phi}\right)/n_2 \\ \vec{v_3} &= \vec{v_1} \times \vec{v_2} \end{aligned} \tag{4.9}$$

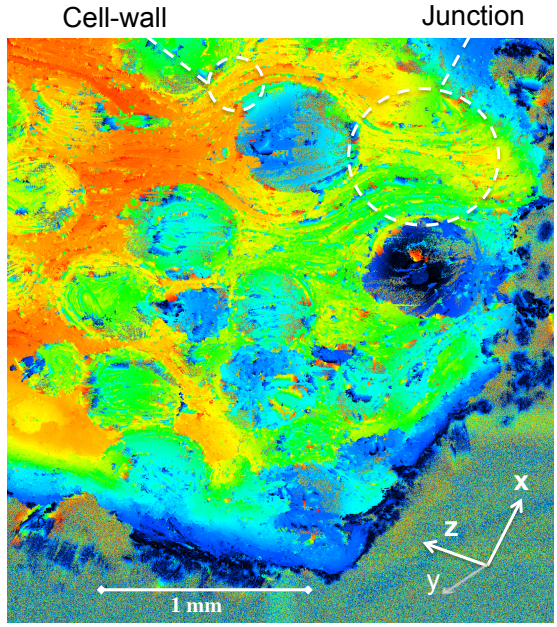

Fig. 4.7: Optical microscopy image of Poco-HTC. The color represents distance from material surface to the camera, enhancing the view of molecular orientations. Red colored parts are closer to the camera.

where n_1 and n_2 are normalization constants to get unit vectors, and $\Gamma_x(\alpha_x)$ and $\Gamma_y(\alpha_y)$ are rotation matrices around the x and y-axes by angle α_x and α_y.

The derivatives in eq. (4.9) can be written in compact form by using eq. (4.2):

$$\frac{\partial \Delta}{\partial i} = \frac{\partial H}{\partial i} r + \frac{\partial r}{\partial i} H \tag{4.10}$$

where i is the spherical angular coordinate, θ or ϕ. The expression for $\partial r/\partial i$ is given in the appendix section A.7.

For each element, the closest bubble is found. The position Δ of the element relative to the bubble centre is found from eq. (4.1), and transformed by inversely rotating around x and y axis by α_x and α_y. Then, it is transformed to spherical polar coordinates[19]. Eqs. (A.18), (4.3) and (4.5) are used in eq. (4.10) to find derivatives at Δ. The tangent vectors are found by using eq. (4.10) in eq. (4.9), and finally the radial direction $\vec{v_3}$ is found by cross product of $\vec{v_1}$ and $\vec{v_2}$. These three vectors define the reference system in which the stiffness matrix K is valid.

[19]Relative angular positions (ϕ and θ) have to be calculated according to the 4 quadrant trigonometric system (between 0-2π).

Static Bending Moment Failure Approach

When the foam is compressed, the cell-walls or ligaments bend and break. This fracture mechanism, Mode-I, was identified as the most important failure mode during foam crushing [101]. Andrews et al. [104] mentioned that the cell-wall curvature has a huge impact on determining the foam compressive strength, and used curvature to adjust strength prediction for various low-density aluminium foams. Following their work, we took the cell-wall curvature as main parameter affecting the bending fracture, along with stress components. The static bending moment factor M given in eq. (4.21) contains both terms and is used to describe Mode-I fracture of graphitic planes for the linear static analysis case.

The 2×2 curvature matrix κ in a specific direction is the rate of change in unit tangent vector $\widehat{\vec{v}}$ with arc length s, with components $\|\partial\widehat{\vec{v}_i}/\partial s_j\|$. The arc length can be calculated by integrating the length of the tangent vector over a certain angular interval [105]. The partial derivative of the arc length becomes the length of the tangent vector, $\partial s_j/\partial j = \|\vec{v_j}\|$. The curvature can then be written in a compact form as:

$$\kappa_{ij} = \left\| \frac{\partial \widehat{\vec{v_i}}}{\partial j} \right\| \frac{1}{\|\vec{v_j}\|} \tag{4.11}$$

In the equation, i and j are in-plane directions of graphitic layers, they are 1 or 2 in literature. But later we label them θ and ϕ to be consistent.

The unit tangent $\widehat{\vec{v_i}}$ is equal to $\vec{v_i}/\|\vec{v_i}\|$. Eq. (4.9) shows that $\vec{v_i} = \partial\Delta/\partial i$ in the non-rotated case. By substituting this term, the unit tangent $\widehat{\vec{v_i}}$ is formulated as:

$$\widehat{\vec{v_i}} = \frac{\partial\Delta}{\partial i} E_i^{-1/2} \tag{4.12}$$

where E_i is:

$$E_i = \|\vec{v_i}\|^2 = \sum_{n=1}^{3} \left(\frac{\partial\Delta_n}{\partial i} \right)^2 \tag{4.13}$$

The partial derivative of the unit tangent $\widehat{\vec{v_i}}$ with respect to j-direction is given as:

$$\frac{\partial \widehat{\vec{v_i}}}{\partial j} = \frac{\partial^2\Delta}{\partial i\,\partial j} E_i^{-1/2} - \frac{1}{2} \frac{\partial\Delta}{\partial i} \frac{\partial E_i}{\partial j} E_i^{-3/2} \tag{4.14}$$

where

$$\frac{\partial E_i}{\partial j} = 2 \sum_{n=1}^{3} \left(\frac{\partial^2\Delta_n}{\partial i\,\partial j} \frac{\partial\Delta_n}{\partial i} \right) \tag{4.15}$$

Taking the partial derivative of eq. (4.10) gives:

$$\frac{\partial^2 \Delta}{\partial i \partial j} = \frac{\partial^2 H}{\partial i \partial j} r + \frac{\partial H}{\partial i}\frac{\partial r}{\partial j} + \frac{\partial^2 r}{\partial i \partial j} H + \frac{\partial r}{\partial i}\frac{\partial H}{\partial j} \tag{4.16}$$

The second partial derivatives of r are given in the appendix section A.7. The first and second partial derivatives of Δ, eqs. (4.10) and (4.16), were substituted into eqs. (4.13) and (4.15). Then, the resultant terms were substituted in eq. (4.14) to evaluate $\partial \widehat{\vec{v}_i}/\partial j$. In eq. (4.11), the norm of tangent vector in the j-direction was also evaluated by using eq. (4.13) as $\|\vec{v_j}\| = \sqrt{E_j}$. Finally, the curvatures in primary and secondary molecular in-plane directions ($\kappa_{\theta\theta}$, $\kappa_{\phi\phi}$, $\kappa_{\theta\phi}$ and $\kappa_{\phi\theta}$) were evaluated by substituting eq. (4.14) in eq. (4.11), and taking the magnitude of the resulting 1×3 vector.

According to Mohr's Circle theory for the 2D planar case, the maximum (σ_{p1}) and minimum (σ_{p2}) principal stresses are related to the in-plane stress components as [106]:

$$\sigma_{p1,p2} = \frac{\sigma_{11} + \sigma_{22}}{2} \pm \sqrt{\left(\frac{\sigma_{11} - \sigma_{22}}{2}\right)^2 + (\sigma_{12})^2} \tag{4.17}$$

The angle γ which is used to transform in-plane stresses onto the principal axes, is given as:

$$\gamma = \frac{1}{2}\tan^{-1}\left(\frac{2\sigma_{12}}{\sigma_{11} - \sigma_{22}}\right) \tag{4.18}$$

The curvatures were transformed onto the principal axes with angle γ as well. The curvatures in the principal axes (κ_{p1} and κ_{p2}) were derived:

$$\begin{aligned} \kappa_{p1} &= c^2\,\kappa_{\theta\theta} - s\,c\,\kappa_{\phi\theta} - s\,c\,\kappa_{\theta\phi} + s^2\,\kappa_{\phi\phi} \\ \kappa_{p2} &= s^2\,\kappa_{\theta\theta} + s\,c\,\kappa_{\phi\theta} + s\,c\,\kappa_{\theta\phi} + c^2\,\kappa_{\phi\phi} \end{aligned} \tag{4.19}$$

where c and s are $\cos(\gamma)$ and $\sin(\gamma)$.

The flexural theory of shells is based on the 8th order differential equation, and it is used to describe the buckling behaviour. In [107], this is simplified by a 4th order differential equation. For the doubly-curved shell, the equilibrium equation in the shell normal direction is [107]:

$$N_{xx}\kappa_{xx} + 2N_{xy}\kappa_{xy} + N_{yy}\kappa_{yy} + p_z = K\Delta\Delta w \tag{4.20}$$

where x and y are the shell in-plane axes, and z is the axis normal to the plane. N is normal or shear load, and κ is curvature or warp in the shell axes. p_z is the distributed load in the z-direction, and K is the flexural rigidity. Δ is the operator of $\frac{\partial^2}{\partial x^2} + \frac{\partial^2}{\partial y^2}$, and w is the displacement in the z-direction. The product of the axial loads and the curvatures induces an apparent loading term in the z-direction causing the shell to bend.

Since the bubbles form graphitic layers in a curved shape, this theory is applicable in the current study. In our study, the graphitic planes are aligned parallel to the ligaments. Under compression, loads are applied along the ligament axis, and the out-of-plane load p_z is small; so the bending occurs due to in-plane loads. Thus, the sum of the products of the in-plane loads[20] and the corresponding curvatures was considered as a static bending moment factor, M, and was used to model graphitic plane fractures under bending. In order to eliminate the shear stress component, the in-plane stresses were transformed to the principal axes along with the curvatures in the planar directions. The static bending moment factor was written with the principal stresses and the curvatures in the principal axes as:

$$M = \sigma_{p1}\kappa_{p1} + \sigma_{p2}\kappa_{p2} \tag{4.21}$$

First, the simulation was performed, and element stress resultants were read from Abaqus. Then, in-plane stress components were used in eqs. (4.17) and (4.18) to calculate principal stresses and the corresponding transformation angle. Outcomes were used to transform the curvatures in planar directions found from eq. (4.11) onto the principal axes by using eq. (4.19). Then, transformed curvatures were substituted in eq. (4.21) along with the principal stresses to calculate the static bending moment factor of the element. This calculation was done for each element in the model.

4.2.3 Boundary Conditions

Fig. 4.1 indicates material directions corresponding to x, y and z-axes. u along with subscript axis notations is used to define displacement components applied on faces of the foam.

The uniaxial compression state was modelled by prescribing zero displacements i.e. $u_x = 0$, $u_y = 0$ and $u_z = 0$ on the $-x$, $-y$ and $-z$ faces, respectively, to prevent rigid body motion. The uniform axial displacement was enforced at the active compression face. For example, $u_z = c$ displacement was defined on the $+z$ face for out-of-plane compression, ε_{zz}. [108]

The shear state was described based on the in-plane shear on the out-of-plane surface, for example shear state ε_{zx} indicates z face is the shear surface, while x-axis is the shear direction. The shear state was modelled by fixing the displacement at ground through setting $u_x = 0$, $u_y = 0$ and $u_z = 0$ on the $-z$ face, and by applying an in-plane uniform displacement of $u_x = c$ on the $+z$ face [109]. Then, in-plane transverse motion was disabled by defining $u_y = 0$ displacement on the $-y$ face. The out-of-plane and in-plane transverse deformations were prevented by defining $u_z = 0$ and $u_y = 0$ on the $+z$ face, to fix shear plane movement. The out-of-plane deformation was prevented on

[20] In the equation, N is line load in N/mm. In our calculations, we took element stresses instead of using line load.

Faces:	$-x$	$+x$	$-y$	$+y$	$-z$	$+z$
ε_{zz}	$u_x = 0$	-	$u_y = 0$	-	$u_z = 0$	$u_z = c$
ε_{xx}	$u_x = 0$	$u_x = c$	$u_y = 0$	-	$u_z = 0$	-
ε_{zx}	$u_z = 0$	$u_z = 0$	$u_y = 0$	-	$u_x, u_y, u_z = 0$	$u_y, u_z = 0,\ u_x = c$
ε_{yx}	$u_y = 0$	$u_y = 0$	$u_x, u_y, u_z = 0$	$u_y, u_z = 0,\ u_x = c$	$u_z = 0$	-

Table 4.2: Boundary conditions for uniaxial compression and shear analysis.

$-x$ and $+x$ faces by defining $u_z = 0$. Boundary conditions were extended for the shear state of ε_{yx}, and summarised in table 4.2.

4.2.4 Material Properties

A homogeneous section with orthotropic anisotropy was defined as a material property. The in-plane Young's modulus E_1 was initially taken from [95]. In turn, this predicted the foam modulus within the 20% range of Roberts and Garboczi's study given in [95]. However, the result was almost 15 times higher than the measurement. Therefore, we use in-plane Young's modulus as a fit parameter. It was set to 1040 MPa in order to get the correct modulus in the out-of-plane direction. The Poisson's ratio ν_{12} was taken as 0.33 [95] resulting in a 390 MPa in-plane shear modulus, G_{12}. The out-of-plane elastic constants (E_3 and G_{13}) were selected by scaling the in-plane properties by 1/40. The density given in [44] for the graphitic ligaments was taken as the material density (ρ).

Fig. 7-3 in [102] lists the tensile strength of various graphite blocks against their densities. Since the conversion from mesophase to graphite releases the gas, the final graphite block product is not pure and contains voids. Thus, the density is lower than the actual graphite and varies from one product to another. By adjusting the data points in [102], the tensile strength σ^* for graphite at 2.23 g/cm^3 density is found to be 250 MPa, which was used as a limit for the in-plane tensile stress. Since relevant data are not available to define the static bending moment factor, a reasonable value, which satisfies the measured crush strength in the out-of-plane direction of Poco-HTC,

Table 4.3: Material elastic constants and strength limits fed for the FEA model.

	Value	Unit
$E_1 = E_2$	1040	MPa
E_3	26	MPa
G_{12}	390	MPa
$G_{13} = G_{23}$	9.75	MPa
ν_{12}	0.33	-
$\nu_{13} = \nu_{23}$	0.33	-
ρ	2.23	g/cm^3
σ^*	250	MPa
M^*	200	MPa/mm

was selected after several trials. The limit for the static bending moment factor M^* was set at 200 MPa/mm. The material properties are summarized in table 4.3.

4.2.5 Computations

The Abaqus CAE package was used to perform the computations. Representative CAD data for a cube of foam with 1.4 mm edges was generated as described in the subsection in page 92. The resultant foam had 62% porosity and consisted of 90 bubbles on average (fig. 4.5). The remaining solid part consisted of 164,000 elements of type 3-dimensional 4-node tetrahedrons (C3D4). Material orientation was set for each element using the vectors defined in eq. (4.9).

Variation of material properties due to planar orientations caused excessive computational effort and computer limits were reached. Including the failure models in Abaqus would require more computing power than was available. Instead, computations were performed for elastic behaviour at low-strain. Results (i.e. stress components) were exported to Matlab software, in which the failure models were included using another algorithm. The Abaqus elastic results were scaled with small increments in a loop. At each increment, the static bending moment factor (M) was evaluated for all elements. When the factor exceeded the pre-defined value, element fails as a result of bending fracture occurring due to in-plane deformations. Stress components of an element were set to zero. In addition, when a cell-wall bends, it is exposed to tensile loads on the convex surface. The tensile failure was considered as a Mode-II fracture mechanism. When the maximum principal stress σ_{p1} exceeded the pre-defined in-plane tensile strength value, elements failed and the stress components were set zero. Failure checks were performed for each element at each increment. After completing an iteration, the bulk compressive load was re-evaluated[21] and destructive stress-strain data were produced.

4.3 Analysis Results and Discussion

Crushing analysis was done in the out-of-plane and in-plane directions, corresponding to z and x-axes, respectively. In addition, shear analysis was performed in the in-plane direction on the out-of-plane face, corresponding to shear state σ_{zx}.

As mentioned, the in-plane Young's modulus of the graphitic layers was tuned to give the measured elastic modulus in the foam out-of-plane direction. The static bending moment factor limit was adjusted to obtain the out-of-plane crushing strength of Poco-HTC. Then, the modulus and the strength in the foam in-plane direction along with the anisotropy ratios were evaluated to determine whether they are in agreement with the measurement.

[21] See section A.8.

	Modulus (MPa)					Strength (MPa)			
	E_z	E_x	G_{zx}	G_{xy}	E_z/E_x	σ_z	σ_x	τ_{zx}	σ_z/σ_x
Measurement	111	75	-	-	1.51	5.30	3.50	1.80	1.51
FEA	112	48	33	18	2.33	5.31	3.78	10.10	1.41

Table 4.4: Compressive and shear modulus and strengths, predicted using the FEA model and measured for Poco-HTC. Compressive Young's modulus was measured with cyclic compression test, while the crushing strength was measured by crushing the samples after cyclic compression. Shear strength was measured with Iosipescu shear test. Since shear strain was not measured, shear modulus could not be calculated. For measurements see [48] (attached in page 155) .

The tuned model was used to produce the results presented in this section. In addition, it was used as a basis for various sensitivity studies that were conducted by tuning the remaining free model parameters to investigate their individual contribution to the bulk properties in both elastic and destructive deformation cases.

The results of this study are presented at both macro- and micro-levels. Macro-level addresses the bulk foam properties, while micro-level addresses results on the elemental scale. At macro-level, elastic constants, strengths, failure behaviour and anisotropy of foam are given. At micro-level, material vectors and stress distribution at an internal section are presented based on sets of elements.

4.3.1 Macro-mechanics

In the tables and figures in this section, E and σ are compressive Young's modulus and crushing strength, and the axis subscript indicates the direction of the properties. The ratio of Young's modulus in z to x-axis (E_z/E_x) gives the elastic anisotropy ratio, while the destructive anisotropy ratio is defined as the ratio of crushing strengths (σ_z/σ_x). ν, G, and τ are the Poisson's ratio, shear modulus and strength on the corresponding face and directions.

Prediction of Modulus and Strength

Table 4.4 lists the compressive and shear moduli, and strengths along with the corresponding anisotropy ratios.

The FEA gives elastic moduli of the bulk material as 112 and 48 MPa for out-of-plane and in-plane directions, with anisotropy ratio of 2.33. While the model is fitted to get the modulus in stiff direction close to the measurement, the modulus in weak direction is significantly lower than the measured modulus. Thus, elastic anisotropy was predicted to be 1.54 times higher than the measured value.

The definition of anisotropy resulted in excessive use of computer memory; therefore, the foam geometry was kept small to reduce the number of elements. The foam had a width of 1.4 mm, with 4-5 bubbles at each side. This made the model sensitive to the edge effects and other micro-topological features, especially number of ligaments. Since the major diameter is effectively higher than the minor side, the foam model contains less ligaments in the in-plane directions, so the in-plane modulus is more affected by the edge effects (e.g. large voids or thinner ligaments at the boundaries).

In order to examine this fact, we simplified the model by replacing anisotropic properties with isotropic properties. This allowed computations with a larger foam size and more elements. Three different cubic foam models with 1.4, 2.0 and 2.4 mm edge sizes were developed[22]. As the edge size is increased, edge effects on the out-of-plane Young's modulus becomes negligible, and the in-plane modulus significantly increased. This resulted in improved prediction of the anisotropy ratio. While 1.4 mm wide foam gave 1.31 elastic anisotropy ratio, 2.0 mm wide foam gave 1.12 anisotropy ratio, reducing the deviation (around 15%) in prediction. Further increase in edge size (in 2.4 mm wide foam) did not affect the anisotropy ratio significantly.

In another study, we tested the effects of element size on the accuracy of the prediction. Two different cubic foam models with 1.4 mm edge size were developed and discretized with 30 and 15 μm element sizes. Both gave a similar anisotropy ratio, suggesting that the element size used in the tuned model is satisfactory, and is not the origin of discrepancy.

Consequently, a larger simulation geometry needs to be used to minimise the microstructural effects. However, analyses can only be performed within computer limits, therefore analyses with anisotropic material model were conducted by using 1.4 mm wide foam.

The primary method of generating foam geometry is to use CAD commands within CAD software. As mentioned in section 4.2.1, we used Abaqus CAE for this task, which created many unwanted geometric features and later on caused the meshing process to fail. Then, we developed a foam geometry by element deletion process, which gives a poor discretization at cell-walls. It is highly recommended to use the first method with a suitable CAD tool to have clear geometric data. This provides better discretization at solid sections.

The crushing strength was taken as peak of stress-strain curve. The predicted crushing strengths were 5.31 and 3.78 MPa for out-of-plane and in-plane directions, along with the anisotropy ratio of 1.41. The strengths were predicted within 7 % of the measured values for both crushing cases. Since the Young's modulus is found to be lower in the in-plane direction, crushing strain (i.e. strain corresponding to crushing stress) was calculated at higher strain values (see green curve in fig. 4.8).

[22] Major/minor diameters ratio was kept constant and 1.35 for these models. Element size was 30 μm, and porosity was 62 %.

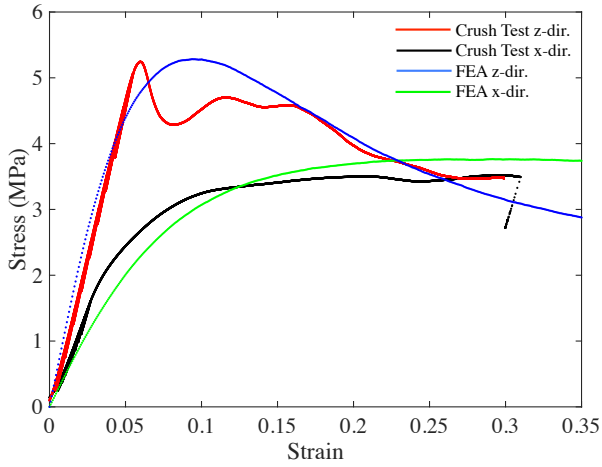

Fig. 4.8: Stress-strain graph for crushing tests and analyses, performed in both directions, i.e. out-of-plane or z-direction, and in-plane or x-direction. The foam is stiffer and stronger in the z-direction. Stress suddenly drops after the fracture (red), this transition is more smooth in the analysed behaviour (blue). In the x-direction, stress continues to increase during the crush, reaches a peak and becomes stable (black). This behaviour is re-produced in the analysis (green); however, the stress plateau zone is shifted to higher strain.

The shear modulus G_{zx} was found to be 33 MPa; however, it is not possible to evaluate the prediction accuracy due to limited test data[23]. The shear strength was predicted to be more than 5 times higher than the measured strength, indicating that the model is not capable to capture it. It is worth noting that cell-wall bending fracture (Mode-I) may be less effective in the shear deformation case. Therefore, the model does not capture element failure from shear loads, predicting a stronger foam than reality.

Crushing Behaviour

Fig. 4.8 illustrates the stress-strain outcomes of the computational compression analysis and the test results for Poco-HTC samples. In the out-of-plane compression test (red), stress suddenly drops after the initiation of crushing, and gradually decreases after the fracture event. In the in-plane compression test (black), stress continues to increase during crushing, and remains slightly stable in the post-failure region after reaching the peak.

As evident in fig. 4.8, calculated crushing behaviour is relatively close to the measured behaviour in both directions. In the out-of-plane crushing analysis (blue), the region in which the stress drops is smoother compared to the sudden decrease observed in

[23]It was not possible to use strain gages in the Iosipescu shear test. Therefore, no strain data was recorded to measure the shear modulus.

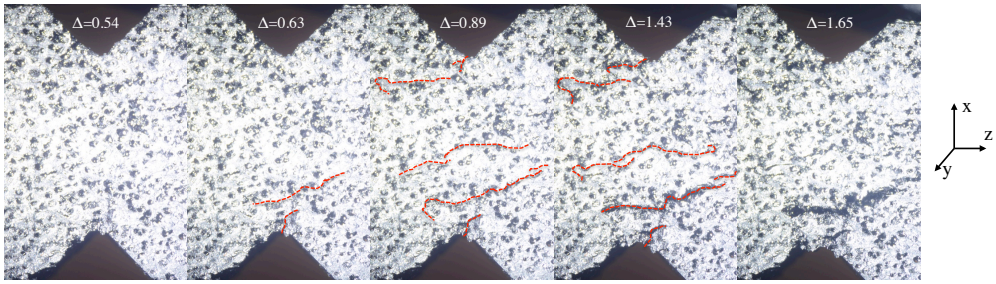

Fig. 4.9: Failure initiation and crack growth during the Iosipescu shear test. Right side of samples are moved down in the $-x$ direction. Shear stress intensifies at the mid-section between the V-notches. Red dashed lines indicate the cracks, which are mostly aligned in the out-of-plane direction between the planes of graphite. Δ is machine head displacement (mm). See [48] (attached in page 155) for details.

the crushing test (red). In the in-plane crushing analysis (green), the crushing stress (peak) is shifted to higher strain values.

The static bending moment factor (Mode-I) defines the peaks in fig. 4.8. This is because cell-wall bending is the most effective fracture mode in foam compression; hence, it determines the characteristic failure behaviour. The tensile failure (Mode-II) just has a small effect after 0.2 strain, and slightly influences stress drop region for the out-of-plane, and stress plateau zone in the in-plane compression cases.

In common computational analysis software, the solver checks whether an element fails. If an element fails, it is removed from the mesh, and the assembly stiffness matrix[24] is updated for use in the next increment of simulation. Removing an element from the model results in higher stress in the neighbouring elements, and failure progressively continues.

Introduction of failure model via external algorithm introduces a weakness to the model. Since assembly stiffness matrix and element connections are not updated in this method, the model does not have the capability to predict the post-failure behaviour accurately. As a result of not removing the failed element from the model, neighbouring elements need more strain increments to reach a failure stress state. Therefore, fracture does not occur as a sudden complete breaking of the ligament, instead the fracturing phase spreads to a wider strain range. Consequently, stress drops smoothly for the out-of-plane compression case (blue curve in fig. 4.8), while stress suddenly decreases in real case (red curve). The strains corresponding to peaks were not determined accurately due to this smooth fracture behaviour. This could be improved by using failure models embedded in the FEA model.

In addition, crushing strain shifted to higher values in the in-plane crushing analysis, since the in-plane modulus was predicted smaller than the measured value (green curve in fig. 4.8).

[24]It is a matrix as a combination of components of stiffness matrices of each element in the model.

ν_{zx}	ν_{zy}	ν_{xz}	ν_{xy}
0.305	0.320	0.124	0.413

Table 4.5: Poisson's ratios evaluated from analyses. Since foam in-plane directions have similar behaviour, $\nu_{zx} \cong \nu_{zy}$.

Although Song et al. [101] identified most of the failure modes in brittle foams, their study was performed for an isotropic material under compression and did not cover all the failure mechanisms in a layered anisotropic material. Moreover, shear deformation may lead to different failure mechanisms. Fig. 4.9 shows the crack formations in the samples used in the Iosipescu shear test, the cracks may have been formed by the separation of graphitic layers. Interlaminar shear failure criteria described in [110] characterise such failures by considering axial and shear loads in the out-of-plane directions (σ_{33}, σ_{13} and σ_{23}). This method could also be used to model separations between graphite layers, and improve the predictive power of the model for the shear deformation case.

Poisson's Ratio

The poisson effect produces slight outward movement of the material transverse to the compression direction. The Poisson's ratio is determined by dividing the strain in the force transverse axis to the compression strain[25]. The Poisson's ratios were calculated for both compression scenarios and are given in table 4.5. In the out-of-plane compression scenario, extension strains in both in-plane directions were almost the same, suggesting that $\nu_{zx} \cong \nu_{zy}$. The ratio of the calculated Poisson's ratios and the Young's moduli are almost equal, i.e. $\nu_{xz}/\nu_{zx} \cong E_x/E_z$.

Parametric Studies

Parametric studies or sensitivity analyses were performed to investigate the effects of individual parameters used in the model on the bulk behaviour. These studies give insight into how different foams would behave, showing which foam properties are important for a particular bulk property. They give some feel for the reliability of any predictions given some uncertainty in a foam parameter.

One parameter is modified at a time. First, the model was modified to use a constant bubble major-to-minor diameters ratio instead of random generation. The ratio was set to 1.35. These studies focused on structural parameters such as porosity and bubble shape, and material properties such as graphitic plane anisotropy. The porosity was tested by generating foam at different relative densities by moving bubbles towards or

[25]The Poisson's ratio can be calculated as $\nu_{ij} = -\varepsilon_j/\varepsilon_i$, where ε is strain, while i and j denote directions.

away from each other. Bubble shape was studied by setting different major-to-minor diameter ratios. Graphitic plane anisotropy was examined by setting different ratios of out-of-plane and in-plane elastic constants, i.e. E_3/E_1. Isotropic properties were defined instead of anisotropic properties in another study.

For all cases investigated, Young's and shear moduli, crushing strengths, and elastic and destructive anisotropy ratios were calculated. Shear moduli in these studies were obtained with different boundary conditions, proper boundary conditions (as given in table 4.2) would result in approximately 1.4 times higher values. The results are plotted against the test parameter and are presented in figs. 4.10 to 4.12. The data points of these graphs are also tabulated in tables 4.6 to 4.8.

- Porosity

Two higher porosities of 69.8 and 74.5 % were modelled in addition to the PocoHTC value of 62.6 %, with results given in fig. 4.10 and table 4.6. The porosity of the foam was set by adjusting parameter F in eq. (4.7) determining the distance between two neighbouring bubbles. When porosity increased from 62.6 to 74.5 %, the foam density decreased by around 30 %, resulting in around 60 % decrease in all moduli in all directions (top left in fig. 4.10). The strength decreased by $30-40$ % for both directions (top right in fig. 4.10). Since the contribution is similar in all directions, there were only slight changes in anisotropy ratios (bottom in fig. 4.10). The characteristics of the stress-strain behaviour remain unchanged (not shown); just the peak position changes.

In [111], the relationship between the foam elastic modulus E, solid material elastic modulus E_s and the relative density ρ_r is described by an empirical formula of $E = CE_s{\rho_r}^n$, known as the Gibson and Ashby model. In general, n is between 1 and 4. It is close to 2 (quadratic), if bending deformation of ligaments defines the behaviour. This occurs, when the cell-wall thickness is very small compared to ligaments in closed-cell foams, or there are no cell-walls as in open-cell foams. The dependence is close to cubic (i.e. $n \approx 3$), if the main deformation mechanism is cell-wall bending. In pocofoam, cell-wall bending governs the behaviour, although the cell-walls contain voids. In such case, n is expected to be between 2 and 3. The data points in table 4.6 were used to derive n, giving 2.62, 2.68 and 2.3 for the foam out-of-plane and in-plane elastic modulus and shear modulus. The calculated n values lie within the expected range.

- Bubble Major/Minor Diameters Ratio

The bubble major-to-minor diameter ratio was set to 1.45, 1.35, 1.20 and 1.00, where the bubble is spherical if the ratio is 1.00. The porosity was kept at about 62 %. The results are given in fig. 4.11 and table 4.7.

As the bubble shape changes from prolate spheroid to sphere, both elastic and destructive anisotropy became closer to 1, i.e. the foam becomes more isotropic. While there

was an increase in the strength in both directions, the impact was significantly higher in the in-plane direction (top right in fig. 4.11). The strength increased in the in-plane direction about 2.5 times larger than increase in the out-of-plane direction.

As the bubble shape goes towards spherical, the alignment of graphite becomes similar in the out-of-plane and in-plane directions. Curvature at the top and bottom of a bubble (i.e. horizontal ligaments) decreases, while curvature at the sides of a bubble (i.e. vertical ligaments) increases. Net result is a small reduction in the out-of-plane modulus, and increase in the in-plane modulus, giving no anisotropy. The shear modulus decreases, but much less than the change in the Young's moduli. Clearly, bubble shape has a significant impact on modulus, strength and bulk anisotropy.

The interpretation of the results regarding solid material distribution is much more complicated. A single bubble volume becomes larger with a lower major-to-minor ratio. Consequently, algorithm places less bubble in the same foam volume to keep porosity constant. Now, the number of ligaments are less, but they are thicker.

Furthermore, the characteristics of the stress-strain curve (example shown in fig. 4.8) were changed for the out-of-plane crushing scenario. The peak of the curve shifted to higher strains, while the post-failure stress increased, resulting in a crushing response similar to the in-plane crushing scenario. In the other direction, the main characteristics remained unchanged, while the peak became higher.

- Graphitic Plane Anisotropy

Graphitic plane anisotropy was tuned by changing the out-of-plane modulus, E_3, while the in-plane modulus, E_1, was kept constant. The out-of-plane modulus was increased from 1/60, 1/40 and 1/20 to 1/1 of the in-plane value. The in-plane shear modulus, G_{12}, was kept constant. The out-of-plane shear moduli, G_{13} and G_{23}, were also adjusted similarly by scaling G_{12} with the same constants. The results are presented in fig. 4.12 and table 4.8. For the isotropic case $E_1 = E_3$ and $G_{13} = G_{23} = G_{12}$, the analyses were done by using isotropic material properties without describing any material orientations, therefore the failure model is invalid, so the stress-strain curves and the strengths were not evaluated.

An increase in the graphite out-of-plane modulus results in an increase in the compressive modulus and strength of the foam in both directions, in particular in the in-plane direction (top row in fig. 4.12). This could be attributed to the placement of the graphitic planes. Since graphitic planes are more aligned in the out-of-plane direction of the foam, increasing the graphite out-of-plane modulus has more effect in the in-plane directions of the foam. Therefore, the bulk anisotropy is decreased (bottom in fig. 4.12).

The characteristics of the stress-strain curve were not significantly affected by the change in the graphite anisotropy ratio.

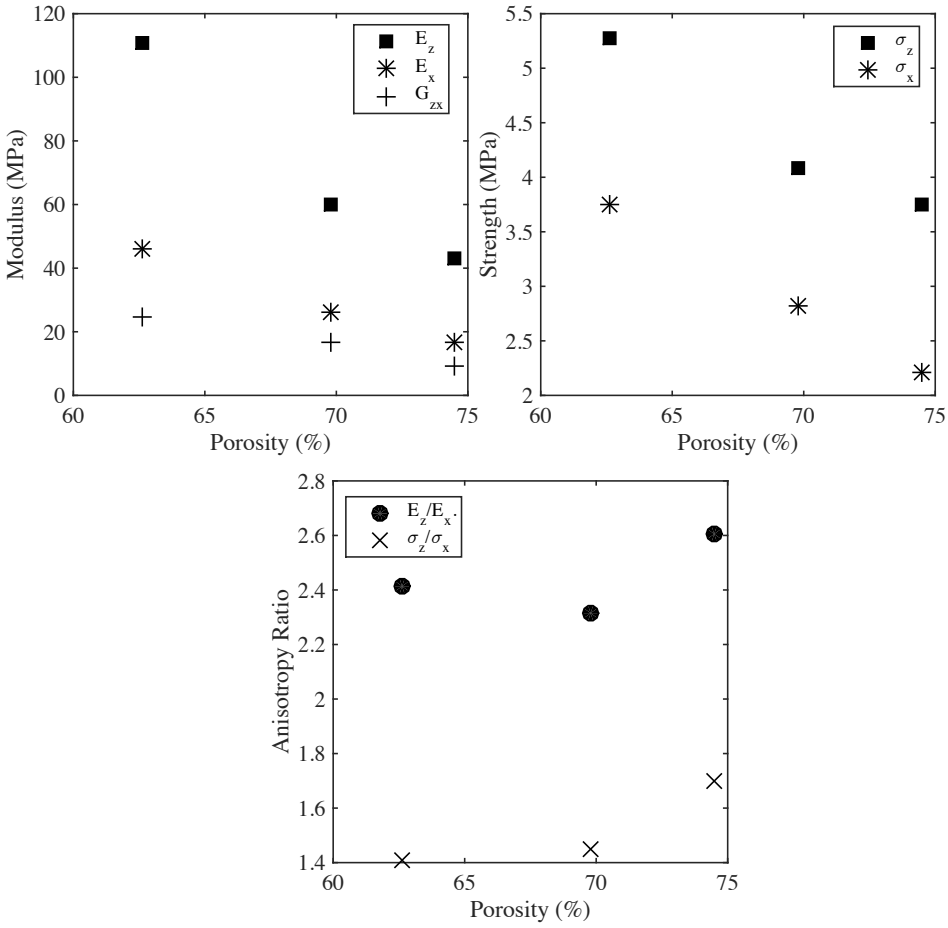

Fig. 4.10: Compressive Young's and shear moduli (top left), crushing strengths (top right), and elastic and destructive anisotropy ratios (bottom) at different porosity, i.e. volume of voids in percent. The models have 1/40 graphite anisotropy and 1.35 bubble major-to-minor diameters ratios.

Porosity (%)	Modulus (MPa)				Strength (MPa)		
	E_z	E_x	G_{zx}	E_z/E_x	σ_z	σ_x	σ_z/σ_x
74.5	43	16.5	9.1	2.61	3.75	2.21	1.70
69.8	60	25.9	16.6	2.32	4.08	2.82	1.45
62.6	111	46.0	24.4	2.41	5.28	3.75	1.41

Table 4.6: Tabulated data of fig. 4.10.

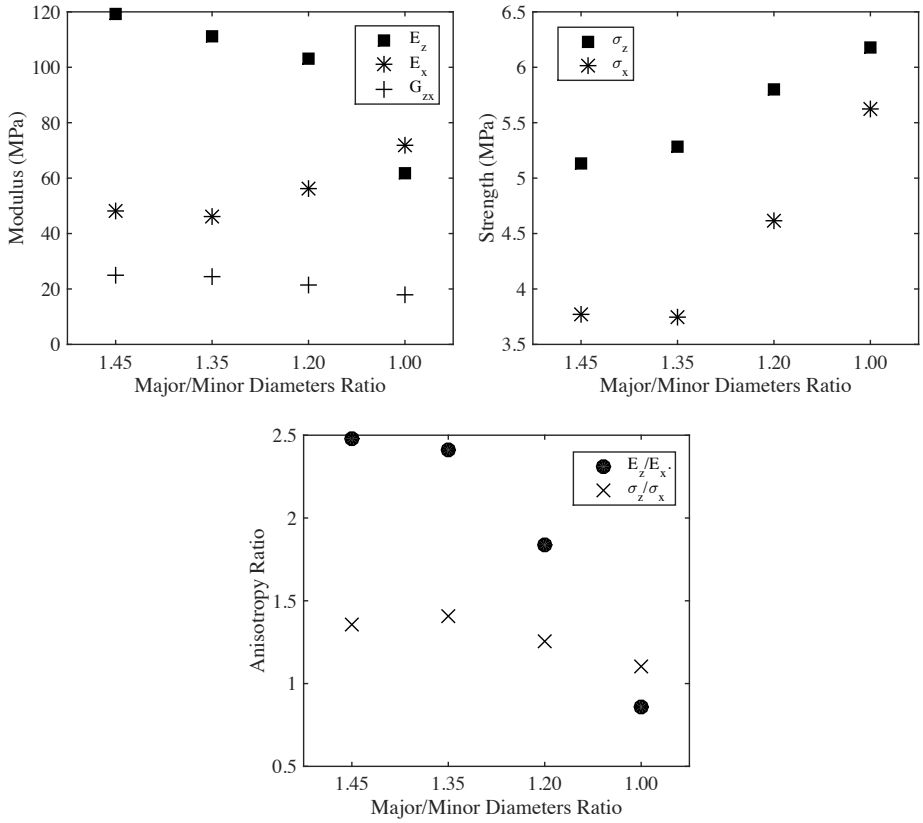

Fig. 4.11: Compressive Young's and shear moduli (top left), crushing strengths (top right), and elastic and destructive anisotropy ratios (bottom) for various bubble major-to-minor diameters ratios. The models have 62 % porosity and 1/40 graphitic material out-of-plane and in-plane elastic constants ratio, E_3/E_1.

Major/Minor Ratio	Modulus (MPa)				Strength (MPa)		
	E_z	E_x	G_{zx}	E_z/E_x	σ_z	σ_x	σ_z/σ_x
1.45	119	48	25.0	2.48	5.13	3.77	1.36
1.35	111	46	24.4	2.41	5.28	3.75	1.41
1.20	103	56	21.6	1.84	5.80	4.62	1.26
1.00	62	72	18.1	0.86	6.18	5.62	1.09

Table 4.7: Tabulated data of fig. 4.11.

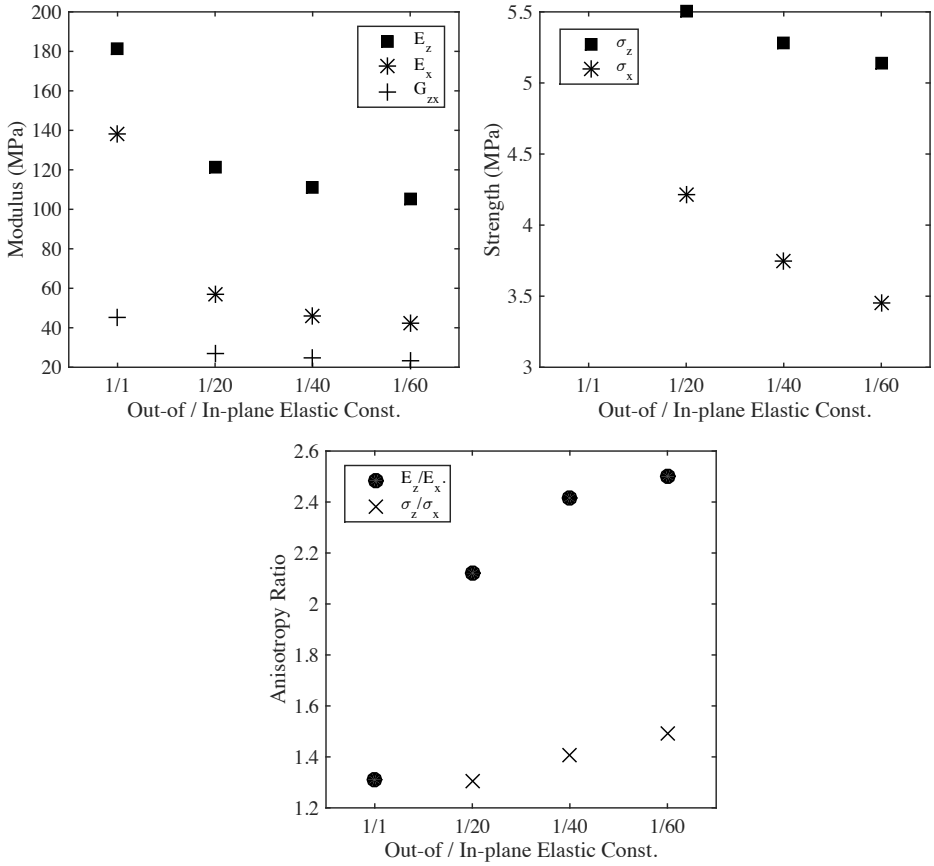

Fig. 4.12: Compressive Young's and shear moduli (top left), crushing strengths (top right), and elastic and destructive anisotropy ratios (bottom) at different graphitic plane anisotropy values, i.e. the ratio of out-of-plane and in-plane elastic constants, E_3/E_1. The models have the porosity of 62 % and bubble major-to-minor diameters ratio of 1.35.

Material Anisotropy	Modulus (MPa)				Strength (MPa)		
	E_z	E_x	G_{zx}	E_z/E_x	σ_z	σ_x	σ_z/σ_x
1/1	181	138	45.3	1.31	-	-	-
1/20	121	57	27.0	2.12	5.50	4.21	1.31
1/40	111	46	24.4	2.41	5.28	3.75	1.41
1/60	105	42	23.1	2.50	5.14	3.45	1.49

Table 4.8: Tabulated data of fig. 4.12.

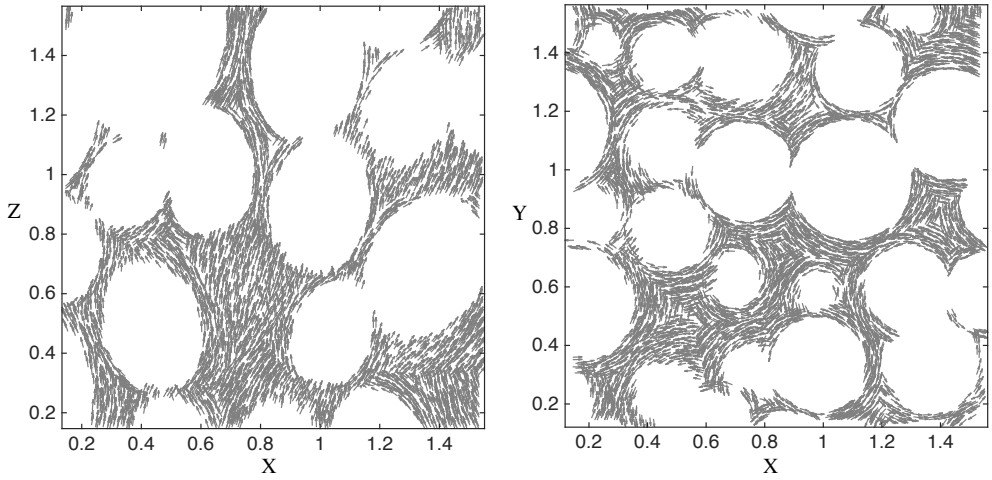

Fig. 4.13: Section cut of the FEA model and projected material vectors. Left: primary in-plane vectors ($\vec{v}_1$) projected onto the zx-plane. Right: secondary in-plane vectors ($\vec{v}_2$) projected onto the xy-plane. Distance units are in mm.

Use of isotropic graphite properties lowers the foam elastic anisotropy considerably (almost 50%), but the out-of-plane direction still has significantly higher modulus compared to the in-plane direction, showing that the elongation of bubbles contributes to the bulk anisotropy. Anisotropy in graphite coupled with its alignment to bubble walls increases the effect on anisotropy coming from the elongation of bubbles.

4.3.2 Micro-mechanics

Alignments of the Graphitic Planes

Fig. 4.13 illustrates sections from the FEA model along with the projected material orientation vectors. Most material vectors are perfectly aligned with the cell-walls, providing a good stress estimation at the cell-walls. The method also describes molecular layers in junctions according to the closest bubble wall formation, resulting in parallel molecular layers to the cell-walls. In real case, graphite sheets have low-alignment and more folded structure at the junctions, and contain interlayer gaps (see figure 2 in [48] (attached in page 155) and fig. 2.4). If these formations can be adapted to the local anisotropy model, stress distribution and deformation can be evaluated at junctions more accurately.

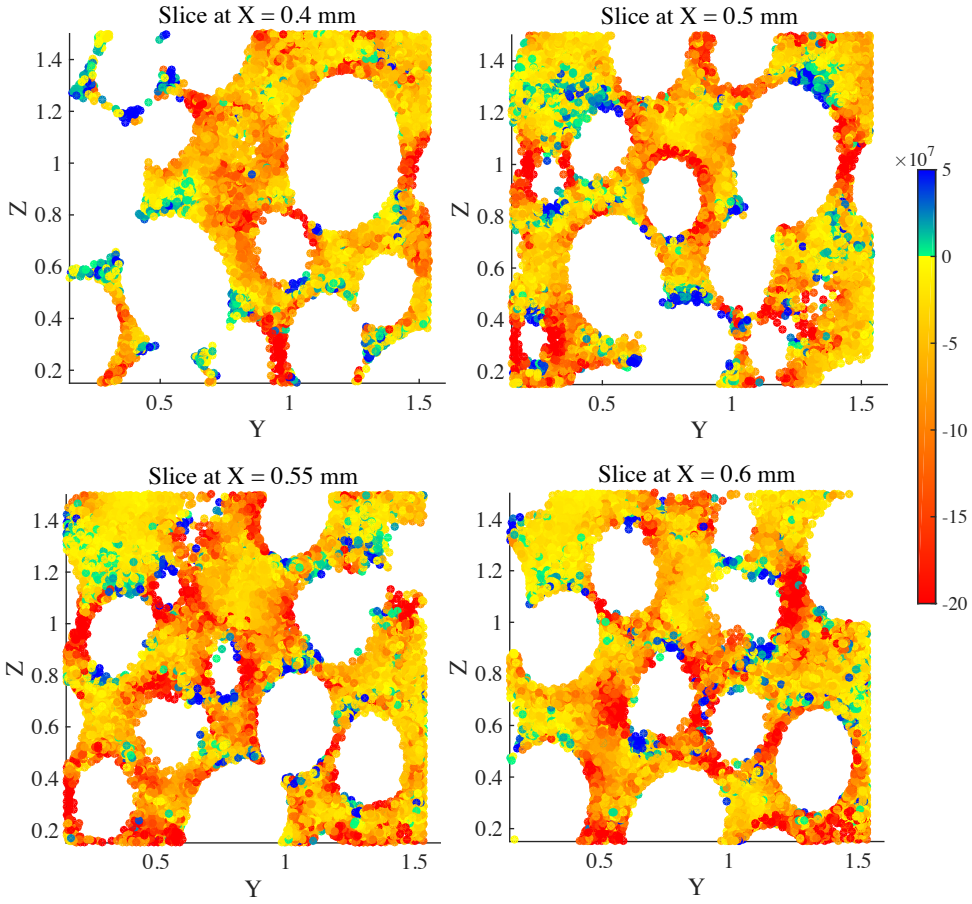

Fig. 4.14: Illustration of the static bending moment factor (in Pa/mm) during out-of-plane compression. Four internal sections at $x = 0.4$, 0.5, 0.55 and 0.6 mm are shown. The factor is most negative at the dark red elements; these have large bending and tend to Mode-I failure. The highest positive values (blue elements) are regions exposed to tensile stress and possible locations for Mode-II fracture.

Static Bending Moment Factors

Fig. 4.14 presents the static bending moment factor for the out-of-plane compression case. The data is shown for four internal sections of the foam at different x values to identify critical sectors for fracture. Since the factor is calculated by using eq. (4.21), compression forces in the elements give negative factor, while tensile forces result positive factor.

Large negative bending moment factors (dark red) appear at the side ligaments, and are candidate elements for Mode-I (bending) fracture. Large positive factors (blue)

are concentrated at the junctions (top and bottom of the cell-openings), and indicate where Mode-II (tensile) fracture could occur.

4.4 Summary and Conclusion

A series of destructive tests were performed to study fracture mechanics of Poco-HTC graphite foam in compression and shear cases [48]. Destructive compression (crush) tests were performed in both in-plane and out-of-plane directions to characterise anisotropy. These tests were filmed to visually examine crack initiation and propagation at the macro-scale. Images were captured via SEM from the fracture surfaces in crushed samples to examine post-failure formation of material at micro- and meso-scale. In another series of tests, cyclic compressive loads were applied in the elastic regime to characterise the elastic behaviour. The strengths were measured by subjecting some samples to continuously increasing compressive load up to destruction following the cyclic test.

Poco-HTC shows highly anisotropic behaviour in both elastic and fracture cases. It has higher modulus and is stronger in the out-of-plane direction. The SEM images of fracture surfaces indicate that the cracks initiate at cell-walls, and become cleavages between graphitic planes at the junctions. These separations propagate along and between the planes, and spread to neighbouring ligaments. At meso-scale, the initial failure mode is cell-wall bending and fracture followed by propagation to nearby cells up to complete material separation. The highlights of the measurements and examination of crack propagation and fracture surfaces are given in section 4.1.

A computational model for the porous graphite foam was developed to reproduce measured behaviour. A representative geometry was generated by an Abaqus script that uses measured cell dimensions and calculated positions as inputs. The model extended the existing approaches by incorporating the local anisotropy and material failure.

The general stress-strain behaviour was evaluated, and predictions are relatively close to measurements in both directions. Bulk elastic anisotropy was predicted albeit with low accuracy. Predicted compressive modulus in the in-plane direction was smaller than the measured values, leading to a higher foam elastic anisotropy. Though shear modulus was evaluated, measurement was not available for comparison against predicted values. Predicted strength values in both directions were in good agreement with the measured ones, suggesting that the failure model works for the compression case.

Analyses on the foam model based on isotropic solid properties showed that modelling larger cubes minimises edge effects, and gives higher in-plane elastic modulus. This in turn decreases elastic anisotropy, suggesting predictions would get closer to the measurement. Due to limitations on computer performance, it was not possible to increase edge size for foams with anisotropic material properties.

The model was also evaluated for the post-failure response of bulk material. However, the model is not reliable due to the use of a failure model with external code. Moreover, the fracture occurs element-by-element instead of a complete break of a ligament. Consequently, the fracture process spreads to a broader strain zone, and stress decreases smoothly instead of a sudden drop. This can be improved by embedding the failure models in the FEA model along with updating the stiffness matrix after each fracture case.

The model did not capture fractures in the shear deformation case: the shear strength prediction was more than 5 times higher than the measured strength. Cleavages, i.e. the separation of graphite planes are predominant in determining the shear properties of foam. Interlaminar shear failure criteria could be added to the model to improve its shear strength prediction accuracy.

Graphite planes are predominantly arranged parallel to the out-of-plane direction of foam, resulting in a stiffer and stronger foam. The graphite planes are stacked in the in-plane directions of foam. Several analyses were conducted to investigate the influence of structural and material parameters on the foam behaviour. Changing bubbles from prolate spheroids to spheres reduced the elastic and destructive anisotropy ratios, i.e. the foam tended to behave isotropically. In another study, the out-of-plane elastic modulus of graphite was increased, resulting in an increase in the foam moduli by having larger influence on the in-plane directions and reducing the foam anisotropy. In another analysis, isotropic material was used instead of anisotropic material, decreasing the foam elastic anisotropy. However, it remained significantly anisotropic because of the prolate spheroid bubble form. Thus, it can be concluded that the foam anisotropy is governed by the bubble shape, solid material properties and molecular alignments.

The aim of the research was to improve existing models by defining local anisotropy and material failure. Although the model has weaknesses in predicting bulk elastic anisotropy and failure responses, the presented methods significantly extend current foam models, and give a good basis for future works. These weaknesses are open for improvements. Improvements may include:

- The foam size can be increased to make the model less sensitive to edge effects.
- Another computer tool can be used to generate a clear foam CAD geometry, which will give smooth mesh at cell-walls.
- Failure model could be implemented in the FEA software to directly solve fracture problem, instead of in a separate Matlab routine.
- Other failure models such as interlaminar shear failure can be incorporated.
- The local anisotropy model can be improved to capture folded structures of graphite planes at junctions.

The results of this work (especially tables 4.4 and 4.5) will be used to construct a continuum model i.e. a macro-scale model for the foam. The next chapter is dedicated to this development and to mechanically analyse the tube-foam interface.

Chapter 5

Thermo-Mechanics of Tube-Foam Structure

This chapter discusses aspects of the tube-foam cooling structure in a Petal, and investigates whether any fracture may occur.

The cooling tube is sandwiched between two pieces of foam, and the structure is placed between facings of the Petal. The tube is glued in the foam at ambient temperature (around 20°C) and cools down to between −30 and −40°C when in use. The resulting thermal contraction of the tube exerts forces on the carbon foam, which can lead to fracture at the tube-foam interface, deteriorating the thermal performance. At the same time, resistance of foam against deformation can exert forces on the tube, and may lead to tube fracture and leakage of coolant. Early calculations (section 5.1) predicted fracture in the foam, which brought a need for a detailed FEA model to further investigate this issue.

A mechanical continuum model —i.e. macro-scale model— of the foam was developed based on the measurements and the micro-scale model described in the previous chapter. This continuum model was used in a thermo-mechanical model of the tube-foam structure to estimate the stress in the foam and tube due to thermal contraction. The analysis results were compared with the stress measured at the end of the elastic regime for foam samples. This was used to evaluate the risk of local fractures based on the maximum stress failure criterion. Furthermore, the safety factor was calculated via Tsai-Wu orthotropic failure criterion for more reliable evaluation of fracture.

5.1 Description of the Problem

Fig. 5.1 illustrates the tube-foam structure; x, y and z-axes define the alignment of the foam. When the tube shrinks due to the temperature drop, the tube contracts in the radial and longitudinal directions. The contraction directions are indicated with red arrows in fig. 5.1. Radial contraction of the tube exerts force on the foam, which are

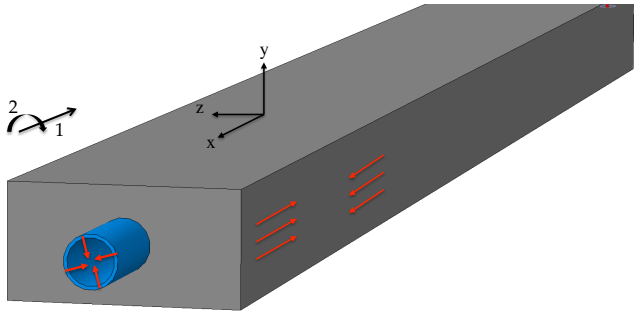

Fig. 5.1: Configuration of tube-foam structure. The foam is constrained since it is glued to facings at top and bottom. The vectors 1 and 2 define tube length and circumferential directions. x, y and z-axes are used to show the alignment of the foam, and define in-plane primary, in-plane transverse and out-of-plane directions. Red arrows illustrate the direction of internal forces due to longitudinal and radial contraction of the tube.

equivalent to stress states σ_z, σ_y and σ_{zy}, while longitudinal contraction produces shear forces along the tube-foam interface, which correspond to σ_{zx} and σ_{yx} shear states.

Longitudinal contraction of the tube is expected to result in higher loads compared to radial contraction. Thus, σ_{zx} and σ_{yx} shear states are expected to be the highest among the stress components, and potential modes for local fractures. The narrowness of the foam above and below the tube (y-direction) makes the σ_{yx} shear mode at these regions the most risky.

Resistance of the foam against deformation leads to internal forces in the tube. Stress in the tube longitudinal direction (σ_1) is the most important parameter to check for rupture.

The worst case scenario for the tube is when the foam is highly rigid and totally restricts the contraction of the tube. Change in the tube length δ at one end resulting from a ΔT temperature change is $\delta = \alpha \Delta T\, l$, where α is the thermal expansion coefficient and l is the half length of the tube. For 60°C temperature drop and 250 mm half tube length, the formula gives 0.138 mm contraction at one end of the structure. Material properties of titanium are given in table 2.2. δ/l gives the strain ε at one end. Multiplying the strain with the Young's modulus of the tube gives the stress along the tube, i.e. $\sigma = \varepsilon E$. The calculation gives 63.5 MPa stress, much less than the yield strength of the tube, indicating the tube design is safe.

The worst case for the foam fracture is when it has the highest deformation. This occurs when the foam does not have any resistance against tube contraction and is fully distorted with the tube. The foam thickness above the tube is $t = 1.35$ mm. The shear stress can be found as $\sigma_{yx} = (\delta/t)\, G_{yx}$, where in-plane shear modulus G_{yx} is 18 MPa, taken from results of FEA analysis, table 5.2. Calculation gives shear stress

1.8 MPa, much higher than the estimated shear strength (table 5.2). This oversimplified calculation predicts fracture in the foam, requiring a detailed FEA model to further study the design regarding the structural risks.

5.2 Continuum Mechanical Model for Carbon-Foam

Continuum modelling simplifies the description of behaviour of non-continuous material such as foams. Properties of a fictitious continuous material are estimated, and the foam is modelled with this, omitting the micro-structural properties used in the micro-scale model. It is used for large scale analysis, where the unit element size is larger than the pore size. Therefore, the model based on continuum material is also called macro-scale model. The continuum model uses the "constitutive equations" to describe material response. These equations are developed using measurements and/or evaluated behaviour from micro-scale models. In our case, the continuum material properties are based on the results of chapter 4.

The purpose of this study was to determine whether the stress resultants would exceed the elastic limits. Therefore, the continuum model is developed only to capture linear elastic behaviour of the foam. This requires a 6×6 material compliance matrix $[C]$ to set up relations between 1×6 stress and strain tensors. Then, the elastic limits, where the material starts to have local fractures, are determined, and compared to the predicted elastic stresses.

5.2.1 Compliance Matrix

Analyses with the micro-scale FEA model showed that both in-plane properties are similar, i.e. $E_x \cong E_y$. Consequently, the shear modulus in both in-plane directions on the out-of-plane face are similar, $G_{zx} \cong G_{zy}$. We assume that, shear stress only depends on strain of the same state, so the lower right 3×3 part of the compliance matrix becomes diagonal, and only two shear moduli are needed. Along with the equality of elastic properties in the in-plane material axes, the compliance matrix is significantly reduced and consists of the following six elastic constants: E_z, E_x, G_{zx}, G_{yx}, ν_{zx} and ν_{xy}. The compliance matrix is:

$$C = \begin{bmatrix} \frac{1}{E_x} & -\frac{\nu_{yx}}{E_x} & -\frac{\nu_{zx}}{E_z} & 0 & 0 & 0 \\ -\frac{\nu_{xy}}{E_x} & \frac{1}{E_x} & -\frac{\nu_{zx}}{E_z} & 0 & 0 & 0 \\ -\frac{\nu_{xz}}{E_x} & -\frac{\nu_{xz}}{E_x} & \frac{1}{E_z} & 0 & 0 & 0 \\ 0 & 0 & 0 & \frac{1}{G_{yx}} & 0 & 0 \\ 0 & 0 & 0 & 0 & \frac{1}{G_{zx}} & 0 \\ 0 & 0 & 0 & 0 & 0 & \frac{1}{G_{zx}} \end{bmatrix} \tag{5.1}$$

Values for the six elastic parameters were taken from measurements and the micro-scale FEA foam model: The Young's moduli, E_z and E_x, were taken from the measurements presented in table 4.4; while the shear moduli, G_{zx} and G_{yx}, and the Poisson's ratios, ν_{zx} and ν_{xy}, were taken from the analysis results summarised in tables 4.4 and 4.5.

The relation between a Poisson's ratio with reversed indices can be expressed as $\nu_{ij} = \nu_{ji} E_i / E_j$. Since $E_x = E_y$, $\nu_{yx} = \nu_{xy}$. The other Poisson's ratio is found as $\nu_{xz} = \nu_{zx} E_x / E_z$. Although ν_{xz} was evaluated via FEA (given in table 4.5), we preferred to calculate it by using both measured moduli along with evaluated ν_{zx} to ensure symmetry in the compliance matrix. The elastic constants are listed in table 5.2.

5.2.2 Tsai-Wu Safety Factor

Applying the Tsai-Wu tensor polynomial failure criterion is one of the most commonly-used methods to predict failure for a 3D orthotropic material [112]. The criterion has been used for PVC closed cell-foams with orthotropic properties to predict the strengths for multiaxial loading cases in [113], and the predictions showed good agreement with measurements. For our study, the same criterion was used to evaluate the safety factor within the foam. The Tsai-Wu failure criterion in compact form is [112]:

$$P_i \sigma_i + P_{ij} \sigma_i \sigma_j = 1 \tag{5.2}$$

$i \,\&\, j = 1,2,...,6$, specifying the material directions x, y, z, yx, zx, zy [26]. The parameters P are related to the measured stress limits in the material axes. These P coefficients are[27]:

$$\begin{aligned} P_i &= \frac{1}{\sigma^*_{it}} - \frac{1}{\sigma^*_{ic}} \\ P_{ii} &= \frac{1}{\sigma^*_{it}\,\sigma^*_{ic}} \\ P_{ij} &= \frac{-1}{2\sqrt{\sigma^*_{it}\sigma^*_{ic}\sigma^*_{jt}\sigma^*_{jc}}} \quad ;\ when\ \ i \neq j\ \ and\ \ i \,\&\, j = 1,2,3 \end{aligned} \tag{5.3}$$

where the subscripts t and c specifies tensile and compressive mode, and the superscript $*$ specifies stress limit or strength of the stress component σ_i.

In total, required measures are three shear strengths, and tensile and compression strengths in the three axial modes, giving 9 modes in total. The shear strengths in the

[26] For the criterion, we used the notations from the literature. They should not be confused with the stress tensor order used in the other parts of the dissertation.

[27] The P_{ij} coefficients with $i \neq j$ condition (e.g. P_{12}, P_{13} and P_{23}) are related to other strength quantities measured via equal biaxial tensile loading test. Due to complexity of the measurement, there is no exact data for these coefficients. They are expressed in the form of common axial strength terms as an approximation [114].

material axes are independent of the signs of the shear stresses, this makes P coefficients of the first power shear stress terms zero [114]: P_4, P_5 and $P_6 = 0$; moreover P_{14}, P_{24}, ..., $P_{64} = 0$ except P_{44} for σ_4 component, and the same applies for the other shear terms.

The left side of eq. (5.2) is the failure index. This index is separated into two terms:

$$\begin{aligned} C_1 &= P_i \sigma_i \\ C_2 &= P_{ij} \sigma_i \sigma_j \end{aligned} \tag{5.4}$$

P coefficients are substituted in eq. (5.4), and the notation system $i \& j = 1,2,...,6$ is replaced by the material directions x, y, z, yx, zx and zy. C_1 and C_2 can be written in expanded form:

$$\begin{aligned} C_1 &= \sigma_x \left(\frac{1}{\sigma^*_{xt}} - \frac{1}{\sigma^*_{xc}} \right) + \sigma_y \left(\frac{1}{\sigma^*_{yt}} - \frac{1}{\sigma^*_{yc}} \right) + \sigma_z \left(\frac{1}{\sigma^*_{zt}} - \frac{1}{\sigma^*_{zc}} \right) \\ C_2 &= \left(\frac{\sigma_x^2}{\sigma^*_{xt}\,\sigma^*_{xc}} + \frac{\sigma_y^2}{\sigma^*_{yt}\,\sigma^*_{yc}} + \frac{\sigma_z^2}{\sigma^*_{zt}\,\sigma^*_{zc}} + \frac{\sigma_{yx}^2}{{\sigma^*_{yx}}^2} + \frac{\sigma_{zx}^2}{{\sigma^*_{zx}}^2} + \frac{\sigma_{zy}^2}{{\sigma^*_{zy}}^2} \right) \\ &\quad - \left(\frac{\sigma_x \sigma_y}{\sqrt{\sigma^*_{xt}\sigma^*_{xc}\sigma^*_{yt}\sigma^*_{yc}}} + \frac{\sigma_x \sigma_z}{\sqrt{\sigma^*_{xt}\sigma^*_{xc}\sigma^*_{zt}\sigma^*_{zc}}} + \frac{\sigma_y \sigma_z}{\sqrt{\sigma^*_{yt}\sigma^*_{yc}\sigma^*_{zt}\sigma^*_{zc}}} \right) \end{aligned} \tag{5.5}$$

The safety factor S_f can be calculated by C_1 and C_2 [115]:

$$S_f = \frac{-C_1 + \sqrt{|\,{C_1}^2 + 4C_2\,|}}{2C_2} \tag{5.6}$$

First, determined strength terms (i.e. end of elastic regimes) were substituted in eq. (5.5) to calculate constants. Then, evaluated stresses were used in the same equation to calculate C_1 and C_2, and both were used in eq. (5.6) to find Tsai-Wu safety factor.

5.2.3 End of Elastic Regime

In eq. (5.5), the compression state stress limits in the out-of-plane (σ^*_{zc}) and in-plane (σ^*_{xc} and σ^*_{yc}) directions are directly taken from measurements made in [48] (attached in page 155) and given in table 5.1. The stress values at the initiation of local fractures are taken as stress limits, instead of using the crushing strengths.

The tensile strengths σ^*_{zt} and σ^*_{xt} were not measured during this study. The literature review has been done on similar type of carbon-foams. The reported data shows that tensile mode is weaker than the compressive mode, and tensile strengths are usually 40-70% of compressive strengths [97, 116]. Although these proportions are not precise

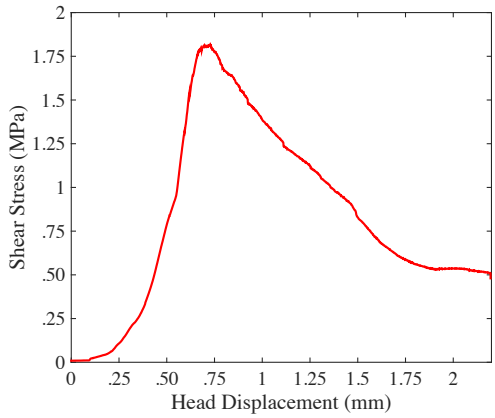

Fig. 5.2: Shear stress σ_{zx} vs. machine head displacement measured with Iosipescu shear test made on a Poco-HTC sample. Taken from [48] (attached in page 155).

for the current material, they can define a range to calculate tensile strengths based on measured compressive strengths. Then, various studies can be made within this range to validate the conclusion. The tensile strength is written as a fraction of compressive strength:

$$\sigma^*_{it} = k_i \, \sigma^*_{ic} \tag{5.7}$$

Fig. 5.2 presents the stress-displacement curve for the shear test in σ_{zx} mode (the data represents σ_{zy} mode as well due to in-plane equality). The peak of the curve is the shear strength, which is 1.8 MPa. Local fractures start before reaching this point; the slope of the curve starts to change around 1.6 MPa, which is taken as the end of the elastic regime σ^*_{zx}.

Measurements for σ_{yx} mode are not available. We estimate the elastic limit of σ_{yx} state as follows. Analyses show that G_{yx} is around half of G_{zx} (see table 4.4). The axial compression tests indicated that fracture in the in-plane direction started at slightly higher strain ε_x compared to the out-of-plane direction ε_z, see table 5.1. We assume

	Modulus MPa	Stress MPa	Strain %	Strength MPa
Out-of-plane, z	111	3.0	3.2	5.3
In-plane, x	75	1.5	3.5	3.5
Shear, zx	-	-	-	1.8

Table 5.1: Parametric results from compression (top and middle row) and shear (bottom row) tests. Taken from [48] (attached in page 155). The stress and strain are given at where local fractures start. The strength is the maximum stress the foam reached.

that the in-plane shear mode is also more flexible than the out-of-plane shear mode by a factor $\varepsilon_x/\varepsilon_z$. Then, stress at the end of the elastic regime for σ_{zx} state can be scaled with the ratio of shear moduli and axial compressive strains to determine σ^*_{yx}, so $\sigma^*_{yx} = \sigma^*_{zx}(G_{yx}/G_{zx})(\varepsilon_x/\varepsilon_z)$. The stresses at the end of the elastic regime are summarised in table 5.2.

5.3 Tube-Foam Thermo-Mechanical Model

The CAD model for the tube-foam structure was developed based on the drawing given in fig. A.6 using the Abaqus CAE software. The three-dimensional model is illustrated in fig. 5.1. The length of the structure was set to 500 mm, very close to the length of the foam used in the Petal.

Homogeneous orthotropic material with linear elastic properties was selected for the foam region (grey component in fig. 5.1). The lowest intended operation temperature of the structure is $-40°C$, and the low temperature condition is not expected to result in significant changes on the foam's mechanical behaviour[28]. Elastic constants given in table 5.2 were used in eq. (5.1) to calculate components of the compliance matrix, which was used in Abaqus to set material properties. The thermal expansion coefficient (CTE) of the Poco-HTC is given in [24] for various temperature ranges above room temperature for both out-of-plane and in-plane directions. Trend curves were fitted with the given data points, and the CTEs were calculated in both directions, resulting in -1.94 and 0.27 ppm/C at $-40°C$ and -1.07 and 1.02 ppm/C at $20°C$ for the out-of-plane and in-plane directions. These CTE values were used to define a linear behaviour

Elastic Constants					
E_z	E_x	G_{zx}	G_{yx}	ν_{zx}	ν_{xy}
$111^{\blacktriangle}$	$75^{\blacktriangle}$	$33^{\dagger}$	$18^{\dagger}$	$0.305^{\dagger}$	$0.413^{\dagger}$

Stress Limits					
σ^*_{zc}	σ^*_{xc},σ^*_{yc}	σ^*_{zt}	σ^*_{xt},σ^*_{yt}	σ^*_{zx},σ^*_{zy}	σ^*_{yx}
$3.0^{\blacktriangle}$	$1.5^{\blacktriangle}$	$k\sigma^*_{zc}$	$k\sigma^*_{xc}$	$1.6^{\blacktriangle}$	$0.95^{\bullet}$

Table 5.2: Elastic constants (E and G are given in MPa) used in continuum model developed for Poco-HTC, and stress limits in MPa defining where the local fractures start. ▲ : measured values; • : calculated values; † : from FEA.

[28] There is no direct measurement data showing the temperature dependent mechanical properties of the pocofoam. In [116], the thermal conductivity of the pocofoam is measured at various low temperature points, and the change in properties remains small. This indicates that there are no significant internal fractures. Therefore, we also do not expect significant changes in fracture stress levels for the foam.

	Temperature Derivative	At 20°C	At −40°C
Elastic modulus	−66.3 MPa/C	115 GPa	119 GPa
Poisson's ratio	2.8×10^{-4}/C	0.32	0.303
CTE	-	9.2 ppm/C	8.3 ppm/C

Table 5.3: Temperature dependent material properties of pure titanium alloy. Room temperature properties were taken from [64, 65]. Temperature derivatives of mechanical properties were taken from [117], and used to calculate properties at −40°C. The coefficient of thermal expansion at −40°C was taken from [118].

within the analysis temperature range. Material orientations were described in the model to align the foam out-of-plane direction with respect to the z-axis as shown in fig. 5.1.

The tube is made of T40 titanium alloy and was modelled as homogeneous isotropic material with non-linear elasticity based on temperature change. The elastic modulus and poisson's ratio are 115 GPa and 0.32 at room temperature. The temperature derivatives of the elastic constants are given in table 3 in [117] for pure titanium, and the derivatives stay constant down to −100°C . By using them, the mechanical properties were calculated at −40°C . The coefficient of thermal expansion was taken 9.2 and 8.3 ppm/C at 20°C and −40°C (the latter taken from [118]). Both values were used to define material thermal expansion characteristics with linear-trend within the analysis temperature range. Table 5.3 gives the values of temperature dependent material properties for titanium used in the model.

The foam is glued between two facesheets. The thermal expansion coefficient of the prepreg in the facesheet is −0.76 ppm/C. Since this is very low, the thermal deformation is neglected. The facings are much stiffer than the foam, and are assumed not to deform with the tube-foam structure when it is cooled down. That is, the foam is constrained by the facings, and this is modelled by prescribing zero displacement to the top and bottom surfaces of the foam, i.e. $u_x = 0$, $u_y = 0$ and $u_z = 0$ at the $+y$ and $-y$ faces. Initial temperature of the system was set to 20°C using the predefined temperature field in Abaqus. Then, the temperature was lowered to −40°C. The temperature drop was applied in a single step with 10 substeps to solve the non-linearity problem.

A single layer of shell elements was used to model the tube. A boundary region of foam 0.3 mm thick around the tube was divided into 5 layers of linear solid elements. The sensitivity of model predictions to this choice was investigated:

- The number of element layers in the foam at the interface region was increased; this changed the shear stresses by less than 5%.
- Quadratic elements were used in the foam region; the change in the shear stresses remained very small by less than 2%.
- The tube was modelled by 3 layers of solid elements; this had no significant effect on the evaluated stress.

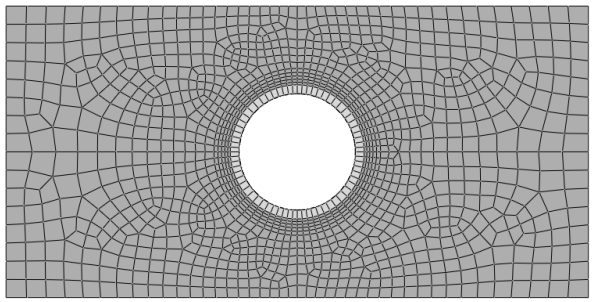

Fig. 5.3: Mesh used in the tube-foam model.

Therefore, the first mesh configuration was sufficient and used to produce the final results, fig. 5.3 shows the mesh.

5.4 Results and Discussion

Thermo-mechanical analysis was performed to examine the internal stresses in the tube-foam structure due to the 60°C temperature drop. First, stress fields both in the foam and the tube were examined to define which regions are susceptible for fracture. Safety factors in the foam were calculated based on maximum stress failure criterion in the out-of-plane (σ_{zx}) and the in-plane shear (σ_{yx}) directions[29]. Then, the elemental stress results were exported to Matlab, and the safety factor was calculated based on the Tsai-Wu failure criterion via eqs. (5.5) and (5.6). The von Mises yield criterion was used to calculate the safety factor in the tube component. Safety factors are given in table 5.4.

Figures 5.4 and 5.5 give the stress distributions through the foam and tube. The shear stresses get higher towards both ends of the foam, and it reaches maximum value at the interface at just a few mm before the end point (top and middle pictures). While the highest σ_{yx} is observed in the foam at the bottom side of the tube, the maximum σ_{zx} is in the elements diagonal to the tube. The end of the foam has high compressive stresses in the σ_z and σ_y modes near the interface, and they are locally concentrated (bottom pictures). The edges of the constrained top and bottom faces of the foam have tensile stresses (bottom right picture). The other shear term σ_{zy} and the axial term σ_x are very low compared to the other components, therefore their contour-plots are not given here. Along the tube, the von Mises stress[30] is highest in the middle sector (fig. 5.5), where the contraction of the tube is totally restricted by the foam. The total longitudinal contraction of the tube was evaluated at around 20 μm at one end.

[29]The safety factor was calculated by dividing stress limit to evaluated stress, i.e. σ_i^*/σ_i.

[30]Since the longitudinal contraction of the tube is the highest among the other modes, von Mises stress is almost the same as σ_1.

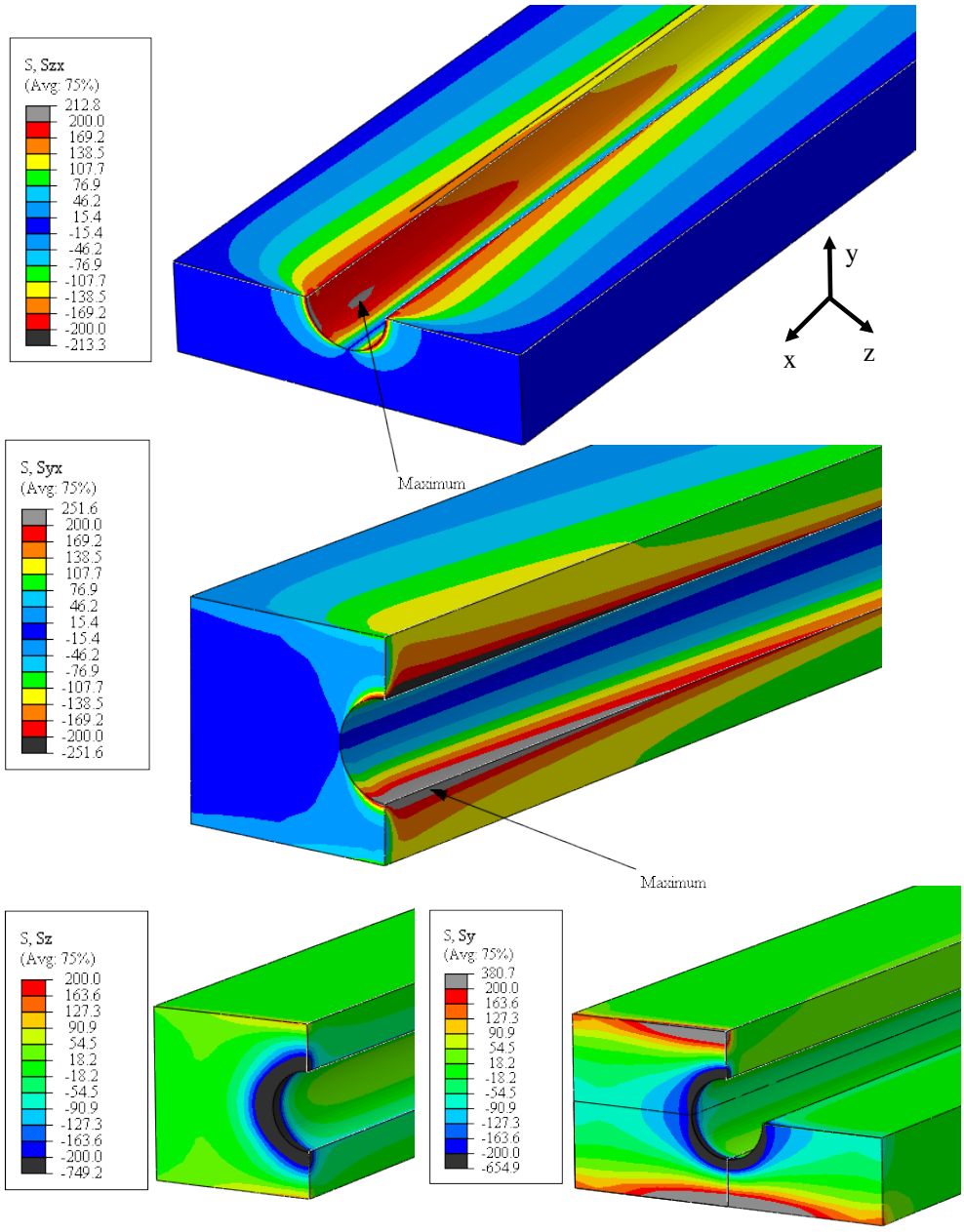

Fig. 5.4: Stress distributions within the foam for the 500 mm long structure: from top to bottom, σ_{zx}, σ_{yx}, σ_z and σ_y. Stresses are given in kPa. The contour-plots are symmetric in the x-direction. The foam has higher stresses at both ends, indicating the regions deformed.

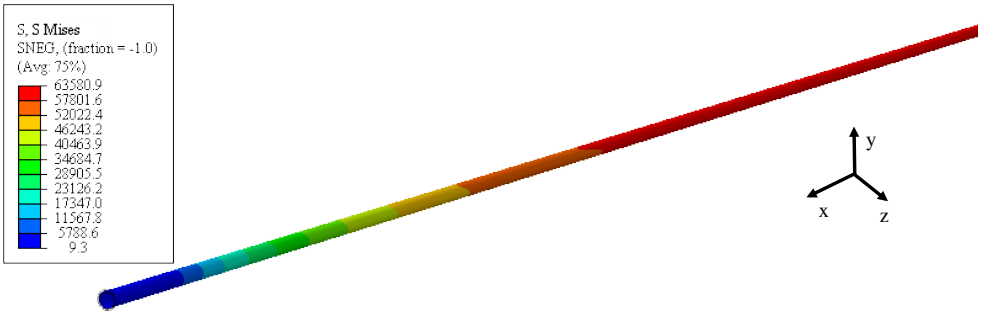

Fig. 5.5: Stress distribution through the tube for the 500 mm long structure. Stresses are given in kPa. The contour-plot is symmetric in the x-direction. The tube has higher stress at middle sector, showing where its deformation is restricted by the foam.

Based on the maximum stress failure criterion, the in-plane shear mode σ_{yx} of the foam gives the highest potential risk for local fractures by having the lowest safety factor, table 5.4. The Tsai-Wu criterion gives a slightly lower safety factor at the same location where the in-plane shear stress is the highest, since the other stress components have very low contribution to failure. This location is dominated by the shear mode.

Value of the unknown parameter k in eq. (5.7) was changed within $0.4-0.9$ range. The change in the safety factor was not significant (about 2%). Since the axial stresses —which are the multiplier of k— do not affect the damage factor strongly, the safety factor is insensitive to change in the factor-k.

However, this fact is only valid in this specific in-plane shear dominant zone. There are other regions with different stress combinations. For example, at the sides of the tube where the foam is thicker, the shear stresses are lower. Also, the shear mode

	Mode	**Stress (KPa)**	**Limit (KPa)**	**Safety Factor**
Foam	Max. Stress Criterion, Out-of-plane Shear, σ_{zx}	204	1600	7.84
	Tsai-Wu Criterion, max. σ_{zx} location	-	-	6.16
	Max. Stress Criterion, In-plane Shear, σ_{yx}	253	950	3.75
	Tsai-Wu Criterion, max. σ_{yx} location	-	-	3.71
	Tsai-Wu Cr., σ_{yx} shear and compressive stress	-	-	3.72
Tube	von Mises Yield Criterion, σ_m	63600	350000	5.50

Table 5.4: Maximums of the evaluated stresses and safety factors for the 500 mm long structure. Stresses are taken from figs. 5.4 and 5.5. Stress limits are also given for comparison. Tsai-Wu safety factors were calculated at $k = 0.5$. Since the Tsai-Wu safety factor is a combination of all stress components, there is no stress and limit to give. The variation of safety factor based on k is given in fig. 5.6.

σ_{zx} of the foam has higher strength (table 5.4). As a consequence, the contribution of the shear terms to the failure index reduces, increasing the importance of the axial contribution. So, safety factor is affected by both axial and shear stresses. Similarly, by moving away from the shear dominated zone and getting closer to the end of the structure, the shear stresses are lower and compressive stresses become higher (see bottom picture in fig. 5.4). Then, the failure index is determined by both shear and axial terms, and becomes more sensitive to change in k. Based on value of the factor-k and stress combination, location of the lowest safety factor changes.

Three main regions with different stress combinations were taken into account for comparative study. The first one is the shear dominated zone, where in-plane shear stress σ_{yx} is maximum. The second one is at the end of the foam, where compressive stresses are at their highest value and shear stresses exist. The third region is the edge of the constrained top face of the foam, where only tensile stresses are effective. Three elements were selected from the most critical location of each identified zone, and the safety factors were calculated at different values of k varying below 1. The results are presented with a graph given in fig. 5.6, and following facts were observed:

- When k is 0.5, the lowest safety factor is at the in-plane shear dominated zone, and the safety factors from the other zones are almost the same. As explained above, the shear dominated area is insensitive to k (red-line).
- By reducing k, the structure becomes weaker in tensile mode, and the safety factor dramatically decreases in the tensile stress region (green-line). Now, the lowest safety factor is observed here.
- By making structure stronger in tensile mode by increasing k, the safety factor is expected to increase naively, and it does in the tensile stress region. However, in contrast, the safety factor gets lower where shear and compressive effects are combined (blue-line). This can be explained by the contribution of the first order term in eq. (5.2). The tensile strength is lower than the compressive strength in carbon-foam ($\sigma_t^* < \sigma_c^*$), therefore P_i is always positive. The stresses are compressive (i.e. negative), so the first order term $P_i\sigma_i$ has a negative contribution to the failure index. By increasing k and getting closer to one, difference between the tensile and compressive strengths decreases, P_i gets closer to zero and the negative contribution diminishes. As a consequence, the overall failure index becomes higher, reducing the safety factor. Now, the lowest safety factor in the foam shifts towards this region, and it was calculated at a few mm away from the element where the shear stress σ_{yx} is maximum.
- Last of all, under the uncertainty of k, safety factors throughout the structure are still far away from the fracture point.

Though the local fractures may lead to deterioration in thermal performance, this does not mean complete failure of the foam. It can still sustain cooling support for the silicon sensors and electronics. In addition, the hole in the foam is machined with a radius $50\,\mu$m less than the outer radius of the tube. This crushes the foam at interface layer,

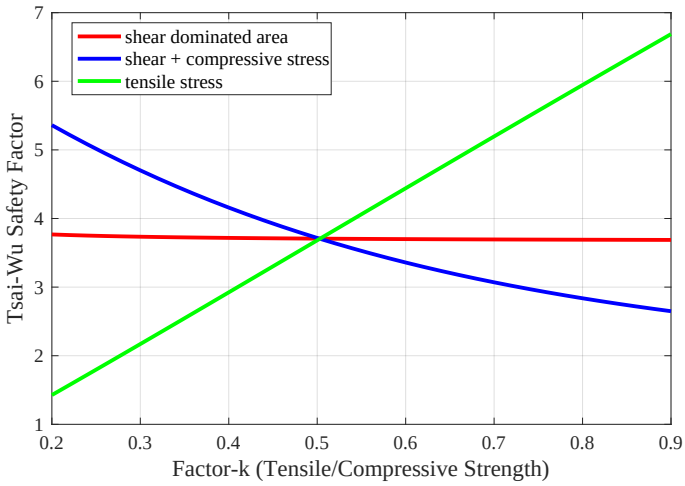

Fig. 5.6: Change in the Tsai-Wu safety factor by based on k. The results were produced at three elements, each selected from regions with different stress combinations.

providing good contact with tube to improve thermal transportation at this interface. Furthermore, the glue does not lie between the foam and tube, it fills the pores near the interface and makes the foam stiffer and stronger. Furthermore, the glue transfers the stress to a larger area, reducing apparent stress. These all will result in a higher safety factor than the prediction.

The safety factor of the tube is large enough not to be a design problem. As discussed, even the worst case scenario is not expected to cause fracture through the tube. Since the tube contraction is totally restricted by the foam in the middle sector, the evaluated von Mises stress is very close to the value calculated in section 5.1.

The actual Petal developed for the ATLAS upgrade uses Allcomp foam, which has higher elastic modulus and lower strength (table 2.2). Lower strength will decrease the safety factor in the foam. Since we did not perform any experiments to measure shear properties of Allcomp foam, we did not do any FEA studies with this configuration.

Miller and Gilchriese et. al [100] studied this case for the pixel stave prototype. Here, the steel tube was sandwiched in graphite coated RVC foam (Allcomp product). The base skeleton of the foam shows non-linear stress-strain behaviour before failure. Therefore, they used non-linear elasticity to construct a continuum model for the foam. Furthermore, the adhesive penetrated 0.5 to 1 mm into the foam at the tube/foam interface. This is quite thick compared to our configuration. Thus, they implemented the properties of the foam while filled by glue. In the model, the coefficient of thermal expansion was independent of temperature for the foam and facesheet, but dependent for the foam filled by glue and the tube. They used the model to predict stresses for

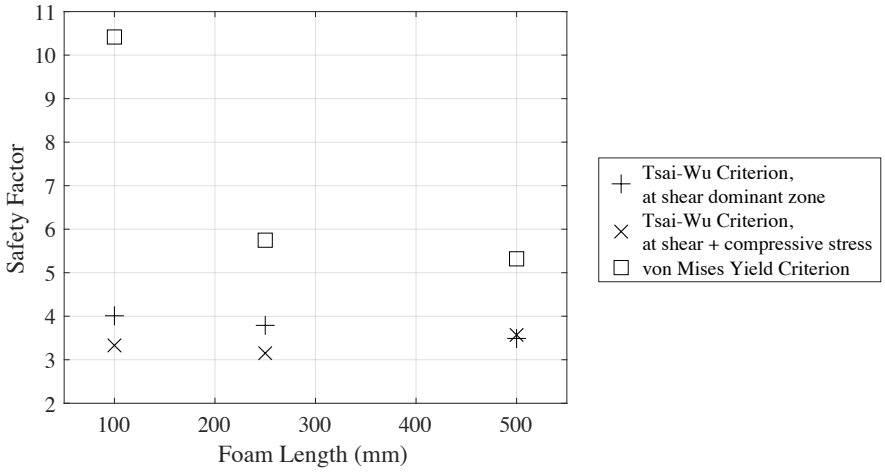

Fig. 5.7: Variation of minimum safety factors with tube/foam length. The Tsai-Wu safety factor in the foam is given at two critical locations at $k = 0.5$. The safety factor in the tube is given based on von Mises yield criterion. The safety factor decreases in the tube with a longer structure. However, beyond a specific length, it does not have a significant change. The behaviour is more complex in the foam. The lowest safety factor is where the in-plane shear stress is maximum, while the length is 500 mm. Below this length, the lowest safety factor is where shear and compressive stresses are combined.

a 60°C temperature drop, and the work concluded that the stress within the foam is below the permanent deformation state.

In order to improve cooling performance and radiation length of petals, there is a discussion to reduce the tube diameter while keeping the wall thickness the same. This implementation will make the contact area smaller, resulting in higher stress. Since the glue distributes the stress over a larger area, this is unlikely to be a problem but should be checked.

In another series of studies, the analysis was repeated for structures having 100, 250 and 500 mm foam length. The material properties were linear (independent of temperature), and the room temperature values were used. Fig. 5.7 gives the calculated safety factors. The safety factor in the tube decreases going from 100 to 250 mm length. However, beyond 250 mm length, it stays almost the same. As seen in fig. 5.5, the tube has higher stress at the middle section, where the foam cannot deform. In contrast, the foam is able to distort along with the tube at both ends, giving low stress in the tube and high stress in the foam. Examining the stress distribution along the length shows that the distortion zone in the foam stays constant with an increasing length of the structure. Therefore, the total contraction of the tube remains at 40 μm for the structures longer than 250 mm. The maximum stress in the middle of the tube did not increase, but the length of high stress region (red in fig. 5.5) does increase.

The Tsai-Wu safety factor in the foam is given at two critical locations: shear dominated zone and a region affected by in-plane shear stress in combination with compressive stresses. Factors were calculated by taking k as 0.5. In the structure with 500 mm length, the lowest safety factor occurs where the in-plane shear stress is maximum. In a shorter structure, shear stresses get lower, so the safety factor at shear dominated zone becomes higher. Now, the lowest safety factor shifts towards where the shear and compressive stresses have a combined effect at the end of the structure.

5.5 Conclusion

Early oversimplified calculations predicted that the foam will break, and this led to the need for a detailed finite element model of the tube-foam structure to further study structural risks. A continuum model for the carbon-foam was developed based on measurements and a micro-scale computational model described in the previous chapter. This model was used to construct a thermo-mechanical finite element model for the tube-foam structure. The model was used to analyse stresses through foam and tube resulting from a 60°C temperature drop. Stress results were compared with the maximum stresses before local fractures occur to evaluate design safety. Then, the Tsai-Wu orthotropic failure criterion was used for more reliable prediction of the safety factor within the foam.

According to the analysis results, the current configuration of the structure is not expected to fracture, and will reliably maintain the performance. However, there are some design issues that have to be taken into account for a final assessment of the structure:

- The foam is expected to behave stiffer and stronger due to glue. Inherently, this will increase the safety factor in the foam.
- It is desirable to reduce the thickness of this glue layer as much as possible in future, to improve the radiation length. Analysis without including glue takes the worst case in account, and the design safety is validated for future design scenarios with very little glue.
- The actual Petal design uses Allcomp foam, which is stiffer but weaker than Poco-HTC. This will reduce the safety factor in the foam.
- If the tube diameter is reduced for a new design configuration, the calculation should be repeated with the new dimensions.

Chapter 6

Conclusion

The mechanics of the Petal design for the ATLAS tracker upgrade, graphitic foams and the tube-foam cooling element have been investigated in great detail, creating a solid knowledge base to solve design issues in the ATLAS Inner Tracker.

Regarding the ATLAS petal design, the design was reduced to a sandwich beam consisting of two thin facings glued on top and bottom of a thick core, and its bending stiffness was analytically modelled. The calculations agree within 3 % with the computational results from a finite element model (FEM). The analytical model was used to compare different prepregs and angular configurations for the facings and different honeycomb materials for the core. The target was to improve bending stiffness, and reduce weight to reduce the radiation length of the structure. The study led to a recommendation of using 3 layers of a 45 gsm K13C2U/EX1515 prepreg with $[0/90/0]^\circ$ angular configuration in the facings, and Plascore Kevlar honeycomb with a moderate shear modulus in the core. The proposed configuration resulted in 16 % improvement in the fractional radiation length for the base petal.

A FEM of the Petal prototyped at Nikhef (LoI-design) was developed to reproduce measured bending behaviour and modal frequencies. The model predicts bending stiffness and the lowest modal frequencies within 5 % agreement with experimental measurements. This model was applied to the Petal designed by the DESY group (LTF-design), and used to evaluate improvements resulting from material recommendations above.

The analyses show that the recommended prepreg gives a significant reduction in mass (~ 30 g), while angular configuration in the facings and use of the Kevlar core increase bending stiffness of the Petal. Through the computations on the Petal with ATLAS conditions (i.e. containing modules and fixed to the end-cap frame), both improvements resulted in a 5 % increase in the lowest natural frequency, which was evaluated 64 Hz, belongs to the bending mode, and still sustains stability requirements.

Despite the improvements of the recommended configuration, the petal design updated in 2016 does not contain the selected core. The design uses the UCF carbon-fibre honeycomb core, which is 1.5 times denser and having an almost 3 times higher shear modulus than the Kevlar. Changing to the recommended Kevlar core will reduce the

weight 8 g more at the cost of 2 % reduction in the lowest natural frequency. Furthermore, making the close-outs from carbon-fibre composite is expected to save up to 20 g, which will further reduce the fractional radiation length by 11 % for the base petal.

Regarding the graphitic foams, a series of destructive tests were performed to study fracture mechanics of Poco-HTC graphitic foam in compression and shear cases [48]. The destructive compression, i.e. crush tests, were carried out in both out-of-plane and in-plane directions of the foam to characterise anisotropy. Some of these tests were also used to characterise the elastic behaviour.

Poco-HTC shows highly anisotropic behaviour in both elastic and fracture cases. It has higher modulus and strength in the out-of-plane direction. This comes from two separate effects: the graphite planes of carbon atoms are aligned along the out-of-plane (z) direction; and the cells are elongated in the out-of-plane direction.

The initial failure mode is cell-wall bending and fracture followed by propagation to nearby cells up to complete material separation. In the out-of-plane crushing, the fracture plane propagates diagonally in both in-plane directions with a slightly larger component in the out-of-plane direction. This is very close to the 45° crack line in typical brittle shear failure. Cracks tend to grow between layers of graphite resulting in a slightly larger component in the z-direction. In the in-plane (x) crushing, the propagation is horizontal in the out-of-plane (z) direction in line with the graphite planes, while it is around the 45° diagonal in the in-plane transverse (y) direction. In the shear test, cracks appear in the foam out-of-plane direction, as cleavages between the planes of graphite. These observations showed that alignment of graphitic planes affects the behaviour of macro-cracks.

The SEM images of the fracture surfaces of the crushed samples indicate that the cracks emerge at cell-walls, becoming cleavages between graphitic planes at the junctions. These separations propagate between the planes and spread to neighbouring ligaments.

A computational micro-model for the porous graphite foam was developed to reproduce measured behaviour. The aim of the research was to improve existing models by defining local anisotropy and material failure. The general stress-strain characteristic was evaluated and predicted relatively close to measurements in both directions. Predicted compressive modulus in the in-plane direction was smaller than the measured values, leading to a higher foam elastic anisotropy. Predicted strength values in both directions were in good agreement with the measured ones, suggesting that the failure model works for the compression case. Due to low in-plane modulus, crushing strain was predicted higher than the measured value. Increasing the foam edge size reduces the micro-structural effects and gives higher in-plane modulus, bringing prediction closer to the measurement. Although the anisotropy model shows weaknesses in predicting bulk elastic anisotropy and failure responses, the method presented here sufficiently extends current foam models, and gives a good basis for future work. Furthermore, potential improvements are described in this thesis which should improve prediction accuracy.

Regarding the tube-foam structure, the elastic constants found as a result of experimental and computational studies on graphitic foam were used to construct a macro-scale continuum model. This model was used to develop a FEM of the tube-foam element for structural analysis. Computations showed that internal stresses arising due to a 60°C temperature drop are not expected to cause any fracture at the tube-foam cooling element. Consequently, the design is safe to use in the Petal.

In summary:

- The Petal design was described in detail with respect to the structural aspects. Materials are recommended to improve the design.
- A verified FEM of the ATLAS Petal design was delivered. This can be used by other groups within the ATLAS team for further studies.
- The fracture mechanism in anisotropic graphitic foam were investigated in detail [48].
- A computational micro-model of the graphitic foam was developed extending existing methods by incorporating local material anisotropy and failure models.
- The design safety in the tube-foam cooling element of the Petal was analysed in terms of structural risks.

Appendices

A.1 Description of Terms in Radiation Length X_0

The definitions of the symbols used in multiple scattering and radiation length formulas, eqs. (1.1) to (1.3), are:

Θ	Angular deviation from the incoming particle trajectory,
k	Charge of the particle divided by the proton charge,
P	Momentum of the incoming particle (MeV/c),
c	Speed of light (m/s),
β	Speed of the particle as a fraction of the speed of light,
X_0	Radiation length (g/cm^2),
t	Thickness of material along particle trajectory (cm),
r_0	Classical electron radius ($r_0 = 2.82 \times 10^{-15}$ m),
ρ	Material density (g/cm^3),
α	Fine structure constant ($\alpha \approx 1/137$),
N_A	Number of scattering centers or atoms per mole (mol^{-1}), i.e. Avogadro's number,
A_r	Relative atomic weight (g/mol),
Z	Nuclei number i.e. number of protons.

A.2 Calculating Radiation Length of Materials

This section gives a method to calculate the fractional radiation length $\%X_0$ of the structures. The radiation length (X_0) of an element is given in eq. (1.2). Many of the materials used in the petal are molecular mixtures of elements. The radiation length of a molecule is the combined contribution of each individual element and is calculated from [119]:

$$\frac{{A_r}^{(m)} N^{(m)}}{{X_0}^{(m)}} = \sum \frac{{A_r}^{(i)} N^{(i)}}{{X_0}^{(i)}} \tag{A.1}$$

where $A_r^{(m)}$ and $N^{(m)}$ are the averaged atomic mass and the total number of moles in a molecule, $A_r^{(i)}$ and $N^{(i)}$ are the atomic mass and the number of moles of each element.

The radiation length of a composite consisting of multiple materials can be found in a similar way:

$$\frac{1}{{X_0}^{(c)}} = \sum \frac{w^{(i)}}{{X_0}^{(i)}} \tag{A.2}$$

where ${X_0}^{(c)}$ is the radiation length of the composite, and $w^{(i)}$ and ${X_0}^{(i)}$ are the fraction by weight and the radiation length of each constituent.

Total fractional radiation length $\%X_0$ of a structure can be calculated by summing the fractional radiation lengths of each component along the particle's path:

$$\%X_0 = \sum 100 \times \frac{t^{(i)}\rho^{(i)}}{{X_0}^{(i)}} \tag{A.3}$$

where t and ρ are thickness traversed and density of each component indicated by i.

The material traversed depends on the track location and angle: some tracks pass through the cooling pipes and see more material; most do not. As the incident angle increases, tracks pass through more material. To arrive at a single representative number, we use perpendicular incidence and spread material evenly. The area chosen for this spreading is the total active area of sensors on one side of a petal A_{eff}, which is 774 cm^2 calculated from the FEA model. For each item in a petal we calculate its mass $m^{(i)}$ and use eq. (A.4) in eq. (A.3).

$$t^{(i)}\rho^{(i)} = \frac{m^{(i)}}{A_{eff}} \tag{A.4}$$

Molecular composition of materials used in the petal are listed below:

- Carbon-fibers used in the petal are comprised of more than % 99 carbon element, therefore we assume they are purely made of it.
- Both resins, RS3 and EX1515, used in 80 gsm and 45 gsm prepregs are based on cyanate ester with the molecular formula[31] of $C_7H_4NO(C_{21}H_{15}NO)_nH$, where n is between 1 and 50.
- Kevlar honeycomb core is made of para-aramid fiber and phenolic resin. Para-aramid fiber is known as poly(para-phenylene terephthalamide) with molecular formula of $(C_{14}H_{10}N_2O_2)_n$ [121]. Phenolic resin, also called phenol-formaldehyde resin, can have different molecular structures in polymerised form based on cross-linking network, but the simplest repeating unit is $(C_7H_8O_2)_n$ [122].
- Nomex honeycomb core is made of poly(meta-phenylene isophthalamide) (i.e. meta-aramid) fibers with same molecular formula as in para-aramid fibers [123], and phenolic resin.
- Carbon-fiber honeycomb core uses cyanate ester resin with molecular formula given above.
- Araldite and Hysol are two-component epoxy-adhesives. The most known epoxy prepolymer is bisphenol A diglycidyl ether with the most representative molecular unit of $C_{21}H_{24}O_4$ [124]. The molecular composition of the curing agent is not known.
- PEEK, poly(ether ether ketone), has the molecular composition of $C_{21}H_{18}O_3$ [125].
- As mentioned earlier in the text, cooling tubes are made of pure titanium alloy.

[31] The molecular formula of cyanate ester resin depends on synthesis process, and may vary from one producer to another. Since, companies do not share their product's molecular formula, we do not know exact formula. Instead, the formula 5 given in the patent application [120] is used here.

Element	**Atomic Number,** Z	**Atomic Weight,** A_r (g/mol)	**Radiation Length** X_0 ($\mathrm{g.cm^{-2}}$)
H	1	1.008	63.04
C	6	12.011	42.70
N	7	14.007	37.99
O	8	15.999	34.24
Ti	22	47.867	16.16

Table A.1: Radiation length and nuclei properties of common elements within the molecular structure of materials used in the Petal. Radiation length values are based on experimental data and taken from [119].

Material	**Mol. Formula**	**Rad. Length** X_0 ($\mathrm{g.cm^{-2}}$)
Cyanate ester resin	$C_7H_4NO(C_{21}H_{15}NO)_nH$	42.57
Aramid fibers	$(C_{14}H_{10}N_2O_2)_n$	41.29
Phenolic resin	$(C_7H_8O_2)_n$	40.95
Epoxy resin	$C_{21}H_{24}O_4$	41.72
PEEK	$C_{21}H_{18}O_3$	41.91

Table A.2: Molecular formulas and calculated radiation lengths of the materials.

Component	**Constituents & Weight Fractions**	**Rad. Length** X_0 ($\mathrm{g.cm^{-2}}$)
80 gsm prepreg	0.71/0.29 carbon-fiber / cyanate ester resin	42.66
45 gsm prepreg	0.57/0.43 carbon-fiber / cyanate ester resin	42.64
Nomex hc.	0.50/0.50 aramid-fiber / phenolic resin	41.12
Kevlar hc.	0.50/0.50 aramid-fiber / phenolic resin	41.12
Carbon-fiber hc.	0.50/0.50 carbon-fiber / cyanate ester resin	42.64
Close-out composite	0.50/0.50 carbon-fiber / epoxy resin	42.14
Close out plastic	PEEK	41.91
Glue bus-to-facing	Hysol, epoxy	41.72
Glue - in bare petal	Araldite, Epoxy Resin	41.72
Carbon-foam	Carbon	42.70
Tube	Titanium	16.16

Table A.3: Radiation lengths of the components used in the petal. hc. is the abbreviation for honeycomb core.

Table A.1 gives the radiation length and nuclear properties of elements in the petal. Instead of using eq. (1.2), we directly took measured radiation lengths from [119]. Then, the radiation lengths of the materials were calculated using eq. (A.1) according to the molecular formula of the material, and results are given in table A.2.

Eq. (A.2) was used to calculate the radiation length for the components by accounting for the mass fractions and the radiation lengths of each individual constituent material. Mass fraction of the items in prepregs are already found in section 3.3.1. For the honeycomb cores and the composite close-outs, there is no clear data expressing how much of the mass comes from fiber or resin. Since the radiation lengths of both constituents are relatively close to each other, we took mass fractions 0.5. Calculated radiation lengths for the components are summarised in table A.3.

Finally, data presented in table A.3 was used in eqs. (A.3) and (A.4) to calculate fractional radiation lengths $\%X_0$ of components and the petal. The results are presented in table 3.10.

A.3 Prototyping Nikhef LoI-Petal

The petal prototype was made at Nikhef as an assembly of parts. All components were supplied by the manufacturers except the close-outs, which were made in Nikhef. The prototyping steps are as follows:

- Close-outs were made with hand lay-up technique. Firstly, a foil was placed on one side of a U-channel mould with peel ply on top. Bidirectional carbon-fibre weave was added and resin matrix was applied with a brush. This was covered by another layer of peel ply and foil. The other half of the mould was forced in to the U channel. The matrix was cured at ambient temperature. The close-outs were cut to length (10 close-out pieces in total).
- All close-outs were glued on the first facesheet on one side.
- Meanwhile, smaller rectangular foam pieces were machined from the larger block. A cylindrical hollow was formed on one side with machine milling, using a custom-ordered tool to give precisely the desired radius (1st-2nd images in fig. A.1). Since the original foam block was small, the foam block was made in several short sections.
- The tube was placed in the hollow and glued (3rd image).
- The foam/tube part was glued onto the first facesheet (3rd image).
- Another layer of adhesive was applied on top of tube/foam block and the another foam piece were placed on top. Thus, the tube was sandwiched between two sets of foam (4th image).
- The top of the foam was machined to the same height as the honeycomb and close-outs.

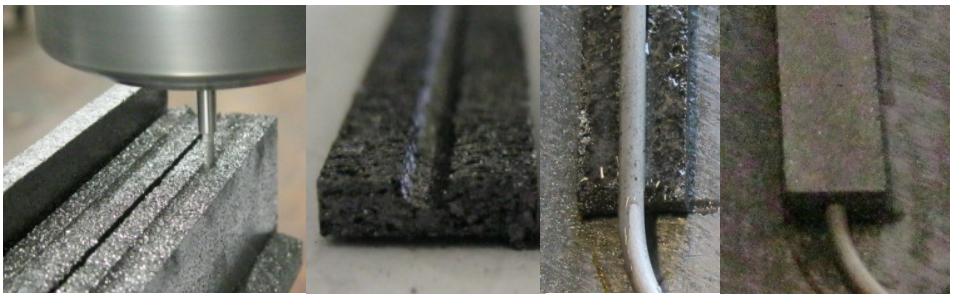

Fig. A.1: Tube/foam component assembly steps.

- A bath of glue was prepared with 0.1 mm deep. The honeycomb core was dipped in bath for 5 seconds, and then the other side was dipped for the same duration. The honeycomb was placed on the first facesheet (see fig. 1.6).
- The glue was applied on top of the close-outs with a brush.
- The second facesheet was placed on the honeycomb and close-outs, weighted down with a tool plate and vacuum bagging technique.

A.4 Boundary Conditions for Three-point Bending Analysis of LTF-Petal

Fig. A.2 shows the points and lines used to define loads and boundary conditions. Line-A and curve-B are the inner and outer ends of the petal on the neutral plane, and pinned by prescribing zero displacements to all axial directions, i.e. $u_x = 0$, $u_y = 0$ and $u_z = 0$. The point-C defines the corner of the petal at the side without cooling tubes. The concentrated force is applied to the point-D, and the deflection is read at the point-E. The concentrated load may lead to high deformation on the node where it is applied, so having E offset from D is more reliable. The locations of points D and E with respect to the point-C are given in fig. A.2.

A.5 Boundary Conditions for Constrained Body Modal Analysis

Constrained-body modal-analysis evaluates modal frequencies of a structure, while the supports restrict its movement. This is a more realistic study case for the petal installed in an End-cap structure. Fig. A.3 gives the locking points of LTF-Petal to the End-cap disk frames. The following boundary conditions were applied to model such an installation:

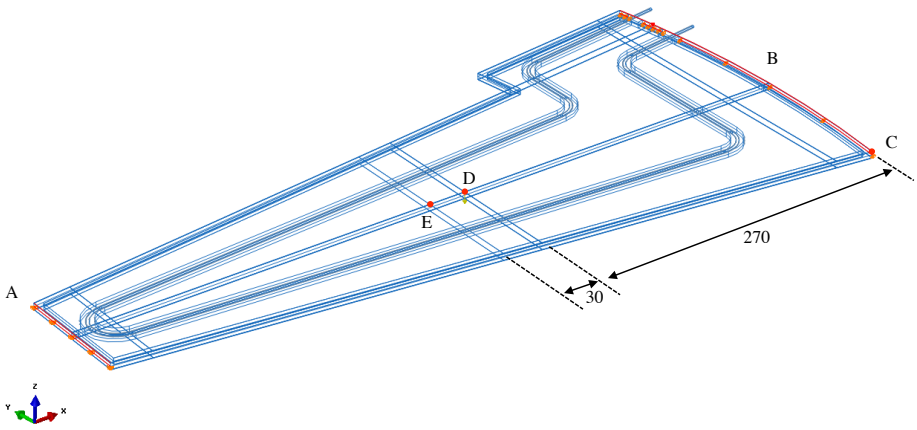

Fig. A.2: Boundary conditions for three-point bending analysis of LTF-Petal. Dimensions are in mm.

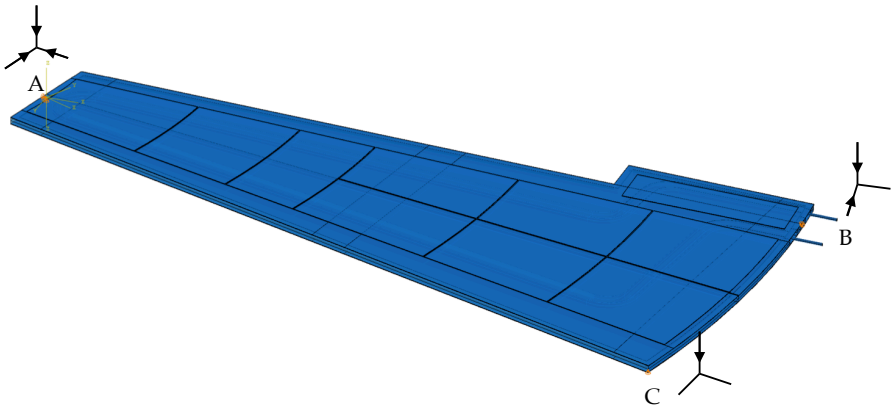

Fig. A.3: Boundary conditions for constrained body modal analysis. The conditions model the petal, when it is installed into the End-cap structure.

- Node-A was pinned by prescribing zero displacements to all three directions, i.e. $u_x = 0$, $u_y = 0$ and $u_z = 0$.
- Node-B was released to slide on the axis from node-A to B, and constrained from the remaining translations, i.e. $u_1 =$ free, $u_2 = 0$ and $u_3 = 0$. The subscript 1, 2 and 3 defines translations in the local coordinate system, where the axis-1 is the vector from node-A to B, and the axis-2 is perpendicular to the axis-1 in the petal in-plane direction. The axis-3 is the petal out-of-plane direction.
- Node-C was only constrained in the petal out-of-plane direction, i.e. $u_z = 0$.

A.6 Unforced Vibration of Beams

In this section, the free-body and constrained-body modal frequencies are compared by using an analytical approach for a simple beam.

Neglecting rotary inertia and shear effects, the general equation of unforced vibration of a beam can be described by [126, 127]

$$E I \frac{\partial^4 y}{\partial x^4} + \rho A \frac{\partial^2 y}{\partial t^2} = 0 \tag{A.5}$$

where E is the elastic modulus of beam material, I is the area moment of inertia, ρ is the material density and A is the cross-sectional area.

y is the deflection of a beam in the vertical axis. For a statically bent beam, it can be written as a continuous function of the spatial variable x along the beam. The deflection vibrates in time, therefore it also has a time dependent harmonic component. The deflection can be written by separating spatial and temporal components:

$$y(x,t) = w(x)\,u(t) \tag{A.6}$$

The spatial part $w(x)$ has general solution:

$$w(x) = C_1\,sin(kx) + C_2\,cos(kx) + C_3\,sinh(kx) + C_4\,cosh(kx) \tag{A.7}$$

and the temporary part $u(t)$ can be written:

$$u(t) = D_1\,sin(2\pi\omega t) + D_2\,cos(2\pi\omega t) \tag{A.8}$$

where k is the wavenumber specifying the mode shape, and ω is the frequency of the vibration. By writing $y(x,t)$ in full form with eqs. (A.7) and (A.8) and substituting in eq. (A.5), modal frequency ω can be related to the wavenumber k:

$$\omega = \frac{k^2}{2\pi}\sqrt{\frac{E I}{\rho A}} \tag{A.9}$$

The moment M and the shear force V along the beam can be written based on the spatial part of the deflection:

$$\begin{aligned} M(x) &= E I \frac{\partial^2 w}{\partial x^2} \\ V(x) &= \frac{\partial M}{\partial x} = E I \frac{\partial^3 w}{\partial x^3} \end{aligned} \tag{A.10}$$

A.6.1 Beam Free at Both Ends

While the beam is free in space, the moments M and shear forces V at both ends are zero [127]. Applying these boundary conditions in eq. (A.7) gives:

$$\begin{aligned}
&x = 0\,,\ EI\frac{\partial^2 w}{\partial x^2} = 0 \ \Rightarrow\ 0 = -C_2 + C_4\\
&x = L\,,\ EI\frac{\partial^2 w}{\partial x^2} = 0 \ \Rightarrow\ 0 = -C_1\,sin(kL) - C_2\,cos(kL) + C_3\,sinh(kL) + C_4\,cosh(kL)\\
&x = 0\,,\ EI\frac{\partial^3 w}{\partial x^3} = 0 \ \Rightarrow\ 0 = -C_1 + C_3\\
&x = L\,,\ EI\frac{\partial^3 w}{\partial x^3} = 0 \ \Rightarrow\ 0 = -C_1\,cos(kL) + C_2\,sin(kL) + C_3\,cosh(kL) + C_4\,sinh(kL)
\end{aligned} \tag{A.11}$$

By eliminating C_3 and C_4 from the second and fourth equation above, a relationship between C_1 and C_2 can be described by two separate equations.

$$\frac{C_1}{C_2} = -\frac{cosh(kL) - cos(kL)}{sinh(kL) - sin(kL)} \quad \& \quad \frac{C_1}{C_2} = -\frac{sinh(kL) + sin(kL)}{cosh(kL) - cos(kL)} \tag{A.12}$$

By using both relationships, following constraint on the wavenumber k is found:

$$cosh(kL)\,cos(kL) = 1 \tag{A.13}$$

A.6.2 Beam Simply Supported at Both Ends

The kinematic mountings used in the petal is similar to the simply supports, which restricts translational motions and allows rotational motions. The deflection w and the moment M are zero at the supports [127]. By applying these conditions in eq. (A.7), following equations are found:

$$\begin{aligned}
&x = 0\,,\ w = 0 \qquad\ \Rightarrow\ 0 = C_2 + C_4\\
&x = L\,,\ w = 0 \qquad\ \Rightarrow\ 0 = C_1\,sin(kL) + C_2\,cos(kL) + C_3\,sinh(kL) + C_4\,cosh(kL)\\
&x = 0\,,\ EI\frac{\partial^2 w}{\partial x^2} = 0 \ \Rightarrow\ 0 = -C_2 + C_4\\
&x = L\,,\ EI\frac{\partial^2 w}{\partial x^2} = 0 \ \Rightarrow\ 0 = -C_1\,sin(kL) - C_2\,cos(kL) + C_3\,sinh(kL) + C_4\,cosh(kL)
\end{aligned} \tag{A.14}$$

Using the set of equations above gives the following constraint on the wavenumber k:

$$sinh(kL) = 0 \tag{A.15}$$

	Free-Free Beam $k_1 L$	Simply Supported $k_2 L$	Ratio of Freqs. ω_1/ω_2
1st bending	4.7300	3.1416	2.2668
2nd bending	7.8532	6.2832	1.5622
3rd bending	10.9956	9.4248	1.3611
4th bending	14.1371	12.5664	1.2656

Table A.4: The product of the wavenumber k and the beam length L for the first four bending modes for a beam under unforced vibration, and the ratio of modal frequencies. Two type of boundary conditions are considered: free-free and simply supported.

A.6.3 Solution

Eqs. (A.13) and (A.15) are numerically solved in Matlab to find values of kL for the first four bending modes. From eq. (A.9), the ratio of the modal frequencies for free and simply supported beams is found as the square of the ratio of their k values i.e. $\omega_1/\omega_2 = (k_1/k_2)^2$. Table A.4 gives the results, with subscript 1 for the free beam and 2 for the simply supported beam.

When the beam is unsupported, the wavenumber k and the modal frequency is higher. For the first bending mode, the unsupported beam has 2.27 times higher modal frequency than the simply-supported case. The calculated value is consistent with the evaluated modal frequencies for the petal in table 3.10.

A.7 Derivative of Radial Distance

The radial distance $r(\theta,\phi)$ of points on an ellipsoid with radii (R_x, R_y, R_z) given in eq. (4.5) can be rewritten as:

$$r = K^{-1/2} \tag{A.16}$$

where

$$K = \left(\frac{s\theta\, c\phi}{R_x}\right)^2 + \left(\frac{s\theta\, s\phi}{R_y}\right)^2 + \left(\frac{c\theta}{R_z}\right)^2 \tag{A.17}$$

Then, the partial derivatives of r become:

$$\begin{aligned} \frac{\partial r}{\partial i} &= -\frac{1}{2}\frac{\partial K}{\partial i}K^{-3/2} \\ \frac{\partial^2 r}{\partial i \partial j} &= -\frac{1}{2}\frac{\partial^2 K}{\partial i \partial j}K^{-3/2} + \frac{3}{4}\frac{\partial K}{\partial i}\frac{\partial K}{\partial j}K^{-5/2} \end{aligned} \tag{A.18}$$

Taking the partial derivative of K in eq. (A.17) with respect to θ and ϕ we obtain:

$$\begin{aligned} \frac{\partial K}{\partial \theta} &= 2\, s\theta\, c\theta \left[\left(\frac{c\phi}{R_x}\right)^2 + \left(\frac{s\phi}{R_y}\right)^2 - \left(\frac{1}{R_z}\right)^2\right] \\ \frac{\partial K}{\partial \phi} &= 2\,(s\theta)^2\, s\phi\, c\phi \left(\frac{1}{{R_y}^2} - \frac{1}{{R_x}^2}\right) \end{aligned} \tag{A.19}$$

Since we use a prolate sphere as the cell model, $R_y = R_x$. This gives $\frac{\partial K}{\partial \phi} = 0$ and $\frac{\partial r}{\partial \phi} = 0$. However, equations are not simplified in order to be able to use them with $R_y \neq R_x$ if needed. The second derivatives become:

$$\begin{aligned} \frac{\partial^2 K}{\partial \theta^2} &= 2\left[(c\theta)^2 - (s\theta)^2\right]\left[\left(\frac{c\phi}{R_x}\right)^2 + \left(\frac{s\phi}{R_y}\right)^2 - \left(\frac{1}{R_z}\right)^2\right] \\ \frac{\partial^2 K}{\partial \phi^2} &= 2\left[(s\theta\, c\phi)^2 - (s\theta\, s\phi)^2\right]\left(\frac{1}{{R_y}^2} - \frac{1}{{R_x}^2}\right) \\ \frac{\partial^2 K}{\partial \phi\, \partial \theta} &= 4\, s\phi\, c\phi\, s\theta\, c\theta \left(\frac{1}{{R_y}^2} - \frac{1}{{R_x}^2}\right) \end{aligned} \tag{A.20}$$

These formulas are used in eqs. (4.10) and (4.16).

R_x, R_y and R_z here are related to the nearest bubble values by a constant scaling factor $1/t$, which is relevant in the curvature calculation. t is given by rewriting eq. (4.4):

$$\frac{1}{t^2} = \left(\frac{\Delta_x}{R_x^{(B)}}\right)^2 + \left(\frac{\Delta_y}{R_y^{(B)}}\right)^2 + \left(\frac{\Delta_z}{R_z^{(B)}}\right)^2 \tag{A.21}$$

where $R^{(B)}$ are the nearest bubble radii. Then, $R_x = R_x^{(B)}/t$ etc.

A.8 Calculating Foam Stress

For an internal section consisting of n elements, total stress σ_f on the foam section in the normal direction can be written as:

$$\sigma_f = \frac{1}{A_f} \sum_{i=1}^{n} (\sigma_i A_i) \tag{A.22}$$

where σ is the element stress in the normal direction, A is the element area, and A_f is the foam surface area. By assuming all element areas the same, the equation becomes:

$$\sigma_f = \frac{A}{A_f} \sum_{i=1}^{n} \sigma_i \tag{A.23}$$

Solid area of the section is nA, and relative density can be written as $\rho^* = nA/A_f$. In the equation above, replacing A/A_f term with ρ^*/n gives:

$$\sigma_f = \frac{\sum_{i=1}^{n} \sigma_i}{n} \rho^* \tag{A.24}$$

Stress resultants of elements coming from FEA are used in eq. (A.24) to calculate foam stress. The result is divided by strain to calculate Young's modulus of the foam. Calculated Young's modulus is in agreement with the value directly evaluated from FEA.

A.9 2D Petal Drawings

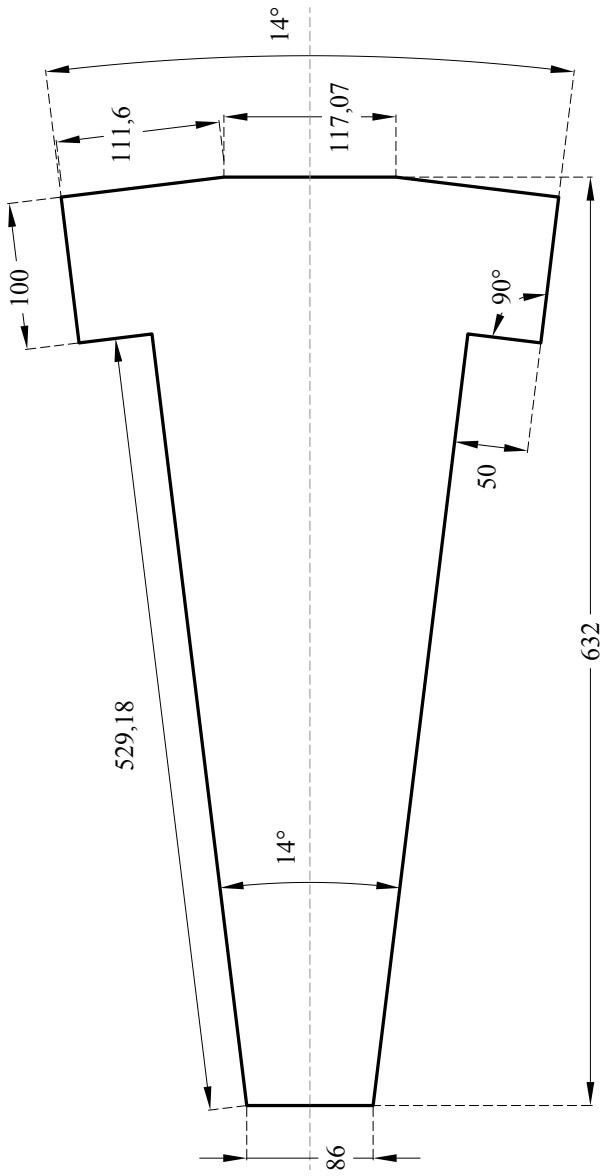

Fig. A.4: Computer drawn sketch of the LoI-Petal. Center line is the petal longitudinal axis. All dimensions are in mm.

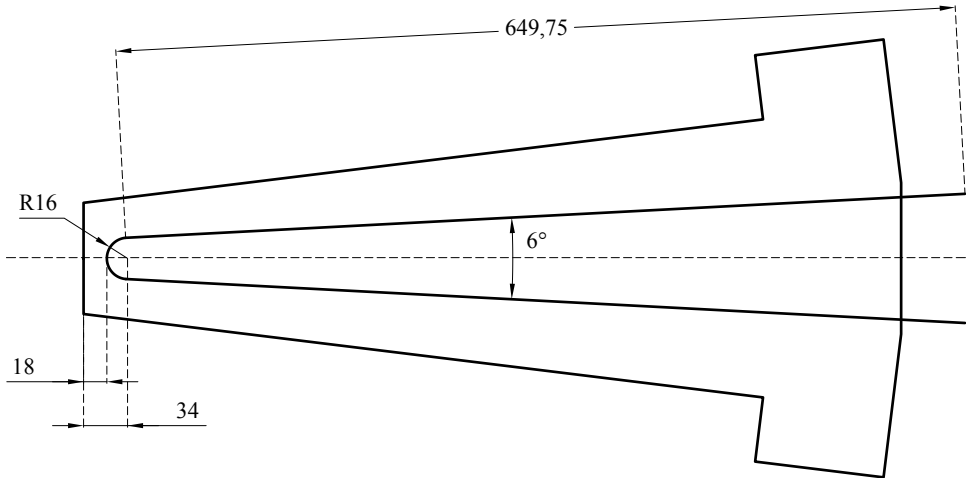

Fig. A.5: Top view of geometric form of the cooling pipe with dimensions and positioning parameters. The line is the centric axis of the tube. All dimensions are in mm. R specifies the radius.

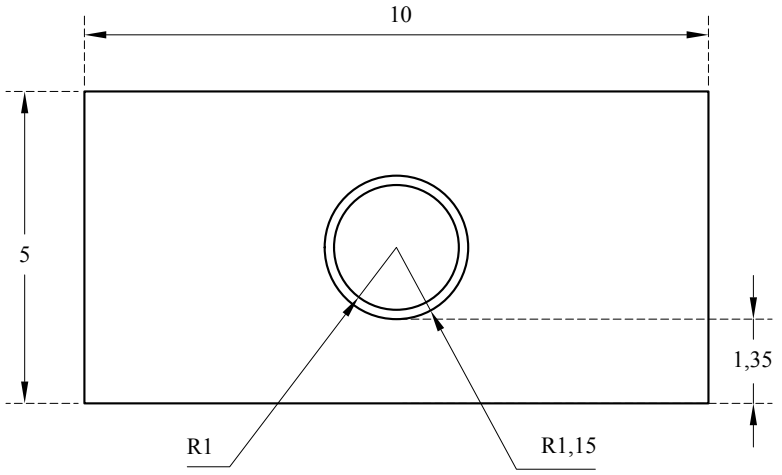

Fig. A.6: Cross-section sketch of tube/foam part. All dimensions are in mm.

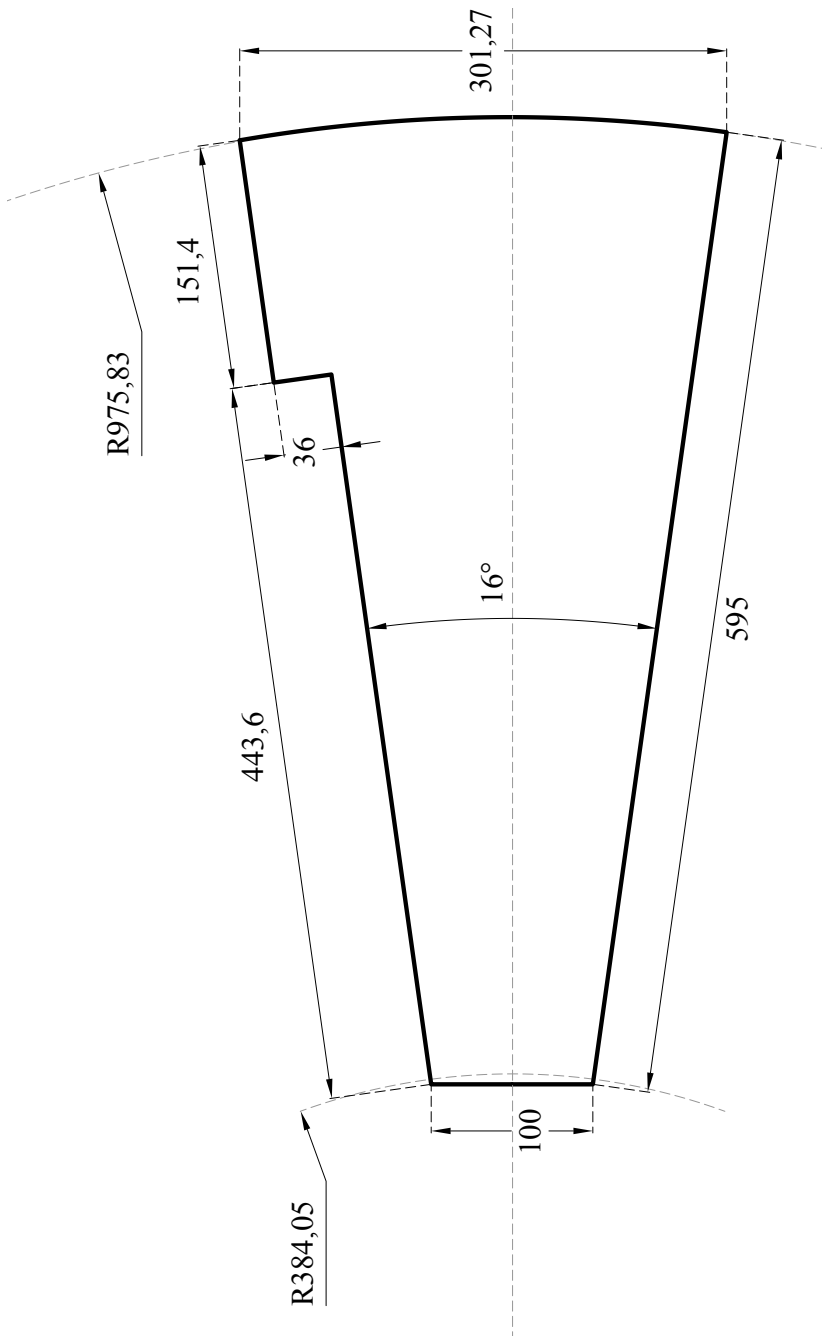

Fig. A.7: Computer drawn sketch of the LTF-Petal.

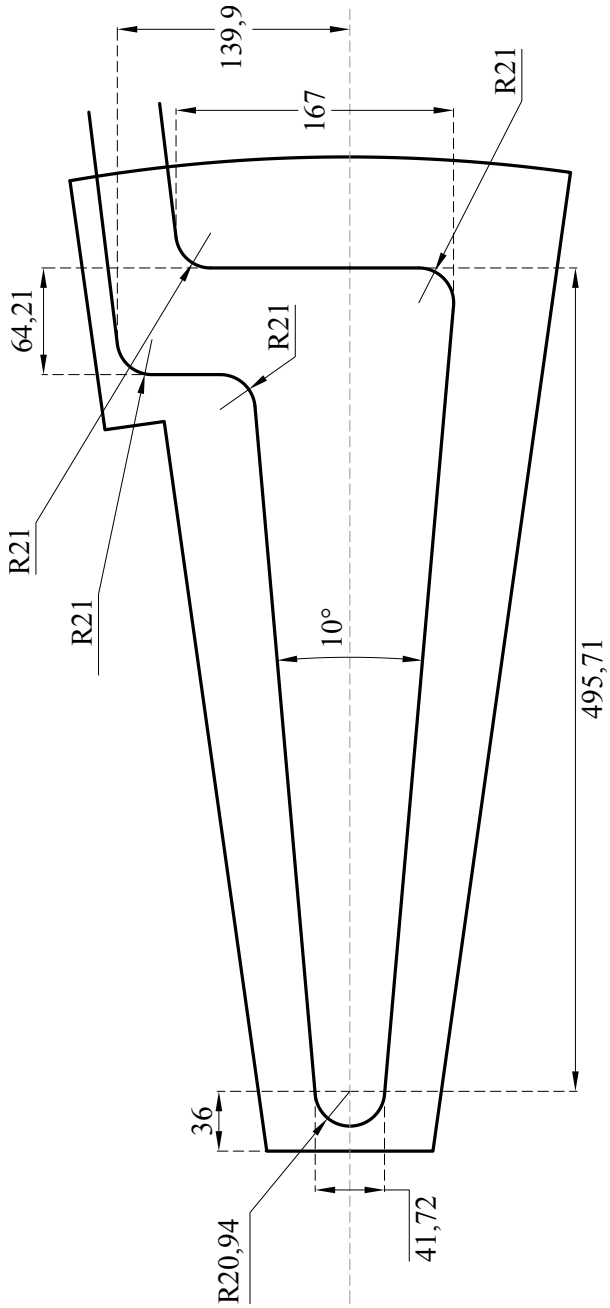

Fig. A.8: The LTF-petal design sketch containing tube dimensions and position relative to the facings.

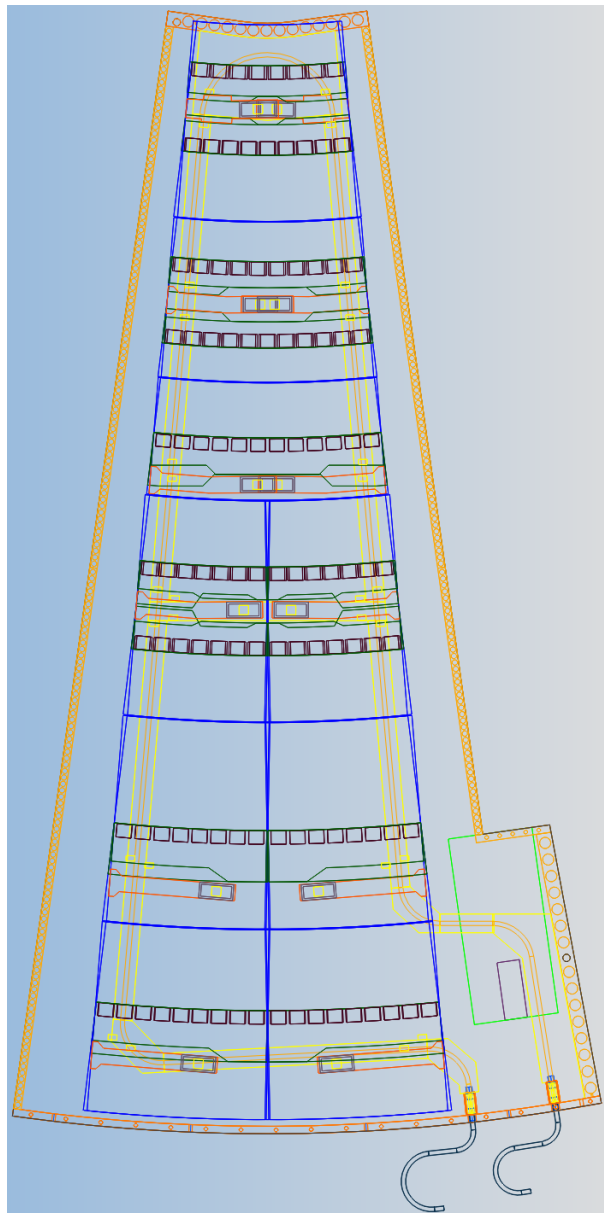

Fig. A.9: The LTF-petal wireframe view including sensor modules and cooling system [6]. Blue is for the Si-sensors, green is for the hybrids, claret red is for ASICs, dark orange in module area is for the DC-DC converters, yellow is for the foam core, orange is for the close-outs and the cooling-pipe.

Publication

Results in Physics 7 (2017) 2043–2053

Contents lists available at ScienceDirect

Results in Physics

journal homepage: www.journals.elsevier.com/results-in-physics

Investigations on anisotropic fracture mechanics of graphitic foams

K. Toptop [a,*], B. van Eijk [a,b], H.J.M. Geijselaers [b], N.P. Hessey [a,1]

[a] NIKHEF, Science Park 105, 1098 XG Amsterdam, The Netherlands
[b] University of Twente, Drienerlolaan 5, 7522 NB Enschede, The Netherlands

ARTICLE INFO

Article history:
Received 21 March 2017
Received in revised form 14 June 2017
Accepted 17 June 2017
Available online 23 June 2017

Keywords:
Graphitic foam
Brittle foam
Fracture mechanics
Anisotropy
Crush

ABSTRACT

This work investigates destructive (crush) compressive and shear behaviour of Poco-HTC™, which is a porous graphitic carbon foam. This material is anisotropic, and compressive measurements were made in both out-of-plane and in-plane directions. A camera filmed the tests to visually study crack formation and growth at macro-scale. Scanning electron microscopy images of fracture surfaces were recorded to examine post-failure material formation at micro- and meso-scales. In another series of tests, cyclic uniaxial compression measurements were performed in the elastic regime to characterise this behavior. Some of the samples were crushed after the cyclic test to measure strength.

1. Introduction

Porous graphitic carbon foam is an emerging material with a very high thermal conductivity to density ratio, that is approximately seven times higher than that of copper [1]. This raises the possibility to make ultra-light and efficient thermal management systems. Highly-aligned graphitised-carbon base material (with 800–1900 W/m.K thermal conductivity) brings high bulk thermal-conductivity to graphitic foams (135–245 W/m.K), while the porous structure reduces density [2,1,3]. Furthermore the bulk material exhibits very low thermal expansion [3], has low atomic number which makes it relatively transparent to radiation, and has high modulus to density ratio [4] compared to other foams.

Carbon foam is currently being considered in the development of a thermo-mechanical support structure for the upgrade of the inner-tracker of the ATLAS detector at the Large Hadron Collider at CERN, Geneva [5]. The above properties make carbon foam an ideal choice for part of this structure. The carbon foam is used to conduct heat from electronics into a 2 mm diameter titanium tube with evaporative CO_2 cooling. The tube is sandwiched between two pieces of foam, and the part is placed between two thin ultra-high-modulus carbon-fiber facings. The detector will sit on the facings in a high radiation area, and must survive more than 10 years without maintenance.

The CO_2 coolant will cool the tube to −30 °C. The thermal contraction of the tube will exert forces on the carbon foam. There is a risk that these forces will lead to fractures at the interface, which would result in deterioration in thermal performance. Since preventing mechanical damage is crucial for maintaining thermal properties, there is a particular interest in the fracture mechanics of the foam.

Most research has focussed on thermal performance, rather than mechanical performance of carbon foams [6–8]. The majority of existing studies on mechanical performance are limited to measurements on elastic bulk parameters such as Young's and shear modulus [9,10]. Chen et al. [11] have measured crush strength resulting from different precursors and manufacturing techniques, but with very little work on understanding graphitic foams under force in detail. One of the most detailed studies on this topic was made by Gowthaman et al. [12,13]. They performed crushing tests on graphitic foams, and presented camera records showing fracture lines and scanning electron microscopy (SEM) records from the fracture surfaces. Since graphitic foams are highly anisotropic, the fracture response is dependent on material direction. Although the work is very useful to describe fracture behavior, the tests were performed in a single material direction and limited to characterisation of fracture in other directions. Consequently, this highlights the need to further investigate fracture mechanics in the anisotropic case. This study extends the understanding of the failure mechanism by presenting measurements made in both material directions, and made with different loading modes.

Destructive compression (crush) and shear tests were performed. The crushing test was conducted in both out-of-plane

* Corresponding author.
E-mail address: koral.toptop@gmail.com (K. Toptop).
[1] Now at TRIUMF, 4004 Wesbrook Mall, V6T 2A3 Vancouver, BC, Canada.

http://dx.doi.org/10.1016/j.rinp.2017.06.024
2211-3797/

Table 1
Properties of Poco–HTC and PocoFoam [8,1,3]. Density and thermal conductivity were taken from datasheets provided by the manufacturer, except the Poco–HTC density which was measured. The ligament density was taken from [8]. Porosity was calculated from the assumed ligament density.

	Poco–HTC	PocoFoam
Density [g/cm^3]	0.85 ± 0.05	0.55
Ligament density	2.23	2.23
Porosity [%]	61.8	75.3
Open porosity [%]	95	96
Therm. cond. [W/(m.K)]		
Out-of-plane (z)	245	135
In-plane (x)	70	45

and in-plane direction to understand anisotropic behavior. The tests were recorded with a video camera to visually analyse fracture mechanics at macro-scale. SEM images were captured from the fracture surfaces to examine post-failure material formation at micro- and meso-scales.[2] In another group of measurements, cyclic compressive loads were applied in the elastic regime to characterise the elastic behavior, such as Young's modulus and elastic limits. Also, the strengths were measured by subjecting some samples to crush after cyclic tests.

1.1. Material and micro-structure

Poco–HTC is a graphitised-carbon foam produced from a mesophase-pitch precursor. It is licensed, and manufactured by Poco Graphite Inc [14]. Poco–HTC is the improved version of Poco-foam with higher thermal conductivity and density. Table 1 gives some properties of both foams.

The precursor and processing details affect the internal structure of the end product, which in turn determines the bulk properties. The structure of the Poco–HTC sample is illustrated in Fig. 1, which was recorded with SEM. This figure highlights what the terms ligaments, junctions, cell-openings (pores), micro-cracks on walls and around cell-openings, and layer-spacings around folded layers refer to. Due to the foaming process, the resultant material has bubbles elongated in the vertical (out-of-plane) direction, which is taken as z-axis, while the x and y-axes are used for the horizontal (in-plane) directions.

Poco–HTC consists of highly graphitised material. The cell walls at mid-height of the bubble have graphite planes parallel to the bubble walls and are perfectly compacted. Where these planes meet at the top and bottom of the bubble (junctions), the graphite structure folds and has many micro-defects. Fig. 2 shows that the molecular layers are much less well aligned at junctions and contain cleavages between planes of graphite. This feature was illustrated in [8] with higher magnification for a graphitic foam similar to the Poco–HTC. It was reported in [8] that higher graphitization rate causes micro-cracks as separation of the graphitic layers. These layer-spacings run parallel to the planes of graphite, affect neither crystal size nor thermal conductivity. However, these defects are expected to mechanically weaken the foam [6].

There are also cracks and defects in the cell-walls probably caused by thermal stresses arising during the heat treatment process. These cracks occur at the boundaries of the planes. However these are much less frequent than the micro-defects at the junctions.

If the gaseous volume is large enough, the bubbles join at holes in the cell walls, making an open-cell foam. These holes in the walls, referred to as cell openings, are initially smooth and circular. However, later heat treatments can lead to fracture and micro-cracks at cell openings.

Both the elongation of bubbles and the alignment of graphite planes along the bubble walls lead to anisotropic behaviour of the bulk material. The micro-cracks, folds, and other defects have a major impact on bulk material properties compared to what would result from perfect graphite.

2. Measurements

Tests were performed to capture material destructive compression and shear behavior. The intention was also to capture elastic behavior for calculating material constants.

The crush tests used monotonically increasing uniaxial compression up to complete failure of material. These tests failed to characterise elastic behavior due to using samples cut from the top (low density) surface of the foam block.[3] A new group of samples were cut from the bottom of the foam block to minimise density variation, and were subjected to a different compressive loading scheme: A cyclic loading scheme, in which the load is increased in stages, and released after each stage, before moving on to the next, higher-load stage (Fig. 3). The Young's modulus was extracted from the cyclic compression test. Both crush and cyclic compression tests were applied in the out-of-plane and in-plane directions to characterise anisotropy.

The Iosipescu shear tests were used to study destructive shear. The material was placed in a fixture to apply shear load in the in-plane direction on the out-of-plane face (Fig. 4). The foam has a porous surface, so it was not possible to install strain gauges, therefore elastic properties could not be derived from shear tests.

A camera filmed the destructive compression and shear tests.

2.1. Samples for compression Tests

Samples were machine-cut from a large foam block (about 300 × 30 × 300 mm^3). The out-of-plane cyclic test samples had 20 × 10 × 20 mm^3 dimensions. The in-plane cyclic test samples were 10 × 20 × 20 mm^3. The out-of-plane (z) size is always the middle of the three dimensions given here; the surface being compressed is always 20 × 20 mm^2, while the height in the machine is 10 mm. The crush test samples were measured 20 × 20 × 20 mm^3, and cut from the top of the block.

These samples are large enough to minimise edge effects due to open bubbles, debris from machining etc. No cover plates were attached to avoid effects of glue leaking into the surface cells.

2.2. Samples for Iosipescu shear tests

The Iosipescu specimen is a rectangular beam with a symmetric V-notch at its center. A fixture with proper configuration is used to transform applied machine load into the pure shear load acting on a central section [15]. Furthermore, V-notches intensify stress at the center and localise failure at this section.

The Iosipescu sample is 80 × 20 × 8 mm^3 (Fig. 4). V-notches have a 90^o angle and are 12 mm apart. Thus, the shear surface covers a 12 × 8 mm^2 area. Since our Poco–HTC block is only 30 mm thick, we constructed our sample from two aluminium blocks 27.5 mm long, glued either end of the Poco–HTC sample with length 25 mm.

[2] By micro-scale we mean structures smaller than cell walls (but much bigger than atomic scale); by meso-scale we mean structures at the size of a cell; and macro-scale treats the block sample as a whole.

[3] The foam samples used in these tests were cut from the top of the main foam block, where the material has slightly lower density. Local cell crushing occurred at this surface. This in turn introduced sudden changes in the stress–strain response before the actual crushing stress. Consequently, crushing tests showed some irreproducibility when characterising elastic behavior.

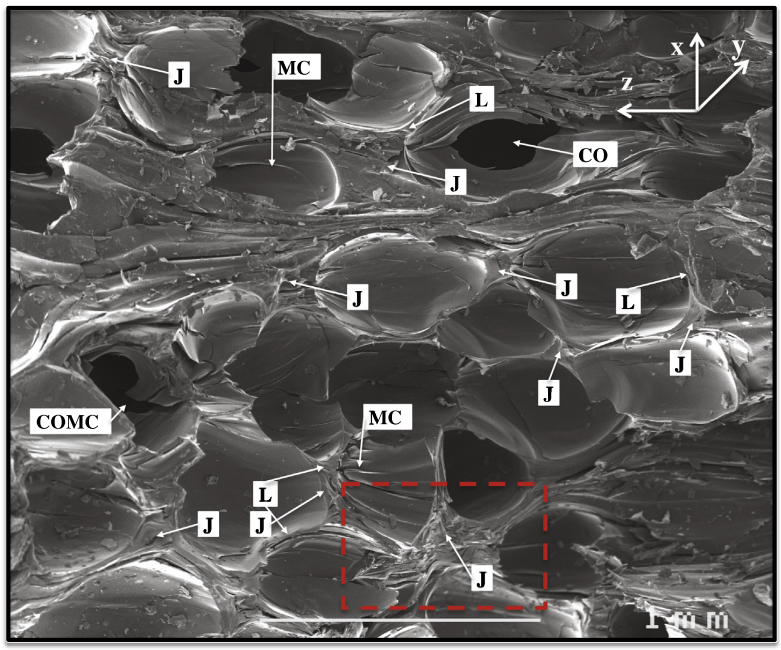

Fig. 1. SEM image of the Poco–HTC with x34 magnification. L - ligaments, J - junctions, MC - micro-cracks, FS - folds (visible in the next figure), CO - cell openings, and COMC - cell-opening micro-cracks refer to different structural features. The layer structure is much less apparent at junctions, indicating a high density of micro-defects there. The z-axis is the bubble elongation and foam out-of-plane direction.

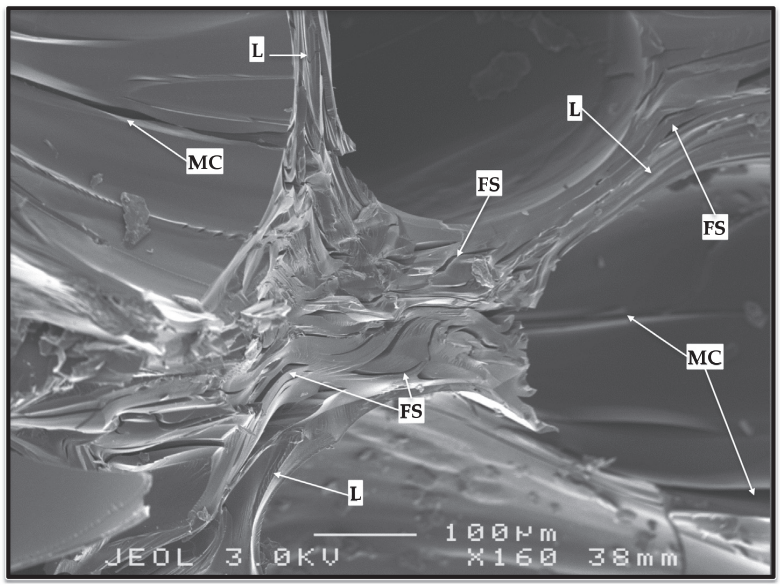

Fig. 2. Zoom into the red-dashed box in Fig. 1 showing a junction with x160 magnification, indicating the high density of micro-defects.

2.3. Data acquisition

The test machine head tool moves vertically down. It measures the reaction force F exerted by the sample and the machine head displacement Δ, and records these along with the test time t. For the compression tests, the force is divided by the initial cross sectional area A_0 of the face where load is applied to obtain the stress σ, i.e. $\sigma = F/A_0$. The displacement is divided by the initial specimen

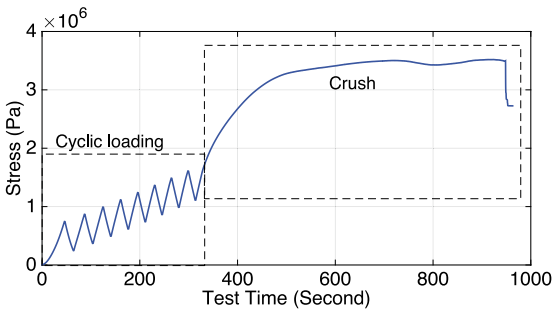

Fig. 3. Example stress vs. time graph for cyclic uniaxial compression test. Maximum stress is increased at each cycle (small dashed box). For some samples, stress is continuously increased up to complete failure after the cyclic test (large dashed box).

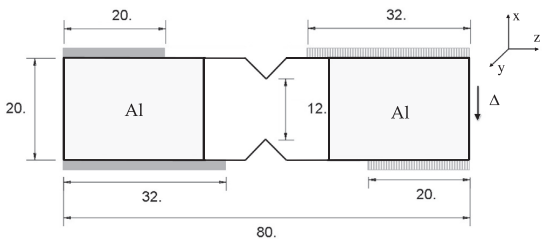

Fig. 4. Iosipescu specimen dimensions and positions of grips (shaded tools). The depth of specimens is 8 mm. The fixture is fixed with a pair of grips at the left side (dark shaded). Displacement (Δ) is applied with another pair of grips at the right side. Axes show alignment of the foam.

height h_0 to obtain the strain ε, i.e. $\varepsilon = \Delta/h_0$. For the shear tests, the force is divided by the initial cross sectional area A_1 between the notches to obtain shear stress τ, i.e. $\tau = F/A_1$. No strain data were available for shear tests.

A camera with 1280 × 720 pixels filmed the crush and Iosipescu shear tests with 24 frames per second. Each pixel of the image covers about 30 × 30 μm^2 of the sample.

2.4. Test procedure – cyclic compression

The cyclic uniaxial compression test captures the mechanical behaviour at low stress–strain $(\sigma - \varepsilon)$ conditions. The machine was programmed to compress the sample by moving down at a constant rate, until it reached a pre-defined load. Then it decompressed by moving upwards, until a pre-programmed lower limit was reached. These cycles were repeated, each going to a slightly higher load than the previous cycle (Fig. 3). Each cycle then measures a hysteresis loop in a different $\sigma - \varepsilon$ region for the first time a sample is compressed. The machine head displacement rate was 0.25 mm/min for both compression and decompression phases. Typically eight cycles were made.

In total, ten samples were tested, five in each loading direction. For the in-plane case, the first two samples were tested at a high stress (1.5–3 MPa), with a rapid drop in Young's modulus indicating fracture occurred. Further samples were measured at lower stresses (0.75–1.5 MPa). Some samples were compressed to destruction immediately after the completion of the cyclic tests.

2.5. Test procedure – crush

Another group of foam samples were subjected to continuous uniaxial compressive load until the material reached complete failure, using five for out-of-plane and five for in-plane measurements. In the out-of-plane tests, samples were placed with the face corresponding to the top side of the block during manufacture on the bottom jaw. The machine head displacement rate was set to 1.2 mm/min. Samples were not subjected to any pre-load.

2.6. Test procedure – Iosipescu shear

Two samples were used in the Iosipescu test. Samples are held by two pair of grips, each supporting the sample from the top and bottom, at both ends (Fig. 4). The grips at the left fix the position of samples, while the grips at the right continuously move down. The rate of displacement was set to 0.5 mm/min.

3. Results and discussion

Three types of measurements were made: 1) Cyclic uniaxial compression tests to measure elastic behavior, 2) Crush tests to measure strength and characterise the compressive failure, and 3) Iosipescu shear tests to measure shear strength and study failure in the shear mode.

3.1. Material constants

3.1.1. Cyclic compression

A single cycle consists of compression followed by an unloading phase. The compression is divided into two phases, reloading and incremental-loading. In the reloading phase, the material is

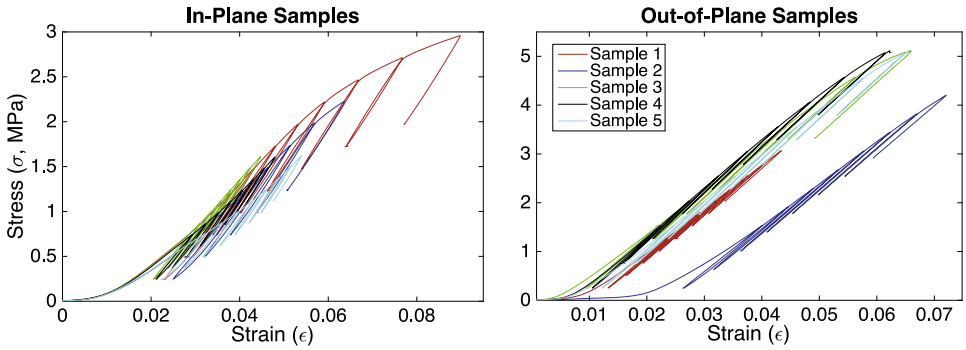

Fig. 5. Stress vs. strain curves for the cyclic tests on each sample. Five samples were measured in each loading direction. The samples behave quite similarly. Sample 2 in the out-of-plane case has a long initial movement before building up any stress, but is otherwise similar to the rest.

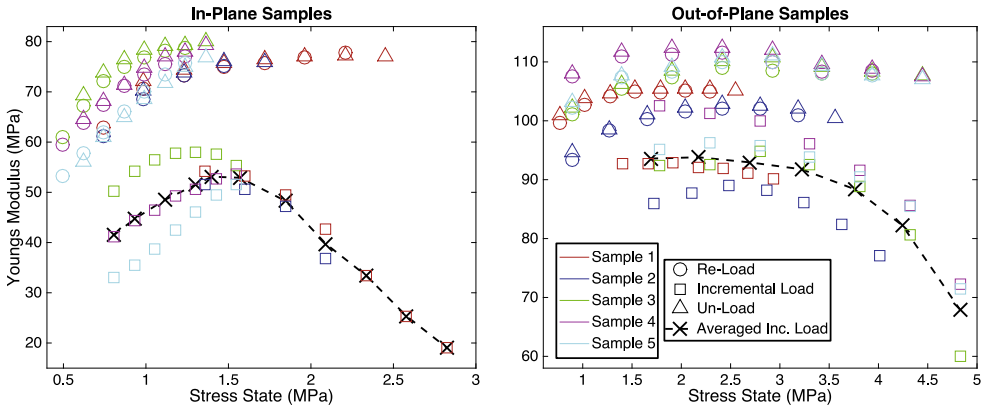

Fig. 6. Young's moduli for the three loading phases of each cycle vs. stress. These phases represent reloading, incremental-loading and unloading. Stress states were calculated as the mean stresses during the phases. The dashed lines are the mean of the incremental phase Young's moduli which, are used to determine where the elastic regime ends.

compressed from the beginning of the cycle up to the maximum stress state of the previous cycle. In the incremental-loading phase, the material is compressed from the end of the reloading phase up to the maximum load defined for the current cycle. In this phase the material is subjected to additional load. In the unloading phase, the material is decompressed until the minimum load defined for the cycle, which is also the beginning of the next cycle.

Fig. 5 shows the $\sigma - \varepsilon$ curves measured for all samples. The Young's moduli E are calculated from the slope of the $\sigma - \varepsilon$ curve at each phase of each cycle. The stress state of a phase is calculated as the mean of the stress during that phase. Fig. 6 shows the modulus results versus the stress states.

The incremental phase Young's modulus is much lower than for reloading and unloading. It increases at low stress, peaks and starts to decrease at high stress (black dashed line in Fig. 6).

After the incremental phase, the unloading and reloading moduli are similar and slightly higher than the moduli in the previous cycle.

Samples used in the tests do not have a perfect surface finish; surfaces show small bumps. As the bumps are compressed, the machine head tool gets into contact with a wider area at each displacement step, which results in slightly higher apparent modulus as strain increases. This is the reason for the steep rise in Fig. 5 for low strains. This effect continues until the surface is perfectly flat and there is no further increase of the contact area. This occurs at 0.01–0.02 and 0.03–0.04 strain for the out-of-plane and in-plane compressed samples. The difference between the strains is caused by the different surface flatness of the samples. The out-plane compressed samples have better surface flatness, so their Young's modulus changes less with applied stress (Fig. 6). Simultaneously during the incremental load phase, ligaments break at the bumps and local crushing occurs. This gives a false low reading of the Young's modulus. However, during unloading and reloading, no more crushing occurs, and so the cyclic test makes it possible to extract the true Young's modulus from the reloading phase.

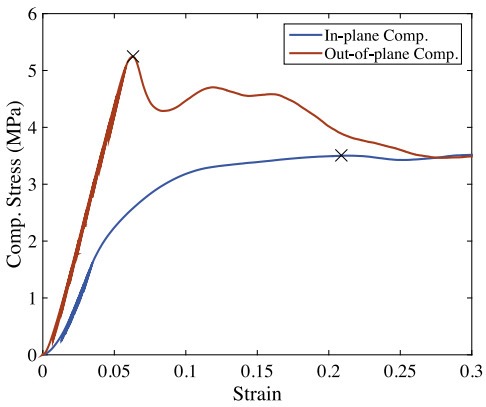

Fig. 7. Stress vs. strain curve to destruction. Both samples had previously undergone a cyclic compression test. The plots show the second cyclic compression test followed by continuous compression to destruction. Crosses mark the points used in Table 2.

The intention during cyclic compression was to stay within the elastic regime, however some last cycles demonstrated some inelastic deformation. Consequently, the incremental phase modulus starts to decrease after a certain stress. Out-of-plane fracture starts at 3 MPa and in-plane fracture starts at 1.5 MPa (Fig. 6). This is apparently very localised, since there is no sudden drop in the unloading moduli (Fig. 6) and in the stress–strain graph (Fig. 5). Therefore, these stress states are where the elastic regime ends and initial fracture starts, but are not the actual crush strength of the foam. The corresponding strains to these stress states were found from Fig. 5, corrected for the take up of slack at the start of the curves (subtracting 0.005 and 0.010 for out-of-plane and in-plane cases) and averaged for the samples to calculate elastic strain limits.

The Young's modulus of the foam was calculated during the unloading phase at the elastic limit. The crush strength of the foam was measured by subjecting the samples to continuous compression up to destruction immediately after the cyclic test (Fig. 7). The maximum stress (i.e. peak) in the tests was taken as crush strength. Table 2 summarises these measurements.

Table 2
Parametric results from compression (top and middle row) and shear (bottom row) tests. Stress and strain are taken at the elastic regime limit. Strain is taken into account by including the slack at the beginning.

	Modulus MPa	Stress MPa	Strain %	Strength MPa
Out-of-plane, z	111	3.0	3.2	5.3
In-plane, x	75	1.5	3.5	3.5
Shear, zx	–	–	–	1.8

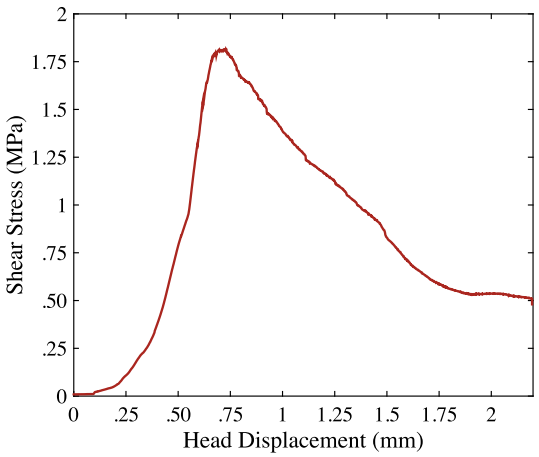

Fig. 8. Shear stress vs. machine head displacement measured with Iosipescu shear test. The shear stress continuously increases up to the peak, where failure starts, and then steadily decreases until complete failure. The steepening curve below the peak shows the shear modulus increases up to failure.

3.1.2. Shear test

Both samples used in Iosipescu shear tests gave similar behavior. Fig. 8 gives the stress vs. displacement for one of the samples. Since no strain data was available, the shear modulus was not measured. The graph was only used to extract the shear strength, which was assumed to be the maximum stress reached. The strength is given in Table 2.

3.2. Anisotropy

Poco–HTC is highly anisotropic in its compression behaviour. It has about 1.5 times higher Young's modulus and strength in the out-of-plane direction than in the in-plane direction. The observed anisotropy can be attributed to two features of the foam: shape of the pores, and alignment of the graphitic material.

An amorphous material with spherical holes would have isotropic bulk properties. The foam contains ellipsoidal bubbles, which are elongated in the z-direction. The elongated side-walls are thinner and the crystals in them tend to be more aligned. Under z-direction loading, these side walls are primarily loaded by membrane stresses, whereas under in-plane loading they are mostly subjected to bending. This explains the higher out-of-plane Young's modulus compared to the in-plane one.

The solid base material is not amorphous. Graphite crystal planes have high modulus in the plane of the hexagonal arrangement of carbon atoms, and much lower modulus in the plane normal. In Poco–HTC, the graphite sheets tend to be aligned with the elongation direction, further enhancing the Young's modulus in the foam out-of-plane direction.

3.3. Fracture

A camera set up filmed destructive compression and shear tests. Selected frames of the videos were compiled to give a clear impression of the failure initiation and growth of the cracks from meso- to macro-scale. Fig. 9 shows the frames captured during the crush tests and Fig. 11 gives the frames recorded during the destructive shear test. Crush tests were performed up to complete fracture with high levels of material separations, shown in Fig. 10. The fracture surfaces where material separated were recorded via SEM and are illustrated in Figs. 12–14. Since the shear tests were stopped before complete fracture, no open fracture surface was available for examination.

3.3.1. Out-of-plane crush

In the out-of-plane case, the failure occurs along the bottom face of the sample as local cell layers collapse. The upper part of the sample moves down with little distortion, with more and more cells at the bottom edge disappearing. Eventually the material at the bottom starts flowing outwards. At about 20% strain, a single macro-crack appears with a big vertical component but growing diagonally (upper row in Fig. 9). This is very close to the 45° characteristic of shear failure in brittle materials. The characteristics of crack growth are the same in both in-plane directions. After complete progression of the crack through the whole material, large pieces of carbon foam break off sideways (upper row in Fig. 10).

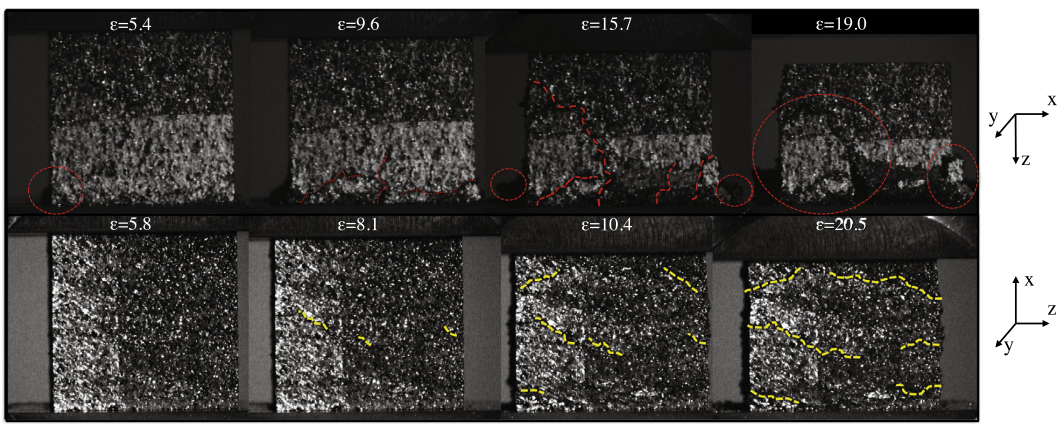

Fig. 9. Failure initiation and growth during compression tests (out-of-plane in upper row and in-plane in bottom row). The compression direction is from up to down. Stress and strain increase from left to right. ε shows the calculated strain. Red dashed lines highlight the crack paths in the out-of-plane case; ovals highlight the material separation. Yellow dashed lines highlight regions of cell collapse in the in-plane case, which propagate sideways. (The difference in grey shades across the samples are a by-product of the machining process). Direction of the foam is given with x, y and z-axis at sides. (For interpretation of the references to colour in this figure legend, the reader is referred to the web version of this article.)

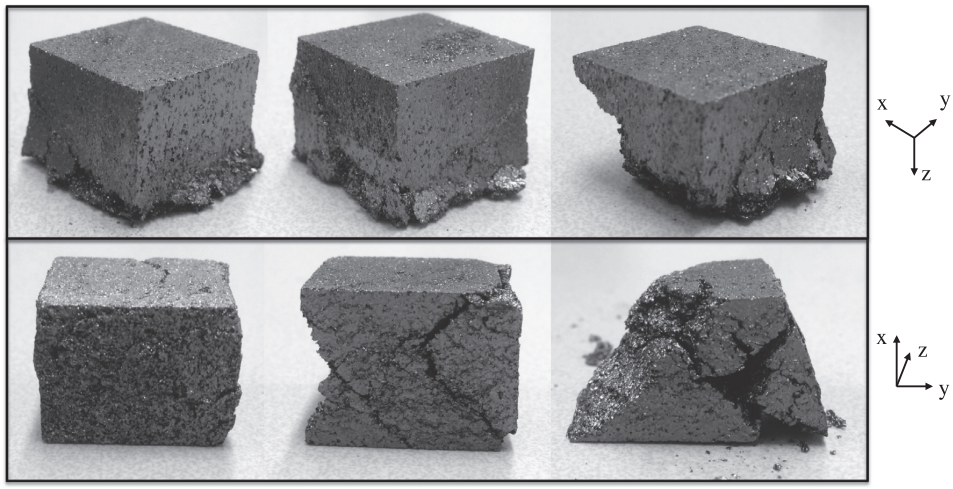

Fig. 10. Step-by-step crushing up to complete loss of material for three out-of-plane (upper row) and in-plane (bottom row) samples. At high strain cracks join up and cause complete material separation at sides. Out-of-plane fracture occurs as material separation to sides at the edges, especially at corners, and propagates vertically and diagonally.

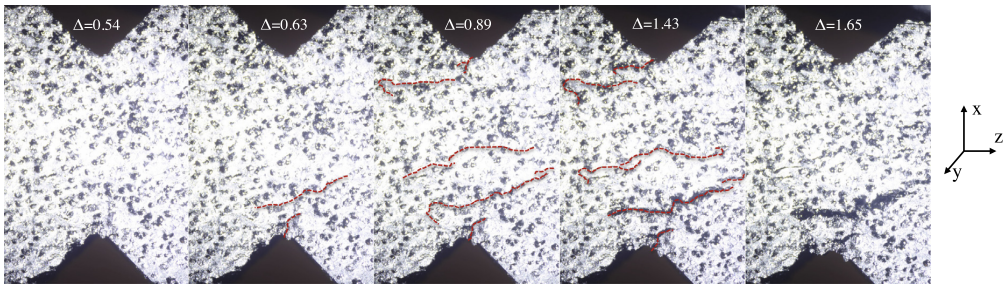

Fig. 11. Failure initiation and crack growth during losipescu shear test. Right side of samples are moved down in the $-x$ direction. Shear stress intensifies at the mid-section between the V-notches. Red dashed lines indicate the cracks, which are mostly aligned in the out-of-plane direction. (For interpretation of the references to colour in this figure legend, the reader is referred to the web version of this article.)

In all five samples, collapse occurred at the bottom jaw, which was the top side of the foam block during manufacture. The images show an intact upper-block moving down about 2 mm, with all crushing occurring at the bottom layer, before large cracks appear. This indicates that the samples have weaker structure here. When the foam is manufactured, gases flow in the out-of-plane direction and accumulate at the top, leading to a less dense and weaker structure compared to the rest of the body. Therefore, the fracture always starts in this region. The local layer collapse could be avoided by filling the face with glue as suggested in [12,13], and reduced by avoiding the top face when cutting samples.

One of the cyclic test samples, cut from the bottom of the block, was also tested to destruction. It had qualitatively different behaviour, with no local crush and collapse of the face at a jaw. Instead, it just suffered from a single diagonal crack similar to the macro-crack described above. This suggests that the local layer crushing is not predominantly effective on macro-cracks.

There are two stages in the fracture mechanism, covering gradual transition of cracks from meso-scale to macro-scale. First, cell walls bend and break (see [16]), causing the load to increase in adjacent cells. As a result, the damage spreads to neighboring cells making cracks, which grow until complete separation of material occurs. The cracks initially expand more or less horizontally, as bend/fracture of neighbouring cells. Eventually bulk shear stress causes a more vertical crack growth; the cracks spread through the whole sample, allowing the shear forces to push material out sideways. Cracks usually tend to grow parallel to the crystal planes, leading to a larger vertical component aligned with planes in the z-direction. The resultant cracks lie at slightly larger than 45° to the horizontal axis.

3.3.2. In-plane crush

For the in-plane x compression, the fracture mechanism is similar to the out-of-plane compression. Contrarily, there is a difference in fracture growth in the transverse directions of the compression axis. Horizontal regions of cracks appear throughout the face viewed from the in-plane y-direction (bottom row in Fig. 9). Looking from the out-of-plane direction, the cracks appear diagonal (around 45°) starting from the corner of the sample (bottom row in Fig. 10). Most separation of material becomes apparent only when the specimen is released from the jaws of the press. There is complete material separation at the sides in the in-plane y-direction, while the foam maintains its structural integrity in the out-of-plane direction.

Since cracks tend to grow parallel to the crystal planes, they appear as horizontal lines in the out-of-plane direction, and do

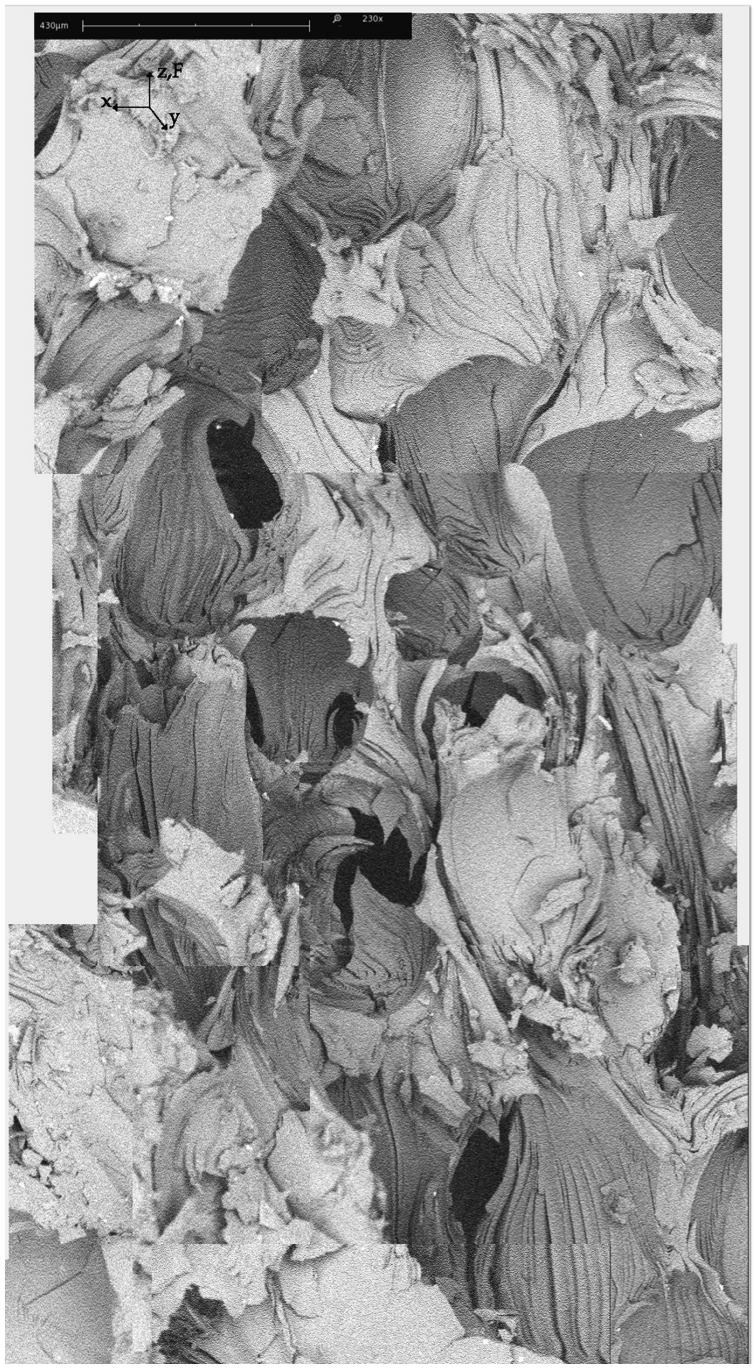

Fig. 12. SEM capture of a fracture surface for out-of-plane crushing. The out-of-plane z direction and load F are up the page. The fracture plane cuts foam through the bubbles, therefore cells are open for view. Compared to Fig. 13, there is much less debris.

not break down structural integrity in this direction. The shear forces are predominant in the in-plane y-direction, which has low modulus and strength, and cause cracks to grow diagonally with an angle of 45° from the corners.

3.3.3. Destructive shear

The internal section parallel to the out-of-plane face was subjected to shear in the in-plane direction, corresponding to shear state σ_{zx}. Cracks appear in the out-of-plane direction, as cleavages

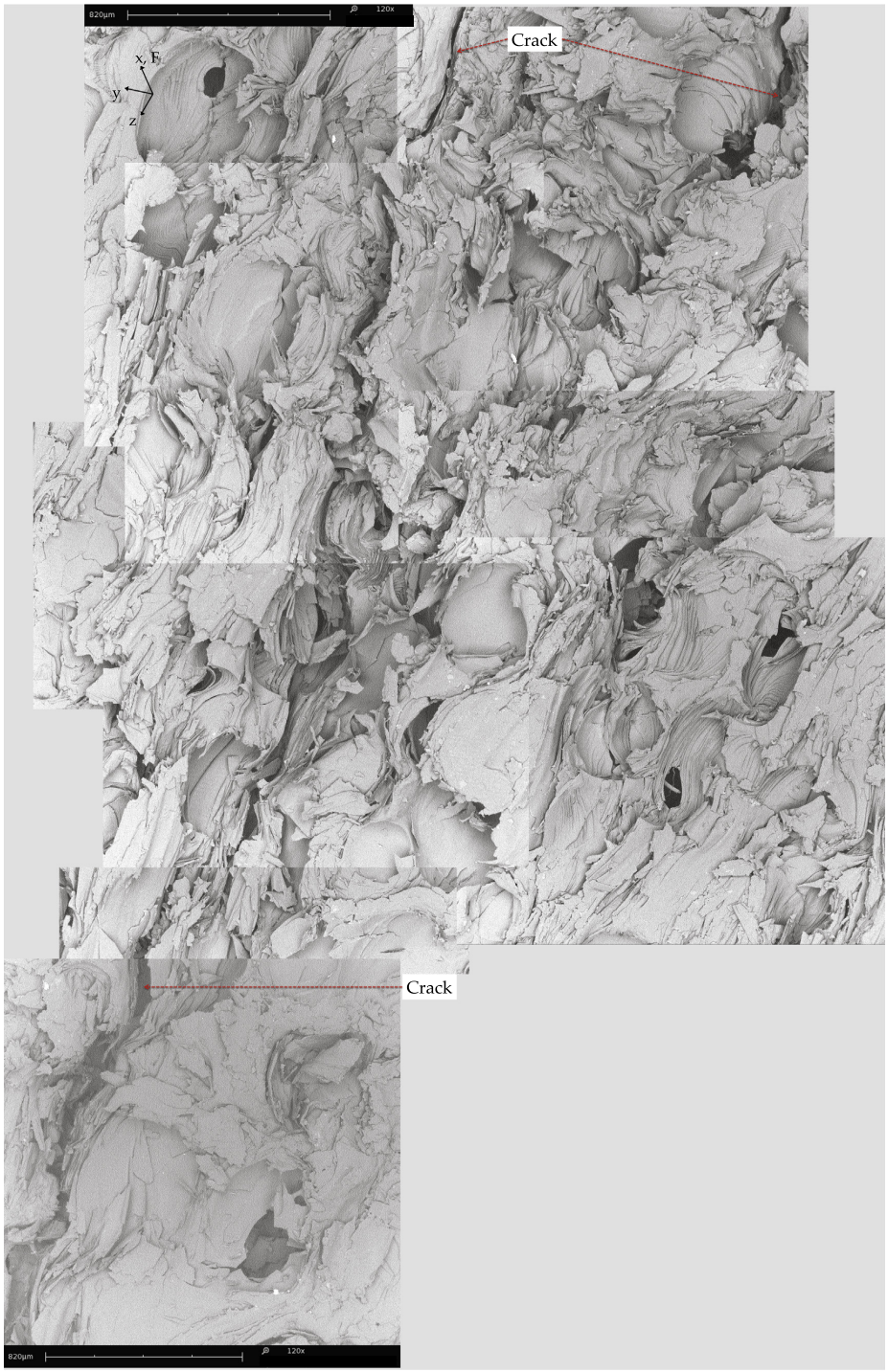

Fig. 13. SEM capture of a fracture surface for in-plane crushing. The surface is at about 45° to the loading direction, which is *F* shown in the top left corner. The cell structure is almost obscured by the presence of a large amount of debris. There is a clear crack running parallel to the out-of-plane direction. The fracture plane is also the cell-collapse layer.

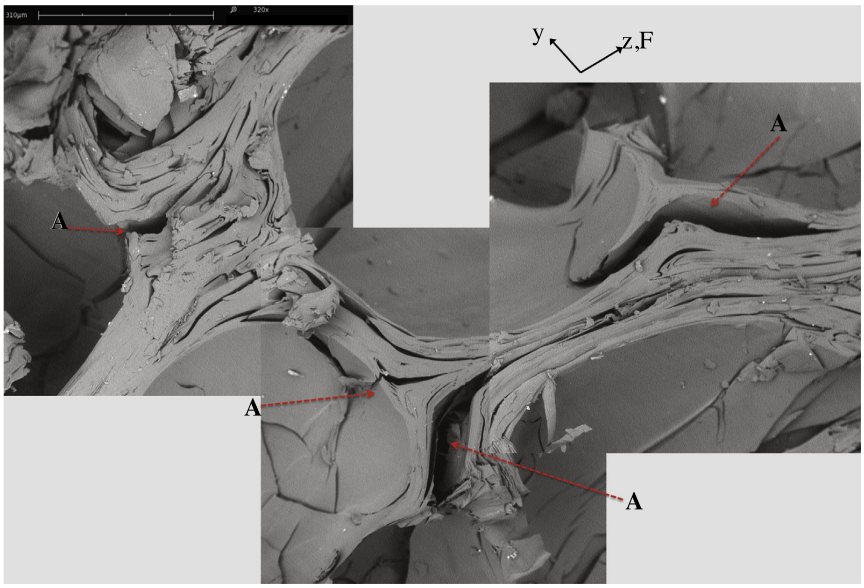

Fig. 14. SEM record of the junction captured from the fracture surface for out-of-plane crushing, showing post-failure formation. *A* indicates the cracks initiated at cell-wall, and propagates into junctions as cleavages of the graphitic planes. *x*-axis is normal to image.

(Fig. 11). This is probably due to separation of graphitic layers as a result of shear force. These cleavages propagate between the planes. Video record showed that the material at the top and bottom of these cleavages slide on each, indicating the direction of shear forces. Diagonal cracks also appear at the edges of the central-section, where the V-notches are. Had the test been continued these diagonal cracks would have propagated to the horizontal cracks, and resulted in complete failure.

3.3.4. Fracture planes

The SEM device was not able to record at low magnification. Therefore, we recorded images from adjacent areas and combined them to produce a single record showing a larger area. The fracture surface is not flat, so each image has a different focus. This gives slight discontinuity at the edges of individual images.

Fig. 12 shows a fracture plane after crushing in the out-of-plane direction. The cells and walls are clearly visible. The fracture plane has a large component parallel to the compression force (right at upper row in Fig. 9). Material does not compact. Instead, it separates sideways at the macro-crack. Consequently, friction forces are low and the material pore structure is not badly degradated.

Fig. 13 shows a fracture plane for the in-plane crushed sample. The cells, walls and junctions are distorted and covered by smashed graphitic material. The smashed particles are dragged in the in-plane *y*-direction, indicating the direction of shear and resultant friction force. It also contains a long crack along the out-of-plane direction, which is one of the horizontal cracks illustrated in the right at the bottom row in Fig. 9. Cell-collapse compacts material at the fracture plane and increases friction forces. Shear forces build up in the direction perpendicular to the applied force. The shear strength in the in-plane *y* direction was exceeded first, leading to the fracture plain propagating in this direction. Material movement occurs in the same direction, dragging smashed particles along the fracture plane, causing a high level of material degradation.

Fig. 14 illustrates junctions and cells with larger scale for the out-of-plane crushed samples. There are many micro- and meso-scale cracks, as cleavages between layers. Studying the images suggests cracks are initiated at cell-walls, propagate to the junctions where they widen, and spread to neighbouring ligaments. Probably they initiate in the pre-existing micro-defects at the cell-walls as seen in Figs. 1 and 2.

Song et. al. [16] performed destructive compression tests on a AlSi closed-cell brittle foam, in which the solid material has a homogeneous structure and does not contain micro-defects. The fracture plane in AlSi foam propagates more or less at 45° diagonally (see Fig. 7 in [16]), very similar to what is observed in Poco–HTC. This indicates that the pre-existing defects do not have a dominant effect on the bulk failure mode.

However, the macro-crack in the out-of-plane compressed Poco–HTC sample has a larger vertical component compared to the crack in AlSi foam. As mentioned above, cracks tend to grow between layers of graphite resulting in a slightly larger component in the *z*-direction. Consequently, the alignment of graphitic planes affects the macro-crack behavior.

It would be very interesting to investigate effects of pre-existing micro-defects on the crack initiation and crack transition from micro- to meso-scale for both loading scenarios. However, this would require tests inside a scanning electron microscope as in [16] to simultaneously capture the crack propagation.

4. Conclusion

A series of destructive tests have been performed to study fracture mechanics of Poco–HTC graphitic foam in compression and shear modes. Compressive measurements were made in both out-of-plane and in-plane to characterise anisotropy. Cyclic uniaxial tests were performed to study elastic behaviour. Some samples were compressed up to complete failure to measure the strength. Destructive tests were filmed to visually examine crack initiation and propagation at macro-scale. At the end, SEM records were captured from the fracture surfaces to examine material at micro- and meso-scales after failure.

Poco–HTC shows highly anisotropic behaviour in both elastic and fracture cases. It has higher modulus and is stronger in the out-of-plane direction. This comes from two separate effects: the graphite planes of carbon atoms are aligned along the out-of-plane direction; and the cells are elongated in the out-of-plane direction.

The local fractures start at 3.0 and 1.5 MPa, and strengths are 5.3 and 3.5 MPa in the out-of-plane and in-plane directions. Shear strength is 1.8 MPa, measured with Iosipescu shear test (Table 2).

The initial failure mode is cell-wall bending and fracture followed by propagation to nearby cells up to complete material separation.

In the out-of-plane crushing, the fracture plane propagates diagonally in both in-plane directions with a slightly larger component in the out-of-plane direction. This is very close to the 45° crack line in typical brittle shear failure.

In the in-plane (x) crushing, the propagation is horizontal in the out-of-plane (z) direction, while it is around 45° diagonal in the in-plane transverse (y) direction.

In the shear test, cracks appear in the foam out-of-plane direction, as cleavages between the planes of graphite. These observations showed that alignment of graphitic planes affects the behaviour of macro-cracks.

The SEM images of fracture surfaces clearly indicate that the cracks initiate at cell-walls and become cleavages between graphitic planes at the junctions. These separations propagate along and between the planes, and spread to neighbouring ligaments (Fig. 14).

These investigations give insight to the fracture mechanism in anisotropic graphitic foams.

Acknowledgements

This research was granted and funded by the European Commission Research Executive Agency under the FP7 MC ITN 'TALENT' (project grant 289161 Training for Career Development in High-Radiation Environment Technologies) and local partner Dutch Foundation for Fundamental Research on Matter (FOM).

References

[1] Klett J. Cellular ceramics: structure, manufacturing, properties and applications, chapter 2.6-carbon foams. Weinheim: WILEY-VCH Verlag GmbH & Co. KGaA; 2005. ISBN: 3-527-31320-6.
[2] Straatman AG, Gallego NC, Thompson BE, et al. Thermal characterization of porous carbon foam-convection in parallel flow. Int J Heat Mass Transfer 2006;49:1991–8.
[3] PocoGraphite. PocoGraphite Thermal Management Material - Poco HTC, 2008.
[4] Maruyama B, Spowart JE, Hooper DJ, et al. A new technique for obtaining three-dimensional structures in pitch-based carbon foams. Scripta Materialia 2006;54:1709–13.
[5] Collaboration A. The ATLAS experiment at the CERN Large Hadron Collider. J Instrum 2008;3.
[6] Klett J, Hardy R, Romine E, et al. High-thermal-conductivity, mesophase-pitch-derived carbon foams: effect of precursor on structure and properties. Carbon 2000;38:953–73.
[7] Gallego NC, Klett JW. Carbon foams for thermal management. Carbon 2003;41.
[8] Klett JW, McMillan AD, Gallego NC, et al. The role of structure on the thermal properties of graphitic foams. J Mater Sci 2004;39:3659–76.
[9] Bonad I. Thermo-mechanical characterisation of low density carbon foams and composite materials for the ATLAS upgrade PhD thesis. University of Glasgow; 2011.
[10] Sarzynski MD. Carbon foam characterization: sandwich flexure, tensile and shear response Master's thesis. Texas A&M University; 2003.
[11] Chen C, Kennel EB, Stiller AH, et al. Carbon foam derived from various precursors. Carbon 2006;44:1535–43.
[12] Gowthaman S, Shivakumar KN. An improved method of compression testing of foam materials. In: Conference Proceedings: Structural Dynamics and Material Conference, Denver, 2011.
[13] Gowthaman S, Shivakumar K, Mathiyalagan P. End-potting concept for compression testing of open-cell carbon foams. Experimental Techniques 2013.
[14] Herdcastle LE, Sheppard RG, Dingus D. US Patent 6776936: Process For Making Porous Graphite and Articles Produced Therefrom, 2004.
[15] Xavier JC, Garrido NM, Oliveira M, et al. A comparision between the Iosipescu and off-axis shear test methods for the characterization of Pinus Pinaster Ait. Composites: Part A 2004;35:827–40.
[16] Song HW, He QJ, Xie JJ, et al. Fracture mechanism and size effects in brittle metallic foams: In situ compression tests inside SEM. Compos Sci Technol 2008;68:2441–50.

Bibliography

[1] "Atomic theory". In: *UXL Encyclopedia of Science*. Ed. by A. H. Blackwell and E. P. Manar. 3rd ed. UXL, (2015).

[2] T. Jevremovic. "Atomic theory - Basic principles, evidence and examples". In: *Nuclear Principles in Engineering*. 2nd ed. Springer Science & Business Media, (2009). Chap. 2.

[3] J. Uythoven (for the LHC team). "First 13 TeV collisions: Reporting from the CCC". In: *CERN Bulletin* 22-23 (2015), pp. 1–2.

[4] CERN. *About CERN: The accelerator complex, experiments*. URL: `http://home.cern/about`.

[5] N. P. Hessey, H. Schuilenberg, and E. Hennes. "ATLAS end-cap stave upgrade plans at Nikhef". ATLAS, Technical Report. (2009).

[6] S. D. Cornell. "Petal core structures for the strips Phase-II upgrade of ATLAS". In: *Forum on Tracking Mechanics*. University of Bonn, (2016). URL: `https://indico.cern.ch/event/469996/contributions/2148106/attachments/1278026/1898068/Diez_ATLAS_strips_petals.pdf`.

[7] A. Koutoulaki. PhD thesis. University of Twente, (in preparation).

[8] M. C. Morone. "Evaluation of silicon sensors for the ATLAS silicon tracker, and TPC reconstruction in the HARP experiment". PhD thesis. University of Geneva, (2003).

[9] K. Schindl. "The injector chain for the LHC". In: *9th LEP Performance Workshop*. Chamonix, France, (1999), pp. 47–52.

[10] L. Evans. "The Large Hadron Collider". In: *Philosophical Transactions of the Royal Society A* 370 (2012), pp. 831–858.

[11] The ATLAS Collaboration. "Observation of a new particle in the search for the Standard Model Higgs boson with the ATLAS detector at the LHC". In: *Physics Letters B* 716.1 (2012), pp. 1–29.

[12] A. Castelli. "Measuring the Higgs boson mass using event-by-event uncertainties". PhD thesis. University of Amsterdam, (2015).

[13] The ATLAS Collaboration. "The ATLAS experiment at the CERN Large Hadron Collider". In: *Journal of Instrumentation* 3 (2008).

[14] N. Valencic. "Fusing the vector bosons - Higgs production through VBF and WW scattering at the current and future LHC". PhD thesis. University of Amsterdam, (2015).

[15] The ATLAS Collaboration. "Letter of intent for the Phase-II upgrade of the ATLAS experiment". CERN, Technical Report, CERN-LHCC-2012-022. (2012).

[16] The ATLAS Collaboration. "ATLAS Phase-II upgrade scoping document". CERN, Technical Report, CERN-LHCC-2015-020. (2015).

[17] CERN. *ATLAS Experiment: Detector & Technology*. URL: `https://atlas.cern/discover/detector`.

[18] C. G. Argos. "The ATLAS ITk strip detector. Status of R&D". In: *Nuclear Instruments and Methods in Physics Research Section A* 845 (2017), pp. 80–83.

[19] I. M. Gregor. "The ATLAS tracker upgrade". In: *Mass, Spectrum, Symmetry Graduate College - Block Courses*. Humboldt University of Berlin, Course Talk, (2011). URL: `https://www.physik.hu-berlin.de/de/gk1504/block-courses/autumn-2011/program_and_talks/23_2011-10_gregoringrid_paralell.pdf`.

[20] D. Lavicka and J. Knourek. "Investigation of heat transfer in the petal detector structure". In: *EPJ Web of Conferences* 114.02066 (2016).

[21] S. Tavernier. "Interactions of particles in matter". In: *Experimental Techniques in Nuclear and Particle Physics*. Springer, (2010). Chap. 2, pp. 23–32.

[22] C. Patrignani et al. (Particle Data Group). "Review of particle physics - 33. Passage of particles through matter". In: *Chinese Physics C* 40.10 (2016), p. 447.

[23] J. Klett. "Carbon foams". In: *Cellular Ceramics: Structure, Manufacturing, Properties and Applications*. Ed. by M. Scheffler and P. Colombo. 1st ed. Wiley-VCH, (2005). Chap. 2.6.

[24] PocoGraphite. *PocoGraphite thermal management material - Poco HTC*. Product datasheet. (2008). URL: `http://poco.com/Portals/0/Literature/Semiconductor/78961v3PocoHTCFlyer.pdf`.

[25] L. Warnet and R. Akkerman. "Composite Course, Lecture Notes". University of Twente. (2013).

[26] F. C. Campbell. "Introduction to composite materials". In: *Structural Composite Materials*. ASM International, (2010). Chap. 1.

[27] M. S. A. Rahaman, A. F. Ismail, and A. Mustafa. "A review of heat treatment on polyacrylonitrile fiber". In: *Polymer Degradation and Stability* 92.8 (2007), pp. 1421–1432.

[28] P. J. Walsh. "Carbon fibers". In: *ASM Handbook*. Vol. 21: Composites. ASM International, (2001). Chap. 3 Constituent Materials, pp. 35–40.

[29] Toray Industries Inc. *High-performance carbon fiber Torayca®*. Product datasheet. URL: `http://www.torayca.com/en/download/pdf/torayca.pdf`.

[30] Hexcel Corporation. *HexPly® prepreg technology*. Technical Document. (2013). URL: `https://www.ethz.ch/content/dam/ethz/special-interest/mavt/design-materials-fabrication/composite-materials-dam/Education/Manufacturing_of_Polymer_Composites/FS2017/Prepreg_Technology.pdf`.

[31] K. Majerski, B. Surowska, and J. Bienias. "Tensile properties of carbon fiber/epoxy laminates at low and room temperatures". In: *Polish Society of Composite Materials* 12.3 (2012), pp. 182–185.

[32] Tencate Advanced Composites. *TenCate BT250E-1*. Product datasheet. (2018). URL: https://www.tencatecomposites.com/media/bae1bd51-424c-4836-9698-b9a3a7fde06d/2MO8BQ/TenCate%20Advanced%20Composites/Documents/Product%20datasheets/Thermoset/UD%20tapes%20and%20prepregs/BT250E-1_Epoxy_PDS.pdf.

[33] S. Sanchez Saez et al. "Static behavior of CFRPs at low temperatures". In: *Composites Part B: Engineering* 33.5 (2002), pp. 383–390.

[34] R. M. Crane and J. W. Gillespie Jr. "Characterization of the vibration damping loss factor of glass and graphite fiber composites". In: *Composites Science and Technology* 40.4 (1991), pp. 355–375.

[35] J. Zhang, R. J. Perez, and E. J. Lavernia. "Documentation of damping capacity of metallic, ceramic and metal-matrix composite materials". In: *Journal of Materials Science* 28.9 (1993), pp. 2395–2404.

[36] E. J. Graesser and C. R. Wong. "The relationship of traditional damping measures for materials with high damping capacity". David Taylor Research Center, Technical Report, DTRC-SME-91/05. (1991).

[37] Y. Gao et al. "Modeling of the damping properties of unidirectional carbon fibre composites". In: *Polymers & Polymer Composites* 19.2 & 3 (2011), pp. 119–122.

[38] Hexcel Composites. *HexWeb^{TM} honeycomb sandwich design technology*. Technical Document. (2000). URL: http://www.hexcel.com/user_area/content_media/raw/Honeycomb_Sandwich_Design_Technology.pdf.

[39] F. E. Penado. "Effective elastic properties of honeycomb core with fiber-reinforced composite cells". In: *Open Journal of Composite Materials* 3.4 (2013), pp. 89–96.

[40] G. A. Hoffman. "Poisson's ratio for honeycomb sandwich cores". In: *Journal of the Aerospace Sciences* 25.8 (1958), pp. 534–535.

[41] A. G. Straatman et al. "Thermal characterization of porous carbon foam - convection in parallel flow". In: *International Journal of Heat and Mass Transfer* 49.11 (2006), pp. 1991–1998.

[42] B. Maruyama et al. "A new technique for obtaining three-dimensional structures in pitch-based carbon foams". In: *Scripta Materialia* 54.9 (2006), pp. 1709–1713.

[43] C. Chen et al. "Carbon foam derived from various precursors". In: *Carbon* 44.8 (2006), pp. 1535–1543.

[44] J. W. Klett et al. "The role of structure on the thermal properties of graphitic foams". In: *Journal of Materials Science* 39.11 (2004), pp. 3659–3676.

[45] N. C. Gallego and J. W. Klett. "Carbon foams for thermal management". In: *Carbon* 41.7 (2003), pp. 1461–1466.

[46] W. Shih. "Allcomp foam development experience and plan". In: *Pixel and Strip ATLAS Upgrade Mechanics Meeting*. CERN, (2010). URL: http://physics.lbl.gov/MaKaC/

getFile.py/access?contribId=27&resId=1&materialId=slides&confId=12.

[47] ERG Aerospace Corporation. *Duocel® reticulated vitreous carbon (RVC) foam*. Product Catalogue. (2017). URL: http://ergaerospace.com/wp-content/uploads/2017/08/ERG-Data-Sheets-3.pdf.

[48] K. Toptop et al. "Investigations on anisotropic fracture mechanics of graphitic foams". In: *Results in Physics* 7 (2017), pp. 2043–2053. DOI: 10.1016/j.rinp.2017.06.024.

[49] Cfoam Ltd. *Touchstone CFOAM® carbon foams*. Product datasheet. URL: http://www.cfoam.com/data-3/.

[50] W. Shih (from Allcomp). *Private communication by e-mail*. (August 2016).

[51] ERG Aerospace Corporation. *Duocel® foam materials*. URL: http://www.ergaerospace.com/index.html.

[52] J. Klett et al. "High-thermal-conductivity, mesophase-pitch-derived carbon foams: effect of precursor on structure and properties". In: *Carbon* 38.7 (2000), pp. 953–973.

[53] Mitsubishi Chemical Carbon Fiber and Composites Inc. *Pitch fiber selector guide*. URL: http://mccfc.com/pitch-fiber/.

[54] Tencate Advanced Composites. *RS-3 cyanate ester resin*. Product datasheet. (2017). URL: https://www.tencatecomposites.com/product-explorer/products/o90%7C2D/RS-3.

[55] C. Gargiulo. "Studies on composite light structures for the ALICE silicon tracker upgrade". In: *Forum on Tracking Detector Mechanics*. CERN, (2012). URL: https://indico.cern.ch/event/192033/contributions/1468436/attachments/275118/385101/Gargiulo_detector_forum_july2012.pdf.

[56] Tencate Advanced Composites. *EX-1515 resin system*. Product datasheet. (2019). URL: https://www.tencatecomposites.com/product-explorer/products/T3GL/EX-1515.

[57] N. Baral et al. "High modulus carbon fibre composites: Correlation between transverse tensile and mode I interlaminar fracture properties". In: *Materials Letters* 62.6 (2008), pp. 1096–1099.

[58] Goodfellow Co. *Polyaramid honeycomb material information*. URL: http://www.goodfellow.com/A/Polyaramid'-Honeycomb.html.

[59] Plascore Inc. *PK2 para-aramid fiber honeycomb*. Product datasheet. (2019). URL: http://www.plascore.com/download/datasheets/honeycomb_data_sheets/Plascore_PK2.pdf.

[60] Ultracor Inc. *Carbon fiber honeycomb core UCF-304-3/8-2.0*. Product datasheet. URL: http://ultracorinc.com/assets/uploads/files/files/UCF-304-3-8-2_0.pdf.

[61] Huntsman Advanced Materials. *Araldite® AY 103-1 / HY 991 low viscosity two component epoxy adhesive system*. Technical Document. (2004). URL: http://www.dawex.cz/userFiles/technicke-listy/huntsman/araldite-ay103-1hy991.pdf.

[62] Henkel Corporation Aerospace Group. *Hysol® EA9396 epoxy paste adhesive*. Technical Document. URL: http://www.chemcenters.com/images/DATA%20SHEET/EA9396%20Hysol%20Henkel%20DATA%20SHEET.pdf.

[63] Krayden Inc. *Dow® SE4445*. URL: http://krayden.com/dow-corning-se-4445/.

[64] Aubert & Duval Co. *Titanium alloy - T40*. Product datasheet. (2012). URL: http://www.ukadforge.com/wp-content/uploads/2012/09/t40_gb1.pdf.

[65] Arnold Magnetic Technologies. *Titanium Grade 2 (Commercially Pure) UNS R50400*. Product datasheet. (2017). URL: http://www.arnoldmagnetics.com/wp-content/uploads/2017/10/Arnold_SpecSheet_A4_Titanium-Grade-2_Final.pdf.

[66] Solvay. *APC-2-PEEK thermoplastic polymer*. Product datasheet. (2017). URL: https://www.solvay.com/en/product/apc-2-peek-thermoplastic-composite-tapes#product-documents.

[67] Solvay. *Torlon® 4203L polyamide-imide*. Product datasheet. (2016). URL: http://catalog.ides.com/Datasheet.aspx?I=92041&FMT=PDF&U=0&CULTURE=en-US&E=1455.

[68] G. R. Trott and A. Shorey. "Glass wafer mechanical properties: A comparison to silicon". In: *6th International Microsystems, Packaging, Assembly and Circuits Technology Conference (IMPACT)*. IEEE, (2011), pp. 359–362.

[69] S. D. Cornell (from DESY). *Private communication by e-mail*. (September 2016).

[70] H. Miyagawa et al. "Comparison of experimental and theoretical transverse elastic modulus of carbon fibers". In: *Carbon* 44.10 (2006), pp. 2002–2008.

[71] A. K. Kaw. "Micromechanical analysis of a lamina". In: *Mechanics of Composite Materials*. 2nd ed. CRC Press, (2005). Chap. 3.

[72] H. Miyagawa et al. "Transverse elastic modulus of carbon fibers measured by Raman spectroscopy". In: *Materials Science and Engineering: A* 412.1 (2005), pp. 88–92.

[73] D. Loidl et al. "Poisson ratio of carbon fibers at the microscopic and nanoscopic scale". In: *Proceedings, Carbon Conference*. Brown University, (2004).

[74] R. Haynes et al. "On plane stress and plane strain in classical lamination theory". In: *Composites Science and Technology* 127 (2016), pp. 20–27.

[75] D. Roylance. "Laminated composite plates". Massachusetts Institute of Technology, OpenCourseWare. (2000). URL: https://ocw.mit.edu/courses/materials-science-and-engineering/3-11-mechanics-of-materials-fall-1999/modules/MIT3_11F99_laminates.pdf.

[76] Wikipedia. *Sandwich Theory*. URL: https://en.wikipedia.org/wiki/Sandwich_theory.

[77] H. G. Allen. "Introduction, Sandwich beams". In: *Analysis and Design of Structural Sandwich Panels*. 1st ed. Pergamon Press, (1969). Chap. 1 & 2.

[78] B. P. Russel et al. "Quasi-static three-point bending of carbon fiber sandwich beams with square honeycomb cores". In: *Journal of Applied Mechanics* 78.3:031008 (2011).

[79] B. J. Schwarz and M. H. Richardson. "Experimental modal analysis". In: *CSI Reliability Week*. Orlando, (1999).

[80] P. Avitabile. "Experimental modal analysis, a simple non-mathematical presentation". In: *Sound and Vibration* 35.1 (2001), pp. 20–31.

[81] I. Aydıncak. “Investigation of design and analyses principles of honeycomb structures”. MA thesis. Middle East Technical University, (2007).

[82] Hexcel Corporation. *HexWeb® HRH-10 Aramid Fibre/Phenolic Honeycomb*. Product datasheet. (2017). URL: https://www.hexcel.com/user_area/content_media/raw/HexWeb_HRH10_DataSheet_eu(1).pdf.

[83] L. Poley and T. Jones. “Material studies for the ATLAS Phase-II Upgrade for the High Luminosity LHC: Carbon fibre laminae measurements and investigation of moisture expansion of an adhesive used in support structures”. In: *Forum on Tracking Detector Mechanics*. Bonn, (2016). URL: https://indico.cern.ch/event/469996/contributions/2148133/attachments/1277763/1898254/Material_Studies.pdf.

[84] G. G. Barnafoldi et al. “First report of long term measurements of the MGGL laboratory in the Mátra mountain range”. In: *Classical and Quantum Gravity* 34.11-114001 (2017).

[85] D. Santoyo. “End-cap Support Structure”. In: *Atlas Phase II Strip tracker meeting*. Valencia, (2014).

[86] S. Li et al. “The Tsai-Wu failure criterion rationalised in the context of UD composites”. In: *Composites Part A: Applied Science and Manufacturing* 102 (2017), pp. 207–217.

[87] S. K. Nammi, P. Myler, and G. Edwards. “Finite element analysis of closed-cell aluminium foam under quasi-static loading”. In: *Materials and Design* 31.2 (2010), pp. 712–722.

[88] Y. X. Gan, C. Chen, and Y. P. Shen. “Three-dimensional modeling of the mechanical property of linearly elastic open cell foams”. In: *International Journal of Solids and Structures* 42.26 (2005), pp. 6628–6642.

[89] S. Santosa and T. Wierzbicki. “On the modeling of crush behavior of a closed-cell aluminum foam structure”. In: *J. Mech. Phys. Solids* 46.4 (1998), pp. 645–669.

[90] S. A. Meguid, S. S. Cheon, and N. El-Abbasi. “FE modelling of deformation localization in metallic foams”. In: *Finite Elements in Analysis and Design* 38.7 (2002), pp. 631–643.

[91] A. Czekanski, M. A. Elbestawi, and S. A. Meguid. “On the FE modeling of closed-cell aluminum foam”. In: *International Journal of Mechanics and Materials in Design* 2 (2005), pp. 23–34.

[92] M. De Giorgi et al. “Aluminium foams structural modelling”. In: *Computers and Structures* 88.1 (2010), pp. 25–35.

[93] W. Y. Jang, A. M. Kraynik, and S. Kyriakides. “On the microstructure of open-cell foams and its effect on elastic properties”. In: *International Journal of Solids and Structures* 45.7 (2008), pp. 1845–1875.

[94] M. Gilchriese et al. “Carbon foam measurements and comparison to FEA”. In: *Local Support Working Group (LSWG) - Mechanics*. LBNL. (2011) (Limited Access). URL: https://indico.cern.ch/event/155345/contributions/1396735/attachments/167226/235898/Carbon_Fiber_Measurements_and_Parameters.pdf.

[95] M. Kırca et al. “Computational modeling of micro-cellular carbon foams”. In: *Finite Elements in Analysis and Design* 44.1 (2007), pp. 45–52.

[96] J. Lamontie et al. “Modeling the principle physical parameters of graphite carbon foam”. In: *Carbon* 48.9 (2010), pp. 2418–2424.

[97] I. Bonad. “Thermo-mechanical characterisation of low density carbon foams and composite materials for the ATLAS upgrade”. PhD thesis. University of Glasgow, (2011).

[98] S. Sihn and A. K. Roy. “Modeling and prediction of bulk properties of open-cell carbon foam”. In: *Journal of Mechanics and Physics of Solids* 52.1 (2004), pp. 167–191.

[99] S. Choi and B. V. Sankar. “Fracture toughness of carbon foam”. In: *Journal of Composite Materials* 37.23 (2003), pp. 2101–2116.

[100] W. B. Miller (from Allcomp). *Private communication by e-mail*. (April 2018).

[101] H. W. Song et al. “Fracture mechanisms and size effects of brittle metallic foams: In situ compression tests inside SEM”. In: *Composites Science and Technology* 68.12 (2008), pp. 2441–2450.

[102] Entegris Inc. “Properties and characteristics of graphite”. Technical Document. (2013).

[103] I. E. Berinskii and F. M. Borodich. “Elastic in-plane properties of 2D linearized models of graphene”. In: *Mechanics of Materials* 62 (2013), pp. 60–68.

[104] E. Andrews, W. Sanders, and L. J. Gibson. “Compressive and tensile behavior of aluminum foams”. In: *Materials Science and Engineering: A* 270.2 (1999), pp. 113–124.

[105] D. Joyce. “The unit tangent vector and curvature, Math 131 Multivariate Calculus”. Clark University, Lecture Note. (2014). URL: `https://mathcs.clarku.edu/~djoyce/ma131/curvature.pdf`.

[106] D. Roylance. “Transformation of stresses and strains”. Massachusetts Institute of Technology, Lecture Notes. (2001). URL: `http://web.mit.edu/course/3/3.11/www/modules/trans.pdf`.

[107] C. G. J. Vreedenburgh. “The shell with double curvature considered as a plate on an elastic foundation”. In: *Heron* 10.1 (1962).

[108] K. M. Ryu et al. “Mechanical modeling of Al-Mg alloy open-cell foams”. In: *Materials Transactions* 46.3 (2005), pp. 622–625.

[109] J. Doherty and M. Fahey. “Three-dimensional finite element analysis of the direct simple shear test”. In: *Computers and Geotechnics* 38.7 (2011), pp. 917–924.

[110] A. Muc. “Interlaminar failure and buckling of doubly-curved laminated composite shells”. In: *Mechanics of Composite Materials* 31.3 (1995), pp. 238–246.

[111] A. P. Roberts and E. J. Garboczi. “Elastic moduli of model random three-dimensional closed-cell cellular solids”. In: *Acta Materialia* 49.2 (2001), pp. 189–197.

[112] J. Galicki and M. Czech. “A new approach to formulate the general strength theories for anisotropic discontinuous materials. Part A: The experimental base for a new approach to formulate the general strength theories for anisotropic materials on the basis of wood”. In: *Applied Mathematical Modelling* 37.3 (2013), pp. 815–827.

[113] E. E. Gdoutos, I. M. Daniel, and K. A. Wang. "Multiaxial characterization and modeling of a PVC cellular foam". In: *Journal of Thermoplastic Composite Materials* 14.5 (2001), pp. 365–373.

[114] I. M. Daniel and O. Ishai. "Strength of unidirectional lamina - Interactive tensor polynomial theory (Tsai-Wu)". In: *Engineering Mechanics of Composite Materials*. Oxford University Press, (1994). Chap. 4, pp. 118–119.

[115] M. Akbulut and F. O. Sonmez. "Design optimization of laminated composites using a new variant of simulated annealing". In: *Computers & Structures* 89.17 (2011), pp. 1712–1724.

[116] R. Bates and T. Jones. "Material studies for HL-LHC strip stave design". In: *Forum on Tracking Detector Mechanics*. Oxford, (2013). URL: `https://indico.cern.ch/event/233332/contributions/1546104/attachments/388984/540994/MaterialsTalk.pdf`.

[117] E. R. Naimon, W. F. Weston, and H. M. Ledbetter. "Elastic properties of two titanium alloys at low temperatures". In: *Cryogenics* 14.5 (1974), pp. 246–249.

[118] P. Hidnert. "Thermal expansion of Titanium". In: *Journal of Research of the National Bureau of Standards* 30 (1943), pp. 101–105.

[119] M. Gupta. "Calculation of radiation length in materials". CERN, Technical Report, PH-EP-Tech-Note-2010-013. (2010). URL: `https://cds.cern.ch/record/1279627`.

[120] Y. Sugano et al. "Novel cyanate ester compound, flame-retardant resin composition, and cured product thereof". Pat. US20050182203A1. Mitsubishi Gas Chemical Co. Inc. (2005).

[121] K. K. Chang. "Aramid fibers". In: *ASM Handbook*. Vol. 21: Composites. ASM International, (2001). Chap. 3 Constituent Materials, pp. 41–45.

[122] M. Sohoni. "Phenolic resins". In: *Polymer Data Handbook*. Oxford University Press, (1999), pp. 239–244.

[123] C. E. Lin et al. "Poly(m-phenylene isophthalamide) (PMIA): A potential polymer for breaking through the selectivity-permeability trade-off for ultrafiltration membranes". In: *Journal of Membrane Science* 518 (2016), pp. 72–78.

[124] R. F. Lane et al. "Bisphenol diglycidyl ethers and bisphenol A and their hydrolysis in drinking water". In: *Water Research* 72 (2015), pp. 331–339.

[125] J. R. Fried. "Poly(ether ether ketone)". In: *Polymer Data Handbook*. Oxford University Press, (1999), p. 466.

[126] C. L. Kirk and S. M. Wiedemann. "Natural frequencies and mode shapes of a free-free beam with large end masses". In: *Journal of Sound and Vibration* 254.5 (2002), pp. 939–949.

[127] S. E. Motaghian, M. Mofid, and P. Alanjari. "Exact solution to free vibration of beams partially supported by an elastic foundation". In: *Scientia Iranica* 18.4 (2011), pp. 861–866.

Summary

This dissertation aims to create a solid knowledge base regarding design issues in the ATLAS Inner Tracker, and presents technical information to be used in the design of the detector support structures. Studies are primarily based on computations conducted on developed finite element analysis (FEA) models. Experimental studies have been performed to confront the computational results for some cases. Overall, this research deals with three topics related to each other. The first subject is to improve the ATLAS Petal design in terms of its radiation length. The second subject focuses on the fracture mechanics of graphitic carbon-foam and its micro-scale computational model. The results of this model is then used to derive a macro-scale i.e. continuum model for a carbon-foam. The third topic investigates the foam-tube structure —an essential element of the Petal in terms of cooling performance— regarding the structural risks, and checks whether any fracture may occur.

Currently, the Large Hadron Collider (LHC) is operating. It is planned to be shut down in 2019 for improvements, and reoperate with higher luminosities (i.e. collisions per unit time). New conditions brought a need for replacing the entire innermost subsystem of the ATLAS detector, the Inner Detector, with a far higher radiation tolerant construction. In addition, new construction should minimise multiple scattering of the charged particles and other particle-matter interactions to increase accuracy in the reconstruction of particle trajectories. Both requirements can be achieved by reducing the fractional radiation length $\%X_0$ of the detectors, detector supports and services. Since detectors and electronics are not very flexible to reconfigure, most of the effort to lower $\%X_0$ is focused on the design of supports. Reducing $\%X_0$ simply means using low atomic number materials, such as carbon, and minimising the amount of all materials used. At the same time, supports must be rigid to prevent detector motion which would deteriorate the precision of position measurements of particles, setting a lower limit to material reduction.

The thermo-mechanical support units carrying detector modules are known as Petals. The petal is a sandwich structure, made of high-modulus thin facings glued on both sides of a light core material. The petals cool the detector modules with evaporative CO_2 flow in a tube surrounded by carbon foam and embedded in the Petal's core. While the facings and the core are essential elements for the structural rigidity, the tube-foam structure and the facings are prime elements to cool detectors.

The petal design was reduced to a rectangular sandwich beam model in combination

with composite theory, and its three-point bending stiffness was formulated. The formula was used to compare two different prepregs with two different angular configurations for the facings along with varying core shear properties. Fig. 1 gives the longitudinal bending stiffness of the sandwich beam versus core shear modulus.

The current petal configuration (Nikhef LoI design) uses facings made of 3 plies of a 80 gsm K13D2U/RS3 unidirectional prepreg laid up in $[60/0/-60]^\circ$ angles from the petal longitudinal axis, and Nomex honeycomb core.

The target is to improve the bending stiffness, while reducing weight to reduce the radiation length of the structure. The angular configuration was replaced with $[0/90/0]^\circ$, which almost doubled the longitudinal bending stiffness. The improvement in the facing rigidity allows thinner facings to be used, therefore 45 gsm K13C2U/EX1515 prepreg was used. Core shear modulus has a diminishing contribution to the bending stiffness; therefore it is not the predominant factor in determining bending stiffness of the petal beyond a specific modulus. After about 70 MPa shear modulus, there is little improvement for the recommended facesheet material (continuous red line). Therefore, Plascore Kevlar honeycomb was chosen as an available core material on the market offering a moderate modulus (about 70 MPa) and a lighter structure.

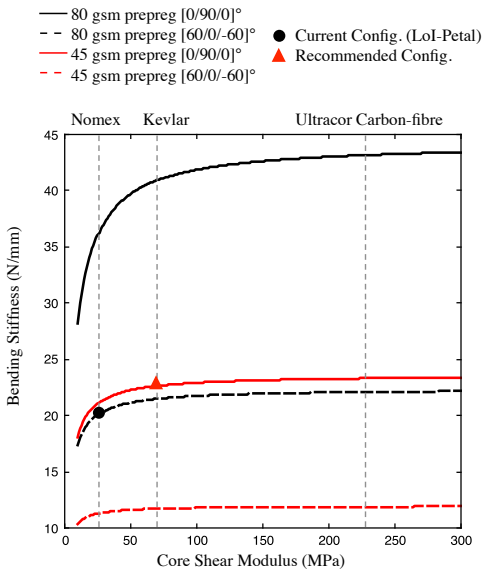

Fig. 1: Three-point bending stiffness versus core shear modulus in the panel longitudinal direction. Vertical dashed-lines correspond to available core materials of interest. Filled-markers indicate the current and recommended material configurations.

A FEA model of the Nikhef Petal prototype (LoI-design) was developed, which predicts the bending stiffness and the lowest modal frequencies within 5 % agreement with the measurements. Later, this model was applied to the petal designed by the DESY group (LTF-design, which is the actual product being used for the future ATLAS tracker) and used to evaluate improvements resulting from the above material recommendations.

The recommended configuration gives a significant reduction in mass of about 30 g, resulting in 16 % improvement in the fractional radiation length for the base petal. Through the analyses on the petal with conditions for use in the ATLAS detector (i.e. with modules mounted and constrained to the End-cap frame), the lowest natural frequency was evaluated at 64 Hz in the longitudinal bending mode, with a 5 %

improvement.

Graphitic carbon foam is used to transfer heat from electronics mounted on the facings of the petal to the cooling tube. The thermal contraction of the tube will exert forces on the carbon-foam. Early oversimplified calculations predicted fracture in the foam, and mechanical damage in the tube-foam interface can have adverse impacts on thermal transportation through the structure and its long-term reliability. This brought a need for a detailed study of fracture mechanics of the foam, and a FEA model of the tube-foam structure to further investigate this issue.

A series of destructive tests were performed to study fracture mechanics of Poco-HTC graphitic foam in compression and shear cases. The destructive compression (crush) tests were carried out in both out-of-plane and in-plane directions of the foam to characterise anisotropy. These tests were filmed to visually examine crack initiation and propagation at macro-scale.

The initial failure mode is cell-wall bending fracture (called Mode-I) followed by propagation to nearby cells up to complete material separation. Fig. 2 shows the crack lines for both crushing tests. In the out-of-plane (z) crushing, the fracture plane propagates diagonally in both in-plane directions (x and y) with a slightly larger component in the out-of-plane direction. This is very close to the 45° crack line in typical brittle shear failure. In the in-plane (x) crushing, the propagation is horizontal in the out-of-plane direction (z), while it is around 45° diagonal in the in-plane transverse (y) direction.

In the shear test (zx), cracks appear in the foam out-of-plane direction, as cleavages. These cleavages are probably due to separation of graphitic layers as a result of shear forces, and propagate along the planes. These observations showed that alignment of graphitic planes affects the behaviour of macro-cracks.

Then, scanning electron microscopy (SEM) images of fracture surfaces were recorded to examine post-failure formation of material at micro- and meso-scales. The SEM images indicate that the cracks initiate at cell-walls, becoming cleavages between graphitic planes at the junctions. These separations propagate along the planes and spread to neighbouring ligaments.

In another series of tests, cyclic compressive loads were applied in the elastic regime to characterise the elastic behaviour, such as measuring Young's modulus and elastic limits. Also, strengths were measured by subjecting some samples to continuous compression load up to destruction after the cyclic test.

Poco-HTC shows highly anisotropic behaviour in both the elastic and fracture cases. Measurements showed that the local fractures start at 3.0 and 1.5 MPa, and strengths are 5.3 and 3.5 MPa in the out-of-plane and in-plane directions. The Young's modulus was measured 113 and 75 MPa in the same directions. The shear strength is 1.8 MPa, measured with the Iosipescu shear test.

A computational micro-model for the porous graphite foam was developed to reproduce measured behaviour. The aim of the research was to improve existing models by taking

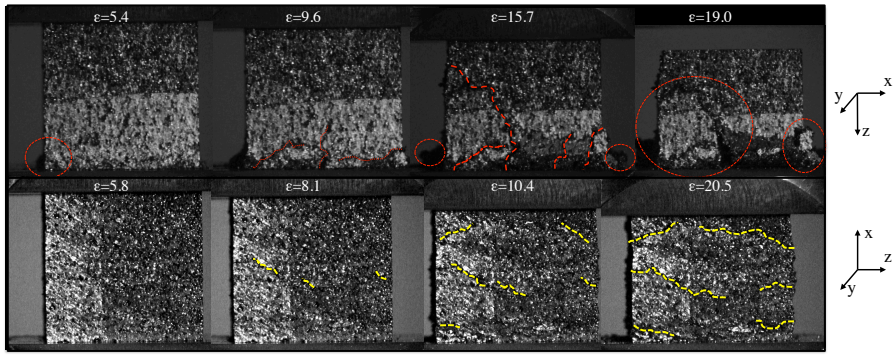

Fig. 2: Failure initiation and growth during compression tests (out-of-plane in upper row and in-plane in bottom row). The compression direction is from up to down. Stress and strain (ε) increase from left to right. Red dashed lines highlight the crack paths in the out-of-plane case; ovals highlight the material separation. Yellow dashed lines highlight regions of cell collapse in the in-plane case, which propagate sideways. Direction of the foam is given with x, y and z-axis at sides.

local anisotropy and material failure into account. A geometric model was obtained by taking a prolate spheroid bubble as the unit-cell, and placing many cells in an enclosed volume via computer script by targeting a certain porosity. The cell dimensions were selected to match measurements on various Poco-HTC samples. Thus, topological anisotropy and cell irregularity were accounted. The generated geometry was discretized to small elements, and material directions (alignment of graphitic planes) were defined in each to introduce local anisotropy to predict macroscopic anisotropy. Here, plane orientations at each elements were formulated based on the wall formation of the nearest bubble. Failure criteria for finite elements are included in the model to predict strength. In-plane loads and curvatures result in a static loading term in the plane normal direction. A factor (called static bending moment factor) directly proportional to this static term was used to model cell-wall bending fracture, Mode-I, for linear static analysis case.

Fig. 3 gives the stress-strain graph for the crushing tests and analyses. The analyses predicted stress-strain characteristics relatively close to the measurements in both directions. The predicted compressive modulus in the in-plane direction was smaller than the measured values, leading to a higher foam elastic anisotropy. The predicted strength values in both directions were in good agreement with the measured ones, suggesting that the failure model works for the compression case. Increasing the foam edge size reduces the micro-structural effects and gives a higher in-plane modulus, bringing the prediction closer to the measurement. Although the anisotropy model shows weaknesses in predicting bulk elastic anisotropy and failure responses, the method presented here sufficiently extends current foam models, and gives a good basis for future work. Failure analysis was performed with an external code due to computational limits. If the failure model can be used within the finite element model, this could improve

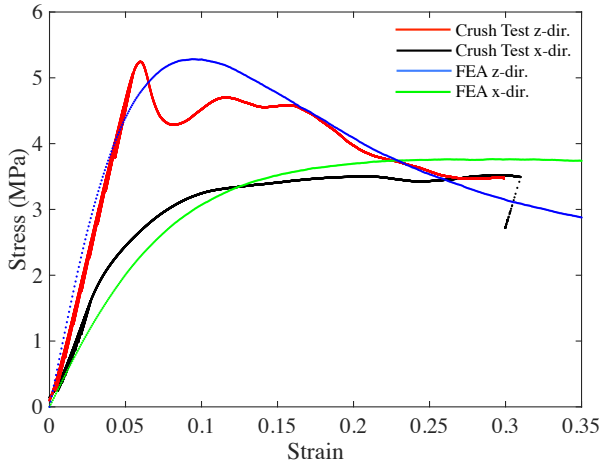

Fig. 3: Stress-strain graph for crushing tests and analyses, performed in both directions, i.e. out-of-plane or z-direction, and in-plane or x-direction. The foam is stiffer and stronger in the z-direction.

prediction accuracy.

The elastic constants found from measurements and computations with a micro-scale foam model were used to construct a macro-scale continuum model of the foam. This continuum model was used in a thermo-mechanical FEA model of the tube-foam structure to evaluate if any fracture occurs. According to analysis for a 60°C temperature drop, the current configuration of the structure is not expected to fracture, and will reliably maintain the performance.

Samenvatting

Dit proefschrift heeft als doelstelling het creëren van een gedegen basiskennis over vraagstukken rondom het ontwerp van de ATLAS Inner Tracker, en presenteert technische informatie die ingezet kan worden voor het ontwerpen van de detector ondersteunende structuren. Onderzoeken zijn voornamelijk gebaseerd op berekeningen gemaakt met behulp van ontwikkelde Finite Element Analysis (FEA) modellen. Experimenten zijn uitgevoerd om de berekeningen voor sommige casussen te confronteren. In zijn totaliteit behandelt dit onderzoek drie met elkaar in verbinding staande onderwerpen. Het eerste onderwerp gaat over het verbeteren van het ATLAS Petal ontwerp op het gebied van stralingslengte. Het tweede onderwerp legt nadruk op de breukmechanica van grafiet koolstofschuim en bijbehorend micro-schaal rekenmodel. De resultaten van dit model werden vervolgens gebruikt om een macro-schaal af te leiden, namelijk een continuüm model voor koolstofschuim. Het derde onderwerp onderzoekt de structuur van de buis-schuim - een essentieel element van de Petal op het gebied van koelfunctie - met betrekking tot de structurele risico's, en bekijkt of er breuken kunnen voorkomen.

Op dit moment is de Large Hadron Collider (LHC) operationeel. Deze zal in 2019 stilgelegd worden voor verbeteringen en is gepland om weer te openen met hogere lichtsterkte (botsingen per eenheid tijd). Nieuwe omstandigheden brachten de noodzaak van het vervangen van het gehele binnenste subsysteem van de ATLAS detector, de Inner detector, door een constructie die beter bestand is tegen veel hogere straling, met zich mee. Daarnaast zou nieuwe constructie het verspreiden van verstrooiing van de geladen deeltjes en andere deeltjes-materie interacties minimaliseren, om nauwkeurigheid bij het reconstrueren van deeltjestrajecten te verhogen. Beide eisen kunnen bereikt worden door te verminderen de fractionele stralingslengte $\%X_0$ van de detectoren, detector ondersteuning en diensten. Aangezien detectoren en elektronica niet erg flexibel zijn voor het configuratie is het meeste van de poging $\%X_0$ te verlagen, gericht op het ontwerp van ondersteuning. Vermindering van $\%X_0$ betekent simpelweg het gebruik van materialen met lage atomische waarden zoals koolstof, en het minimaliseren van de hoeveelheid van alle gebruikte materialen. Tegelijkertijd moet ondersteuning rigide zijn om detector beweging, die de precisie van positiemetingen van deeltjes kan verslechteren, te voorkomen, daarbij een lager limiet aan materiaalreductie in te stellen.

De thermo-mechanische ondersteuningseenheden die de detector modules bevatten worden Petal genoemd. Een petal is een sandwich structuur, gemaakt van hoge modulus dun beplatingsmateriaal dat aan beide zijden van een licht kern materiaal gelijmd is. De petal verkoelen de detector modules door middel van een verdampende CO_2 stroom

in een buis omhuld met koolstofschuim, in het midden van het Petal's kern. Hoewel de beplating en de kern essentiële elementen voor de structurele stevigheid zijn, de buis-schuim structuur en de buitenbeplating zijn de primaire elementen om detectoren te koelen.

Het petal ontwerp werd verkleind tot een rechthoekig sandwich-balk model in combinatie met composiet theorie, en de driepunts buigstijfheid werd geformuleerd. De formule werd gebruikt om twee verschillende geïmpregneerde vezels met twee verschillende hoekige configuraties voor de beplating samen met verscheidene kern schuif eigenschappen te vergelijken. Fig. 1 geeft de buigstijfheid in de lengte van de sandwich-balk versus de kern's schuifmodulus weer.

De huidige petal configuratie (Nikhef Lol ontwerpen) maakt gebruik van beplatingen bestaande uit 3 lagen van 80 gsm K13D2U/RS3 unidirectionele geïmpregneerde vezels, in hoeken gelegd op $[60/0/-60]^\circ$ van het petal's lengteas, en Nomex honingraat kern.

Het doel is het verbeteren van de buigstijfheid, daarbij gewicht verminderen om de stralingslengte van de structuur te verminderen. De hoek instelling werd vervangen door $[0/90/0]^\circ$, dat de lengte buigstijfheid bijna verdubbelde. De verbetering van de buitenstevigheid staat het gebruik van dunnere beplatingsmateriaal toe, daarom worden 45 gsm K13C2U/EX1515 geïmpregneerde vezels gebruikt. De kern schuifmodulus levert een afnemende bijdrage aan de buigstijfheid; daarom is het niet de meest hoofdzakelijke factor bij het bepalen van buigstijfheid van de petal voorbij een specifieke modulus. Na ongeveer 70 MPa schuifmodulus is er weinig verbetering in het aanbevolen beplatingsmateriaal (doorlopende rode lijn). Daarom kiezen we een Plascore Kevlar honingraat als een in de markt beschikbaar kernmateriaal dat een gemiddelde modulus (ongeveer 70 MPa) biedt en een lichtere structuur heeft.

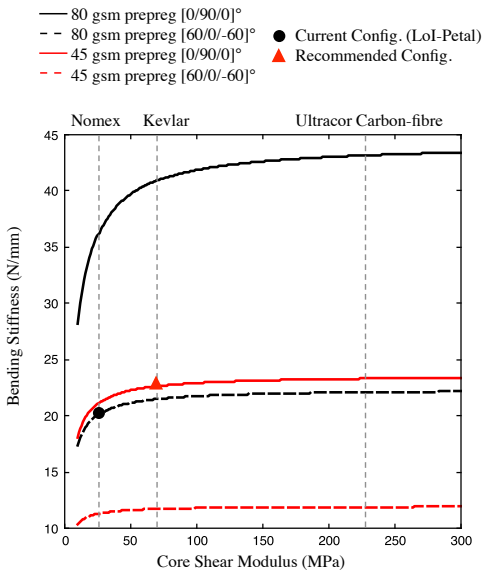

Fig. 1: Driepunts buigstijfheid versus kern schuifmodulus in de lengte van het paneel. Verticale stippellijnen geven beschikbare interessante kern materialen weer. Gevulde punt geven de huidige en aanbevolen materiaal configuraties weer.

Een FEA model van het Nikhef Petal prototype (Lol-ontwerpen) werd ontwikkeld, welke de buigstijfheid en de laagste modale frequenties binnen een 5 % overeenkomst met de metingen voorspelt. Later werd dit model toegepast op het petal ontwerp van

de DESY groep (LTF-ontwerp, het echte product dat gebruikt wordt voor de toekomstige ATLAS tracker) en gebruikt om verbeteringen die uit de bovenstaande materiaal aanbevelingen voortkomen te evalueren.

De aanbevolen configuratie geeft een aanzienlijke massareductie van ongeveer 30 g, resulterend in een verbetering van 16 % van de fractionele stralingslengte voor de basis van het petal. Door analyze van het petal, met instellingen voor gebruik in de ATLAS detector (met modules gemonteerd aan, en gefixeerd op het End-cap frame), werd de laagste natuurlijke frequentie waargenomen op 64 Hz in de lengtebuigings modus, met een verbetering van 5 %.

Grafiet koolstofschuim wordt gebruikt om hitte van de elektronica die op de petal gemonteerd is naar de koelbuis te verplaatsen. De thermische krimp van de buis zal kracht uit oefenen op het koolstofschuim. Eerdere simplistische berekeningen voorspelden breuk in het schuim, en mechanische schade aan het buis-schuim raakvlak kan nadelige effecten hebben op thermische geleiding door de structuur en de betrouwbaarheid ervan op lange termijn. Dit bracht de noodzaak van gedetailleerde studie naar de breukmechanica van het schuim, en een FEA model van de buis-schuim structuur met zich mee om dit vraagstuk verder te onderzoeken.

Een serie van destructieve testen werden gedaan om breukmechanica van Poco-HTC grafietschuim in gevallen van compressie en afschuiving te bestuderen. De destructieve drukproeven werden uitgevoerd in zowel evenwijdige als loodrechte richtingen van het schuim om anisotropische kenmerken vast te stellen. Deze testen werden gefilmd om scheurvorming en verspreiding op macro-schaal visueel te onderzoeken.

De initiële faal modus is celwand breuk door buiging (Mode-I genoemd) gevolgd door verspreiding naar omliggende cellen tot complete scheiding van materiaal. Fig. 2 laat de breuklijnen van beide drukproeven zien. Bij de loodrechte (z) drukproef verspreidt het breukvlak diagonaal in beide evenwijdige richtingen (x and y) met een enigsinds groter gedeelte in de loodrechte richting. Dit is heel dicht bij de 45° breuklijn in typisch broos afschuiving falen. Bij de evenwijdige (x) drukproef is de verspreiding horizontaal in de loodrechte richting (z), terwijl het rond de 45° diagonaal in de evenwijdige dwarsrichting (y) is.

Bij de schuifspanningstest (zx) verschijnen barsten, als spleten, in de loodrechte richting van het schuim. Deze spleten worden waarschijnlijk veroorzaakt door scheiding van de grafietlagen als resultaat van schuifkrachten en verspreiden over de vlakken. Deze waarnemingen lieten zien dat uitlijning van grafietlagen het gedrag van macro-barsten beïnvloedt.

Daarna werden Scan Elektronenmicroscopie (SEM) beelden van breukvlakken opgenomen om materiaalformatie na het falen te analyseren op micro en meso-schalen. De SEM beelden tonen aan dat de breuken beginnen in celwanden en grote spleten tussen grafietlagen op de knooppunten worden. Deze scheidingen vermeerderen langs de lagen en spreiden naar aangrenzende celwanden.

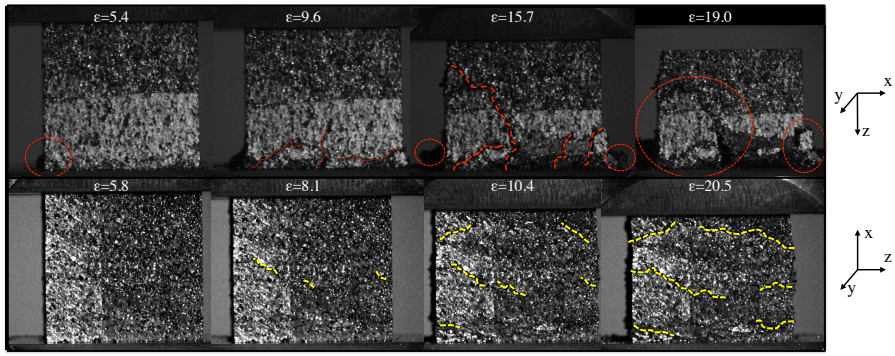

Fig. 2: Begin van het falen en de groei gedurende drukproeven (loodrecht in de bovenste rij en evenwijdig in de onderste rij). De drukrichting is van boven naar beneden. Drukspanning en rek (ε) vermeerderen van links naar rechts. Rode stippellijnen benadrukken de barstpatronen in het loodrechte geval; ovalen geven de materiaalscheiding weer. Gele stippellijnen benadrukken de gebieden van celinstorting die zich zijdelings verspreiden, in het evenwijdige geval. Richting van het schuim is weergegeven door middel van x, y en z-assen aan de zijkanten.

Gedurende een andere serie testen werden cyclische drukkrachten toegepast in het elastische regime om het elastische gedrag in kaart te brengen, zoals het meten van Young's modulus en elastische limieten. Ook werden druksterkte gemeten door enkele monsters na de cyclische test aan doorlopende drukkrachten bloot te stellen tot vernietiging volgde.

Poco-HTC laat zeer anisotropisch gedrag zien in zowel de elastische als de breuk gevallen. Metingen toonden aan dat de lokale breuken starten bij 3.0 en 1.5 MPa en krachten zijn 5.3 en 3.5 MPa in de loodrechte en evenwijdige richtingen. De Young's modulus werd gemeten op 113 en 75 MPa in dezelfde richtingen. De schuifsterkte is 1.8 MPa, gemeten met de Iosipescu methode.

Een rekenkundig micro model voor poreus grafietschuim werd ontwikkeld om gemeten gedrag te herberekenen. Het doel van het onderzoek was bestaande modellen te verbeteren door lokale anisotropie en materiaalfalen mee te omvatten. Een geometrisch model werd bereikt door een prolate sferoïde zeepbel als de eenheidscel te nemen, en veel cellen in een gesloten volume te plaatsen via een computerscript door een bepaalde poreusheid te richten. De celdimensies werden geselecteerd op basis van metingen van verscheidene Poco-HTC monsters. Dus, topologische anisotropie en cel onregelmatigheid werden omvatten. De gegenereerde geometrie werd gediskretizeerd tot kleine elementen, en materiaalrichtingen (uitlijning van grafietlagen) werden in elke gedefinieerd om lokale anisotropie te introduceren om macroscopische anisotropie te voorspellen. Daarbij werden lagenrichtingen van elk element geformuleerd gebaseerd op de wandformatie van de meest nabije zeepbel. Criteria van falen van eindige elementen zijn opgenomen in het model om kracht te voorspellen. Evenwijdige druklast in het lagenrichting en kromming resulteren in een statische drukladings waarde in de

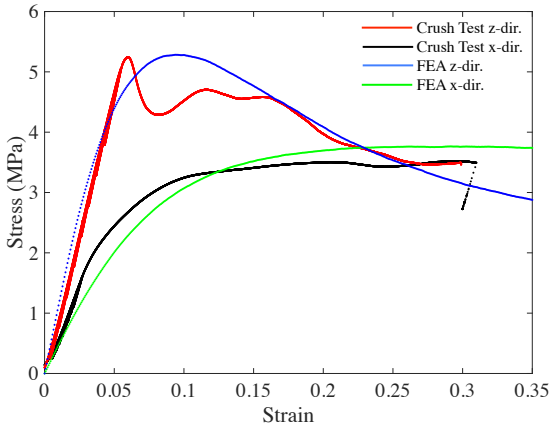

Fig. 3: Drukspanning en rek grafiek van de drukproeven en analyses, gedaan in beide richtingen, bv. loodrecht ofwel z-richting en evenwijdig ofwel x-richting. Het schuim is stijver en sterker in de z-richting.

normale richting van het lagen. Een factor (genaamd statisch buigmoment factor) in directe verhouding met deze statische waarde werd gebruikt om de celwand buigbreuk te simuleren, Mode-I, voor lineaire statische analyse.

Fig. 3 geeft de drukspanning en rek grafiek van de drukproeven en analyses weer. De analyses voorspelden drukspanning en rek relatief dicht bij de metingen in beide richtingen. De voorspelde drukmodulus in de evenwijdige richting was kleiner dan de gemeten waarden waardoor een hogere schuim elastische anisotropie ontstond. De voorspelde krachtwaarden in beide richtingen waren in goede overeenkomst met de gemeten waarden, hetgeen suggereert dat het model voor falen succesvol is in het geval van druk. Het vergroten van de schuimrand vermindert de micro-structurele effecten en produceert een hogere evenwijdige modulus, daarmee de voorspelling dichter bij de meting brengend. Hoewel het anisotropie model zwakke punten bevat bij de voorspelling van bulk elastische anisotropie en reacties op falen, de hier gepresenteerde methode breidt huidige schuimmodellen voldoende uit en is een goede basis voor toekomstig werk. Breukanalyse werd uitgevoerd met een externe code vanwege rekenkundige limieten. Als het breukmodel gebruikt kan worden binnen het eindige elementen model, zou dit voorspellingsaccuraatheid kunnen verbeteren.

De elastische constanten die gevonden werden door metingen en berekingen met een micro-schaal schuimmodel werden gebruikt om een macro-schaal continuum model voor het schuim te ontwikkelen. Dit continuum model werd gebruikt in een thermisch-mechanisch FEA model van de buis-schuim structuur om te beoordelen of er breuken voorkomen. Volgens analyse van een 60°C temperatuursdaling is een breuk in de huidige configuratie van de structuur niet te verwachten en zal de prestatie betrouwbaar kunnen volhouden.

Acknowledgements

The last few years have been the most intense years of my life. I have gained various experiences and new capabilities. Of all these experiences, the most special one was the training I received to become an independent research engineer. At the end of this challenging but incredibly valuable journey, I am about to receive my PhD degree. In this stage, I would like to finish my dissertation by thanking all the people without whom I would not come to this point.

First of all, I owe my deepest gratitude to my supervisors: prof. dr. ing. Bob van Eijk and dr. Nigel P. Hessey.

Nigel, I am very grateful for your support since the beginning until the end of my PhD program. You guided the program, led me into the correct path, and had valuable contributions to my research in terms of technical aspects. Even though you moved to another country for a new job, you did not leave me alone and kept supporting me.

Bob, we did not start the program together, but eventually, our paths have crossed. Thank you for taking charge of my research program and helping me to reach the finish line. Hence I am grateful for your contributions to the dissertation. I had lots of ups and downs during the PhD program. I would like to extend special thanks to both of you for keeping me in line by motivating and focusing me through the program.

I would also like to thank prof. dr. ir. Ton van den Boogaard, prof. dr. ir. Marcel ter Brake, prof. dr. Auke-Pieter Colijn, prof. dr. Gerhard Raven, dr. ir. Bert Geijselaers, dr. ir. Arnoud van der Stelt and dr. Frank Cadoux for being in my doctorate committee, sparing time to read my thesis and providing me with important comments, which helped me to improve it further.

I would like to give special thanks to dr. ir. Bert Geijselaers for helping me during the experiments and for his valuable contributions in the publication entitled *'Investigations on anisotropic fracture mechanics of graphitic foams'*. I also appreciate the help of ing. Bert Vos and dr. ir. Laurent Warnet in preparing the test set-ups in the University of Twente. I also want to thank dr. ir. Timo Meinders for being my supervisor during the first year of the program and for initiating the research. It was unfortunate that we could not work together afterwards.

I can not forget two names from the Nikhef. I am grateful for your help, Mr. Geritt Brouwer and Mr. Joop Rovekamp, with the technical works in the facilities and in the Nikhef laboratories. Dr. Heinz Pernegger and Mrs. Hanna Poikela, I appreciate both

of your support in this research program and for providing contact between me and CERN.

During my PhD, I have met with great colleagues making ground office floor a social area. Panos, Afroditi, Stergios and Rolf, I am very pleased with your social support. Especially thank you, Afroditi, for sharing an office with me more than four years without any complaints.

Leaving my hometown and beginning a new life abroad was never easy for me. I would like to thank Okan and Gerben for being good life coaches during my life in Amsterdam. Moreover, BAUISC sailing club with its members has always been a good friend for me when I went back to my home city Istanbul; I am glad for your long-standing friendship.

I can not forget my MSc program supervisor dr. Kamuran Kadıpaşaoğlu, who has been a good educator prior to PhD program. He taught me most of the things I know about how to conduct a research independently and prepared me for this PhD program.

Lastly, but most importantly, I am grateful to my family for their life-long support and always being with me to solve problems whenever I needed.

Koral Toptop, Amsterdam, March 2019.